

# Degenerate Bose Gases: Tuning Interactions & Geometry

---

**Alexander Lloyd Gaunt**  
Trinity College, October 2014

A dissertation submitted for the  
degree of Doctor of Philosophy



Cavendish Laboratory

# Declaration

I declare that this thesis is my own work and is not substantially the same as any that I have submitted or am currently submitting for a degree, diploma or any other qualification at any other university. No part of this thesis has already been or is being concurrently submitted for any such degree, diploma or any other qualification. This thesis does not exceed the word limit of sixty thousand words, including tables, footnotes, bibliography and appendices, set out by the Faculty of Physics and Chemistry.

2014 Alex Gaunt

Cavendish Laboratory  
University of Cambridge  
J J Thomson Avenue  
Cambridge CB3 0HE  
UK

# Abstract

This thesis describes experiments carried out on a dilute cloud of Bosonic atoms cooled to quantum degeneracy. It is divided into two parts: Part I describes experiments in which we tune the inter-particle interactions to explore the system's dynamics in both weakly and strongly interacting limits. Part II describes novel optical trapping geometries for cold atomic gases, with an emphasis on the first ever realisation of an atomic Bose-Einstein condensate in a uniform potential.

Part I employs a method in which inter-particle interactions in a nanokelvin gas of  $^{39}\text{K}$  atoms are tuned via a Feshbach resonance. Using this technique we explore the non-equilibrium dynamics of a weakly interacting Bose-condensed gas in a dissipative system. The highlight of this study is the observation of a “superheated” Bose-Einstein condensate persisting at temperatures up to 1.5 times higher than the equilibrium critical temperature. In a second study, we investigate the opposite regime of maximal interaction strength (the “unitary” regime). Here we experimentally demonstrate scaling laws governing the dynamics of clouds undergoing atom loss and heating by multi-particle collisions.

In Part II, we demonstrate holographic techniques for shaping laser beams to produce new atom trap geometries. We concentrate on the theoretically important and experimentally novel uniform geometry and review our first experiments performed in this system. In equilibrium we study both the thermodynamics of a homogeneous  $^{87}\text{Rb}$  gas held in our novel trap and perform spectroscopic measurements of its ground-state. In a dynamical study we investigate the coherence properties of a Bose-Einstein condensate formed after a rapid thermal quench of a homogeneous gas. We observe Kibble-Zurek dynamics following this quench, and are able to make the first measurement of the dynamical critical exponent for the 3D Bose-Einstein condensation transition using our homogeneous system.



# Acknowledgements

“Writing is difficult: only some people are good at it.” This diplomatic phrase posited by a wise man rings in my ears as I struggle to eloquently pen my heartfelt gratitude to the people who have supported me over the last three years. My Ph.D. has taught me that where the pen can stutter, the keyboard can triumph. Therefore I will attempt to forego the unfamiliar world of vocabulary, sentence structure and punctuation by distilling my gratitude into a more manageable Excel bar chart.

Fig. 0.1 shows the average flux of emails that I received from contemporaneous lab members normalised to a reference flux from my wife, Beth. This bar chart provides a good starting point for objectively dividing my acknowledgements among the key characters who helped me with the work presented in this thesis<sup>1</sup>.

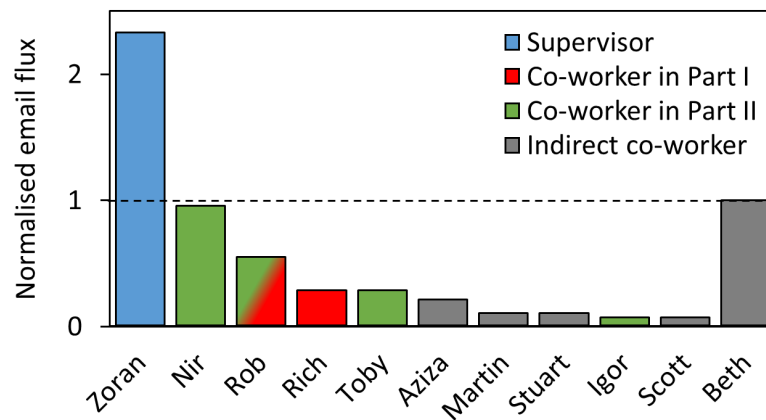


**Fig. 0.1.:** Normalised email flux from lab members. We count the total number of emails received from each lab member and divide by the overlap time with my Ph.D. For reference, the resulting fluxes are normalised to that from my wife, Beth.

Zoran's unerring dedication and enthusiasm irrefutably shines out of Fig. 0.1. As my supervisor, his active influence and impact on every aspect of the lab's progress is exemplified by the only score greater than unity. An analysis of the length and depth of the emails is beyond the scope of this thesis, but I am certain that Zoran would

<sup>1</sup>In my analysis of this data I will mitigate any potential offense by mentioning systematic errors arising from the use of email volume as a metric for gratitude.

again claim victory in these statistics. There is nothing more reassuring for a Ph.D. student than knowing that your supervisor is always available with deeply insightful comments on the experiments. Furthermore, Zoran has gone out of his way to support the progress of my career and I am truly grateful to Zoran for everything that he has done to help me over the years.

The next highest bars in Fig. 0.1 are the postdocs, Rob Smith and Nir Navon, who were directly involved in the experiments presented in this thesis. Rob's contribution is vastly under-represented in Fig. 0.1. As a man of quiet brilliance, he exemplifies the systematic problem with the email metric. His uncanny ability to understand everything and make anything work, has been pivotal to every success in this thesis. Nir has injected great enthusiasm and "rock and roll" into the lab. As one of the most badass physicists in the group, he played an essential role in the uniform-system experiments, and was a key antagonist in the on-going dialogue concerning the quality of my software, PIDs, and general persona.

I have been proud to be part of a motley band of Ph.D. students alongside Richard Fletcher, Tobias Schmidutz and Igor Gotlibovych. Rich formed part of the original Dream Team and many happy nights were spent watching cartoons as we super-heated some BECs. A lot of thanks have to go to Tobias and Igor (as a strong but silent type, Igor's contribution is again underestimated by the email tally). Their months of hard work (including an unfortunate incident involving my laser and a drill) meant that I could hit the ground running in Part II of this thesis. Thanks also go to the former members of the lab, Naaman Tammuz, Robbie Campbell, Stuart Moulder and Scott Beattie who built the machine used in Part I of this thesis.

Aziza Suleymanzade and Martin Robert-de-Saint-Vincent have been busy working on experiments which are not covered in this thesis, but their presence has completed the daily life that I have enjoyed in the group. Regardless of experimental allocation, all group members (including the Ghost) are bonded by TheQuiz, and it has been a pleasure to MC TheQuiz for such an enthusiastic bunch of budding historians.

Finally, even though "working from home doesn't count", I have been supported outside the lab by my parents, Mary and Stephen, my siblings, Jo and Steph and my wife Beth. Beth's contribution to this work is difficult to overstate. Without her concern for my well-being, I would have rapidly devolved into a cave-dwelling creature surviving solely on Cherryade and prawn cocktail crisps. Her unerring optimism that I will one day share her delight in a picturesque sunset or a bright rainbow and her contagious enthusiasm for life infinitely brighten up my life outside the lab. I am truly grateful to her for being my companion through everything.

# Contents

<b>Outline</b>	<b>1</b>
<b>I Tuneable Interactions</b>	<b>5</b>
<b>1 Introduction</b>	<b>7</b>
1.1 Tuneable s-wave scattering . . . . .	7
1.2 Producing $^{39}\text{K}$ condensates . . . . .	11
1.3 Extreme interactions . . . . .	12
<b>2 A Superheated Bose-condensed Gas</b>	<b>15</b>
2.1 Qualitative picture . . . . .	16
2.2 Experimental procedure . . . . .	20
2.3 Experimentally measuring chemical potentials . . . . .	21
2.4 Observation of a superheated state . . . . .	28
2.5 Dynamical model of superheating . . . . .	31
2.6 Limits of superheating . . . . .	36
2.7 Conclusion . . . . .	38
<b>3 Stability of a Unitary Bose Gas</b>	<b>39</b>
3.1 Can a unitary bose gas be stable at degeneracy? . . . . .	41
3.2 Scaling Law 1: $NT^\beta = \text{const.}$ . . . . .	43
3.3 Scaling Law 2: $L_3 \propto 1/T^2$ at unitarity . . . . .	50
3.4 Extraction of the rate parameter $\zeta$ . . . . .	51
3.5 Conclusion . . . . .	53
<b>II Trap Geometry</b>	<b>55</b>
<b>4 Introduction</b>	<b>57</b>
4.1 Atom-light interactions . . . . .	58
4.2 Outline . . . . .	63
<b>5 Robust Digital Holography for Ultracold Atom Trapping</b>	<b>65</b>
5.1 Digital holography . . . . .	66
5.2 Vector-holography . . . . .	68
5.3 Raster-holography . . . . .	72
5.4 Conclusion . . . . .	75

<b>6 Bose-Einstein Condensation of Atoms in a Uniform Potential</b>	<b>77</b>
6.1 Building an optical box . . . . .	78
6.2 First realisation with atoms . . . . .	86
6.3 Conclusion . . . . .	96
<b>7 Observing Equilibrium Properties of a Homogeneous Bose Gas</b>	<b>97</b>
7.1 Thermodynamic experiments . . . . .	97
7.2 Ground state measurements . . . . .	105
7.3 Conclusion . . . . .	115
<b>8 Critical Dynamics of Spontaneous Symmetry Breaking in a Homogeneous Bose gas</b>	<b>117</b>
8.1 Domain size in Kibble-Zurek theory . . . . .	118
8.2 Quantitative measurement of domain sizes . . . . .	122
8.3 Direct observation of Kibble-Zurek freeze-out . . . . .	131
8.4 Kibble-Zurek scaling and universal critical exponents . . . . .	136
8.5 Conclusion . . . . .	138
<b>9 Conclusions and Outlook</b>	<b>139</b>
9.1 Thermodynamics with tuneable interactions . . . . .	139
9.2 Kibble-Zurek with tuneable interactions . . . . .	140
9.3 Interferometry . . . . .	140
<b>Appendices</b>	<b>145</b>
<b>A Experimental Sequence Overview</b>	<b>147</b>
A.1 Rubidium-87 $D_2$ Lines . . . . .	147
<b>B Raster Holography</b>	<b>151</b>
B.1 MRAF: Mixed-region amplitude freedom . . . . .	151
B.2 Optical vortices . . . . .	152
B.3 Experimental realisation with laser light . . . . .	154
B.4 Fourier vs Helmholtz . . . . .	155
<b>C Graphics Card Acceleration of Computations for Ultracold Atom Experiments</b>	<b>159</b>
C.1 Image processing: AnalysisGpUI . . . . .	160
C.2 Physical simulation: EvolveGPuE . . . . .	162
<b>D Numerical Simulation of Kibble-Zurek Dynamics</b>	<b>167</b>
D.1 Dynamical evolution of $\xi$ . . . . .	167
D.2 Simulation results . . . . .	169
<b>Bibliography</b>	<b>173</b>

# Outline

Single atoms are well understood quantum objects. However, when a macroscopic number of interacting atoms come together, an exact treatment of the ensemble can become impossible. The fundamental difficulty with many-body quantum mechanics stems from the exponential scaling of the system's Hilbert space with particle number<sup>2</sup>. Some analytical and computational methods such as the mean-field approximation or Monte-Carlo techniques allow us to probe weakly interacting systems. However, *strongly* interacting many-body systems are at the heart of many of the most fascinating and least understood phenomena in modern physics, ranging from high temperature superconductivity and superfluidity to exotic forms of magnetism. Moreover, we are often interested in dynamical effects in out-of-equilibrium systems, which can again be difficult to describe exactly with theory.

One fruitful approach to understand many-body quantum systems is to use experimental rather than theoretical simulations, as envisioned by Feynmann in 1982 [1, 2]. This is the route pursued here, where we use an experimental simulator based on an ultracold atomic gas cloud. A "quantum simulator" is simply a very clean quantum system which is easily accessed and tuned in the laboratory. The dynamic and static properties of our simulator are defined by a many-body Hamiltonian over which we have excellent control. By observing the behaviour of our simulation as we tune the parameters of the Hamiltonian, we can probe the many-body physics of our system, and any other quantum system described by the same Hamiltonian.

At the core of our experimental simulator is a dilute gas of ultracold Bosonic atoms. In Einstein's textbook picture of a 3D Bose gas (discussed in detail in chapter 7), this system undergoes a phase transition to form a Bose-Einstein condensate (BEC) at the critical point  $n\lambda_T^3 \approx 2.612$ , where  $n$  is the atom density and  $\lambda_T$  is the thermal

---

<sup>2</sup>The intractability of macroscopic quantum systems is best exemplified by trying to write down an exact description of a state, even before we start to tackle any evolution. Whereas in the classical case, recording the 3D position and velocity of  $N$  particles requires only  $6N$  real numbers, to write the state vector for a quantum system containing  $N$  distinguishable particles occupying  $M$  levels in an arbitrary superposition requires  $M^N$  complex numbers. Computationally, if we have 1 GB of computer RAM, this means we can store a classical state containing  $N \sim 10^7$  particles, but only the state of  $N \approx 26$  particles in the simplest  $M = 2$  level system.

wavelength<sup>3</sup>. Below the critical temperature, the characteristic wavepacket size,  $\lambda_T$ , is larger than the interparticle spacing,  $n^{-1/3}$ , meaning quantum effects dominate and our simulator probes many body quantum mechanics.

In general, the anatomy of a many-body Hamiltonian,  $\hat{H}$ , to be simulated in our experiments is as follows:

$$\hat{H} = \underbrace{\hat{H}_{\text{Kin}}}_{\text{Kinetic energy}} + \underbrace{\hat{H}_{\text{Int}}}_{\text{Interaction energy}} + \underbrace{\hat{H}_{\text{Pot}}}_{\text{Potential energy}} . \quad (0.1)$$

An essential property of a useful quantum simulator is the ability to implement custom Hamiltonians,  $\hat{H}$  in the lab. Dilute atomic gases fulfil this requirement because the response of the individual atoms to electromagnetic fields is well understood. This allows us to use a toolbox of magnetic and optical techniques to synthesise tailored Hamiltonians, and for a dilute Bose gas, any of the three terms in Eq. 0.1 can be experimentally tuned<sup>4</sup>. This thesis describes techniques for tuning the last two terms in Eq. 0.1: the interaction term,  $\hat{H}_{\text{Int}}$ , and the potential term,  $\hat{H}_{\text{Pot}}$ . We then explore the phenomenon of Bose-Einstein condensation in the unconventional Hamiltonians that we produce. The thesis is divided into two parts, each of which concentrates on tuning one term, as summarised below.

	Interactions	Potential Geometry	Species
Part I	<b>Tuneable</b>	Traditional harmonic	<sup>39</sup> K
Part II	Fixed	<b>Uniform</b>	<sup>87</sup> Rb
Outlook	<b>Tuneable</b>	<b>Uniform</b>	<sup>39</sup> K

**Tab. 0.1.:** Summary of the emphasis throughout the thesis. A different machine is used for each part with specialisations to handle new interaction regimes or geometries. In the outlook section, we briefly comment on the prospect of a new machine which combines these research strands.

## Part I: $H_{\text{Int}}$ - Tuneable interactions

Since the presence of inter-particle interactions poses many theoretical difficulties in many body quantum physics, it is extremely useful to experimentally tune the interactions and empirically explore the resulting physics. The ability to tune inter-particle interactions in ultracold gases is unparalleled in other systems, and the first half of this thesis will be dedicated to exploring Bose gases in the two extremes of

<sup>3</sup>The ideal value 2.612 is modified slightly in finite-size and interacting systems [3, 4]

<sup>4</sup>The kinetic energy term is not strictly tuneable, however using synthetic gauge fields [5–7], or by trapping the atoms in a lattice, we can modify the dispersion relation of our Bose gas.

interaction strength: In chapter 2, we will explore a very weakly interacting system, and demonstrate a novel non-equilibrium state of a “superheated Bose condensed gas”. In chapter 3, we study the opposite limit where the interaction strength is the maximum allowed by quantum mechanics. This strong coupling limit is particularly interesting because the behaviour of the system ceases to depend on the nature of the interactions and universal behaviour emerges.

## Part II: $H_{\text{Pot}}$ - Flexible geometries

Perhaps the most intuitive term to change in the Hamiltonian is  $\hat{H}_{\text{Pot}}$ . The geometry of the potential energy landscape can play a key role in the physics displayed by a system. By sculpting appropriate potentials for our atoms, we can create race tracks for superfluids [8–10], lattices to model solid-state materials [11–13], and many other interesting geometries. In chapter 5, we present two very versatile optical methods for creating custom atom traps, and demonstrate experimental realisation of high-quality, intricate trapping potentials using these techniques. The development of this optical toolbox inspired us to create one of the most long-sought, and theoretically simplest, potentials: a homogeneous box potential. This potential is abundant in theoretical work because it often offers the simplest understanding of many-body phenomena, and is appropriate for describing several naturally occurring many-body systems. However, this potential is difficult to achieve in experiments with atomic gases. In chapter 6, we overcome these difficulties and present the first realisation of an atomic BEC in a three-dimensional homogeneous potential, and in chapters 7 and 8 we outline the first equilibrium and dynamical results from the fruitful research paths that our uniform trap has opened up.

The following publications are derived from work presented in this thesis:

## Part I

### Chapter 2 **A Superheated Bose-condensed Gas**

A. L. Gaunt\*, R. J. Fletcher\*, R. P. Smith and Z. Hadzibabic

*Nature Phys.* **9**, 271-274 (2013).

### Chapter 3 **Stability of a Unitary Bose Gas**

R. J. Fletcher, A. L. Gaunt, N. Navon, R. P. Smith and Z. Hadzibabic

*Phys. Rev. Lett.* **111**, 125303 (2013).

## Part II

### Chapter 5 **Robust Digital Holography For Ultracold Atom Trapping**

A. L. Gaunt and Z. Hadzibabic

*Sci. Rep.* **2**, 721 (2012).

### Chapter 6 **Bose-Einstein Condensation of Atoms in a Uniform Potential**

A. L. Gaunt, T. F. Schmidutz, I. Gotlibovych, R. P. Smith, and Z. Hadzibabic

*Phys. Rev. Lett.* **110**, 200406 (2013).

### Chapter 7 **Quantum Joule-Thomson Effect in a Saturated Homogeneous Bose Gas**

T. F. Schmidutz, I. Gotlibovych, A. L. Gaunt, R. P. Smith, N. Navon and Z. Hadzibabic

*Phys. Rev. Lett.* **112**, 040403 (2014).

### Chapter 7 **Observing properties of an interacting homogeneous Bose-Einstein condensate: Heisenberg-limited momentum spread, interaction energy, and free-expansion dynamics**

I. Gotlibovych, T. F. Schmidutz, A. L. Gaunt, N. Navon, R. P. Smith, and Z. Hadzibabic

*Phys. Rev. A* **89**, 061604(R) (2014).

### Chapter 8 **Critical Dynamics of Spontaneous Symmetry Breaking in a Homogeneous Bose gas**

N. Navon\*, A. L. Gaunt\*, R. P. Smith, and Z. Hadzibabic

*Science* (in press) (2015).

# Part I

---

Tuneable Interactions



# Introduction

Ultracold atoms, and in particular BECs of atoms, give us a unique opportunity to experimentally access many-body physics in different limits of inter-particle interaction strength. The ability to continuously tune the interaction strength makes cold atom systems both insightful simulators of less accessible quantum systems, and also interesting quantum systems in their own right.

Chapters 2 and 3 will separately detail our experiments exploring two opposite regimes of very weak and very strong interactions. Throughout these chapters we attempt to highlight novel physical phenomena without reviewing an undue volume of background theory. In particular, an understanding of standard methods of laser and evaporative cooling [14] is not required to understand the results in these chapters (the novel stages of the experiments start *after* a degenerate cloud has been prepared). Therefore we have attempted to limit the discussion of the cooling stage of the experiment into section 1.2 and Fig. 1.2. An short pictorial synopsis of the basic steps for laser cooling can also be found in Appendix A.

Aside from the cooling process, another textbook concept, which underpins the novel aspects of these experiments, is the phenomenon of Feshbach resonances. This phenomenon provides the mechanism by which we tune the inter-atomic interactions. Since this is of central importance in our work, we devote a short section below to outlining the basic theory of inter-atomic interactions and Feshbach resonances.

## 1.1 Tuneable s-wave scattering

In order to understand Feshbach resonances, we must first clarify exactly what we mean by "inter-atomic interactions". Below, we briefly describe how the potentially complex process of one atom scattering off another can be entirely characterised by a single parameter known as the s-wave scattering length,  $a$ . We then move on to describe how a Feshbach resonance can be used to tune  $a$ .

### 1.1.1 s-wave scattering

One could set about the daunting task of writing down a very detailed microscopic model for the the Van der Waals interaction between neutral bosonic atoms. However,

we often work in the dilute regime where the typical length scale,  $r_{\text{int}}$ , of the interaction potential is much smaller than the other length scales in the gas (namely the mean distance between atoms,  $n^{-1/3}$ , and the thermal wavelength,  $\lambda_T$ ). This means that the microscopic properties of the interaction potentials are largely irrelevant for describing physical phenomena in an ensemble. In this section, we outline the standard formalism which coarse-grains these microscopic details into a single parameter [3, 15, 16].

The first step of this formalism is to solve the Schrödinger equation,  $(\nabla^2 + k^2)\psi = \frac{2m_r V(\mathbf{r})}{\hbar^2}\psi$ , in relative coordinates,  $\mathbf{r}$ , for the wavefunction  $\psi$  describing the relative motion of two colliding particles with energy  $E$  and reduced mass  $m_r$  in a general interaction potential,  $V$  (note that we have defined  $k = \sqrt{2m_r E/\hbar^2}$ ). Using the Green's function for the Helmholtz operator  $(\nabla^2 + k^2)$ , and applying the first order Born approximation, the solution is as follows<sup>1</sup>:

$$\psi(\mathbf{r}) \approx \underbrace{\phi_{\mathbf{k}}(\mathbf{r})}_{\text{incident}} + \frac{e^{ikr}}{r} \underbrace{\left[ -\frac{m_r}{2\pi\hbar^2} \int e^{-ik\hat{\mathbf{r}}\cdot\mathbf{r}'} V(\mathbf{r}') \phi_{\mathbf{k}}(\mathbf{r}') d^3\mathbf{r}' \right]}_{\text{scattered}}, \quad (1.1)$$

where  $\phi_{\mathbf{k}} = e^{i\mathbf{k}\cdot\mathbf{r}}$  is the particles' wavefunction before the scattering event and  $\hat{\mathbf{r}} = \mathbf{r}/|\mathbf{r}|$ . We can now make the following simplifications:

- The angular momentum of a pair of atoms colliding with impact parameter  $R$  is  $hR/\lambda_{\text{dB}}$  where  $\lambda_{\text{dB}}$  is the deBroglie wavelength associated with the relative motion. In a thermal ensemble at temperature  $T$ , we write  $\lambda_{\text{dB}} \sim \lambda_T$ , where  $\lambda_T$  is the thermal wavelength of the atoms. At degeneracy,  $\lambda_T \sim n^{-1/3}$ , and for the colliding particles to interact, we require  $R < r_{\text{int}}$ . Since we assume  $r_{\text{int}} \ll n^{-1/3}$ , we conclude that  $hR/\lambda_{\text{dB}} \ll h$ , and thus that the colliding pair's angular momentum is small [14]. This means that the amplitude of the scattered spherical wave must be a function,  $f(k)$ , with no angular dependence. This limit is known as the s-wave scattering limit, with higher order angular terms only significant for clouds at  $k_B T > \hbar^2/2mr_{\text{int}}^2 \sim k_B \times 100 \mu\text{K}$ .

For  $k \rightarrow 0$ , we can expand  $1/f(k) = -1/a + bk + \mathcal{O}(k^2)$ , with suitable coefficients  $a$  and  $b$ . In the simplest case ( $|ka| \ll 1$ ), we take  $f(k) = -a$ , thereby reducing the entire scattering problem to the single parameter,  $a$ , known as the

<sup>1</sup>To see this qualitatively, note that the Schrödinger equation is identical to the optical Helmholtz equation with a source term  $\propto V\psi$ . By analogy with Huygens' wavelets and Fraunhofer diffraction, we quote that the far-field solution to this Schrödinger equation is a spherical wave with amplitude proportional to the Fourier transform of this source term. Since the source term explicitly contains  $\psi$  itself, we use the first order Born approximation,  $\psi \approx \phi_{\mathbf{k}}$  to obtain Eq. 1.1.

“s-wave scattering length”. We will return to the second term in this expansion in chapter 3.

- Eq. 1.1 states that the amplitude of the scattered wave is proportional to the Fourier transform of  $V$ . Since  $r_{\text{int}}$  is the smallest length scale in the scattering problem,  $V$  has a very broad Fourier spectrum, which can be treated as a constant for experimentally relevant  $k$ . Therefore, regardless of the true microscopic details of  $V$ , we obtain good results using a delta-function pseudo-potential  $V(\mathbf{r}) = V_0\delta(\mathbf{r})$ .

Using these simplifications in Eq. 1.1, we find:

$$V_0 = \frac{4\pi\hbar^2 a}{m}, \quad (1.2)$$

where we have used  $m_r = m/2$  for atoms of mass  $m$ . Importantly, in this expression, both the sign and magnitude of the scattering potential have been parameterised in terms of a single number,  $a$ .

### 1.1.2 Feshbach resonances

Experimental tuning of  $a$  is achieved by the phenomenon of Feshbach resonances [17]. Feshbach resonances arise from spin-dependent terms in the interaction potential which couple different spin states during elastic scattering. The details of this mechanism are provided below.

When two alkali atoms are brought close together, their atomic orbitals overlap and start to form a molecular orbital. If the (fermionic) electrons in the atom are in a symmetric spin-triplet state, this molecular orbital must be spatially antisymmetric, and the converse is true for electrons in antisymmetric spin-singlet states. Since the spatially symmetric and antisymmetric orbitals experience different degrees of attraction to the nuclei, their energies are different. This means that there is a spin-dependent exchange term  $\chi(r)\mathbf{S}_1 \cdot \mathbf{S}_2$  in the scattering Hamiltonian, which splits the energy depending on the alignment of the electron spins  $\mathbf{S}_1$  and  $\mathbf{S}_2$  ( $\chi$  captures the dependence of this term on inter-atomic separation). The total Hamiltonian,  $H$ , for the two atoms can then be written:

$$H = H_{\text{hf},Z}^1 + H_{\text{hf},Z}^2 + \chi(r)\mathbf{S}_1 \cdot \mathbf{S}_2 + H_{\text{VdW}}(r), \quad (1.3)$$

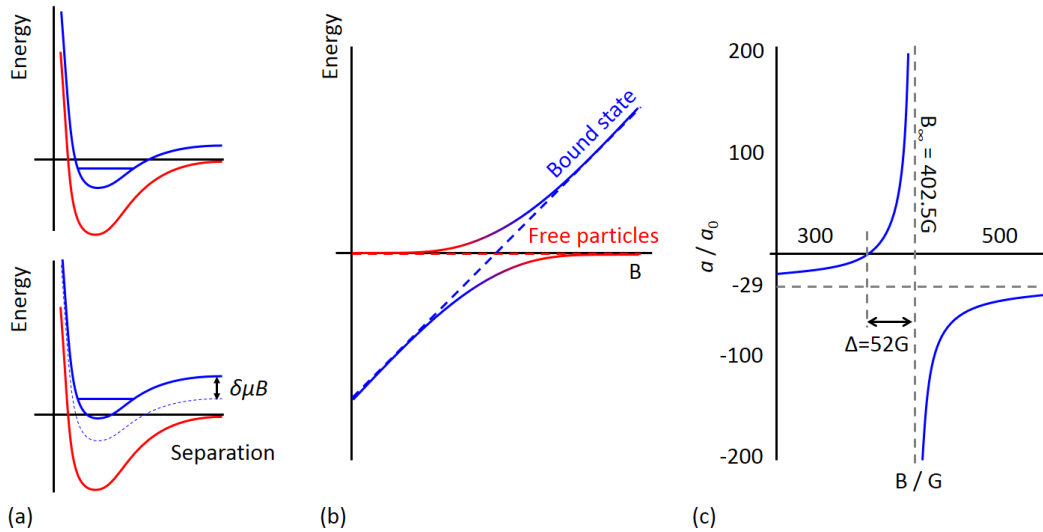


**Fig. 1.1.:** Using a Feshbach resonance to tune the s-wave scattering length. (a) Interaction potential for two states of definite  $F$  at large separation. The red curve shows the incident "open" channel, and the blue curve is the "closed" channel containing a bound state (horizontal line). Using a magnetic field,  $B$ , we can tune the bound state above or below the free particle energy (since the different  $F$  states have a differential magnetic moment,  $\delta\mu$ ). (b) The bound state energy (blue) with respect to the free particle energy (red) as a function of  $B$  at fixed particle separation. The dotted lines show the energy ignoring coupling between these states, and the solid lines show the coupled states. (c) Second-order perturbation theory for the full scattering event gives a resonance in the scattering length when the bound state energy equals the free particle energy. We illustrate the parameters of this resonance for  $^{39}\text{K}$  atoms in the  $|F, m_F\rangle = |1, 1\rangle$  state.

where  $H_{\text{hf,Z}}^i$  are the hyperfine and Zeeman terms for the  $i^{\text{th}}$  atom, and  $H_{\text{vdW}}$  contains any spin-independent parts of the Van der Waals interaction. For large separations,  $\chi$  is small and the spin coupling is a perturbation on the separate eigenstates of the hyperfine terms. For small separations,  $\chi$  dominates, and the hyperfine terms are perturbations to the singlet and triplet eigenstates.

Now suppose we have a collision between two atoms which are both in the hyperfine state  $|F, m_F\rangle$  at large separation. The  $S_1 \cdot S_2$  term is not diagonal in the hyperfine basis, and therefore, can couple different hyperfine states and cause transitions between them. The symmetry of the Hamiltonian means that the total projection of the angular momentum on a quantisation axis is conserved, but  $F$  can change during a scattering event. At low temperatures ( $k_B T \ll$  the hyperfine splitting), spontaneous increases in  $F$  are energetically forbidden. This means that there may be a "closed" channel of higher  $F$  which the atoms cannot make a real transition to.

The closed channel may contain one or more bound states (Fig. 1.1(a)), and even if a real transition to these states is energetically forbidden, a *virtual* transition can be made during a scattering event. This is a second order process (transition in to and then back out of the bound state), and we diagrammatically illustrate the resulting

energy shift in Fig. 1.1(b). We can include this energy shift as an effective change,  $\delta a$ , in the scattering pseudo-potential parameterised by  $a$ . Analytically, we write the magnitude of the shift using the familiar second order perturbation theory "energy denominator" to obtain [3, 18, 19]:

$$\delta a \propto \frac{1}{E - E_{\text{bs}}}, \quad (1.4)$$

where  $E$  is the incident energy and  $E_{\text{bs}}$  is the energy of the virtual bound state. Since the incident and virtual states have different magnetic moments (they have different  $F$ ), the (linear) Zeeman effect allows us to write the energy denominator in terms of an external magnetic field  $B$ :

$$\delta a(B) = -\frac{\Delta}{B - B_{\infty}}, \quad (1.5)$$

where  $B_{\infty}$  is the resonant magnetic field and  $\Delta$  is called the width of the resonance<sup>2</sup>. We plot this form in Fig. 1.1(c) where it is clear that the scattering length can be tuned to any value by varying an external  $B$ .

## 1.2 Producing <sup>39</sup>K condensates

To harness the mechanism in the previous section, we need to work with a species which has a suitably broad Feshbach resonance at an experimentally accessible magnetic field strength. <sup>39</sup>K fits these criteria and is the species which we will use throughout the first part of this thesis. Unfortunately, despite all of its attractive properties, <sup>39</sup>K is comparatively difficult to cool to degeneracy. The methods to overcome this problem are now standard in our lab [24–26], and we describe them only briefly here.

The difficulties with cooling <sup>39</sup>K are:

1. *Standard* sub-Doppler laser cooling techniques are ineffective for <sup>39</sup>K (due to the poorly resolved hyperfine structure in the excited electronic state). This makes the starting conditions for evaporative cooling unfavourable.
2. Evaporative cooling relies on the inter-atomic interactions to continuously re-equilibrate the gas to lower temperatures as we remove the highest energy

---

<sup>2</sup>In our experiment, we use <sup>39</sup>K atoms in the  $|F, m_F\rangle = |1, 1\rangle$  state. In this case,  $\Delta = 52$  G, and  $B_{\infty} = 402.5$  G [20–23]

atoms. Alongside the Feshbach shift,  $\delta a(B)$ , each atomic species has a background scattering length,  $a_{\text{bg}}$  such that  $a = a_{\text{bg}} + \delta a(B)$ . Unfortunately,  $a_{\text{bg}} = -29 a_0$  for  $^{39}\text{K}$  [23] (where  $a_0$  is the Bohr radius). This means that potassium is a very weakly interacting gas at  $B = 0$ , which makes conventional evaporative cooling in low-field magnetic traps inefficient. Moreover, even if a BEC could be achieved by standard low field evaporation, the negative scattering length means it would be unstable against collapse [3, 27–29].

A combination of these two facts makes  $^{39}\text{K}$  comparatively hard to cool to degeneracy. While these problems can in principle be overcome, and both sub-Doppler cooling of K and direct evaporation of this species to degeneracy have recently been reported [30–32] (see also chapter 9), we take a different approach, originally inspired by [20]. We use an easy-to-cool gas of  $^{87}\text{Rb}$  to sympathetically cool  $^{39}\text{K}$  down to a point ( $\sim 5 \mu\text{K}$ ) where we can effectively trap it in a standard optical dipole trap. In the dipole trap, we can exploit the Feshbach resonance to tune  $a$  to a large positive value ( $135 a_0$ ). We finally achieve condensation by standard evaporative cooling at this high scattering length. The stages of this cooling are schematically outlined in Fig. 1.2. Further details of the apparatus can be found in the PhD theses of Robert Campbell [25], Naaman Tammuz [26] and Stuart Moulder [33], who, along with post-doctoral researchers Scott Beattie and Robert Smith, are credited with the construction of most of the setup. Since all the novel experiments described in the following two chapters start after the cooling process has been completed, we will not include technical details of the inherited apparatus here and instead direct the reader towards the builders' theses for description beyond the schematic presented in 1.2.

### 1.3 Extreme interactions

The two experiments discussed in the first part of this thesis concentrate the extremes of a very weakly interacting and very strongly interacting gas:

In chapter 2 we will tune the interactions to sufficiently small values to observe a gas far from equilibrium. By stalling the transfer of atoms between the condensate and its thermal surroundings, we will prevent the decay of the BEC even as the system rises above the critical temperature. We refer to this BEC stranded above the critical temperature as a "superheated" BEC.

In chapter 3, we tune the interactions to the opposite regime, where the gas is as strongly interacting as quantum mechanics allows. In this so-called "unitary" limit, we can probe universal physics which is hard to describe theoretically. In this limit, collisions involving more than two particles become more frequent and can

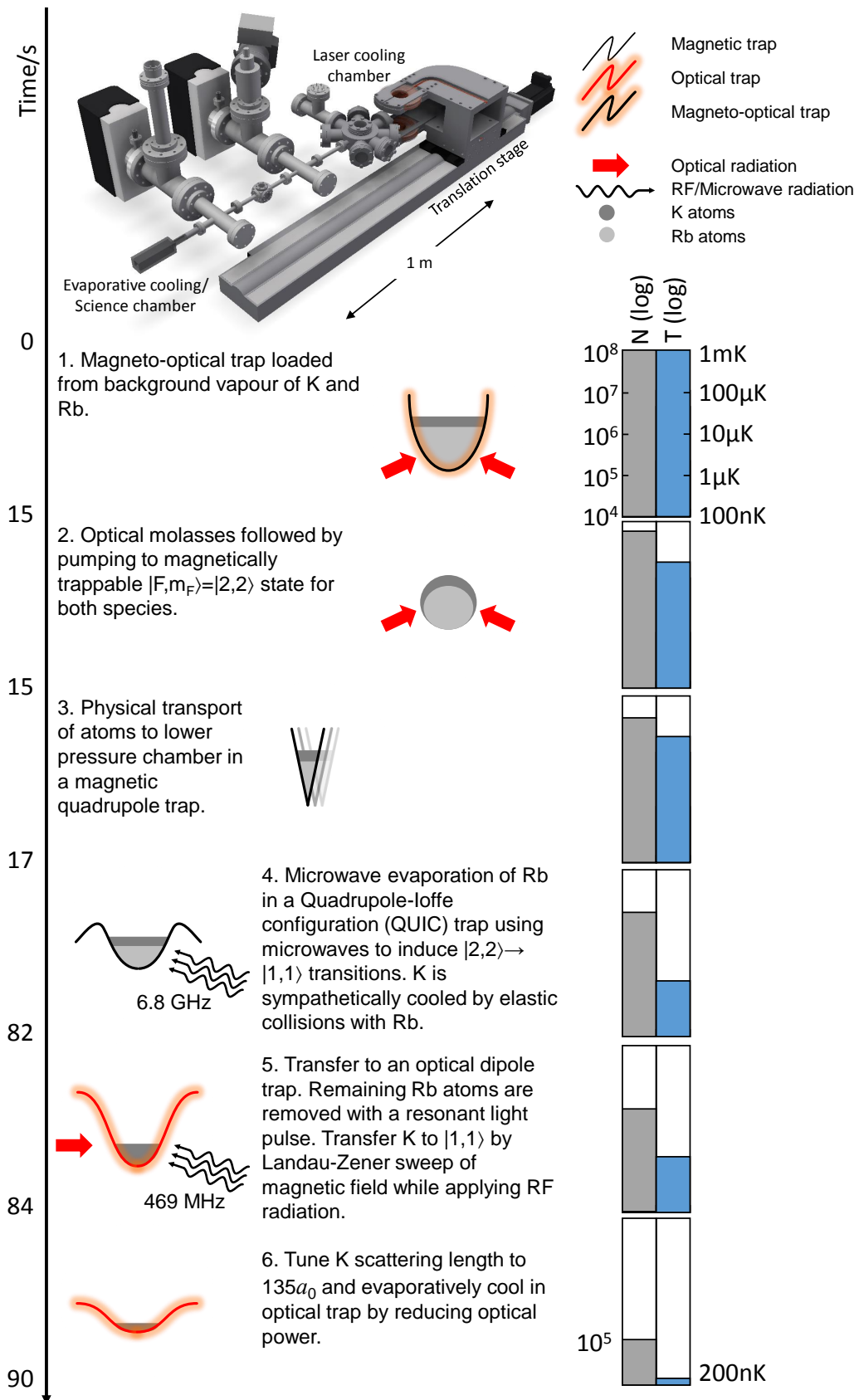


**Fig. 1.2.:** Summary of our experimental sequence for cooling  $^{39}\text{K}$  [24–26]. At the top we show a schematic of the experimental apparatus, containing two vacuum chambers (we omit all electromagnetic coils and optics for clarity). Cartoons of the trapping potential for each cooling stage are drawn below the part of the apparatus where the stage takes place. The bars on the right show the approximate atom number and temperature (log scales) at the end of each step.

destabilise the cloud. We observe the dynamics of a cloud where this few-body physics dominates, and by characterising this dynamics (particularly concentrating on three-body physics), we address the question of whether a degenerate unitary Bose cloud can ever be stable.

# A Superheated Bose-condensed Gas

Without any inter-particle interactions, individual particles in a closed system travel indefinitely on a fixed trajectory. Only by introducing interactions can particles redistribute their energy and change their dynamics, ultimately tending towards an equilibrium steady state. Interactions therefore play a key role in attaining and maintaining thermodynamic equilibrium, and systems can be stranded out of equilibrium if interactions are turned off or modified.

In this chapter we will study the non-equilibrium dynamics of a BEC of very weakly interacting  $^{39}\text{K}$  atoms. The most striking phenomenon we will observe in this regime is the persistence of a condensate stranded in a system far out of equilibrium at a temperature approximately 1.5 times higher than the equilibrium BEC transition temperature. We can draw parallels between this novel superheated state and traditional superheated systems such as very pure water heated to over  $100^\circ\text{C}$ . In a sample of superheated water, the particle motion is microscopically characteristic of a temperature over  $100^\circ\text{C}$ , whereas macroscopically, the system is not in the thermodynamically stable phase. This is directly analogous to what we observe in our superheated Bose-condensed gas.

An important difference is that whereas superheated water is an example of a stalled first-order transition, our Bose gas is superheated relative to the *second*-order BEC transition. First order transitions can be easily stalled by rendering the system incapable of overcoming the activation energy for the transition (in pure water we remove all nucleation sites for the formation of steam bubbles). Meanwhile, second order transitions have no activation energy, and instead, we exploit a dynamical method for making our novel superheated state. Specifically, our experimental system is dissipative (technical heating and atom loss gradually deplete the cloud), and by tuning the inter-particle interaction strength, we render the system incapable of keeping up with the rate of dissipation, and we allow the system to diverge away from equilibrium.

This chapter is organised as follows: In the first section, we will clarify the processes which move atoms and energy around our system, and describe a simple qualitative picture of our dissipative system. We then move on to present the experimental procedure for realisation of the superheated state in section 2.2, and the quantitative

techniques for analysing the experimental data in section 2.3. We show experimental results comparing the dynamics of a superheated state to an equilibrium system in 2.4. Finally, we build a quantitative model for the non-equilibrium dynamics of our superheated state in section 2.5, and test it by predicting the limits of superheating seen in the experiment.

## 2.1 Qualitative picture

To construct a simple picture in which superheating may occur, we consider a “two-fluid” model of our partially condensed Bose gas held in a trap (Fig. 2.1). In this model, we have two equilibrium subsystems - the thermal bath and the condensate. We consider the dissipation of each of these subsystems and the mechanisms for atom and energy transfer between them in the following sections.

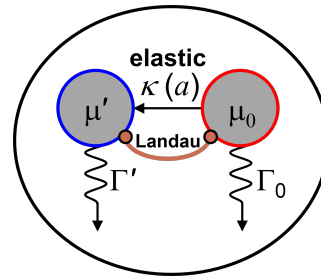


**Fig. 2.1.:** The two fluid model for our Bose gas. The components of this model will be explained individually in sections 2.1.1 - 2.1.4 and figures 2.2 - 2.5.

### 2.1.1 Equilibrium subsystems

In the two-fluid model, we conceptually divide our degenerate cloud into (1) the condensate and (2) its surrounding thermal cloud. In the Bogoliubov picture, we crudely imagine this division to be at the transition from the linear phonon spectrum to the free particle spectrum. In real space the condensate appears as a dense object embedded in the thermal cloud. We schematically represent the two subsystems in Fig. 2.2.

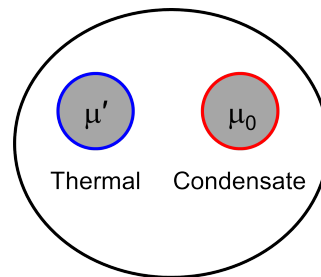


**Fig. 2.2.:** Division of the system into degenerate and non-degenerate subsystems. We treat each subsystem as individually in equilibrium and study non-equilibrium effects arising from imbalance between the subsystems.

Empirically (see section 2.4.3 for more justification), we find that these subsystems can be individually described by equilibrium properties (excluding  $|a| < 1 a_0$ ), and it is the balance *between* these two systems which can be driven out of equilibrium (even at much larger interaction strengths  $\gg 1 a_0$ ). Specifically, there are two key aspects to the equilibrium between these subsystems:

1. *Thermal equilibrium*: In thermal equilibrium, the temperature,  $T'$ , describing the thermal cloud is the same as the temperature,  $T_0$ , describing the excitations of the condensate. We explain in section 2.1.4 that in almost all cases that we study (more precisely, for  $|a| > 1 a_0$ ), thermal equilibrium holds. This means we always consider a state with a single well defined temperature,  $T' = T_0 \equiv T$ .
2. *Phase equilibrium*: In phase equilibrium, the chemical potential,  $\mu'$ , describing the thermal cloud is the same as the chemical potential,  $\mu_0$ , describing the condensate. In particular, phase equilibrium forbids there to be a condensate present if the number of atoms in the system,  $N$ , is less than a critical number,  $N_c$ , or equivalently if  $T$  is greater than a critical temperature,  $T_c(N)$ . This form of equilibrium will be violated in our superheated system.

### 2.1.2 Dissipation

At the start of the experiment, the two subsystems are in global equilibrium. However, dissipation plays a key role in their subsequent evolution. Dissipation in our experiment is primarily caused by scattering of atoms with photons from the laser beams used to trap the cloud. This drives both particle loss and heating on a characteristic timescale of 35 s in our system (see Eq. 2.25).

By continuously changing the atom number and temperature of the two subsystems at different rates, dissipation causes their chemical potentials to diverge away from the phase equilibrium condition  $\mu' = \mu_0$ . In the absence of any further processes,  $\mu'$  always falls faster than  $\mu_0$  (see Eq. 2.19). This imbalance breaks phase equilibrium unless an additional process acts to continuously re-equilibrate the chemical potentials (see below).

### 2.1.3 Atom transfer - Elastic scattering

If the two subsystems interact, they will exchange atoms with the aim of equilibrating their chemical potentials. This exchange proceeds by elastic

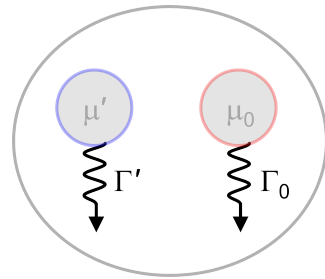


**Fig. 2.3.:** Dissipation in our system (namely technical heating and atom loss) causes the chemical potentials of the two subsystems to become unbalanced at a rate dictated by the per particle loss rates  $\Gamma'$  and  $\Gamma_0$ . An additional imbalance of  $\mu' < \mu_0$  due to heating of the cloud by the laser beams is also taken into account in our calculations.

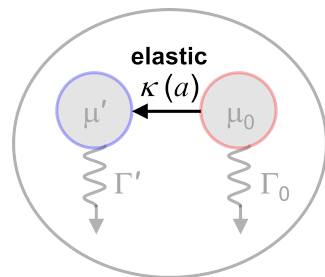


**Fig. 2.4.:** Elastic scattering between the subsystems proceeds at a rate  $\kappa$  to try to continuously re-equilibrate the chemical potentials in response to dissipation.

s-wave scattering between atoms, with the dissipation-induced imbalance  $\mu' < \mu_0$  tending to drive a net flow of atoms out of the BEC into the thermal cloud.

The rate,  $\kappa$ , at which atoms are transferred depends on the strength of inter-atomic interactions, parameterised by  $a$ . Indeed, we will see in Eq. 2.24 that  $\kappa \propto a^2$ .

For sufficiently large  $a$ , re-equilibration by elastic scattering will be faster than the dissipation rate. In this large- $a$  case, we will simply observe quasi-static equilibrium decay of the cloud and the condensate will vanish when the atom number falls below the equilibrium critical number  $N_c$ . However, in a very weakly interacting system, elastic scattering cannot keep up with the dissipation and a non-equilibrium state will form (for reference, the characteristic time scale for elastic scattering at  $a = 5 a_0$  is 16 s in our experiment). In this non equilibrium state, atoms are stranded in the condensed state, and the phase transition to a purely thermal state is dynamically inhibited even as the atom number falls below the equilibrium critical number  $N_c$  (or equivalently the temperature rises above  $T_c$ ). We then refer to the state in which atoms are still stranded in the condensate as a “superheated Bose-condensed gas”.

## 2.1.4 Energy transfer - Landau damping

The final process we consider in the two-fluid picture is concerned with thermal equilibrium: If we take a thermos flask of cold water and put it in a room full of steam at over 100°C, then we have successfully stranded the water out of phase equilibrium with the steam by reducing the interactions between the two phases. However, this is not an interesting superheated system because microscopic inspection of the particles reveals that the water in the flask is still below its boiling point. Crucially, this analogy tells us that it is not only the absence of phase equilibrium, but also the presence thermal equilibrium which defines a superheated state.

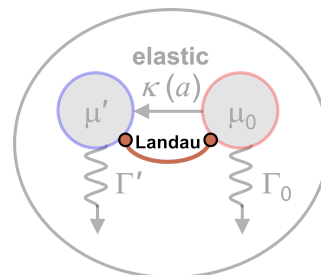


**Fig. 2.5.:** Landau damping maintains thermal equilibrium between the two sub-systems for all interaction strengths (excluding  $|a| \ll 1 a_0$ ).

In our Bose-condensed gas, we define the temperature of the thermal cloud from the occupation of free particle energy levels, and we define the temperature of the BEC from the occupations of collective modes (i.e. phonons). Consider artificially amplifying one phonon mode in a condensate originally at thermal equilibrium with its surrounding thermal cloud. Through mean-field interactions, this condensate phonon modifies the thermal cloud density distribution, and in turn, the mean-field

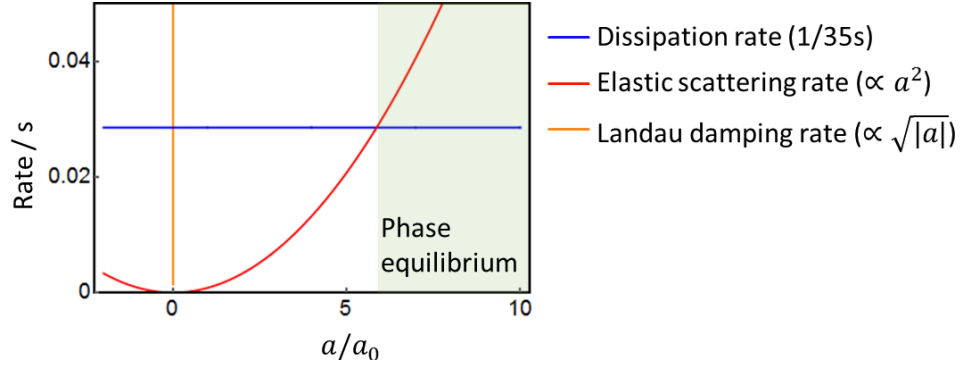


**Fig. 2.6.:** Comparison of the characteristic rates of relevant processes in our system for typical initial conditions. In this plot we adjust the elastic scattering rate based on the assumption that  $\sim 3$  collisions are required to achieve equilibrium [36–38]. This very simple picture taken at the start of the cloud’s evolution predicts phase equilibrium for  $a > 6a_0$ . As the system evolves, the atom number and temperature change, which changes the elastic scattering rate and extends the range of  $a$  in which we can observe non-equilibrium behaviour. In order to capture these effects, we need the fully dynamical model in section 2.5.

effect of this modified thermal cloud alters the spectrum of the condensate. The ultimate result of this “back-action” on the condensate is that the original phonon is damped back to equilibrium. The rate at which this damping occurs depends on the interaction strength,  $a$ . A more complete description of this process (known as Landau damping) can be found in [3, 34, 35]. By analytically modelling this back-action in a homogeneous system<sup>1</sup>, one arrives at the following phonon damping rate<sup>2</sup>:

$$\tau_L(\omega_p) = \frac{8}{3\pi^{3/2}} \frac{n_0^{1/2} \lambda_T^2}{\omega_p} \frac{1}{|a|^{1/2}}, \quad (2.1)$$

where  $\tau_L(\omega_p)$  is the Landau damping time for a phonon at frequency  $\omega_p$ ,  $n_0$  is the condensate density and  $\lambda_T$  is the thermal wavelength at the equilibrium temperature.

We insert our empirical peak density,  $n_0 \approx 5 \times 10^{14} \text{ cm}^{-3}$ , into the homogeneous gas result in Eq. 2.1 to estimate the thermal equilibration time scale in our trapped system<sup>3</sup>. The lowest frequency phonon mode in our trapped system is  $\omega_p = \sqrt{2}\omega_{\text{ho}}$  [3] where  $\omega_{\text{ho}} \approx 2\pi \times 71 \text{ Hz}$  is the trap frequency of our isotropic harmonic trap. At

<sup>1</sup>Note that here we are resorting to homogeneous system results to avoid the complications of the inhomogeneous trapping potential. Exactly these sorts of simplifications motivate the work to produce an experimental uniform system in chapter 6.

<sup>2</sup>Here we assume that the kinetic energy of the thermal cloud is greater than the interaction energy of the condensate, which is appropriate for our experiments.

<sup>3</sup>Handled in this way, the homogeneous expression should give an upper bound on  $\tau_L$  for our harmonically trapped gas [35].

typical experimental temperatures of  $\sim 180$  nK, this gives a Landau damping time of  $\tau_L < 1$  s even for  $a$  as low as  $1 a_0$ .

Since Landau damping occurs on a timescale ( $< 1$  s) much faster than the dissipation ( $\approx 35$  s), we can be confident that our gas is almost always in thermal equilibrium. Only for  $a \rightarrow 0$ , where the Landau damping time diverges, is the assumption of thermal equilibrium unjustified (exactly at  $a = 0$  we have a situation similar to the thermos flask analogy). Therefore, throughout this investigation, we assume thermal equilibrium  $T_0 = T' \equiv T$ , and anticipate that this assumption will only fail to capture the correct behaviour for  $|a| < 1 a_0$ .

We stress that the key point in our experiments is that  $1/\tau_L \propto \sqrt{a}$ , while  $\kappa \propto a^2$ . It is this difference in scaling with  $a$  that allows us to find a large parameter space where the two subsystems are in thermal equilibrium, but not in phase equilibrium (see Fig. 2.6).

### 2.1.5 Summary

We have described how the inter-particle interaction strength sets the rate at which our system can respond to being driven out of phase equilibrium by dissipation. For sufficiently strong interactions, particle transfer between the BEC and thermal cloud proceeds quickly enough to keep the system in global equilibrium. Under these conditions, the BEC disappears when the system crosses the equilibrium critical point. However, in a weakly interacting gas, particles are stranded in the BEC, meaning we can observe a BEC at a temperature higher than the equilibrium critical temperature - i.e. we see a superheated state.

## 2.2 Experimental procedure

To put our discussion on a concrete footing, it is helpful to immediately introduce the experimental procedure which is illustrated in Fig. 2.7(a).

The experiment starts after cooling the atoms to degeneracy at  $T \approx 160$  nK (see section 1.2). We stop the evaporative cooling by raising the dipole trap depth to  $2 \mu\text{K}$ , and wait at  $a = 135 a_0$  for 2 s to ensure the cloud has reached global equilibrium. Then we use a Feshbach resonance (see section 1.1.2) to tune the interactions by ramping an external uniform magnetic field over 50 ms to create a weakly interacting system. Finally we wait for a hold time,  $t$ , to allow the system to evolve under the influence of dissipation.

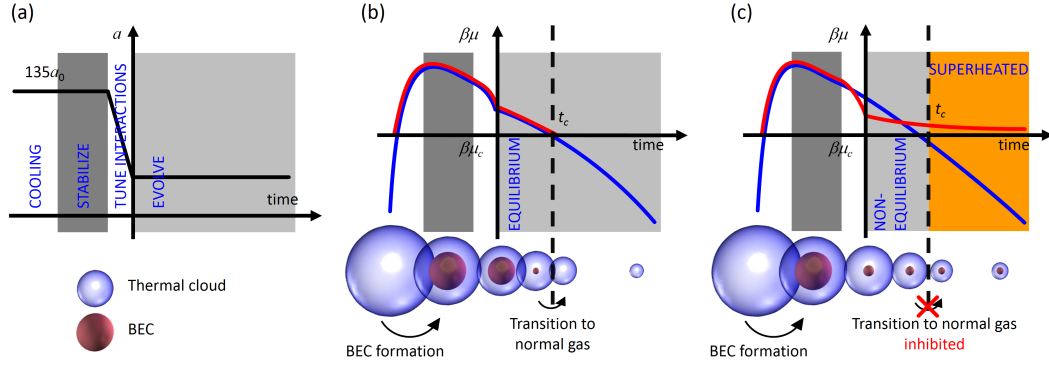


**Fig. 2.7.:** Experimental sequence. (a) We prepare a BEC and then reduce  $a$  over a period of 50 ms to study the cloud as it evolves at low  $a$ . (b) Schematic illustration of  $\mu_0$  (red) and  $\mu'$  (blue) in an equilibrium system (large  $a$ ).  $\mu_0$  and  $\mu'$  are locked together until  $\mu' = \mu_c \approx 0$  and the BEC disappears. (c) Schematic illustration of the chemical potentials when  $a$  is insufficient to maintain phase equilibrium. We define the superheated regime as the region with  $\mu' < \mu^{\text{eq}} < \mu_c$  but  $\mu_0 > \mu_c$ .

To probe the properties of the gas created in this procedure, we reduce the interaction strength all the way to  $2.2 a_0$  (i.e. essentially non-interacting) and release the cloud from the trap, allowing it to expand ballistically for a time-of-flight (ToF) of  $t_{\text{ToF}} = 18$  ms. After this time, an atom with momentum  $\mathbf{p}$  is at  $\mathbf{r} \approx \mathbf{p}t_{\text{ToF}}/m$  (ignoring the small initial size of the cloud). Therefore, when we image the cloud using absorption imaging [25, 26, 39, 40], we obtain its momentum distribution.

By repeating this whole sequence for different hold times,  $t$ , we can measure the momentum distribution as a function of time in the presence of dissipation. In the next section, we will see how the momentum distributions can be converted into the chemical potentials  $\mu'$  and  $\mu_0$  which we use to track the superheating of our system.

## 2.3 Experimentally measuring chemical potentials

We already indicated that the balance between chemical potentials  $\mu'$  and  $\mu_0$  is of central importance in defining whether a system is in phase equilibrium. In the language of chemical potentials, the arguments of our qualitative picture run as follows: For large interaction strengths<sup>4</sup>, we expect  $\mu' = \mu_0$  always, and a BEC exists whenever  $\mu' > \mu_c$  where  $\mu_c$  is the critical chemical potential (see section 2.3.2). For "small" interaction strengths, we will show in Eq. 2.19 that dissipation causes  $\mu'$  to diverge away from  $\mu_0$ . Eventually  $\mu' < \mu^{\text{eq}} < \mu_c$  while  $\mu_0 > \mu_c$  (where  $\mu^{\text{eq}}$  is the chemical potential that a cloud of the observed total atom number and

<sup>4</sup>We empirically find that (approximately)  $a > 50 a_0$  is sufficiently large in our system to observe predominantly equilibrium effects (see Fig. 2.13).

energy would have in phase equilibrium). These inequalities define the superheated regime, and this behaviour is schematically illustrated in Fig. 2.7.

Since we cannot assume that our partially condensed gas is in global equilibrium, extraction of  $\mu$  and  $\mu_0$  from the absorption images that we record is not immediately simple. We proceed by considering that regardless of whether a system is in equilibrium or not, two extensive variables are always well defined: the total atom number,  $N = N' + N_0$ , and the total cloud energy,  $E$ . We will first explain how we extract these two extensive variables from the absorption images in the following section, and then in section 2.3.2 we take the next step of calculating  $\mu$  and  $\mu_0$  from  $N$  and  $E$ .

### 2.3.1 Extraction of $N$ and $E$

We use absorption imaging to probe our atom clouds. The light absorbed from an imaging beam of intensity  $I$  propagating in the  $z$  direction through an atom cloud can be linked to the cloud of density  $n(\mathbf{r})$ , using the Beer-Lambert law:

$$\frac{dI}{dz} = -n(\mathbf{r})\sigma(I)I, \quad (2.2)$$

where the cross section  $\sigma$  is given on resonance by the Optical-Bloch equations [14]:

$$\sigma = \sigma_0 \frac{1}{1 + I/I_{\text{sat}}}. \quad (2.3)$$

Here  $I_{\text{sat}}$  is the saturation intensity for the imaging transition and<sup>5</sup>  $\sigma_0 = 3\lambda^2/2\pi$  where  $\lambda$  is the wavelength of the resonant imaging light. Integrating 2.2 gives:

$$-\log\left(\frac{I}{I_0}\right) + \frac{I - I_0}{I_S} = \sigma_0 \int n dz, \quad (2.4)$$

where  $I_0$  is the initial intensity of the beam before entering the cloud, which we measure by taking an additional image with no atoms present. For our low intensity beam ( $I < I_S$ ), to good approximation, we can keep only the logarithmic term on the left-hand-side of Eq. 2.4 (in section 6.2 we will keep both terms).

<sup>5</sup> $\sigma_0$  can deviate from this theoretical value due to (among other factors) components of incorrect polarisation in the imaging light. To eliminate these uncertainties we calibrate the value of  $\sigma_0$  by measuring the critical atom number for a cloud at  $a = 62a_0$  and comparing to the theoretical value assuming that the cloud is in equilibrium at this value of  $a$  [41, 42].

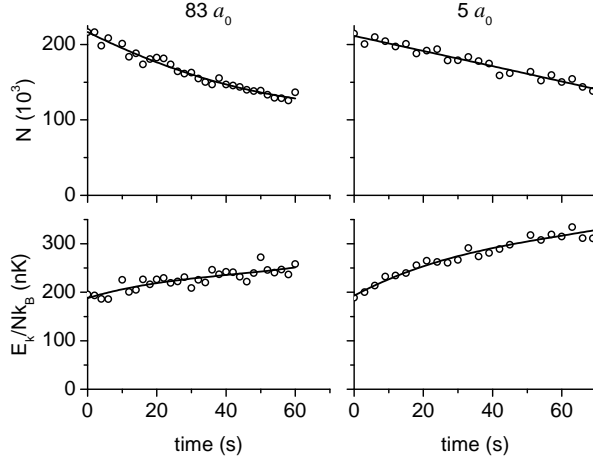


**Fig. 2.8.:** Raw measurement of  $N$  and  $E_k$  after tuning  $a_0$  as in Fig 2.7 (single experimental run per point; scatter indicates random error scale). These series at  $83 a_0$  and  $5 a_0$  are put through the analysis in section 2.3.2 to extract  $T^{\text{eq}}$  and  $\mu'$  in Fig. 2.9. To calculate  $\mu^{\text{eq}}$  and the theoretical curves in Fig. 2.13, we parameterise  $N$  and  $E_k/N$  using the polynomial fits shown by solid lines.

With this link between  $n$  and  $I$ , the extensive variables  $N$  and  $E$  can be calculated from the image as follows:

$$N = \int n d^3\mathbf{r} = \frac{1}{\sigma_0} \int \log\left(\frac{I_0}{I}\right) dx dy \quad (2.5)$$

$$E \approx 2E_k = m \frac{\int r^2 n d^3\mathbf{r}}{t_{\text{ToF}}^2} = \frac{3\pi m}{\sigma_0 t_{\text{ToF}}^2} \int \rho^3 \log\left(\frac{I_0}{I}\right) d\rho, \quad (2.6)$$

where  $m$  is the mass of a  $^{39}\text{K}$  atom and  $\rho$  is the radial coordinate in the 2D camera image centred on the cloud. Note that we have assumed spherical symmetry and ignored the interaction energy in the expression for  $E$  (we assess its contribution to be  $< 1\%$  for  $a < 100 a_0$ ). Furthermore, we have assumed that the total energy,  $E$ , is simply twice the kinetic energy,  $E_k$  (the mean kinetic and potential energy are equal in a non-interacting harmonic oscillator). Any initial size effects from the finite in-trap size can be accounted for by rescaling the energy by a factor  $\omega_{\text{ho}} t_{\text{ToF}}^2 / (1 + \omega_{\text{ho}} t_{\text{ToF}}^2)$ , which effectively un-does the effect of convolving the momentum distribution with the in-trap cloud size (assuming gaussian-like cloud profiles).

Example plots of  $N$  and  $E_k/N$  curves during experimental sequences for clouds evolving with strong ( $83a_0$ ) and weak ( $5a_0$ ) interactions are shown in Fig. 2.8. These curves can be converted into chemical potentials and temperatures (see Fig. 2.9) by the operations summarised in the next section.

## 2.3.2 Calculation of chemical potentials

The process to obtain  $\mu'$  and  $\mu_0$ , from the extensive variables,  $N$  and  $E$ , is not simple and requires several numerical steps. Below we outline the basic procedure (which could be omitted on first reading) and in section 2.3.3 we use some of the results presented here to provide a satisfactory answer to the question of why dissipation should necessarily tend to drive particles in the direction from the BEC to the thermal cloud. We leave a full dynamical calculation of the rate of this particle flow until section 2.5.

We start the task of relating  $\mu'$  to  $N'$  and  $E$  by integrating the Bose distribution for a *non interacting* gas to obtain theoretical form for the density,  $n'$ , of the excited states under the semi-classical approximation [3]:

$$\begin{aligned} n'(\mathbf{r}, \mu', T) &= \int \frac{d^3\mathbf{p}}{(2\pi\hbar)^3} \frac{1}{\exp\left[\frac{1}{k_B T} \left(\frac{p^2}{2m} + \frac{1}{2}m\omega_{\text{ho}}^2 r^2 - \mu'\right)\right]} - 1 \\ &= \frac{1}{\lambda_T^3} g_{3/2} \left[ \exp\left(-\frac{m\omega_{\text{ho}}^2 r^2}{2k_B T} + \frac{\mu'}{k_B T}\right) \right], \end{aligned} \quad (2.7)$$

where  $g_\alpha(z)$  is the polylogarithm function. This allows us to calculate the theoretical forms for  $N'$  and  $E_k$  as functions of  $\mu'$  and  $T$ :

$$N'(\mu', T) = \int n(\mathbf{r}, \mu', T) d^3\mathbf{r} = \frac{N_c^0}{\zeta(3)} g_3 \left( e^{\mu'/k_B T} \right) \quad (2.8)$$

$$\frac{E_k(\mu', T)}{N'(\mu', T)} = \frac{1}{N'} \int \frac{1}{2} m\omega_{\text{ho}} r^2 n(\mathbf{r}, \mu', T) / d^3\mathbf{r} = \frac{3}{2} k_B T \frac{g_4 \left( e^{\mu'/k_B T} \right)}{g_3 \left( e^{\mu'/k_B T} \right)} \quad (2.9)$$

where  $N_c^0 = \zeta(3) \left( \frac{k_B T}{\hbar\omega_{\text{ho}}} \right)^3$  is the critical atom number, and  $\zeta(\alpha) = g_\alpha(1)$  is the Riemann zeta function. These non-interacting expressions are modified in a finite-sized interacting system by two corrections:

- *Finite-size corrections:* The maximum value of  $N' = N_c^0$  in Eq. 2.8 occurs at  $\mu = 0$ . However, the semi-classical description does not capture the quantum mechanical zero-point energy  $\epsilon_0 = 3\hbar\omega_{\text{ho}}/2$  of a trapped system. When we include this in the Bose factor, we find that the maximum (i.e. critical) value of  $N'$  is actually reached when  $\mu$  rises to  $\mu = \mu_c^0 \equiv \epsilon_0$ . The correction to the

critical number,  $\tilde{N}_c^0$  in a trapped system can then be calculated by expanding  $N'(\mu_c^0, T) = N'(0, T) + \mu_c^0 \partial_{\mu'} N'$ :

$$\tilde{N}_c^0 = N_c^0 \left( 1 + \frac{\zeta(2)}{\zeta(3)} \frac{\mu_c^0}{k_B T} \right) \quad (2.10)$$

- *Interaction shift*: Mean-field interactions shift the critical chemical potential in a harmonic trap to  $\mu_c = \mu_c^0 + 4\zeta(3/2)a/\lambda_T$ , and the resulting shift in the critical number has been measured (including beyond mean-field terms) as [41, 42]:

$$N_c = \tilde{N}_c^0 \left( 1 - 3.426 \frac{a}{\lambda_T} + 42 \left( \frac{a}{\lambda_T} \right)^2 \right)^{-3} \quad (2.11)$$

These corrections transform Eq. 2.8 and 2.9 into:

$$N'(\mu', T) = \frac{N_c}{\zeta(3)} g_3 \left[ \exp \left( \frac{\mu' - \mu_c}{k_B T} \right) \right], \quad \frac{E_k(\mu', T)}{N'(\mu', T)} = \frac{3}{2} k_B T \frac{g_4 \left[ \exp \left( \frac{\mu' - \mu_c}{k_B T} \right) \right]}{g_3 \left[ \exp \left( \frac{\mu' - \mu_c}{k_B T} \right) \right]} \quad (2.12)$$

Finally, the key step in this procedure is to numerically invert this pair of equations:

$$\begin{cases} N'(\mu', T) \\ E(\mu', T) \end{cases} \xrightarrow{\text{invert}} \begin{cases} \mu'(N', E) \\ T(N', E) \end{cases}. \quad (2.13)$$

Since these expressions for  $\mu'$  and  $T$  are in terms of  $N'$  rather than the measured  $N$ , there are two routes to proceed:

1. In the column densities retrieved from the absorption images, the BEC stands out as a sharp peak at low momentum on top of the broader thermal distribution (see Fig. 2.11(a)). We can remove the thermal cloud by fitting and subtracting the theoretical thermal profile:

$$\int n'(\mathbf{r}, \mu', T) dz = \sqrt{\frac{2\pi k_B T}{m\omega^2}} g_2 \left[ \exp \left( \frac{\mu'}{k_B T} - \frac{m\omega^2 \rho^2}{2k_B T} \right) \right] \quad (2.14)$$

leaving only the residual BEC atoms,  $N_0$ , to be counted. We can then calculate  $N' = N - N_0$  to find  $\mu'(N, N_0, E)$  and  $T(N, N_0, E)$ .

To establish whether the system is in phase equilibrium, we also need to know  $\mu_0$ . To find  $\mu_0$ , we use a modified Thomas-Fermi law for the condensate subsystem, which interpolates between  $\mu_0 = \mu_c^0 = 3\hbar\omega_{\text{ho}}/2$  for  $N_0 = 0$  and the infinite particle Thomas-Fermi limit [43]:

$$\mu_0 - \mu_c = \frac{\hbar\omega_{\text{ho}}}{2} \left[ 15 \frac{N_0 a}{a_{\text{ho}}} + 3^{5/2} \right]^{2/5} - \frac{3\hbar\omega_{\text{ho}}}{2}, \quad (2.15)$$

where  $a_{\text{ho}}$  is the harmonic oscillator length.

So, by this route, we measure  $\{N, N_0, E\}$  and calculate  $\{\mu', \mu_0, T\}$ .

2. An alternative route would be to ask how the measured  $N$  atoms would be distributed if the system was in global equilibrium ( $\mu' = \mu_0 \equiv \mu^{\text{eq}}$ ) at energy  $E$ . In this case, we know from [44, 45] that the harmonically trapped gas has an equilibrium equation of state<sup>6</sup>:

$$\frac{N'}{N_c} \approx 1 + \frac{\zeta(2)}{\zeta(3)} \frac{\mu'}{k_B T} \quad (2.16)$$

More precisely, in our calculations we include the next order term  $\propto (\mu^{\text{eq}})^2 \sim N_0^{4/5}$ , found experimentally in [45] as:

$$N' = N_c + S_0(N_0)^{2/5} + S_2(N_0)^{4/5}, \quad (2.17)$$

where  $S_0$  and  $S_2$  depend on  $a$  and  $T$ , and we used Eq. 2.15 to link  $\mu'$  and  $N_0$ . Using  $N_0 = N - N'$ , Eq. 2.17 becomes an implicit equation for  $N'(N, T)$ . Inserting this into Eq. 2.13 allows us to calculate  $\{\mu^{\text{eq}}, T^{\text{eq}}\}$  from  $\{N, E\}$  via  $\{N'^{\text{eq}}, N_0^{\text{eq}}\}$ .

Empirically, we find  $T^{\text{eq}} \approx T$  (i.e.  $T(N'^{\text{eq}}, E) \approx T(N', E)$ ) for all the experimental sequences we measure (because the condensate atom number is always small). This allows us to drop the notation  $T^{\text{eq}}$  and simply refer to the temperature of the cloud as  $T$ .

<sup>6</sup>The derivation of Eq. 2.16 is outlined in section 7.1.1

By comparing the ‘true’ chemical potentials (calculated via route 1) with their equilibrium counterparts (calculated via route 2), we are able to see which range of  $a$  is well described by the equilibrium theory and which range of  $a$  shows large deviations from it.

### 2.3.3 Direction of the particle flow

Having introduced the basic expressions for calculating chemical potentials, it is worth returning to the question raised in section 2.1.2 and 2.1.3 of why the dominant motion of atoms in response to dissipation is out of rather than into the BEC.

Imagine a system which is infinitesimally displaced from equilibrium ( $\mu' \approx \mu_0$ ). In the absence of elastic processes, we can write:

$$\left\{ \begin{array}{l} \dot{\mu}'/\mu' = -\alpha'\Gamma' \\ \dot{\mu}_0/\mu_0 = -\alpha_0\Gamma_0 \end{array} \right. \quad \text{where} \quad \left\{ \begin{array}{l} \Gamma' = -\dot{N}'/N' \\ \Gamma_0 = -\dot{N}_0/N_0 \end{array} \right. . \quad (2.18)$$

We can calculate  $\alpha_0 \approx 2/5$  (from Eq. 2.15), and  $\alpha' \approx (1 - N_c/N')^{-1}$  (from Eq. 2.16). Therefore, without any elastic effects, the instantaneous ratio of the rates of decay of  $\mu'$  and  $\mu_0$  when the system starts to depart from equilibrium is:

$$\frac{\dot{\mu}_0/\mu_0}{\dot{\mu}'/\mu'} = \frac{2}{5} \underbrace{\left(1 - \frac{N_c}{N'}\right)}_{<1} \underbrace{\frac{\Gamma_0}{\Gamma'}}_{\approx 1} . \quad (2.19)$$

Assuming three-body effects do not dominate (see Eq. 2.26 and chapter 3), energy inselective inelastic processes should give a ratio of  $\Gamma_0/\Gamma' \sim 1$ , and since we start with an equilibrium condensate ( $N' > N_c$ ), the right-hand side of Eq. 2.19 is always smaller than 1, meaning  $\mu'$  always falls faster than  $\mu_0$ . Atoms will tend to flow down this dynamically growing chemical potential gradient by elastic processes in the direction from the BEC to the thermals.

Now that we have shown that elastic processes necessarily deplete our BEC in the presence of energy-inselective dissipation, we are justified in our notion that limiting the elastic scattering rate will preserve the condensate in a superheated state.

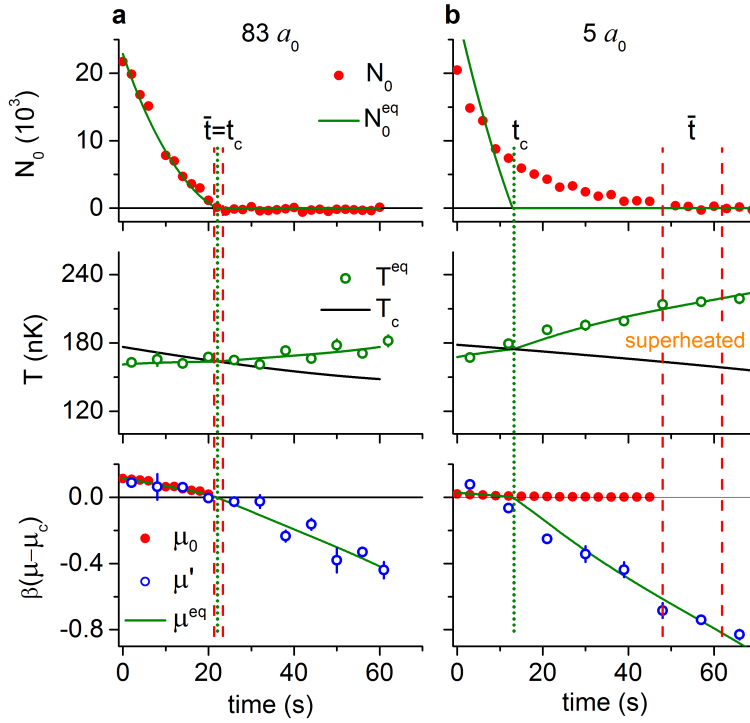


**Fig. 2.9.:** Equilibrium vs. non-equilibrium BEC decay. (a) At  $a = 83 a_0$  the cloud is always in quasi-static equilibrium. The measured  $N_0$  is in excellent agreement with the predicted  $N_0^{\text{eq}}$ , and vanishes when  $T^{\text{eq}} = T_c$ ; the three separately calculated chemical potentials,  $\mu_0$ ,  $\mu'$  and  $\mu^{\text{eq}}$ , all agree with each other. The dotted green line marks the equilibrium critical time,  $t_c$ , and the dashed red lines show the experimental bounds on the time  $\bar{t}$  when the BEC actually vanishes. (b) At  $5 a_0$ , the BEC persists in the superheated regime ( $T^{\text{eq}} > T_c$ ) for  $\bar{t} - t_c \approx 40$  s. Note that we are careful to start both the  $83 a_0$  and  $5 a_0$  series with the same initial conditions. The raw data for  $N_0$  are shown with one experimental run per point, and the extracted values of  $T$  and  $\mu'$  are shown with three experimental runs per point; error bars indicate the uncertainty in the mean.

## 2.4 Observation of a superheated state

The previous sections take us from absorption images to chemical potentials for the two subsystems. In this section, we present experimental trajectories of  $\mu_0$  and  $\mu'$  for the examples of an equilibrium decay at  $83 a_0$  and a non-equilibrium decay at  $5 a_0$ . After analysing this data within the two-fluid model, we then verify the validity of this model *a posteriori* in section 2.4.3.

### 2.4.1 Equilibrium decay vs. superheating

Using the methods of sections 2.2 and 2.3.2, Fig. 2.9 shows the trajectories of  $N_0$ ,  $T$ ,  $\mu'$  and  $\mu_0$  as we hold the gas at fixed  $a$  (this figure can be compared with the predictions of Fig. 2.7). By contrasting data taken at a "high" scattering length ( $a = 83 a_0$ ) and at a "low" scattering length ( $a = 5 a_0$ ) we can compare the cases of equilibrium and non-equilibrium decay, which are discussed separately below.

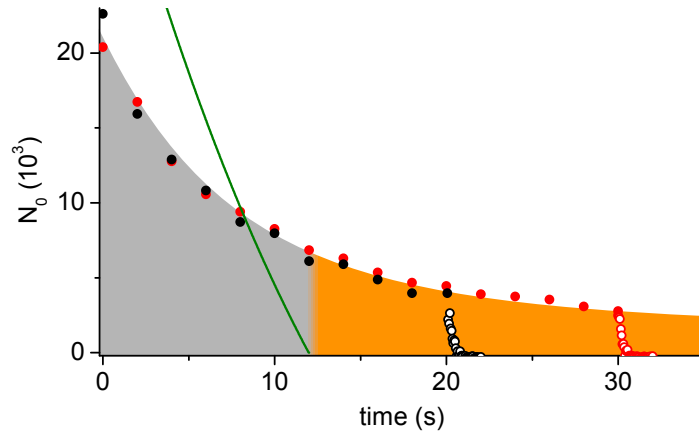


**Fig. 2.10.:** Quenching the superheated Bose-condensed gas. Solid symbols show the evolution of  $N_0$  at  $a = 3a_0$  (single experimental run per point), the green solid line shows  $N_0^{\text{eq}}$ , and orange shading indicates the superheated regime. Open symbols show the rapid decay of the BEC after it is strongly coupled to the thermal bath by an interaction quench to  $a = 62a_0$  at time  $t_q$ . We show two experimental series in which  $t_q = 20$  s (black) and 30 s (red).

### Equilibrium: $a = 83 a_0$

At  $a = 83 a_0$  (Fig. 2.9(a)) we find excellent agreement between the measured  $N_0$  and the predicted  $N_0^{\text{eq}}$ . The BEC vanishes exactly at the equilibrium “critical time”,  $t_c$  (dotted green line), at which  $T = T_c$ . Furthermore, the separately calculated  $\mu_0$ ,  $\mu'$  and  $\mu_{\text{eq}}$  all coincide exactly as predicted for a system in global equilibrium.

### Superheated: $a = 5 a_0$

At  $a = 5 a_0$  (Fig. 2.9(b)) we observe strikingly different behaviour. The BEC now survives much longer than it would in true equilibrium;  $\bar{t} - t_c \approx 40$  s. We also see that  $\mu_0$  and  $\mu'$  diverge from each other for  $t > t_c$ , so the system is moving away from the global phase equilibrium rather than towards it. The non-equilibrium behaviour is thus not just a transient effect. Explicitly, since  $T > T_c$  for  $t > t_c$  while  $N_0 > 0$ , we have direct evidence that our non-equilibrium state is a superheated Bose-condensed gas.

## 2.4.2 Quenching the superheated state

We can further confirm our observation of a superheated state by suddenly reintroducing strong interactions into the system. In Fig. 2.10, we show the effect of quenching the interaction strength from  $3 a_0$  to  $62 a_0$ . The quench is performed within  $\sim 10$  ms, and for the experimental sequences shown, we either perform the quench at hold times  $t = 20$  s or 30 s.

When we suddenly increase in the elastic scattering rate, we are giving the atoms which were stranded in the BEC a mechanism (elastic scattering) to rapidly flow

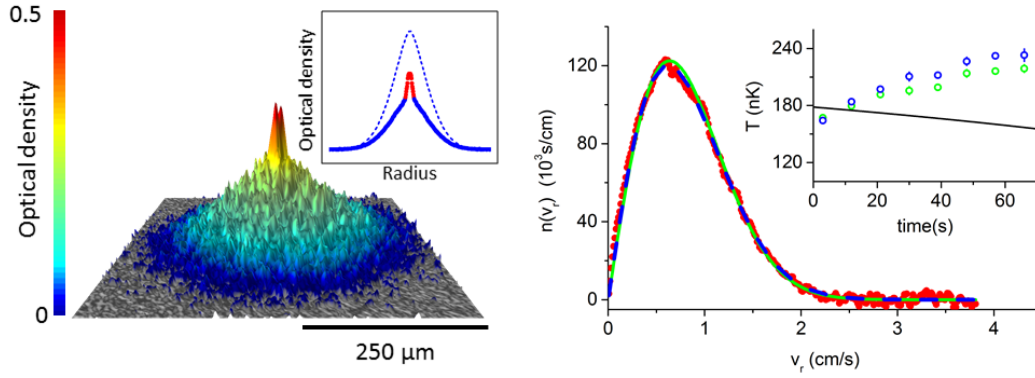


**Fig. 2.11.:** Thermal distribution in a gas out of global phase equilibrium. (a) Absorption image of the of a BEC in a system at  $5 a_0$  in the superheated regime after 18 ms ToF. Inset: the same image azimuthally averaged. The red peak shows the condensed part of the cloud, with the thermal part in blue. The dotted blue line shows the expected profile for the critical number of atoms at the temperature of our superheated cloud. (b) From the profile in (a), we can extract (1) the radial velocity distribution (red), (2) the theoretical distribution corresponding to the measured  $N$ ,  $E$  and calculated  $T^{\text{eq}}$  (green), and (3) the temperature from a fit,  $T^f$ , (blue). Even though the gas is not in true equilibrium, the distribution still looks thermal and  $T^f$  and  $T^{\text{eq}}$  agree to within a few percent. Inset: Comparison of  $T^f$  (blue) and  $T^{\text{eq}}$  (green) for the whole  $5 a_0$  series (error bars analogous to Fig 2.9). The solid black line shows the equilibrium  $T_c(N)$ . Note that  $T^f$  (blue) and  $T^{\text{eq}}$  agree within a few percent and both differ significantly from equilibrium.

down the chemical potential gradient into the thermal cloud, leading to rapid decay of the BEC in  $< 1$  s. This is the second-order transition analogy to sprinkling grit into a sample of superheated water: the water suddenly boils when the grit surface provides a nucleation site with lower activation energy.

### 2.4.3 Verification of the two-fluid model

Throughout the data analysis above, we employed a key feature of our two-fluid model: the assumption that the thermal and BEC subsystems are individually in equilibrium. This is essential because out of equilibrium temperature and chemical potential are potentially ill-defined concepts. In this section, we give evidence which supports this assumption.

In our experiment, we only measure extensive variables, and then calculate intensive variables from these. If the thermal subsystem is individually in equilibrium, then we should recover the same intensive variables (e.g. temperature) by fitting the cloud with a suitable polylogarithm function (Eq. 2.14). In Fig. 2.11(b) we show the radial velocity distribution ( $n(r)r/t_{\text{ToF}}$ ) of a cloud deep in the superheated regime ( $a = 5 a_0$ ,  $t = 45$  s). Overlaid on this figure are two curves:

- A fitted profile (Eq. 2.7) with temperature  $T^f$  as one of the free parameters (blue).
- The distribution expected based on the temperature,  $T^{\text{eq}}$ , derived from the total kinetic energy of the cloud (Eq. 2.13) (green).

We find that the data is fitted almost perfectly by the equilibrium distribution characterised by  $T^{\text{eq}}$ , and the fit for  $T^f$  gives only very slightly different shape. In Fig. 2.11(c), we compare the calculated  $T^{\text{eq}}$  with the fitted  $T^f$  for the whole  $5 a_0$  series;  $T^f$  always agrees with  $T^{\text{eq}}$  to within 10%. This indicates that the thermal cloud is itself thermal equilibrium. The very fast rate for Landau damping calculated in 2.1.4 ensures the condensate excitations are also separately in thermal equilibrium (for  $a > 1 a_0$ ), as required for our two-fluid picture.

## 2.5 Dynamical model of superheating

So far we have only observed the superheating effect at  $a = 5a_0$ . To add quantitative understanding, we now explore how the superheating phenomenon varies across a range of interaction strengths,  $a$ . In this section, we first re-cast the two-fluid model in a quantitative framework, and then demonstrate that our quantitative picture captures the main features of the experimental dynamics for almost all values of  $a$ .

The non-equilibrium evolution of  $N_0$  in the two-fluid model is governed by the following equation which combines the dissipative and elastic terms from Fig. 2.3 and 2.4:

$$\dot{N}_0 = -\kappa - \Gamma_0 N_0. \quad (2.20)$$

By evaluating the rates of both the elastic ( $\kappa$ ) and dissipative ( $\Gamma_0$ ) processes in the cloud, we can integrate this expression to extract a predicted trajectory for  $N_0(t)$ . The forms for  $\kappa$  and  $\Gamma_0$  are described in the following sections:

### 2.5.1 2-body elastic term, $\kappa$

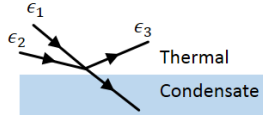
First consider the process in which two thermal atoms collide to form one condensate and one thermal atom. The rate at which this process occurs is calculated in [46]. Here we will give a simple outline which explains the physical origin of each of the terms.

The semi-classical s-wave collision rate,  $n\sigma v$  sets the time scale for elastic scattering:

$$n\sigma v = \frac{8m(k_B T)^2}{\pi \hbar^3} a^2. \quad (2.21)$$

Here  $n \sim \lambda_T^{-3}$  is the atom density of our degenerate gas,  $\sigma = 8\pi a^2$  is the s-wave scattering cross section for indistinguishable bosons<sup>7</sup> and  $v \sim \sqrt{8k_B T/\pi m}$  is the mean velocity of the atoms in the gas.

Alongside this characteristic rate, we need a factor to account for the availability of collision partners and final states. The rate at which atoms in thermal states with energies  $\epsilon_1$  and  $\epsilon_2$  can collide is proportional to the number of atoms,  $f(\epsilon_1)$  and  $f(\epsilon_2)$ , in those states. Indeed, the full collision integral describing the availability of states for this process is:



$$\kappa \propto \int d\epsilon_1 d\epsilon_2 d\epsilon_3 f(\epsilon_1) f(\epsilon_2) (1 + f(\epsilon_3)) (1 + N_0) \Delta(\epsilon_1, \epsilon_2, \epsilon_3), \quad (2.22)$$

where the explicit factors of 1 represent spontaneous collision and their accompanying occupation factors represent stimulated collisions.  $\Delta(\epsilon_1, \epsilon_2, \epsilon_3)$  represents a set of delta functions which ensure energy and momentum conservation. For simplicity, rather than evaluate this collision integral, we will extract the main functional form of the most dominant term: The condensate is macroscopically occupied, so we retain only the stimulated part of  $(1 + N_0) \rightarrow N_0$ , and the thermal cloud levels have small occupation factors so we retain only the spontaneous part<sup>8</sup> of  $(1 + f(\epsilon_3)) \rightarrow 1$ . The collision integral then becomes  $N_0 \int d\epsilon_1 d\epsilon_2 f(\epsilon_1) f(\epsilon_2) \sim N_0 e^{\frac{(\mu' - \mu_c) + (\mu' - \mu_c)}{k_B T}}$ , where for simplicity we use a Boltzmann form for  $f$ , and we deliberately leave the exponent ungathered for later comparison.

Combining Eq. 2.21 and 2.22, we find the total scattering rate *into* the condensate is:

$$\kappa_{\text{in}} \propto \gamma_{\text{el}} N_0 e^{\frac{\mu' - \mu_c}{k_B T}}, \quad (2.23)$$

<sup>7</sup>For distinguishable bosons, the s-wave scattering cross section is  $4\pi a^2$ . The extra factor of 2 in the indistinguishable case arises from symmetrisation.

<sup>8</sup>By ignoring  $f(\epsilon_3)$ , we are taking the lowest order term in  $e^{\frac{\mu'}{k_B T}}$ . Higher order terms have little role once the system becomes superheated ( $\mu' \ll 0$ )

where we define  $\gamma_{el} = n\sigma v e^{\frac{(\mu' - \mu_c)}{k_B T}}$ .

By a similar argument, we can write the collision integral of the reverse process (scattering out of the condensate) as  $\sim N_0 e^{\frac{(\mu_0 - \mu_c) + (\mu' - \mu_c)}{k_B T}}$ . The total rate for two body processes then becomes:

$$\kappa = A\gamma_{el}N_0 \left( e^{\frac{\mu_0 - \mu_c}{k_B T}} - e^{\frac{\mu' - \mu_c}{k_B T}} \right), \quad (2.24)$$

where  $A$  is a theoretically uncertain prefactor in the range  $1 - 10$  [43].

Eq. 2.24 sets the rate at which system can re-equilibrate after being driven out of equilibrium. This rate is to be compared with the dissipation term in the next section to establish whether superheating will take place.

## 2.5.2 Dissipation term

The dominant source of dissipation in our system is spontaneous scattering of atoms with photons in the trapping beam (a ‘‘one-body’’ process). Additional dissipation comes from the finite probability of three atoms simultaneously colliding, with the result that all three atoms ultimately leave the trap. This three-body process becomes more dominant as the interaction strength increases, and will be discussed more when we consider strongly interacting systems in chapter 3. Below we give sufficient details to calculate the rates,  $\Gamma_0^{(1)}$  and  $\Gamma_0^{(3)}$ , of the one- and three-body processes respectively to recover the full dissipation rate  $\Gamma_0 = \Gamma_0^{(1)} + \Gamma_0^{(3)}$

### One-body

Our optical trap is made from two crossed 1.2 W laser beams with waists of  $140 \mu\text{m}$ . The laser light is at  $\lambda = 1070 \text{ nm}$ , which is far red-detuned from the potassium  $\lambda_0 = 767 \text{ nm } D_2$  transition in an effort to minimise the photon-atom scattering rate while maintaining a deep dipole trap. In this far-detuned limit, the scattering rate is given by [15, 47]:

$$\Gamma_0^{(1)} = \frac{3\pi c^2}{2\hbar\omega_0^3} \left( \frac{\omega}{\omega_0} \right)^3 \left( \frac{\Gamma}{\omega_0 - \omega} + \frac{\Gamma}{\omega_0 + \omega} \right)^2 I_{\text{CDT}} \approx \frac{1}{35} \text{ s}^{-1}, \quad (2.25)$$

where  $\Gamma = 2\pi \times 6 \text{ MHz}$  is the linewidth of the transition, and  $I_{\text{CDT}}$  is the intensity of the crossed dipole trap experienced by the atoms. Since the thermal radius at  $200 \text{ nK}$  ( $\approx 14 \mu\text{m}$ ) is much smaller than the beam waist ( $140 \mu\text{m}$ ) we use the peak intensity of the beams to obtain the  $35 \text{ s}$  time scale in Eq. 2.25.

### Three-body

The probability of finding three atoms in the same unit volume scales as the cube of the atomic density. Accounting for all of the thermal-thermal-condensate, thermal-condensate-condensate and condensate-condensate-condensate collisions, the per-particle three-body loss rate from the condensate is [48]:

$$\Gamma_0^{(3)} = \frac{L_3(a)}{6} (\langle n_0^2 \rangle + 6\langle n_0 n' \rangle + 6\langle n'^2 \rangle). \quad (2.26)$$

The behaviour of the rate coefficient,  $L_3$ , for a strongly interacting system is the subject of considerable study in chapter 3. In this section we use the empirical results of [23] for a weakly interacting gas. For the average densities,  $\langle n \rangle$ , we use the following

$\langle n' \rangle$ : In the term  $\langle n'^2 \rangle = \int n^3(\mathbf{r}) d^3\mathbf{r} / \int n(\mathbf{r}) d^3\mathbf{r}$ , we use the expression for  $n'(\mathbf{r})$  in Eq. 2.7. In the term  $\langle n'_0 n' \rangle$  we use the local value of the thermal density at the trap centre,  $n'(0)$ , (where the three-body rate is highest):

$\langle n_0 \rangle$ : We use a functional form which smoothly interpolates<sup>9</sup> between the non-interacting Gaussian ground state,  $\langle n_0 \rangle_{\text{GS}}$  (applicable for  $N_0 a / a_{\text{ho}} \ll 1$ ) and the interacting Thomas-Fermi result,  $\langle n_0 \rangle_{\text{TF}}$  (applicable for  $N_0 a / a_{\text{ho}} \gg 1$ ):

$$\langle n_0 \rangle = \frac{\langle n_0 \rangle_{\text{GS}}}{\left(1 + \left[\frac{\langle n_0 \rangle_{\text{GS}}}{\langle n_0 \rangle_{\text{TF}}}\right]^{5/3}\right)^{3/5}}, \quad \langle n_0^2 \rangle = \frac{\langle n_0^2 \rangle_{\text{GS}}}{\left(1 + \left[\frac{\langle n_0^2 \rangle_{\text{GS}}}{\langle n_0^2 \rangle_{\text{TF}}}\right]^{5/6}\right)^{6/5}}, \quad (2.27)$$

where:

$$\begin{aligned} \langle n_0 \rangle_{\text{GS}} &= N_0 (2\pi a_{\text{ho}}^2)^{-3/2} & \langle n_0 \rangle_{\text{TF}} &= \frac{15\sqrt{2\pi}}{7} \left(\frac{15N_0 a}{a_{\text{ho}}}\right)^{-3/5} \langle n_0 \rangle_{\text{GS}} \\ \langle n_0^2 \rangle_{\text{GS}} &= N_0^2 (3\pi^2 a_{\text{ho}}^4)^{-3/2} & \langle n_0^2 \rangle_{\text{TF}} &= \frac{675\sqrt{\pi}}{56} \left(\frac{15N_0 a}{a_{\text{ho}}}\right)^{-6/5} \langle n_0^2 \rangle_{\text{GS}} \end{aligned} \quad (2.28)$$

### 2.5.3 Integration of non-equilibrium dynamics

Now that we have all the required rates in Eqs. 2.24, 2.25 and 2.26, we can integrate the trajectory of  $N_0$  in Eq. 2.20. The method for this integration is as follows:

<sup>9</sup>The results do not strongly depend on the exact form of the interpolation between these limits.

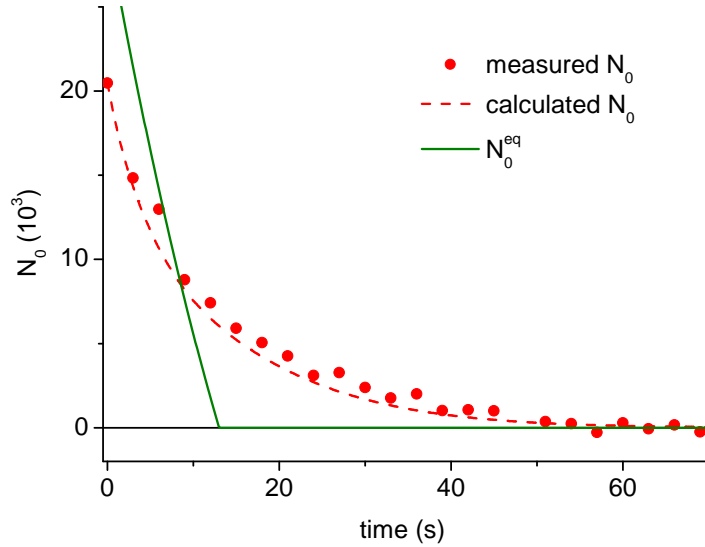


**Fig. 2.12.:** Non-equilibrium  $N_0$  dynamics. We plot the calculated  $N_0(t)$  (dashed red line) together with the measured  $N_0$  (red points; single experimental run per point) for the same  $5 a_0$  data series as in Fig. 2.9. For comparison, we also show the calculated  $N_0^{\text{eq}}(t)$  (solid green line).

1. Take the starting measurements of  $N(t = 0)$ ,  $E(t = 0)$ ,  $N_0(t = 0)$  and evaluate  $\mu'(t = 0)$  as described in section 2.3.2.
2. Using this initial value for  $\mu'$ , evaluate  $\kappa$  in Eq. 2.24 (since the theoretical value of  $A$  is unknown, we repeat this whole integration scheme for several values in the range 1-10, which appear in Fig. 2.13).
3. With this initial  $\kappa$ , take an Euler step to  $N_0(t = \delta t)$ , where  $\delta t$  is the time interval between the experimental measurements on the decay curves.
4. Using the measured  $N(t = \delta t)$ ,  $E(t = \delta t)$  and this calculated  $N_0(t = \delta t)$ , calculate  $\mu'(t = \delta t)$  and iterate back to step 2 to produce entire  $N_0$  and  $\mu'$  decay curves.

The success of our model in reproducing the observed condensate decay at  $5 a_0$  (using  $A=3$ ) is shown in Fig. 2.12.

Since we only included 2-body effects which are stimulated by the macroscopic condensate, the theoretical solutions of Eq. 2.20 can only asymptote to  $N_0 = 0$ , and we can never predict the  $N_0 = 0$  point. A more physical cut-off is to define that the condensate has disappeared when  $N_0$  falls below the thermal occupation of the first excited state, i.e.  $N_0^{\text{cut}} \approx \frac{3k_B T}{\hbar\omega_{\text{ho}}}$ . This cut-off allows us to calculate the time  $\bar{t}$  at which the condensate vanishes.

In the following section, we test the quantitative model derived here by investigating the extremes of the superheating as a function of  $a$ .

## 2.6 Limits of superheating

It is natural to ask how far the system can be heated above the critical temperature and how long this non-equilibrium state can live for. These limits of our superheated state are treated in the sections below where we will see that our dynamical model captures the basic behaviour very well.

### 2.6.1 Maximum temperature

In Fig. 2.13(a) we plot the highest temperature at which we still observe a BEC,  $\bar{T} \equiv T(t = \bar{t})$  scaled to the equilibrium critical temperature  $T_c$  corresponding to the observed  $N(t = \bar{t})$ . For  $a \rightarrow 0$ , the BEC survives up to  $T \approx 1.47 T_c$ . This is analogous to observing superheated water at 275 °C.

We also show the calculated  $\bar{T}/T_c$  derived from our quantitative model. The red line shows the results for  $A = 3$  and the shaded area corresponds to  $A = 1 - 10$ . Our model captures the data well, with  $A = 3$  agreeing everywhere except exactly at  $a = 0$ . We already anticipated that the model would not be accurate at  $a = 0$  because Landau damping vanishes in this limit, so the assumption of thermal equilibrium is no longer valid. Furthermore, our simple model does not include interactions beyond s-wave scattering (e.g. weak dipolar interactions [49]) which become relevant for  $a \rightarrow 0$ . The effect of these residual interactions is to drive  $\bar{T}/T_c$  below the predicted value, as observed.

### 2.6.2 Maximum lifetime

In Fig. 2.13(b), we reconstruct the temporal phase diagram of our non-equilibrium gas. Here, a horizontal cut through the graph corresponds to a time series such as that shown in Fig. 2.9. For each  $a$ , we plot the measured  $\bar{t}$  (red points) and the equilibrium  $t_c$  (green points) together with spline fits to the data. The width of the orange region corresponds to the time that the BEC survives in the superheated regime. For  $a \approx 0$ , this region spans a whole minute. In addition, in the inset, we plot the calculated phase diagram with  $A = 3$  for comparison with the data. Again, the main features are captured well for  $a \neq 0$ .

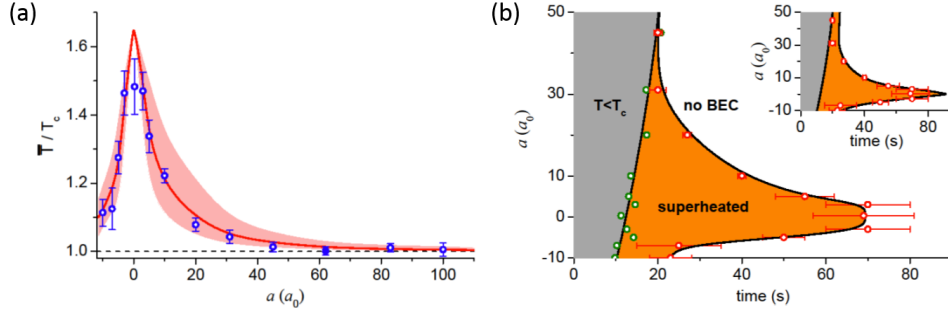


**Fig. 2.13.:** Limits of superheating. (a) The highest temperature at which we observe a BEC,  $\bar{T}$ , scaled to the equilibrium  $T_c$ . Close to  $a = 0$  the BEC survives up to  $\approx 1.47 T_c$ . The red line shows the results of our numerical calculations, with the shaded area indicating the theoretical uncertainty ( $A = 1 - 10$ ). Experimental error bars are statistical. The point at  $62a_0$  is fixed to unity by the absolute atom number calibration [41, 42]. (b) Temporal phase diagram. For each value of  $a$  we plot the equilibrium  $t_c$  (green points) and the time  $\bar{t}$  at which the BEC actually vanishes (red points). The  $\bar{t}$  errors correspond to dashed lines in Fig. 2.9 and the uncertainty in  $t_c$  is indicated by the scatter of points. Solid curves are spline fits to the data. For  $a \approx 0$  the BEC survives in the superheated regime for a whole minute. Inset: numerically calculated phase diagram, with  $\bar{t}$  data overlaid.

### 2.6.3 Independence on the initial conditions

We have now presented the main results of this work: observation of a long lived non-equilibrium BEC above the equilibrium critical temperature. However, before concluding this chapter, we highlight a fortuitous universality in our results.

Non-equilibrium phenomena are usually strongly dependent on the initial conditions. For the data presented here, we were careful to always start with  $N_0(t = 0) \approx 2 \times 10^4$  atoms by holding the cloud at  $a = 135 a_0$  to allow the atom number to decay (in quasi-static equilibrium) to reach this constant starting point. However, empirically, we find that  $\bar{t}$  is essentially constant, within experimental error bars, for initial  $N_0$  in the range  $(1 - 5) \times 10^4$ . Our quantitative model captures this unexpected universality well, and for  $a > 0$ , we attribute this effect to the three body term  $\Gamma_0^{(3)}$ .  $\Gamma_0^{(3)}$  grows with  $N_0$ , and therefore it has a “self-stabilizing” effect, rapidly depleting large condensates to bring them in line with the behaviour of smaller condensates on timescales much shorter than  $\bar{t}$ .

For  $a < 0$ , we attribute the universality to the “Bosenova” phenomenon [3, 27–29], where attractive interactions violently collapse the cloud to a dense point accompanied by rapid atom loss (see Fig. 2.14(a)). By studying the balance of kinetic, potential and interaction energy it can be shown that the collapse continues until the condensate atom number falls below a critical number  $N_{\text{nova}} \approx 0.57 a_{\text{ho}} / |a|$  [3, 27] (see Fig. 2.14(b)). This rapid Bosenova collapses all initial conditions with  $N_0 > N_{\text{nova}}$  to  $N_0 = N_{\text{nova}}$ .

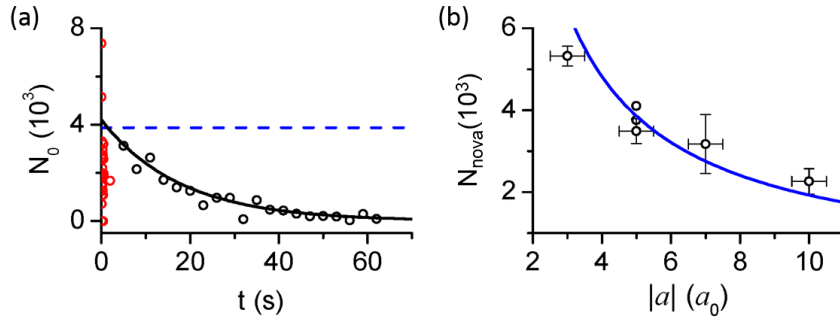


**Fig. 2.14.:** Observation of Bosenovae for  $a < 0$ . (a) We record violent collapse and revival (red points) of  $N_0$  during the early times in of a series at  $a = -5a_0$  (single experimental run per point).  $N_0$  eventually stabilises at  $N_0 \approx N_{\text{nova}}$  (blue dotted line) and then decays slowly. (b) The observed  $N_{\text{nova}}$  agrees well with the theoretical prediction  $N_{\text{nova}} \approx 0.57a_{\text{ho}}/|a|$ . Horizontal error bars are associated with the uncertainty in the Feshbach resonance position and vertical error bars indicate the error in  $N_{\text{nova}}$  from the extrapolation of data for  $t > 5$  s back to  $t = 0$ . (see black line in (a)).

## 2.7 Conclusion

In this chapter, we explored and understood the dynamics of a weakly interacting Bose gas. The highlight of our investigation was the observation of a novel state: a superheated Bose-condensed gas. We demonstrated that this phenomenon arises because the phase transition from a BEC to a normal gas can be dynamically inhibited by the slow atom transfer out of the BEC at low interaction strengths. The state is long lived, lasting up to one minute, and reaches temperatures up to 1.47 times the critical temperature. We mapped out a non-equilibrium phase diagram for this system, and successfully reproduced our measurements using a numerical model based on a two-fluid picture of a partially condensed gas. The success of our calculations supports a conceptually simple way to think about dynamical non-equilibrium effects near a second order transition.

## Stability of a Unitary Bose Gas

The previous chapter concentrated on the dynamics of an extremely weakly interacting Bose gas. Now, we use our ability to tune  $a$  to arbitrarily large values to investigate the opposite limit where interactions are as strong as quantum mechanics allows: the so-called “unitary” regime. This regime is experimentally particularly exciting because the strongly interacting gas is difficult to understand analytically. Many condensed matter phenomena (most famously high temperature superconductivity) exist only in strongly correlated systems. While this physics has been studied extensively in unitary Fermi gases over the past decade (see e.g. [50] and references within), work is only now starting on the unitary regime in a Bosonic gas. The reason for the lack of experimental work on unitary Bose gases is that dissipative three- or more-particle collisions (which are forbidden by the Pauli principle in Fermionic gases) can rapidly destabilise a strongly interacting cloud of Bosons. It is thus an open question to what extent and in what regimes a unitary Bose gas has well defined equilibrium properties. Here we experimentally study a thermal unitary gas of  $^{39}\text{K}$  bosons, and address the viability of bringing this gas to degeneracy at unitary.

In the unitary limit,  $a$  diverges to infinity. Recall that we defined  $a$  in section 1.1.1 from the expansion of the s-wave scattering amplitude,  $1/f(k) = -1/a + bk + \mathcal{O}(k^2)$ . A full treatment of the scattering problem with a regularized  $\delta$  function pseudo-potential [16, 51] shows that  $|b| = 1$ . This means that in the unitary regime ( $ka \gg 1$ ), the scattering amplitude takes the value  $|f(k)| \approx 1/k$ ; i.e. the scattering length is effectively replaced by  $1/k$ .

Extending this argument to a thermal gas of many atoms, we say that if  $a$  is greater than the thermal wavelength,  $\lambda_T$ , then we should replace  $a$  with  $\lambda_T$ . For a condensate, the natural length scale cutoff which replaces  $a$  is the interparticle spacing. This highlights the universality of the physics in the unitary regime: Once  $a$  has dropped out of the problem, the details of the very strong inter-atomic interactions cease to play any direct role in the phenomena we observe, and the two-body interactions are instead characterised by parameters of the gas which are not species-specific.

For Bosons, a particularly important phenomenon arising in this very strongly interacting regime is the dominance of multi-particle collisions. Outside unitarity, we can model low energy collisions as colliding billiard balls of radius  $a$ . The probability

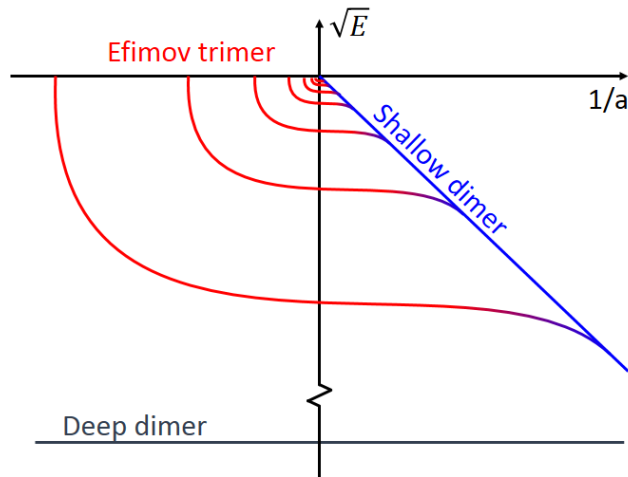


**Fig. 3.1.:** Final states available to three interacting particles. For  $a < 0$ , three particles can form an Efimov trimer which rapidly decays to a deep dimer and a high energy third atom. For  $a > 0$ , two particles can form a shallow dimer with the third carrying away a large share of the excess binding energy. Note that the shallow dimer forms from s-wave interactions which are characterised by the length scale  $a$  and the energy scale  $\hbar^2/ma^2$ , which is linear on these axes.

of a third atom being present in the volume  $\sim a^3$  surrounding the colliding pair grows strongly with  $a$  ( $\propto na^3$ ) until  $a$  is replaced with  $\lambda_T$  at unitarity. The increased likelihood of the presence of a third particle dramatically influences the physics of the collision: At a simple level, conservation of energy and momentum allows many different final states if the conserved quantities can be divided between three particles (e.g. the atoms can leave as three free atoms or as an atom and a dimer). At a more complicated level, the particles can form a 3-particle bound state, known as an Efimov trimer under suitable conditions (see Fig. 3.1) [23, 52–64].

We will see that the net effect of a three-body collision on the atom cloud involves both particle-loss and heating. In this chapter we will study the dynamics of non-condensed Bose gases in and around the unitary regime where we expect these three- (or more generally, few-) body effects to dominate. We will focus on the general scaling laws relating the three-body particle-loss and heating rates to temperature, scattering length and atom number. The dynamics that we uncover can be used to speculate on the stability of a unitary gas at different phase space densities.

The chapter is organised as follows: in section 3.1, we summarise the theory which addresses whether a degenerate unitary Bose gas can be studied in equilibrium. In this theory, a single species-specific parameter,  $\zeta$ , determines whether equilibrium, can be reached at a given phase space density. We measure this parameter for our  $^{39}\text{K}$  system by experimentally recovering two general scaling laws in sections 3.2 and 3.3. The conclusions in section 3.5 show that our measured value of  $\zeta$  makes

<sup>39</sup>K a promising species for further studies of many-body physics in a unitary Bose gas.

### 3.1 Can a unitary bose gas be stable at degeneracy?

In the previous chapter, we assessed the dynamics of a weakly interacting gas by comparing the rate of elastic (two-body) processes with the (one-body) dissipation rate. The same logic can be applied in the opposite limit of strong interactions, but in this limit dissipation is dominated by three-body processes. Below we examine the balance of the two- and three- body scattering rates to quantitatively address whether rapid three-body loss can destabilise a cloud approaching the critical point.

#### Three-body loss rate

For a non-condensed cloud ( $N' = N$ ) we already defined the three-body loss coefficient,  $L_3$ , in Eq. 2.26 such that:

$$\Gamma^{(3)} = -\frac{\dot{N}}{N} = L_3 \langle n^2 \rangle. \quad (3.1)$$

In this chapter, we will be primarily interested in measuring values of  $L_3$  and its scaling with  $a$  and temperature,  $T$ . Theoretically, close to a Feshbach resonance, but still away from unitarity,  $L_3$  can be shown to scale as  $\sim \hbar a^4/m$  [65, 66]. At unitarity we replace  $a \rightarrow \lambda_T$  to reach the asymptotic form  $L_3 \sim \hbar \lambda_T^4/m \propto 1/T^2$ . We will verify this scaling law in section 3.3.

Additionally, species-specific Efimov physics gives a dimensionless prefactor as follows [67]:

$$L_3 = \zeta \frac{9\sqrt{3}\hbar}{m} \lambda_T^4, \quad (3.2)$$

(where we have ignored additional weak log-periodic modulation arising from the Efimov spectrum [23, 54, 62]). The non-universal constant  $\zeta \leq 1$  [67–70] will play an important role in the stability calculations below. Physically,  $\zeta$  describes the fraction of three particle interactions which result in atom loss. A fraction  $1 - \zeta$  of three body collisions form a transient trimer which decays back into free atoms which remain in the trapped gas<sup>1</sup>.

<sup>1</sup> $\zeta$  can be written  $\zeta = 1 - e^{-4\eta}$  where  $\eta$  is known as the Efimov width parameter.  $\eta$  is defined such that the lifetime of a deeply bound effimov trimer is  $\sim \hbar/\eta E_T$ , where  $E_T$  is the trimer state energy [71, 72].

## Two body scattering rate

To assess the stability of a unitary gas, we compare  $\Gamma^{(3)}$  to the two-body elastic scattering rate,  $\gamma_{\text{el}} = n\sigma v$ . We are careful to define  $v$  as the relative velocity of two thermal particles,  $4\sqrt{k_B T/\pi m}$ , and  $\sigma = 8\pi\lambda_T^2$  at unitarity. The ratio of the two- and three-body rates is then locally:

$$\frac{\gamma_{\text{el}}}{\Gamma^{(3)}} = \frac{16\sqrt{2}}{9\zeta\sqrt{3}} \frac{1}{n\lambda_T^3}. \quad (3.3)$$

## Equilibrium criterion

For a system near the ideal-gas critical point<sup>2</sup>  $n\lambda_T^3 \approx 2.612$ , and the ratio of two- to three- body rates is  $\gamma_{\text{el}}/\Gamma^{(3)} \approx 0.56/\zeta$ . This means that for the case  $\zeta = 1$ , a critical gas cannot exist in equilibrium, and if we wish to study the universal strongly correlated physics in a unitary degenerate gas, we need to search for a species which has a non-universal parameter  $\zeta \ll 1$ . Until we have verified  $\zeta \ll 1$ , we work with thermal clouds ( $n\lambda_T^3 \ll 1$ ) for which the equilibrium criterion is satisfied.

## Experimental scheme

The experimental difficulty in finding  $\zeta$  lies in the fact that three-body effects cause both atom number decay *and* heating. Since temperature varies with time, Eq. 3.1 cannot be analytically integrated<sup>3</sup> (temperature enters via  $\langle n^2 \rangle$ , and  $L_3$  at unitarity). One solution offered in [67] is to hold the atoms in a shallow trap such that any heating leads to evaporation which keeps the temperature constant. By modeling this evaporation and assuming  $L_3 \propto 1/T^2$ , the value  $\zeta \approx 0.9$  was measured for  $^7\text{Li}$ . Here, we aim to extract  $\zeta$  for  $^{39}\text{K}$ , and we will use a method which allows us to experimentally verify (rather than assume)  $L_3 \propto 1/T^2$  along the way. The scheme for our approach is summarised as follows:

1. *Scaling Law 1:* We first eliminate  $T$  from the problem by empirically observing a simple scaling law,  $NT^\beta \approx \text{const.}$  in a three-body decay process, and we experimentally determine the parameter  $\beta$ .
2. *Scaling Law 2:* Using scaling law 1, Eq. 3.2 reduces to an integrable form  $\dot{N} = -AN^\nu$ , with a combination of the experimental exponents  $\beta$  and  $\nu$  revealing  $L_3 \propto 1/T^2$  at unitarity.

<sup>2</sup>Note that it is not known whether a phase space density of 2.612 is the condition for criticality at unitarity. We just use this weak-interaction result as a scale where interesting effects may start to occur.

<sup>3</sup>We need to integrate Eq. 3.1 because numerical differentiation of an experimental decay curve of atom number with respect to time leads to large uncertainties in  $\zeta$ .

3.  $\zeta$  *Extraction*: Using the values of  $A$  and  $\nu$  obtained by fitting data to the integrated form of  $\dot{N} = -AN^\nu$ , we can calculate  $\zeta$ .

We now consider each of these steps in the following sections.

## 3.2 Scaling Law 1: $NT^\beta = \text{const.}$

The first scaling law can be considered to be purely empirical for our purposes, but we will attempt to provide some theoretical justification for the values of  $\beta$  we observe in different regimes. We begin by outlining the experimental sequence, and then move on to display results supporting this scaling law. To emphasise the empirical nature of this law, we only suggest theoretical justification for the observed values of  $\beta$  after presenting the experimental results.

### 3.2.1 Experimental sequence

The experimental procedure is similar to the sequence in chapter 2, but here we ramp interactions up rather than down, and watch the system's evolution at the high interaction strength. More precisely, the sequence is:

1. Using the apparatus described in [24], we cool a cloud of  $^{39}\text{K}$  in the  $|F, m_F\rangle = |1, 1\rangle$  state with the interaction strength tuned to  $135 a_0$ . We stop the evaporative cooling when the cloud is still not condensed and then ramp up the trap depth to  $U \approx k_B \times 30 \mu\text{K}$  to prevent any further evaporation. We choose the point at which we stop the evaporation such that we achieve a temperature  $T \approx 1 \mu\text{K}$  ( $\lambda_T \approx 5000 a_0$ ) after the ramp up. At the final trap depth, the trap has an isotropic trapping frequency of  $\omega_{\text{ho}} = 2\pi \times 185 \text{ Hz}$ .
2. We then tune  $a$  to the desired value using the Feshbach resonance centred at 402.5 G. The external magnetic field which achieves this turns on in 10 ms. At this point, we have  $N \approx 10^5$  atoms. Note that these parameters give  $n \approx 3 \times 10^{12} \text{ cm}^{-3}$ , so  $n\lambda_T^3 < 0.1$ , and we can guarantee equilibrium even for  $\zeta = 1$ .
3. We let the cloud evolve at the chosen interaction strength for a variable hold time,  $t$ , of up to 4 s.
4. We simultaneously switch off both the trap and the Feshbach field (within  $\sim 100 \mu\text{s}$ )<sup>4</sup> and image the cloud after 5 ms ToF.

<sup>4</sup>Note that we must switch off the Feshbach field quickly, especially when starting at  $a < 0$ , to prevent atoms adiabatically following the molecular branch as  $a$  changes (see Fig. 1.1(b)). Such

### 3.2.2 Experimental verification of the scaling law

We have taken 19 data series, each at a fixed  $a$ , which span the range  $-12 < \lambda_T/a < 12$ . Fig. 3.2(a) shows an example the particle loss and heating during these sequences. Specifically, we show results for a resonantly interacting ( $\lambda_T/a = 0$ ) series in this figure. Note that we restrict our measurements to  $T < 2 \mu\text{K} \ll U/k_B$  to ensure that evaporative losses and cooling are always negligible.

In the inset of Fig. 3.2(b), we give an example series at  $\lambda_T/a = -5.3$  and  $8.5$  which illustrate that the variation of  $\log(N)$  with  $\log(T)$  is well captured by a straight line. This linear relationship is true for all our measurement series, which indicates the validity of scaling law 1. We extract the constant slope,  $\beta = -d[\log(N)]/d[\log(T)]$ , for all our series and plot this as a function of  $\lambda_T/a$  in Fig. 3.2(b). Note that in the unitary region ( $|\lambda_T/a| < 1$ ) all the measured values of  $\beta$  are the same to within the experimental errors. This is characteristic of the universal ( $a$ -independent) behaviour of a unitary gas.

Having observed evidence for the empirically driven scaling law 1, we now introduce some theoretical concepts to help to explain the numerical values of  $\beta$  in Fig. 3.2(b).

### 3.2.3 Theoretical estimates of $\beta$

Throughout our discussion, it is important to note that in our final analysis the exact values of  $\beta$  are not essential for extracting  $\zeta$ : only the existence of scaling law 1 is required. A very basic understanding of why three body loss should cause heating comes from the fact that three body processes preferentially occur in the densest central part of the trap. Since the potential energy is lowest here, this atom loss leads to heating through what could be considered as the opposite process to evaporative cooling.

Quantitatively, the rate at which the potential energy,  $\mathcal{U}$ , of the cloud varies as atoms are lost is:

$$\dot{\mathcal{U}} = \int \left[ \frac{1}{2} m \omega_{\text{h.o.}}^2 r^2 \right] \dot{n}(r) d^3\mathbf{r} = -L_3 \int \left[ \frac{1}{2} m \omega_{\text{h.o.}}^2 r^2 \right] n^3 d^3\mathbf{r}. \quad (3.4)$$

Using a Gaussian model for the non-degenerate density,  $n \propto \exp(m\omega_{\text{ho}}^2 r^2/2k_B T)$ , gives  $\dot{\mathcal{U}}/\dot{N} = \frac{1}{2}k_B T$ . The mean kinetic energy per atom is  $\frac{3}{2}k_B T$ , so the rate of

---

adiabatic following is undesirable because any molecules which form would not be resonant with the imaging light, and therefore the atom number would appear reduced.

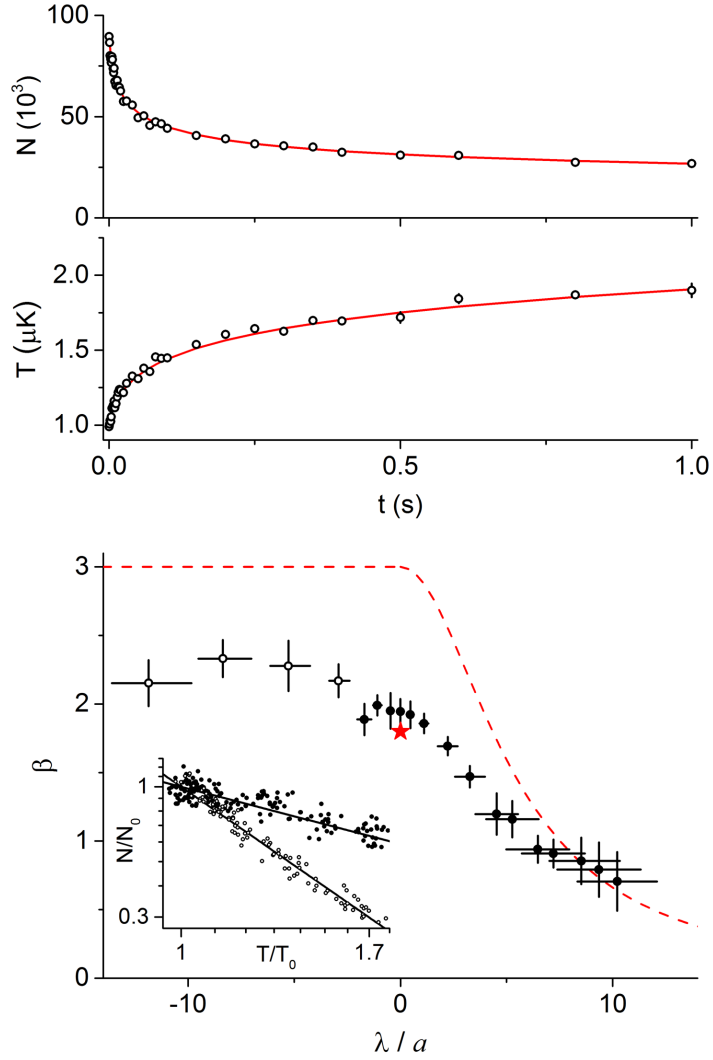


**Fig. 3.2.:** Particle loss and heating in a strongly interacting Bose gas. (a) The time evolution of the atom number and temperature of a resonantly interacting gas ( $\lambda_T/a = 0$ ) held in a deep optical trap. Each point is an average of 5 measurements and error bars show statistical errors. Solid red lines are fits based on Eq. 3.10 and scaling law 1. (b) Heating exponent  $\beta$ , as defined in scaling law 1. The red dashed line is a result of non-unitary three-body theory, while the red star indicates the predicted value of 1.8 at unitarity [67]. Open symbols indicate the region where four-body decay is significant (see text and Fig. 3.4). Note that  $\lambda_T \approx 5 \times 10^3 a_0$  and horizontal error bars reflect its variation during a measurement sequence at a fixed  $a$ . Vertical error bars show fitting uncertainties. Inset: Log-log plots of  $N$  vs.  $T$  (scaled to their values at  $t = 0$ ) for the data series at  $\lambda_T/a \approx -5.3$  (open) and 8.5 (solid).

change of the total energy,  $E = 3Nk_B T$ , of the cloud is  $\dot{E}/\dot{N} = 2k_B T$ . This gives the following scaling law:

$$\frac{3\dot{N}k_B T + 3Nk_B \dot{T}}{\dot{N}} = 2k_B T \quad \implies \quad NT^3 = \text{const.} \quad (\lambda_T/a \ll 0). \quad (3.5)$$

This very simple model predicts the form of the scaling law we observe, and predicts  $\beta = 3$ . However, referring to Fig. 3.2(b), we see that it does not correctly capture the experimental data which shows wide variations of  $\beta$  with  $\lambda_T/a$ . We consider the modifications to this simple theory for  $\lambda_T/a \ll 0$ ,  $\lambda_T/a \gg 0$  and  $\lambda_T/a \rightarrow 0$  cases separately below.

### $\beta$ for $\lambda_T/a \gg 0$

From Fig. 3.1, the closest three-body state to free atoms for  $a > 0$  is the shallow molecular dimer state, with the third atom gaining most of the released binding energy. The fate of the molecule and third atom can be summarised as follows (see Fig. 3.3):

- *Third Atom:* When the dimer forms, it releases binding energy  $\epsilon$  which can be calculated from the length scale  $a$  of the shallow dimer:  $\epsilon = \hbar^2/ma^2$ . For  $a/\lambda_T > 1$ , we ignore the initial kinetic energy of the atoms, meaning that energy and momentum conservation dictate the energy of the third atom after the three-body collision to be  $\frac{2}{3}\epsilon$ . For  $a > 300 a_0$  (i.e.  $\lambda_T/a < 17$ ), this energy is less than our trap depth ( $\approx k_B \times 30 \mu\text{K}$ ) and the atom will remain in the trap. Therefore the cloud is heated by an energy contribution  $\frac{2}{3}\epsilon$  per collision event.

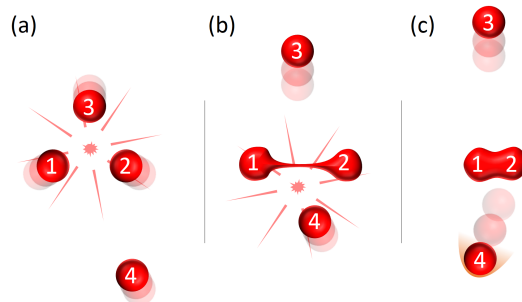


**Fig. 3.3.:** The fate of three atoms colliding with  $a > 0$ . (a) Approach of three atoms within a distance  $a$ . (b) Two atoms form a shallow dimer and the third atom (3) flies away with  $2/3$  of the dimer binding energy (insufficient to knock the atom out of the trap). (c) A fourth atom (4) collides with the dimer allowing it to relax to a deeply bound state. The fourth atom picks up  $\sim 2/3$  of the deep dimer binding energy and is ejected from the trap, along with the deep dimer.

- *Shallow dimer*: The shallow dimer will collide with a fourth atom to decay into a deeply bound state and leave the trap. The fourth atom gains most of the deep binding energy which is sufficient to eject it from the trap.

The net result of this process is to modify our calculation in Eq. 3.5. Whereas in Eq. 3.5, we stated that that three atoms each originally carry average energy  $2k_B T$ , and all this energy is lost when the atoms leave, we have now argued that atom 3 in Fig. 3.3 remains in the trap with energy  $\frac{2}{3}\epsilon$ . Therefore, the total energy of the cloud is reduced by  $[3(2k_B T) - \frac{2}{3}\epsilon]$  in each three body event. Using  $\epsilon = \hbar^2/ma^2$ , we can write:

$$\frac{\dot{E}}{\dot{N}} = k_B T \left[ 2 - \frac{1}{9\pi} \left( \frac{\lambda_T}{a} \right)^2 \right] \implies 3Nk_B \frac{dT}{dN} = -k_B T \left[ 1 + \frac{1}{9\pi} \left( \frac{\lambda_T}{a} \right)^2 \right] \quad (3.6)$$

Strictly speaking, we should integrate Eq. 3.6 as before to extract the law governing the decay. However, the dependence of  $\lambda_T$  on  $T$  complicates this integration. We note that our experimental decay curves cover at most a factor of 2 in temperature range ( $1 - 2 \mu\text{K}$ ). For a modest  $\lambda_T/a = 5$ , as  $T$  increases by a factor of 2, the factor  $[1 + 1/9\pi(\lambda_T/a)^2]$  only falls to 80% of its original value. We therefore treat  $\lambda_T/a$  as a constant in this integration to obtain  $\beta = 3/[1 + 1/9\pi(\lambda_T/a)^2]$ .

We find that this approximate form for  $\beta$  is a good match for the data in the range  $5 < \lambda_T/a < 10$ . For  $\lambda_T/a < 5$ , the data bends away from this crude prediction because the unitarity effects discussed in the next section start to play a role.

### $\beta$ for $\lambda_T/a \rightarrow 0$ (unitarity)

Considerable theoretical work was carried out in [67], leading to the prediction  $\beta = 1.8$  at unitarity. This value arises from two contributions

- As before, preferential removal of atoms from the lowest potential energy regions of the trap gives  $\dot{U}/\dot{N} = \frac{1}{2}k_B T$ .
- At unitarity, three body effects also preferentially remove low kinetic energy particles. The scattering length,  $a$ , is capped by the deBroglie wavelength,  $\lambda_{dB}$  of the atoms, meaning that at unitarity high kinetic energy atoms experience a lower effective interaction strength than low kinetic energy atoms. Thus there is a higher loss rate for low kinetic energy atoms, and it can be shown that the total effective rate of loss of kinetic energy is  $\dot{E}_{\text{kin}}/\dot{N} = \frac{5}{6}k_B T$  [67].

Combining these contributions gives  $\dot{E}/\dot{N} = \frac{5}{6}k_B T$  which can be integrated as in Eq. 3.5 to give  $\beta = \frac{9}{5}$ . Experimentally, we find  $\beta = 1.94 \pm 0.09$  on resonance, which is close to the unitary prediction.

### $\beta$ for $\lambda_T/a \ll 0$

Referring to Fig. 3.1, the closest three-body state to free atoms for  $a < 0$  is an Efimov trimer state. This state is very short lived, rapidly decaying into an un-trapped deeply bound dimer with the third atom gaining most of the released binding energy and also escaping the trap [73]. On its own, this loss mechanism should lead to  $\beta = 3$  as predicted above, but in Fig. 3.2(b), we see that the experimental value of  $\beta$  does not rise to meet this expected value.

One possible reason for this difference is the presence of four-body processes at  $a < 0$ . Studies using  $^{133}\text{Cs}$  have previously observed four-body loss features in the  $a < 0$  region [58], and indirect evidence of four-body decay in a  $^{39}\text{K}$  gas at  $a < 0$  was seen in [23] (but not in [64], where the initial cloud density was significantly lower). We find evidence of four-body processes by analysing the dynamics of the particle loss in the following way:

In the presence of dominant three- and four-body processes, the atom number should evolve according to:

$$\dot{N} = -L_3 \langle n^2 \rangle N - L_4 \langle n^3 \rangle N, \quad (3.7)$$

Where  $L_3$  and  $L_4$  are the three- and four-body rate coefficients respectively, which, far from unitarity, depend only on  $a$ . We numerically evolve Eq. 3.7 for each data series at constant  $a$ , using the measured values of  $T(t)$  to evaluate  $\langle n^i \rangle$  for a calculated  $N(t)$  in a Gaussian model. We then fit the constants  $L_3$  and  $L_4$  to our experimental decays. This allows us to evaluate the relevance of each term. The results are summarised in table 3.1, and illustrated in Fig. 3.4. We compare the cases of  $a < 0$  and,  $a > 0$  below:

For  $a = -850a_0$ , only the decay model which includes both three- and four-body decay captures the data well ( $\chi^2 \approx 1$ ), and a pure four- (three-)body decay in which  $L_3$  ( $L_4$ ) is fixed to 0 does not. This means that *both* the three- and four- body terms are relevant. We find a similar conclusion for all our data with  $-2000 < a/a_0 < -400$ . Furthermore by comparing the fitted values of  $L_3$  and  $L_4$  in the ratio  $L_4 n/L_3$ , we find that  $L_4$  is relevant for densities  $> 10^{12} \text{ cm}^{-3}$  (note that this criterion on density reconciles the observations of [23, 64] in which the experiments were carried out at different densities).

$a/a_0$	$L_3$	$L_4$	$\chi^2$
-850	free	free	1
	free	0	7
	0	free	4
+700	free	free	1
	free	0	1
	0	free	2

**Tab. 3.1.:** Evidence of four-body decay for  $a < 0$ . We try to fit our data at  $a = -850a_0$  and  $+700a_0$  using the numerically evolved form of Eq. 3.7. We allow either or both of  $L_3$  and  $L_4$  to be free parameters or fixed to zero, and measure the goodness-of-fit metric,  $\chi^2$ .

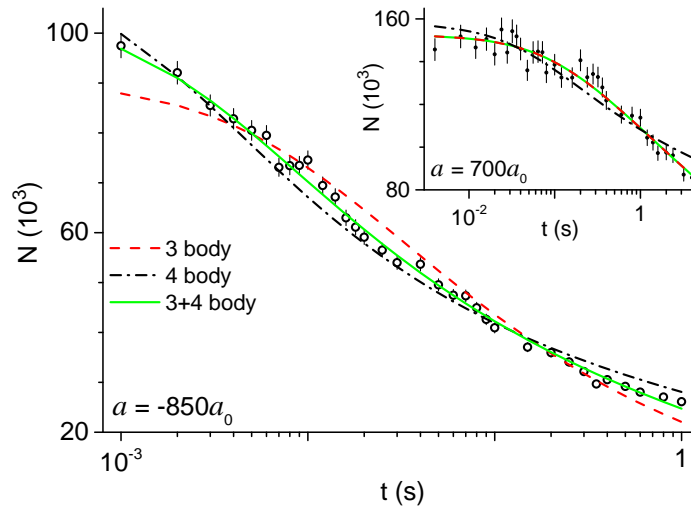


**Fig. 3.4.:** Three- vs four-body decay for  $a < 0$  (away from unitarity). The decay of  $N$  at  $a = -850a_0$  is fitted to a model including both three- and four-body losses (green solid line), as well as to pure three- and pure four-body models (red dashed and black dot-dashed line, respectively). Inset: For comparison, at  $a = 700a_0$ , the solid green and the dashed red lines are indistinguishable, showing that four-body decay does not play a detectable role.

For  $a = +700a_0$ , we find that the model which includes three- and four-body decay gives essentially the same fit as a pure three-body decay (within our 10% fitting errors on  $L_3$ ), with  $\chi^2 \approx 1$  in both cases. A pure four-body decay does not capture the data well ( $\chi^2 \approx 2$ ). This excludes  $L_4$  as a relevant fitting parameter for  $a > 0$ , meaning the decay is three-body dominated. Using a similar procedure, we also checked that we do not detect any five-body decay for either  $a < 0$  or  $a > 0$ .

Since we are ultimately interested in the  $\zeta$  parameter for three-body processes, we exclude the four-body region ( $a/\lambda_T \ll 0$ ) from the remainder of the analysis. Having now experimentally established scaling law 1 between  $N$  and  $T$ , and having understood the limits of  $\beta$ , we may now proceed to the second scaling law in the next section.

### 3.3 Scaling Law 2: $L_3 \propto 1/T^2$ at unitarity

Armed with the experimental result  $NT^\beta = \text{const}$ , we eliminate the varying temperature from the differential equation in Eq. 3.1. Using a Gaussian model for the thermal cloud gives

$$\langle n^2 \rangle = N^2 \left( \frac{m\omega_{\text{ho}}^2}{2\pi\sqrt{3}k_B T} \right)^3, \quad (3.8)$$

and we parameterise the scaling of  $L_3$  with temperature as  $L_3 \propto T^{-\alpha}$ . Combining these parametrisations in Eq. 3.1, we can write  $\dot{N} \propto -N^3 T^{-3-\alpha}$ . Now invoking scaling law 1, this becomes:

$$\dot{N} = -AN^\nu, \quad (3.9)$$

where we introduced  $\nu = 3 + \frac{3+\alpha}{\beta}$ , and  $A$  is constant. Away from unitarity, we expect  $L_3$  to be temperature independent (depending only on  $a$ ), while at unitarity, we expect  $L_3 \propto 1/T^2$ . Explicitly, the onset of this unitary scaling can be detected by a change of  $\nu$  from  $3 + 3/\beta$  to  $3 + 5/\beta$ .

Eq. 3.9 can be integrated to give:

$$N(t) = [A(\nu - 1)t + N(0)^{1-\nu}]^{1/(1-\nu)}. \quad (3.10)$$

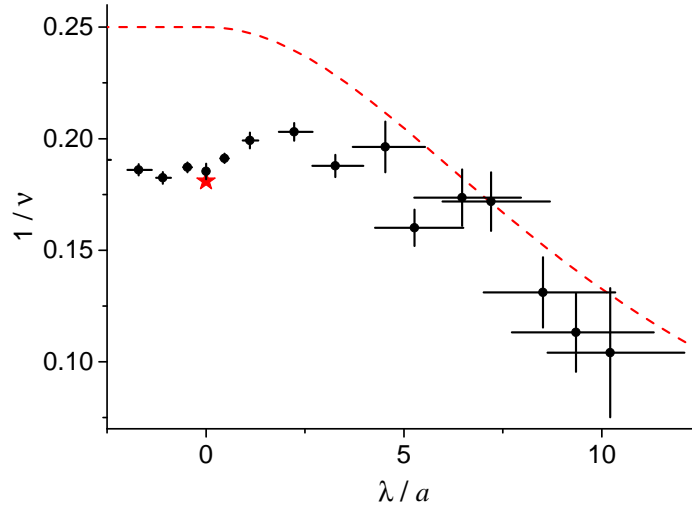


**Fig. 3.5.:** Particle-loss exponent  $\nu$ , as defined in Eq. 3.9. The red dashed line shows the nonunitary theory,  $\nu = 3 + 3/\beta$ , assuming nonunitary theoretical  $\beta$  values. The red star shows the unitary prediction,  $\nu = 3 + 5/\beta$ , corresponding to  $L_3 \propto 1/T^2$  and the measured  $\beta$ . Error bars are analogous to those in Fig. 3.2(b).

We fit the atom decay to this form with  $A$  and  $\nu$  as free parameters. An example fit is shown for the resonant ( $\lambda_T/a = 0$ ) series in Fig. 3.2(a) together with a fit to  $T(t)$  found by combining the fitted  $N(t)$  and the fitted  $\beta$  in scaling law 1.

Fig. 3.5 shows the values of  $\nu$  for all our three-body dominated decays. The dashed line in this figure corresponds to the non-unitary theory,  $\nu = 3 + 3/\beta$  using the theoretical values of  $\beta$  from section 3.2.3. Again, we see surprisingly good agreement in the range  $5 < \lambda_T/a < 10$ . For  $\lambda_T/a < 5$ , we see the data start to diverge away from the non-unitary theory, and instead approach the prediction  $\nu = 3 + 5/\beta$  (using the measured value of  $\beta$  on resonance). From the measured value of  $\nu$  on resonance, we obtain  $\alpha = 1.7 \pm 0.3$  (i.e.  $L_3 \sim 1/T^{1.7 \pm 0.3}$ ), which is in agreement with the expected  $1/T^2$  scaling.

The remaining fit parameter,  $A$ , will be discussed in the next section, where we use its value to extract  $\zeta$ .

### 3.4 Extraction of the rate parameter $\zeta$

Comparing the definition of  $A$  to the definition of  $L_3$  in Eq. 3.1, we obtain:

$$L_3(t) = 3\sqrt{3} \left( \frac{2\pi k_B T(t)}{m\omega_{\text{h.o.}}} \right) N(t)^{\nu-3} A. \quad (3.11)$$

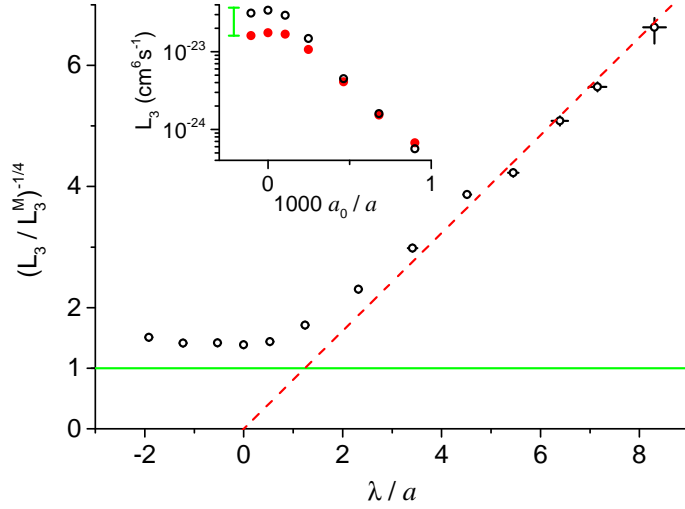


**Fig. 3.6.:** Three-body loss coefficient. Main panel:  $(L_3/L_3^M)^{-1/4}$  (see text) at  $T = 1.1 \mu\text{K}$ . The horizontal green line marks the theoretical upper bound on  $L_3$ , while the red dashed line is a guide to the eye showing the  $L_3 \propto a^4$  nonunitary scaling. At unitarity,  $L_3/L_3^M \propto 0.27$ . Inset:  $L_3$  at  $1.1 \mu\text{K}$  (open symbols) and  $1.7 \mu\text{K}$  (solid symbols). The expected ratio between the two unitary plateaux is indicated by the green vertical bar.

Inserting all of our raw data,  $N(t)$  and  $T(t)$ , with the fitted parameters,  $\nu$  and  $A$ , into this expression, allows us to reconstruct  $L_3(a, T)$ . In Fig. 3.6 we show  $L_3$  at a fixed  $T = 1.1 \mu\text{K}$ , scaled to the theoretical upper bound,  $L_3^M(T)$ , obtained by setting  $\zeta = 1$  in Eq. 3.2. Plotting  $(L_3/L_3^M)^{-1/4}$  vs.  $\lambda_T/a$  clearly reveals two key effects. Firstly, for  $\lambda_T/a > 3$ , we see the non-unitary scaling  $L_3 \propto a^4$ . Secondly, we observe the saturation of  $L_3$  for  $|\lambda_T/a| < 1$  to an  $a$ -independent value  $\approx 0.27L_3^M$  (i.e.  $\zeta \approx 0.27$ ). This saturation is characteristic of the universal behaviour at unitarity, and we have checked that the ratio of the saturated values at different temperatures is in line with expected  $1/T^2$  scaling (see Fig. 3.6 inset).

We refine our estimate of  $\zeta$  by fixing  $\nu = 3 + 5/\beta$  and re-analysing the three data series taken closest to the resonance, ( $|\lambda_T/a| < 0.6$ ). By this method, we obtain  $\zeta = 0.29 \pm 0.03^5$ , with a systematic uncertainty (due to absolute atom-number calibration) of about 30%. This value of  $\zeta$  (approximately three times smaller than the theoretical maximum) makes  $^{39}\text{K}$  a promising candidate for many-body physics in a unitary Bose gas because the ratio of two- to three-body rates becomes  $\gamma_{\text{el}}/\Gamma^{(3)} \approx 5/n\lambda_T^3$ . There are still open questions regarding magnitude of phase space densities at which exotic states first form at unitarity, and the exact number of collisions required to recover equilibrium at unitarity. These questions make it difficult to give precise statements about whether this balance of two- and three-body rates is sufficient to achieve a stable degenerate  $^{39}\text{K}$  gas in unitarity. However,

<sup>5</sup>Recalling the definition of the Efimov width parameter,  $\eta$ , as  $\zeta = 1 - e^{-4\eta}$ , we deduce  $\eta = 0.09 \pm 0.04$ .

we can say that a gas of  $^{39}\text{K}$  atoms can be used to probe phase space densities three times higher than  $^7\text{Li}$  ( $\zeta = 0.9$ ) while remaining in equilibrium at unitarity.

## 3.5 Conclusion

In this chapter, we have characterised the stability of a  $^{39}\text{K}$  gas at and near unitarity. We experimentally verified two general scaling laws characterising particle loss and heating in the unitary regime, namely  $NT^\beta = \text{const.}$  and  $L_3 \propto 1/T^2$ . Using these laws we were able to measure the species-specific three-body loss parameter,  $\zeta$ . We find a value  $\zeta = 0.29 \pm 0.03$  for  $^{39}\text{K}$ , meaning the three body rate in this species is roughly 3 times smaller than the theoretical maximum. This could allow a degenerate unitary  $^{39}\text{K}$  to be observed in (quasi)equilibrium.

Note that since this work was carried out, a study of a degenerate unitary  $^{85}\text{Rb}$  gas was reported in [74].  $^{85}\text{Rb}$  has a 10 G wide Feshbach resonance at 155.05 G [75], and a value of  $\zeta \approx 0.21$  [63] (similar to our observed  $\zeta$ ). This gives us further encouragement that our  $^{39}\text{K}$  system will be useful for future studies into the universal physics at unitarity. However, the work in [74] highlights a further problem with studying unitary systems: the absolute time-scales in a unitary gas are extremely short. For example, three body loss limits the lifetime of the gas in [74] to  $\approx 600 \mu\text{s}$ . Such rapid decays pose many technical challenges, the most notable being the difficulty of ramping the Feshbach magnetic field to the resonance in a time much shorter than the cloud lifetime.



# Part II

---

Trap Geometry



# Introduction

All of the experiments in the first part of this thesis were carried out in parabolic traps. In these experiments considerable effort is put into controlling the frequency, polarisation, intensity, and alignment of the many laser beams which manipulate and probe an atom cloud. However, little attempt is made to sculpt a laser beam's profile beyond the simple Gaussian mode which comes straight out of a commercial source. When used for optical trapping, these Gaussian modes produce a parabolic potential to first order. While a parabolic trap may be the easiest optical geometry to produce, it is not always the most revealing trap shape in which to study many-body quantum mechanics. New trap geometries can produce different forms for the density of states, different dispersion relations [13], different transport properties [76, 77], and (of relevance to chapter 3) different three-body loss rates. This can lead to interesting physics being either highlighted or obscured by the experimental trap geometry.

In this part of the thesis, we will use an optical technique described in chapter 5 for sculpting complex atom traps beyond simple parabolae. In chapters 6, 7 and 8 we will concentrate on one particular novel geometry - the uniform trap - and we will present the first work which experimentally probes a truly homogeneous Bose gas. Many quantum theories, including Einstein's original BEC proposal, are phrased in terms of homogeneous systems, but until now it has been experimentally challenging to produce the sharp walls needed to box off a uniform region of space in which to trap an atom cloud. Our uniform box trap opens many future research paths, and here, we will present two contrasting routes:

**Chapter 7** *Equilibrium* studies of condensation and the ground state in a uniform potential

**Chapter 8** *Dynamical* studies of the BEC phase transition in a uniform potential

Additional ideas for future research directions in our uniform system are presented in chapter 9.

Since optical methods are crucial for realising and probing our flexible trap geometries, we will use this chapter to briefly review the theory of atom-light interaction before embarking on any experimental details.

## 4.1 Atom-light interactions

A full treatment of atom-light interactions can become very complicated, so we will work under a careful set of assumptions which allow us to develop a useful intuition without undue theoretical labour. These assumptions are enumerated explicitly below in the context of a laser beam of frequency  $\omega$  driving an atomic transition between a ground state  $|g\rangle$  and excited state  $|e\rangle$  separated by energy  $\hbar\omega_0$  (see Fig. 4.1(a)).

1. *Semi-classical approximation*: In our treatment we will quantise the atom's energy, but we will treat the laser radiation as a classical electric field  $\mathbf{E} = \mathbf{E}_0 \cos(\omega t)$ . Qualitatively, this is justified by the large occupation of the laser mode.
2. *Dipole approximation*: Since the atom is smaller than the wavelength of incident radiation ( $a_0 \ll \lambda$ ), we ignore the spatial variation of the electric field and treat the microscopic theory as a local picture with spatial variation inserted by hand at the end.
3. *Rotating wave approximation*: We assume that the laser is tuned sufficiently close to resonance such that the detuning  $\delta = \omega - \omega_0$  is much smaller than the laser frequency. Specifically, the rotating wave approximation requires  $|\delta| \ll \omega + \omega_0$
4. *No scattering limit*: From Eq. 2.25, we see that after applying the rotating wave condition, the rate at which an atom incoherently scatters incident photons is proportional to  $(\Gamma/\delta)^2$ , where  $\Gamma$  is the linewidth of the atomic transition. Here, we will work in the limit  $\Gamma \ll \delta$  such that we can ignore these spontaneous scattering events.

Using these assumptions, we can build a framework for describing the behaviour of atoms in off resonant laser light. In particular, in section 4.1.1, we will describe the coherent single photon process which will be used for constructing the potentials and in section 4.1.2, we will discuss two photon processes used to probe the properties of the trapped atom clouds.

### 4.1.1 1-Photon: The AC Stark effect

The AC Stark effect is a phenomenon in which an optical field creates either a trapping or anti-trapping potential for the atoms. The techniques described in the following chapters all rely on this effect to link the optical intensity to the depth of

the potential experienced by the atoms. Once this link is established, the task of producing potentials of complex geometry is reduced to the task of sculpting optical fields. The derivation below explicitly reveals the link between intensity and potential, and is included in detail for comparison with the two-photon theory in section 4.1.2.

The arrangement we use to describe the AC stark effect is illustrated in Fig. 4.1(a), consisting of a single laser illuminating a two-level atom. Under the semi-classical approximation, the laser introduces a term  $-\hat{\mathbf{d}} \cdot \mathbf{E}$  into the two-level atomic Hamiltonian, where  $\hat{\mathbf{d}} = q\hat{\mathbf{r}}$  is the electric dipole operator for the atom. In a simple hydrogen-like atom  $q$  is the electron charge and  $\hat{\mathbf{r}}$  is the position operator for the electron. For basis states with definite parity the diagonal matrix elements of  $\hat{\mathbf{d}}$  are zero, and we can write:

$$\hat{H} = \hbar\omega_0 |e\rangle \langle e| - \left[ \hat{\mathbf{d}} \cdot \mathbf{E}_0 \cos(\omega t) |e\rangle \langle g| + h.c. \right] \quad (4.1)$$

The Schrödinger equation for the time evolution of the two-level atom wavefunction  $|\psi\rangle = c_g |g\rangle + c_e |e\rangle$  in  $\hat{H}$  is then:

$$i\hbar \begin{pmatrix} \dot{c}_g \\ \dot{c}_e \end{pmatrix} = \hbar \begin{pmatrix} 0 & \Omega \cos(\omega t) \\ \Omega \cos(\omega t) & \omega_0 \end{pmatrix} \begin{pmatrix} c_g \\ c_e \end{pmatrix}, \quad (4.2)$$

where  $\Omega = -\langle g | \hat{\mathbf{d}} \cdot \mathbf{E}_0 | e \rangle / \hbar$  is the Rabi frequency for the interaction. Now we make the unitary transformation  $(\tilde{c}_g, \tilde{c}_e)^T = (c_g, e^{i\omega t} c_e)^T$  and apply the rotating wave approximation to remove rapidly oscillating terms<sup>1</sup>:

$$i \frac{d}{dt} \begin{pmatrix} \tilde{c}_g \\ \tilde{c}_e \end{pmatrix} = \frac{1}{2} \begin{pmatrix} 0 & \Omega \\ \Omega & -2\delta \end{pmatrix} \begin{pmatrix} \tilde{c}_g \\ \tilde{c}_e \end{pmatrix} \quad \Longrightarrow \quad \hat{H}_{\text{eff}} = \frac{\hbar}{2} \begin{pmatrix} 0 & \Omega \\ \Omega & -2\delta \end{pmatrix}, \quad (4.3)$$

<sup>1</sup>Strictly speaking, we should first perform the transformation  $(\tilde{\tilde{c}}_g, \tilde{\tilde{c}}_e)^T = (c_g, e^{i\omega_0 t} c_e)^T$  which produces terms oscillating at frequency  $\delta$  and  $\omega + \omega_0$ . At this point we can use the rotating wave approximation to drop the  $\omega + \omega_0$  terms before applying a second unitary transformation  $(\tilde{c}_g, \tilde{c}_e)^T = (\tilde{\tilde{c}}_g, e^{i\delta t} \tilde{\tilde{c}}_e)^T$ . For clarity, we combine the unitary transformations into a single operation in the main text and appeal to the intuitive interpretation of the rotating wave approximation as a removal of "rapidly oscillating terms". This produces the same results.

Diagonalising the effective Hamiltonian,  $\hat{H}_{\text{eff}}$  in Eq. 4.3 reveals a new ground state energy,

$$U = \frac{\hbar\Omega^2}{4\delta} \propto \frac{I}{\delta}, \quad (4.4)$$

Where we have taken the limit of large detuning:  $\delta \gg \Omega$  and  $I \propto \Omega^2$  is the intensity of the laser. This shift of the ground state provides an effective potential for the atoms due to the interaction with the light. Equation 4.4 provides all our qualitative understanding of the optical trapping potential,  $U$ :

- The depth of the potential is directly proportional to the local intensity of the light field.
- The sign of the potential depends on the detuning,  $\delta$ . Red-detuned light (i.e.  $\omega < \omega_0$ ) produces attractive potentials, and blue detuned light ( $\omega > \omega_0$ ) produces repulsive potentials.

Although Eq. 4.4 is conceptually useful, we often do not work in the  $|\delta| \ll \omega_0$  regime required for the rotating wave approximation. Instead, we use large detunings in order to minimise technical heating due photon scattering (see Eq. 2.25). A more careful derivation of the optical potential, which is valid for large detunings, gives [15, 47]:

$$U = -\frac{3\pi c^2}{2\omega_0^3} \left( \frac{\Gamma}{\omega_0 - \omega} + \frac{\Gamma}{\omega_0 + \omega} \right) I, \quad (4.5)$$

where  $c$  is the speed of light and  $\Gamma$  is the linewidth of the transition. This expression retains all the qualitative properties of Eq. 4.4 discussed above, the key result being that the potential experienced by the atoms is proportional to the local intensity of the light. Since the intuition that  $U \propto I$  is sufficient to understand that we can directly sculpt a potential landscape for atoms by shaping the optical field, we can now move on from our 1-photon discussion to start describing 2-photon processes.

### 4.1.2 2-Photon: Stimulated Raman scattering

In chapters 7 and 8, we will use a technique known as Bragg spectroscopy to probe atom clouds produced in our novel trap geometries. At the heart of this technique is a 2-photon process in which the atom absorbs a photon from one laser beam and then emits into a second beam (Raman scattering). Since the theory of this process follows along similar lines to the 1-photon AC Stark effect already described, we

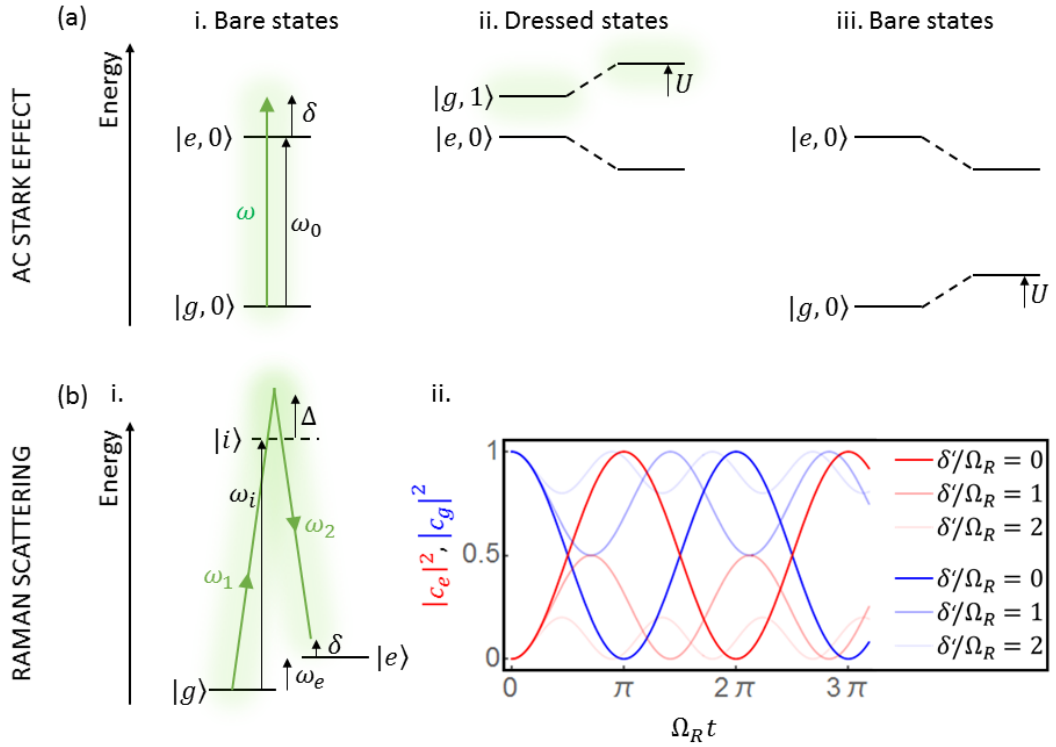


**Fig. 4.1.:** Illustration of atom-light interactions discussed in this chapter. (a) Level diagrams illustrating the AC stark effect. States are labelled with  $|\text{atomic state, photon number}\rangle$ , and  $\hbar$  is omitted for clarity. (a.i.) The bare states illuminated by laser light of frequency  $\omega$ . (a.ii.) Performing a unitary transformation gives the dressed state picture described by  $\hat{H}_{\text{eff}}$  in Eq. 4.3. The dashed lines illustrate the effect of the off-diagonal coupling terms in  $\hat{H}_{\text{eff}}$  on the eigenstates of the diagonal part. (a.iii.) Transforming the coupled states back to the bare state picture reveals a shift  $U$  to the ground state energy, which we treat as an external potential. (b) Illustration of stimulated Raman two-photon scattering. (b.i.) The level diagram for a three state atom absorbing frequency  $\omega_1$  and emitting at  $\omega_2$ . (b.ii.) Solution for the occupation of the ground (blue) and excited state (red) as a function of time according to Eq. 4.12 for different detunings,  $\delta$ .

will derive the basic expressions for the behaviour of an atom in the presence of two laser beams here and then later expand upon theory for application in Bragg spectroscopy in section 7.2.1.

Consider the arrangement shown in Fig 4.1(bi.) where two lasers with frequencies  $\omega_1$  (laser 1) and  $\omega_2$  (laser 2) illuminate a three-level system,  $\{|g\rangle, |i\rangle, |e\rangle\}$  with energy levels  $\{0, \hbar\omega_i, \hbar\omega_e\}$  respectively, ( $0 < \omega_e \ll \omega_i$ ). We assume that the energy levels are sufficiently resolved to allow us to treat the transition  $|g\rangle \rightarrow |i\rangle$  (driven by laser 1) separately from  $|i\rangle \rightarrow |e\rangle$  (driven by laser 2). Under this arrangement, the Hamiltonian for the atom in the laser fields is:

$$\hat{H} = \hbar\omega_i |i\rangle \langle i| + \hbar\omega_e |e\rangle \langle e| - \left[ \hat{\mathbf{d}} \cdot \mathbf{E}_0^1 \cos(\omega_1 t) |i\rangle \langle g| + \hat{\mathbf{d}} \cdot \mathbf{E}_0^2 \cos(\omega_2 t) |i\rangle \langle e| + h.c. \right], \quad (4.6)$$

where  $\mathbf{E}_0^n$  is the electric field envelope produced by laser  $n$  ( $n \in \{1, 2\}$ ). As in the discussion of the AC Stark effect, we immediately write the time evolution of the atomic wavefunction  $|\psi\rangle = c_g |g\rangle + c_i |i\rangle + c_e |e\rangle$  according to the Schrödinger equation:

$$i\hbar \begin{pmatrix} \dot{c}_g \\ \dot{c}_i \\ \dot{c}_e \end{pmatrix} = \hbar \begin{pmatrix} 0 & \Omega_1 \cos(w_1 t) & 0 \\ \Omega_1 \cos(w_1 t) & \omega_i & \Omega_2 \cos(w_2 t) \\ 0 & \Omega_2 \cos(w_2 t) & \omega_e \end{pmatrix} \begin{pmatrix} c_g \\ c_i \\ c_e \end{pmatrix}, \quad (4.7)$$

where  $\Omega_n = -\langle g | \hat{\mathbf{d}} \cdot \mathbf{E}_0^n | e \rangle / \hbar$  is the Rabi frequency for the transition driven by laser  $n$ . Now using the unitary transformation  $(\tilde{c}_g, \tilde{c}_i, \tilde{c}_e)^T = (c_g, e^{i\omega_1 t} c_i, e^{i(\omega_1 - \omega_2)t} c_e)^T$ , and applying the rotating wave approximation, Eq. 4.7 becomes:

$$i \frac{d}{dt} \begin{pmatrix} \tilde{c}_g \\ \tilde{c}_i \\ \tilde{c}_e \end{pmatrix} = \frac{1}{2} \begin{pmatrix} 0 & \Omega_1 & 0 \\ \Omega_1 & -2\Delta & \Omega_2 \\ 0 & \Omega_2 & -2\delta \end{pmatrix} \begin{pmatrix} \tilde{c}_g \\ \tilde{c}_i \\ \tilde{c}_e \end{pmatrix}, \quad (4.8)$$

where  $\Delta = \omega_1 - \omega_i$  and  $\delta = (\omega_1 - \omega_2) - \omega_e$ . In the case  $\Delta \gg \Omega_n, \delta$  Eq. 4.8 predicts that  $\tilde{c}_i$  will oscillate much faster than the amplitudes of the other states, implying that  $d\tilde{c}_i/dt$  will average to zero over timescales in which the other amplitudes change. This allows us to perform a so-called "adiabatic elimination" [78] of the intermediate state,  $|i\rangle$ :

$$\tilde{c}_i = \frac{\Omega_1}{2\Delta} \tilde{c}_g + \frac{\Omega_2}{2\Delta} \tilde{c}_e \quad \Longrightarrow \quad i \frac{d}{dt} \begin{pmatrix} \tilde{c}_g \\ \tilde{c}_e \end{pmatrix} = \begin{pmatrix} \frac{\Omega_1^2}{4\Delta} & \frac{\Omega_1 \Omega_2}{4\Delta} \\ \frac{\Omega_1 \Omega_2}{4\Delta} & \frac{\Omega_2^2}{4\Delta} - \delta \end{pmatrix} \begin{pmatrix} \tilde{c}_g \\ \tilde{c}_e \end{pmatrix}. \quad (4.9)$$

The terms  $\Omega_n^2/4\Delta$  in the diagonal elements of the matrix above arise from the AC Stark shift of the atom's energy levels. Therefore, we define a new detuning,  $\delta'$ , taken with respect to these shifted levels:

$$\delta' = \delta - \frac{\Omega_2^2}{4\Delta} + \frac{\Omega_1^2}{4\Delta} \quad \Longrightarrow \quad i \begin{pmatrix} \dot{\tilde{c}}_g \\ \dot{\tilde{c}}_e \end{pmatrix} = \begin{pmatrix} \frac{\Omega_1^2}{4\Delta} & \frac{\Omega_1 \Omega_2}{4\Delta} \\ \frac{\Omega_1 \Omega_2}{4\Delta} & \frac{\Omega_1^2}{4\Delta} - \delta' \end{pmatrix} \begin{pmatrix} \tilde{c}_g \\ \tilde{c}_e \end{pmatrix} \quad (4.10)$$

Solving the coupled differential equations in Eq. 4.10 gives:

$$\begin{pmatrix} \tilde{c}_g(t) \\ \tilde{c}_e(t) \end{pmatrix} = \begin{pmatrix} \cos\left(\frac{1}{2}\Omega_{\text{eff}}t\right) + i\frac{\delta'}{\Omega_{\text{eff}}}\sin\left(\frac{1}{2}\Omega_{\text{eff}}t\right) & -i\frac{\Omega_R}{\Omega_{\text{eff}}}\sin\left(\frac{1}{2}\Omega_{\text{eff}}t\right) \\ -i\frac{\Omega_R}{\Omega_{\text{eff}}}\sin\left(\frac{1}{2}\Omega_{\text{eff}}t\right) & \cos\left(\frac{1}{2}\Omega_{\text{eff}}t\right) - i\frac{\delta'}{\Omega_{\text{eff}}}\sin\left(\frac{1}{2}\Omega_{\text{eff}}t\right) \end{pmatrix} \begin{pmatrix} \tilde{c}_g(0) \\ \tilde{c}_e(0) \end{pmatrix}, \quad (4.11)$$

where  $\Omega_R = \Omega_1\Omega_2/2\Delta$ ,  $\Omega_{\text{eff}} = \sqrt{\Omega_R^2 + \delta'^2}$  and we have ignored any overall phase factors. This solution is illustrated in Fig. 4.1(bii.) for different values of  $\delta'/\Omega_R$  where we see that the two laser beams drive Rabi oscillations between the states  $|e\rangle$  and  $|g\rangle$  at frequency  $\Omega_{\text{eff}}$ . A particularly important case is the evolution of the excited state population after starting with all the atoms in the ground state:

$$|\tilde{c}_e(t)|^2 = \frac{\Omega_R^2}{\Omega_{\text{eff}}^2} \sin^2\left(\frac{1}{2}\Omega_{\text{eff}}t\right) \quad (4.12)$$

This expression, along with Eq. 4.11 will be used as the starting point for building our theory of Bragg spectroscopy in chapters 7 and 8.

## 4.2 Outline

The remaining chapters of this thesis are based on a holographic trap shaping technique to produce light fields with arbitrary custom profiles (chapter 5). Using the AC Stark effect described in this chapter, we can translate these light fields into tuneable potential geometries of our atom clouds. With recent developments in projector technology (e.g. digital mirror devices and liquid-crystal-on-silicon spatial light modulators), there has been an increased interest in atom traps of complex geometry [12, 76, 77, 79], and our methods provide a very versatile and robust approach.

We will concentrate on a uniform trap geometry and produce the first homogeneous trapped gases (chapter 6). Within this novel geometry, we will study the equilibrium properties of thermal clouds, partially condensed clouds and pure BECs (chapter 7). Using the 2-photon theory presented here, we will also study the dynamics of the homogeneous 3D BEC phase transition (chapter 8). Since six different experiments will be discussed in the remaining chapters, we provide a graphical roadmap in Fig. 4.2 of the topics covered to show the links between the experiments. Throughout these studies, we will highlight the (often dramatic) difference between the behaviour of our homogeneous gas and more conventional harmonically trapped clouds.

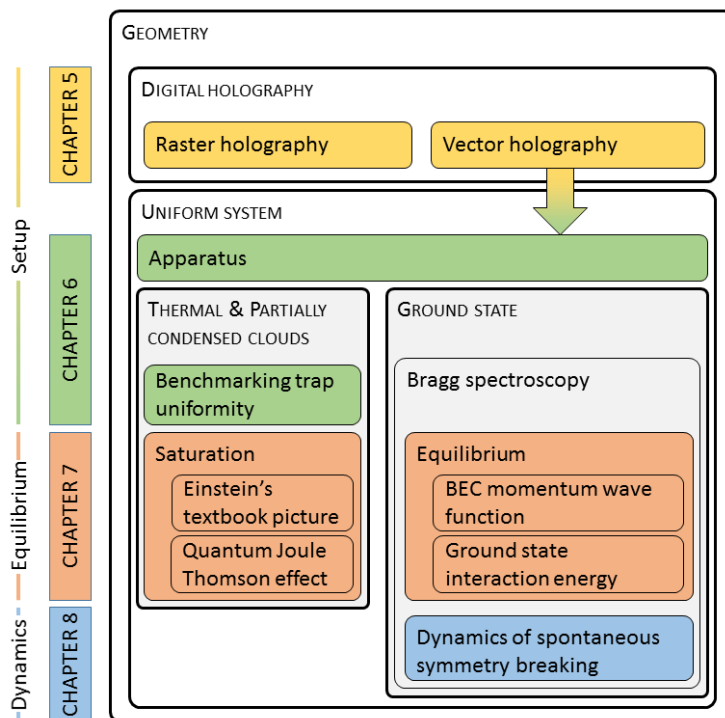


**Fig. 4.2.:** A graphical roadmap for the chapters in this part of the thesis. Colours indicate the content of each chapter and the bounding boxes indicate thematically linked subjects

## Robust Digital Holography for Ultracold Atom Trapping

Whereas theoreticians are free to write down any form for the potential term,  $H_{\text{Pot}}$ , in their Hamiltonian and explore the resulting physics, experimentalists usually require significant investment in new optical and magnetic equipment to construct a new potential geometry. The physics of a quantum gas depends on the connectivity, dimensionality, symmetries and exact form of the geometry in which it is trapped, and considerable work has been put into trapping gases in novel chambers [79–81], channels [9, 76, 77] and lattices [11–13]. One versatile experimental approach is to use configurable arrays of wires or magnetic videotape [82–85] to produce novel *magnetic* trapping geometries on so-called “atom chips”. However, it is often undesirable to use a purely magnetic trap, since these deny the use some of the techniques which make cold atoms an appealing system to study in the first place (a strong external magnetic trapping potential makes tuning interactions via a Feshbach resonance or manipulating atoms’ hyperfine states more complicated). Instead, we ideally need a purely optical method for sculpting the potential geometry.

In this chapter, we describe and experimentally demonstrate two algorithms for producing optical traps which can have arbitrary 2D profiles. These two algorithms serve two complementary roles in cold atom experiments, and we can understand their differences by comparison with vector- and raster-graphics in computer science (see Fig 5.1):

- *Vector-Holography*: Here we first build a toolbox of analytic holograms which sculpt laser beams into simple geometrical profiles in the far field e.g. a ring-shaped beam, or a line-shaped beam. We then find a way to combine these simple shapes to construct our final desired trap shape. This method is very efficient, with almost all the input laser power appearing in the desired trap, but it is only possible to produce relatively simple trap shapes. This is similar to the memory-efficient manner in which simple graphics are stored in vector format on a computer.
- *Raster-Holography*: Here we use a numerical method to directly find the hologram which produces our desired trap shape in the far field. This method is (by construction) not as efficient as vector-holography, but we can produce very intricate trap shapes with details down to the diffraction limit. This is

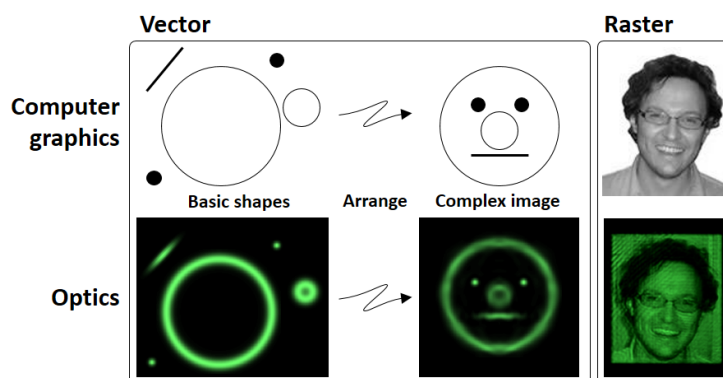


**Fig. 5.1.:** Holographic analogues of vector- and raster-graphics. In a vector-graphics program, we are given a set of basic shapes, and we can arrange them in a complex image (top left). The bottom left row shows a simulation of a complex light fields prepared by a vector-hologram. In contrast, raster-graphics are typically used for storing more complex images, such as the one in the top right, at the expense of memory efficiency. The bottom right image shows a real experimental light field prepared by our optical raster method (the image is approximately 1 mm across).

similar to the memory-inefficient manner in which complex graphics can be stored in a rastered format with pixel-level detail on a computer.

Once a light field has been sculpted by either of these holographic techniques, we can directly associate the optical geometry with a potential landscape using Eq. 4.4.

After defining what we mean by "holography" in section 5.1, we will devote one section to each of the two holographic techniques outlined above. We will place greater emphasis on vector-holography since this technique will be used in later chapters. Technical details of the raster holography method will be relegated to Appendix B with simple proof-of-principle experiments with atoms in raster holograms being outlined in section 5.3.

## 5.1 Digital holography

Holography was originally demonstrated as a means to record both the phase and amplitude of light scattered from an object in order to later reconstruct this light field when the object is absent [86]. Digital holography has now evolved to encompass more than this object reconstruction technique, and refers to any process which uses a computer to reconstruct a desired light field by altering the light's phase and/or amplitude in a single control plane.

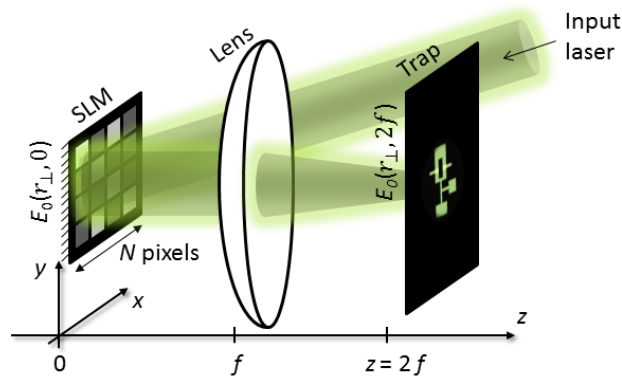


**Fig. 5.2.:** Apparatus for producing holograms using an SLM. The SLM imprints a phase on the incident Gaussian laser beam, and the far field diffraction pattern of this imprinted beam is brought to  $z = 2f$  by the lens.

In this chapter, we will use a phase-only spatial light modulator<sup>1</sup> (SLM) to imprint a phase pattern,  $\phi(\mathbf{r}_\perp)$ , on an incident Gaussian laser beam with the aim of producing a desired custom trapping pattern in the far-field diffraction plane ( $\mathbf{r}_\perp$  spans the plane perpendicular to the propagation direction). We choose an SLM which only affects the laser's phase and does not modify the amplitude of the incident light because we want to produce deep atom traps with lasers of reasonable power (i.e. we do not want to block out any of the incident light by amplitude modulation). Since our phase-only method is vulnerable to any phase aberrations in our system, we keep the apparatus accompanying the SLM in this chapter very simple: A single lens of focal length  $f$  acts to bring the far-field diffraction pattern from infinity to the trapping plane at  $z = 2f$  (see Fig. 5.2).

The techniques presented in this chapter rely on a good understanding of the transfer function which maps the imprinted light field in the SLM plane to the resulting diffraction pattern in the trapping plane. Fraunhofer diffraction theory states that this mapping is approximately a Fourier transform [87]. This approximation will suffice for most of our work, however, in Appendix B.4 we will find that full numerical simulation of the Helmholtz equation describing the light propagation can lead to better experimental results.

Note that we can only imprint the phase  $\phi$  onto a single 2D plane in the light field. Since we can only control one plane of light, we can only make traps which have an arbitrary 2D profile, and we rely on the beam propagation to extrude this pattern in the third direction. Simulations and experiment suggest that the 2D profile we create is preserved up to at least one Rayleigh length on either side of the focus (see Fig. 5.3).

<sup>1</sup>Part number: Hamamatsu X10468-04

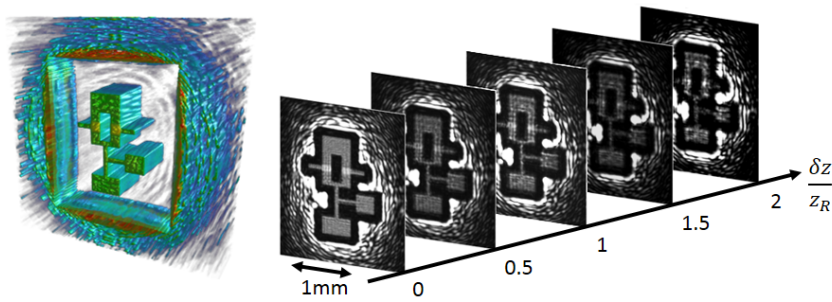


**Fig. 5.3.:** A simulation (left) and experimental images (right) of light fields within  $\delta z < 2z_R$  of the focal plane ( $z$ -axis not to scale,  $z_R \approx 1$  mm is the Rayleigh range of our apparatus). Using these techniques we qualitatively determine that the trap shape persists for  $\sim z_R$  either side of the focal plane before degrading significantly.

The first form of holography that we will consider here is vector-holography, which, despite its simplicity, has great practical use and will form the basis for the work in chapter 6.

## 5.2 Vector-holography

A typical vector-graphics program on a computer provides a toolbox of simple shapes and a method to arrange these shapes on a canvas. In this section we build optical analogues to these features which will allow us to produce and combine several simple atom traps.

### 5.2.1 Toolbox of shapes

We do not intend to give an exhaustive list of primitive shapes constructed in light fields. Instead, we will only illustrate the phase patterns for the shapes which we will use to produce the uniform potential in chapter 6. Alongside the trivial case of a “dot”, the important shapes are the “line” and the “circle”. In table 5.1 we give the details of the analytical holograms for these shapes together with the theoretical and experimental diffraction patterns that they produce. These holograms form the primitive building blocks for our more complex atom traps (note that the face in Fig. 5.1 is built from these primitive shapes).

### 5.2.2 Arranging shapes

Once we can make the basic shapes, we need a method to move the shapes around on our optical canvas and a method to place more than one shape on the canvas using a single hologram. This is the “arrange” stage depicted in Fig. 5.1. We handle the tasks of moving and compositing shapes separately in the sections below:

Shape	Hologram	Theoretical diffraction pattern	Experiment
Dot	$\phi = 0$		
Line	$\phi = -\frac{ky^2}{2F}$		
Circle (pseudo-LG)	$\phi = \ell\theta$		
Circle (axicon)	$\phi = \frac{kR}{f}r_{\perp}$		

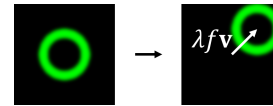
**Tab. 5.1.:** Example primitive beam shapes for use in vector-holography. Here we only mention those shapes which will be useful in chapter 6. In particular, we note that there are many ways to produce a circular beam, and we will discuss the relative merits of two methods which we refer to as the "Axicon beam" and the "Pseudo-Laguerre-Gauss (Pseudo-LG) beam" in chapter 6.

## Moving shapes

Appealing to a familiar property of Fourier transforms, adding a phase gradient in the SLM plane will shift the position of the diffraction pattern in the trapping plane. Explicitly, we can follow through the Fraunhofer theory to obtain the following result (we illustrate the effect of the gradient on an example  $\phi = \ell\theta$ ):

$$\phi \rightarrow \phi - 2\pi\mathbf{v} \cdot \mathbf{r}_\perp$$

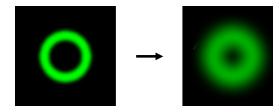
Shifts the pattern corresponding  
to  $\phi$  by  $\lambda f\mathbf{v}$  in the trapping plane



We can also move the shapes in and out of the focal plane by adding a quadratic radial phase pattern (analogous to a lens):

$$\phi \rightarrow \phi + \frac{kr_\perp^2}{2F}$$

Shifts the focal point of the pattern  
by  $\delta z = f^2/F$



## Compositing shapes

Using the shifts above, we can now place a single shape anywhere on the trapping plane, but often we will want to produce a trap which contains several shapes (e.g. the face hologram in Fig. 5.1 consists of five individual component shapes). Suppose we want to produce a trap containing two shapes corresponding to holograms  $\phi_1$  and  $\phi_2$ . For any individual hologram,  $\phi_i$ , the light field at the SLM is given by  $G e^{i\phi_i}$  where  $G$  is the incident Gaussian beam amplitude. The addition rule for Fourier transforms then says that a light field  $G(e^{i\phi_1} + e^{i\phi_2})$  will produce the desired two-shape diffraction pattern. However, since in general  $|e^{i\phi_1} + e^{i\phi_2}| \neq 1$ , our phase-only SLM cannot prepare the required light field since it cannot modulate the amplitude.

Instead, to composite several shapes in the diffraction pattern from a single phase-only hologram, we must appeal to another property of Fourier transforms: the concept of “phase-dominance” [88–90]. This concept is illustrated using an example in Fig 5.4, where we see that the phase part of a Fourier transformed function seems to have a qualitatively greater impact on the modulus of the transform than the amplitude part. There are counter examples to this phenomenon [91, 92], but phase-dominance has proved to be a very useful experimental tool in all the discussions below.

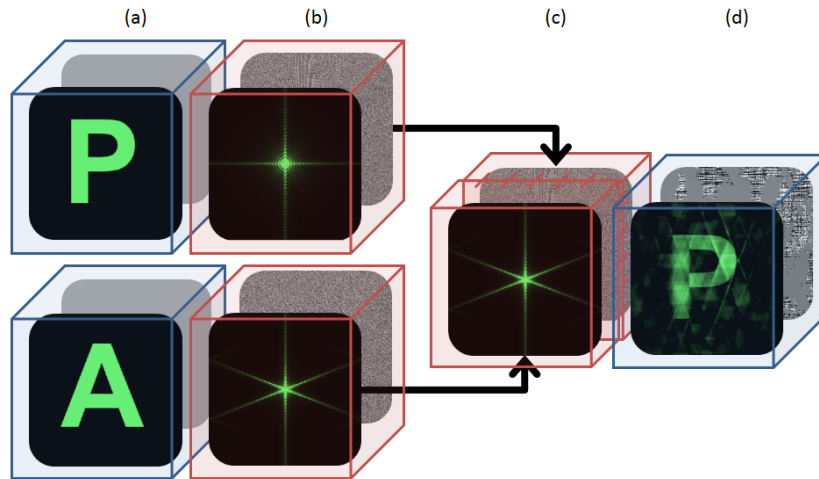


**Fig. 5.4.:** The phenomenon of phase-dominance in Fourier transforms. The green panels represent function amplitudes, and the gray panels give their corresponding phase. If we Fourier transform the two pictures in (a), we obtain the spectra in (b). Now we take the phase of one of these spectra and the amplitude of the other and combine these into a hybrid function, (c). Inverse Fourier transforming this hybrid function gives (d), the amplitude of which closely resembles the picture from which we took the transform's phase information. This phenomenon has counter examples, but it is very useful in almost all experimental cases.

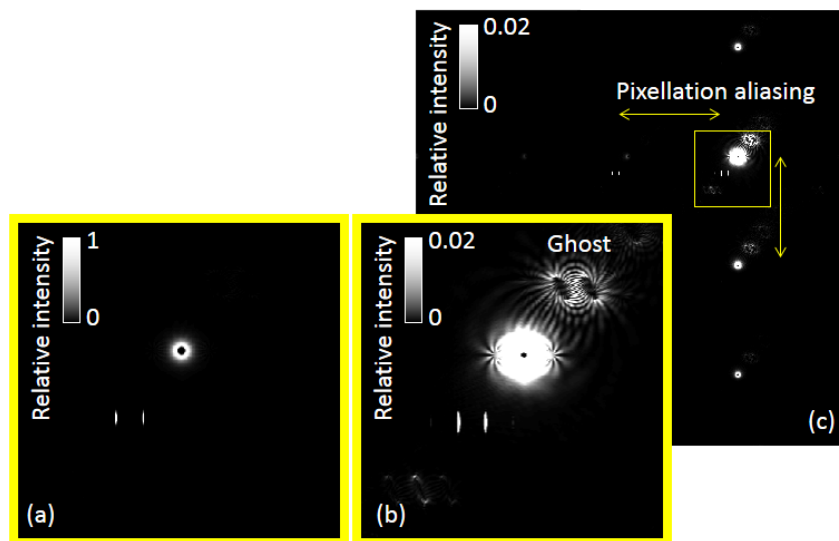


**Fig. 5.5.:** Ghost and alias traps. We make a hologram with three composited shapes: a single circle displaced upwards and two short lines displaced to the left (this trapping pattern will become very relevant in chapter 6). Panel (a) shows a *computer simulation* of the trapping intensity produced by this hologram on an intensity scale  $0 \rightarrow 1$ . Inspecting the trapping plane on a scale  $0 \rightarrow 0.02$  in (b) reveals faint ghost traps which were generated by discarding the amplitude of the hologram sum in Eq. 5.1. (c) Inspecting the simulated trapping plane on a larger scale reveals an array of aliases of the trapping pattern which are artefacts of the finite-sized pixels on the SLM screen.

If we simply discard the troublesome amplitude part of  $G(e^{i\phi_1} + e^{i\phi_2})$ , and just apply the phase:  $\phi_{1+2} = \arg(e^{i\phi_1} + e^{i\phi_2})$ , then phase-dominance says that the (allowed) light field  $Ge^{i\phi_{1+2}}$  almost invariably propagates to produce a diffraction pattern containing the both of the desired shapes (see e.g. Fig. 5.5(a)) [93–95].

In general, to composite  $n$  holograms, we use the expression:

$$\phi_{\Sigma} = \arg\left(\sum_{m=1}^n \alpha_m e^{i\phi_m + i\chi_m}\right), \quad \text{[Diagram: A stack of four square holograms with different phases and intensities, followed by an arrow pointing to a single square containing a complex, multi-colored diffraction pattern.]}$$
 (5.1)

where  $\{\alpha_m\}$  is a set of parameters used to empirically tune the intensity of the individual shapes, and  $\{\chi_m\}$  is a set of random numbers between  $[0, 2\pi]$  which reduce cross-talk between patterns [93] (see next section).

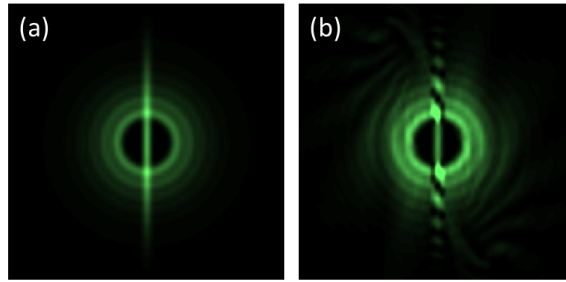
### 5.2.3 Ghost traps

A side effect of discarding the amplitude in our compositing step is the generation of faint “ghost traps”. These are spurious shapes which resemble the desired trap but are severely distorted and misplaced on the canvas (see Fig. 5.5(b)). The peak intensity of the brightest ghost traps is typically  $< 2\%$  of the peak intensity of the desired trap.

In addition to these ghost traps which arise from our compositing technique, the Fourier components of the discrete square pixels on the SLM cause both the desired and ghost traps to be aliased across the trapping plane (see Fig. 5.5(c)). This diverts light away from the desired trap, but even with the combined losses of ghost traps and aliasing, we still retain  $\approx 80\%$  of the incident power in the desired trap. This high efficiency, combined with the method’s simplicity, make this the most suitable technique to produce the homogeneous optical box discussed in detail in the next chapter.

## 5.3 Raster-holography

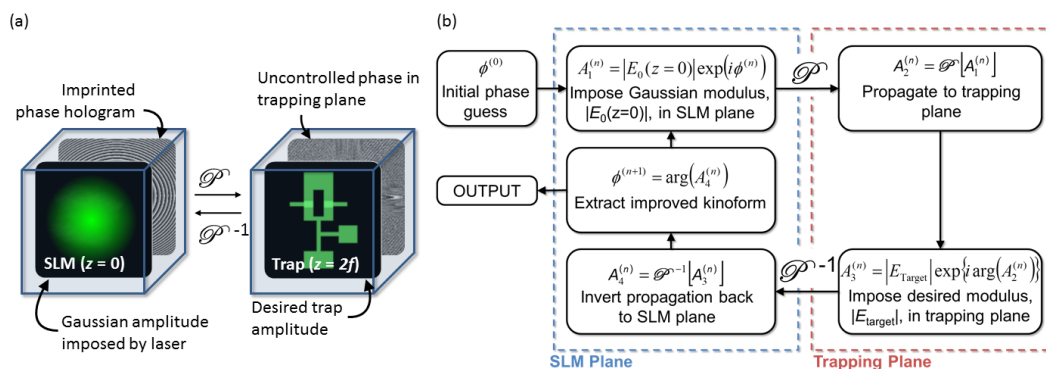
The major limitation of the vector-holography method described above is that we cannot make a trap in which shapes overlap. Since all the shapes are derived from the same laser, they are all coherent and generally produce interference patterns if overlapped (see Fig. 5.6). To make complex traps with overlapping geometries, we need to devise an alternative algorithm.



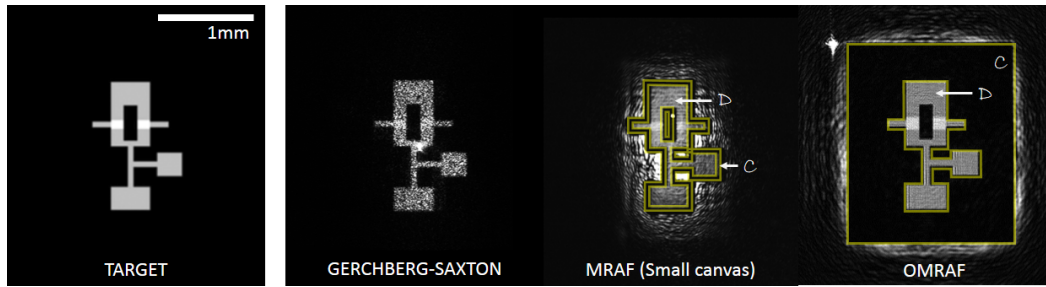
**Fig. 5.6.:** Limitations of the vector-holography method. Suppose we want a trap which consists of an overlapping circle and line (a). Since the two patterns are coherent, they interfere when they overlap and we simulate the resulting pattern in (b). We need to use the raster method in section 5.3 for any complex pattern with overlapping geometries.

Figure 5.7(a) summarises the problem that we are trying to solve: we want to find the phase pattern which when applied to our Gaussian input beam produces the desired trapping intensity in the trapping plane. Since the potential depends only on the intensity of the light, we place no constraint on the phase in the trapping plane. This gives us sufficient degrees of freedom to use a numerical method to self consistently solve for the phase in both the SLM and trapping planes subject to the amplitude constraints in each plane. Many numerical methods have been used to approach this problem, ranging from steepest-descent optimisation [96–98] to genetic algorithms [99]. We choose the iterative Gerchberg-Saxton algorithm [100] (illustrated in Fig. 5.7(b)) because it is very computationally efficient, and is easily executed on a fast graphics processing unit.

It is well documented that the convergence of the naïve Gerchberg-Saxton algorithm is highly erratic because the amplitude constraints in each plane are non-convex



**Fig. 5.7.:** The Gerchberg-Saxton algorithm. (a) A cartoon of the constraints and the variables to be solved for. The modulus of the light field is fixed in the SLM plane, and we wish to solve for the phase hologram which produces the correct modulus with no constraints on the phase in the trapping plane. (b) Diagrammatic representation of the iterative Gerchberg-Saxton algorithm.



**Fig. 5.8.:** Motivation for an improved algorithm. We try to make a light field in the shape shown on the far left (this shape is also used in [103]). Real experimental light fields produced using different algorithms are recorded on the right. A naïve implementation of the Gerchberg-Saxton algorithm fails to converge to the desired pattern. MRAF improves on this by only asking for convergence inside regions  $\mathcal{C}$  and  $\mathcal{D}$ . In the original MRAF paper, the canvas region,  $\mathcal{C}$  was shrunk to a tight fit around  $\mathcal{D}$ , which is experimentally impractical. We developed an improved algorithm, OMRAF, which allows  $\mathcal{C}$  to be expanded to approach the Nyquist limit.

[101, 102]. For this reason, Pasienski and DeMarco modified the algorithm to the so-called MRAF algorithm [103–106], and we have made further improvements in Appendix B to create the OMRAF algorithm. Fig. 5.8 shows the evolution of the trap quality between these algorithm upgrades.

Using OMRAF we have generated complex optical patterns in laser light with only  $\sim 7\%$  root mean square deviation from the target potential. Furthermore, since our phase-only method essentially "steers" light into the desired pattern, and does not block out any of the incident light, we manage to direct approximately 20 – 30% of the incident laser power into the final trapping potential (the remaining light is scattered outside region  $\mathcal{C}$  shown in Fig. 5.8). This is considerably higher than the efficiency of more traditional amplitude-modulation techniques (e.g. digital projectors) which would be less than 1% efficient for the target pattern shown in Fig. 5.8.

While our OMRAF algorithm, has the potential to produce more complex trap geometries than can be achieved with only vector-holography, it has not yet been put to use in an extended project. However by adapting and repurposing the apparatus described in Stuart Moulder's PhD thesis [33], we have produced some preliminary  $^{87}\text{Rb}$  atom clouds trapped in simple OMRAF traps (see Fig. 5.9). These very basic trials serve to show that this moderately sophisticated holographic technique has genuine promise for trapping real atom clouds in flexible geometries. Note that the quality of the traps shown in Fig. 5.9 is at present primarily limited by our current optical setup, which was originally designed to create small ring-traps for study of superfluid flow [9, 33]. Re-purposing this apparatus without modification meant that a typical BEC only covers  $\sim 10 \times 10$  pixels of the trapping plane, so we can currently only trap atoms in simple shapes.

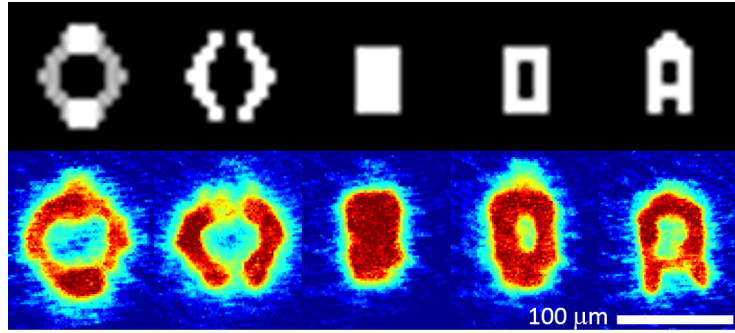


**Fig. 5.9.:** Preliminary trials trapping  $^{87}\text{Rb}$  BECs using OMRAF traps in the apparatus described in [33]. The top row shows the target potentials, and the bottom row shows a BEC of atoms trapped in 805 nm laser light shaped into these potentials (blue to red indicates optical density of 0 to 3). The apparatus in [33] was not explicitly designed for testing OMRAF, and the geometry of this apparatus is such that the atom cloud covers only  $\sim 10 \times 10$  pixels in the trapping plane.

## 5.4 Conclusion

The two holographic methods in this chapter have opened an entirely new research path with an unprecedented control over the trap geometry. In the following chapters, we will concentrate on one particular geometry - the uniform trap - where our vector holographic method proves to be a very versatile technique for trapping and condensing real clouds of atoms.



## Bose-Einstein Condensation of Atoms in a Uniform Potential

In an undergraduate quantum mechanics course, the first system that students tackle is the *uniform*, square well. Later, as an introduction to the BEC transition, students study quantum statistics in an infinite *uniform* gas of Bosons. Even for difficult concepts in this thesis, such as Landau damping rates in chapter 2, we have quoted the simplest *uniform* system results. It seems that whenever we want to understand complex phenomena, it is often best to approach them in a uniform environment where there are no additional length scales to complicate the problem.

With its simple and fundamental description, the uniform system has a very special place in theoretical physics. However, experimentally, it is very difficult to achieve a three-dimensional homogeneous potential for cold atoms. Most existing experiments instead use simple optical or magnetic apparatus to produce parabolic traps. While the apparatus for parabolic traps may be simple, the many-body physics we wish to study can be complicated by the inhomogeneous trapping potential, and the fundamental phenomena at play can become obscured by trapping artifacts [41, 45, 107–109].

Various methods have been developed to overcome the problems with inhomogeneous traps and to extract uniform-system properties from a harmonically trapped sample [42, 110–117]. These methods generally rely on the local density approximation (LDA) [42, 110–115] or selective probing of a small central portion of the cloud [42, 116, 117]. In some cases, this can work extremely well, particularly if a single experimental run in a harmonic system can be mapped onto many uniform-system runs with different (local) particle densities. However, some experimental signatures are still difficult to separate from relics of the trap geometry, and some signals simply cannot be recovered using the LDA. In particular, the LDA breaks down close to phase transitions where the correlation length diverges (see chapter 8). In these situations it is of central importance to construct a genuinely uniform atom trap.

Motivated by this, we will describe the preparation and observation of the first atomic BEC in a truly uniform potential. We start in section 6.1 by designing a holographic method based on the techniques in the previous chapter to create a uniformly dark 3D optical box with steep repulsive walls. Atoms are loaded into this trap using a

single-chamber apparatus described in detail elsewhere [118], and schematically illustrated in Fig. 6.1 and Appendix A. This machine was originally constructed by Igor Gotlibovych and Tobias Schmidutz to create *harmonically* trapped BECs of  $^{87}\text{Rb}$  atoms in a hybrid magnetic and optical trap (introduced in [6]). A more complete description of the apparatus can be found in the PhD theses of Igor and Tobias [39, 40]. We adapt this apparatus to transfer atoms out of this harmonic trap into the novel uniform trap as described in section 6.2. Since this is the first realisation of a homogeneous atomic Bose gas, we will spend most of this chapter explaining and benchmarking the technical details of the uniform trap. In particular, we will verify the uniformity of our trap (section 6.2.2) and verify that we can condense in our trap (section 6.2.3). Chapters 7 and 8 will give more details of the physics that we have explored using this apparatus. These experiments reveal phenomena which could not have been observed in a more conventional harmonic trap.

## 6.1 Building an optical box

We will use the simpler vector-holography method from chapter 5 to produce the uniform trap which is used throughout the remaining sections of this thesis. Our chosen trapping arrangement must fulfill the following criteria:

- *3D*: In chapter 5, we concentrated on 2D optical traps, and assumed that these 2D profiles are typically extruded in the third direction by  $\sim 1$  Rayleigh length before significant distortion. In section 6.1.2, we will describe the modifications to the holography apparatus which allow us to properly handle the third direction and produce a 3D region of uniform potential.
- *Dark traps*. We can either trap the atoms in a uniformly dark region surrounded by steep, blue-detuned (repulsive<sup>1</sup>) walls, or in a uniformly bright, red-detuned (attractive) region. On the bench we can produce dark regions uniform to  $< 1\%$  of the total trap depth (see Fig. 6.4(e)), or bright regions uniform to within 6% of the total trap depth (see Fig. B.3). We therefore strongly favour a method which creates a uniformly dark region surrounded by sharp, high, repulsive (blue detuned) walls.

Below we briefly describe the historic progression of the technique which satisfies both of these criteria.

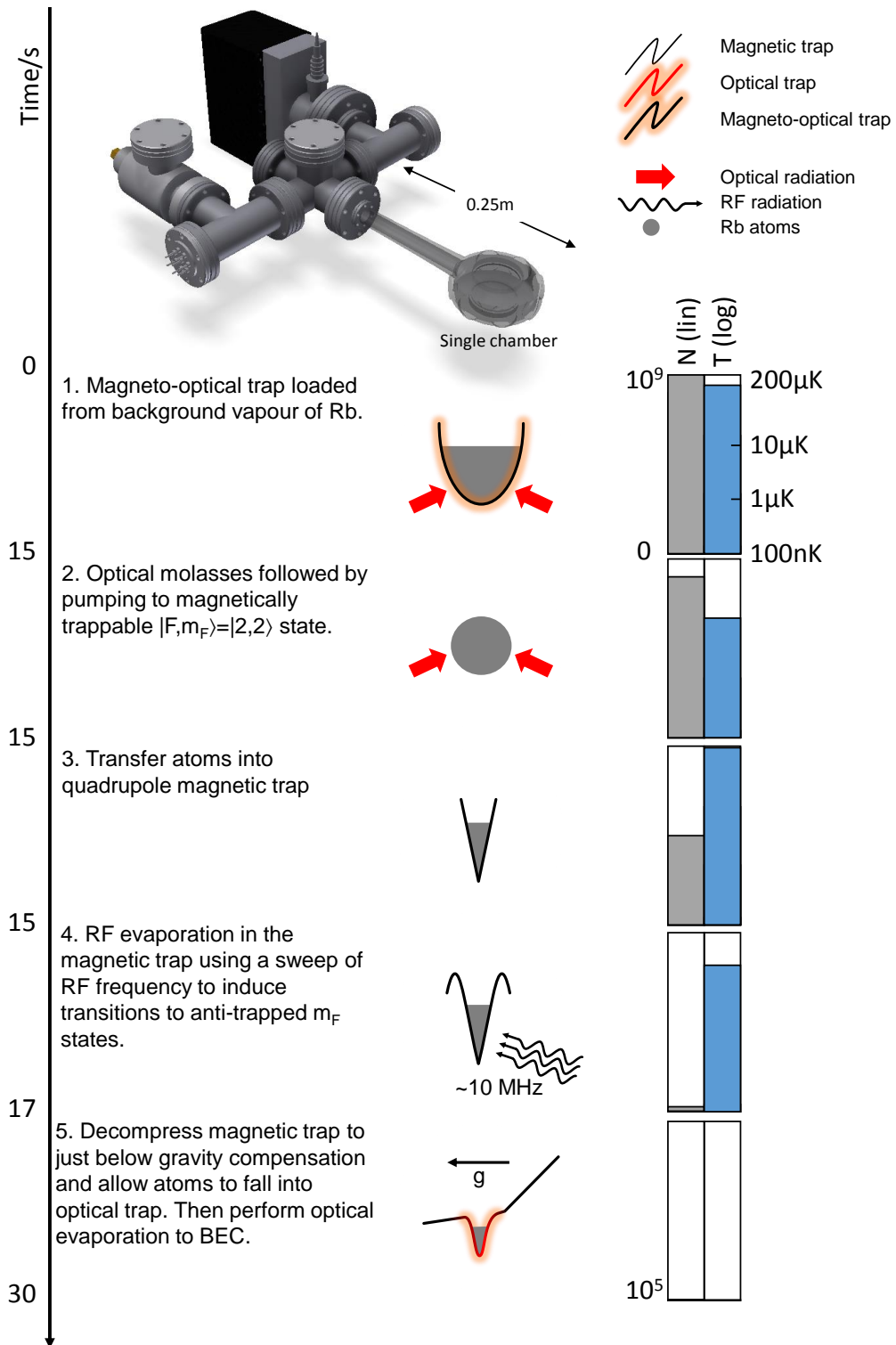


**Fig. 6.1.:** Summary of the experimental sequence for cooling  $^{87}\text{Rb}$  in a simple single-chamber apparatus [118] inspired by the hybrid optical/magnetic trapping technique in [6]. We show a schematic of the experimental apparatus at the top (we omit all electromagnetic coils and optics for clarity), and underneath we show cartoons of the trapping potentials which the atoms experience. The bars on the right show the approximate atom number and temperature (log scale) at the end of each step.

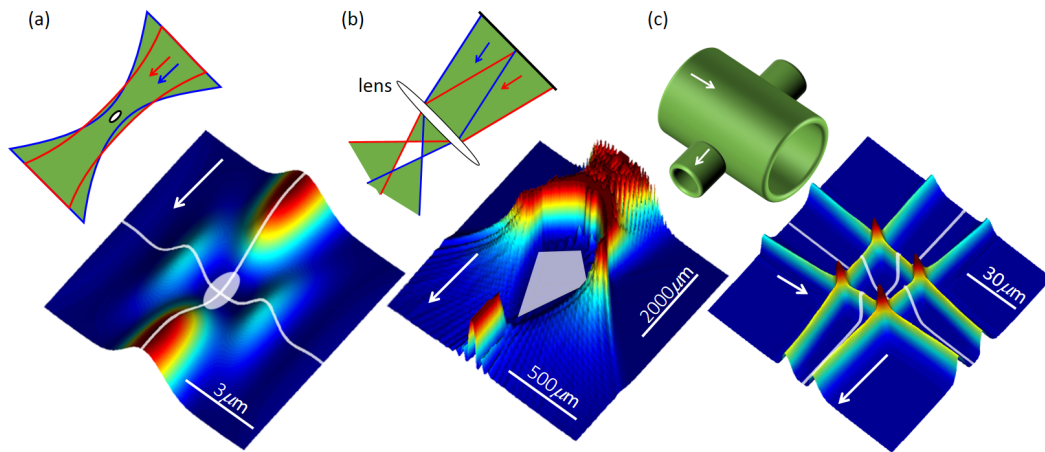


**Fig. 6.2.:** Possible methods for producing dark optical traps in 532 nm (green) light. (a) and (b) show co-propagating beam methods: Using an appropriate hologram, we can (a) create co-propagating coherent Gaussian beams of different waists, or (b) radially offset the focus of a beam in the axially symmetric manner shown. These both produce the dark traps indicated by white shading. However, the trap in (a) is parabolic in the propagation direction, and the walls of the trap in (b) are very diffuse which wastes most of the input power. Instead, we will use a crossed-beam method illustrated in (c). The original proposal was to use two crossed tubes of differing diameter to create a dark arena at their intersection as shown here. This was later modified to a geometry in which a tube of light is capped by two sheet beams (see Fig. 6.3).

### 6.1.1 The evolution of our box

To minimise the number of optics which can introduce aberrations into our laser beam, and for ease of alignment, we want to make the trap using only one SLM. Furthermore, ideally, we would create our dark 3D optical box using only one optical axis. This can be achieved using methods which we refer to as "co-propagating beam methods" (see Fig. 6.2(a) and (b)). Unfortunately, these methods either produce parabolic dark traps [119] or are extremely inefficient in their use of light [120, 121] (see Fig. 6.2), meaning we are forced to use a second optical axis to make a 3D trap.

Originally we planned to generate two "tube" beams using a single SLM and then intersect these tubes at right-angles to trap atoms in the central cavity (see Fig. 6.2(c)). If the tube walls are sufficiently sharp, then the enclosed region will be uniformly dark. Much of the preliminary optical work was carried out based on this two-tube geometry, and the first realisation of a uniform Bose-condensed gas was achieved using this arrangement. However, as work progressed with atoms, the original choice of optical geometry evolved to optimise the atomic cloud shape (see section 6.1.3). The final geometry used is constructed with the following beams:

<sup>1</sup> $\delta > 0$  in 4.4 gives a repulsive potential

*Tube beam* Along one optical axis we shine a "pseudo-LG" beam (see table 5.1) with a circular profile to form a steep-walled tube.

*Capping beam* The tube is capped at both ends by sheets of light formed from the extrusion of the "line" beam in table 5.1 and propagating perpendicular to the tube.

This capped tube forms a uniformly dark "optical tin-can" in which to trap atoms (see Fig. 6.3(b)). Since all the experimental images from the preliminary optical trials are based on the two-tube approach, we include simulated images of the final geometry alongside the experimental images in Fig. 6.3.

In either the two-tube or final geometry, the beams along both optical axes are shaped using a single SLM as described below.

### 6.1.2 Beam-shaping apparatus

The central principle behind our apparatus is to use a single vector-hologram on the SLM to generate a plane (referred to as "focal plane A") which contains two spatially separated sets of optical geometry: one set for the tube beam and one for the capping beam (see Fig. 6.3(a)). We then use a sharp-edged mirror covering half of focal plane A to split the capping beam away from the tube beam. The simple optical components shown in Fig. 6.3 steer and refocus the two beams until they intersect at right angles to form the optical box in focal region B which coincides with the atoms in the vacuum chamber.

Approximate positions of the relay lenses are given in Fig. 6.3. However as we have seen in section 5.2.2, a particularly elegant feature of the SLM is that each beam can be independently digitally focused by adding a lens-like parabolic phase term of focal length  $F_m$  to each component hologram:

$$\phi_{\Sigma} = \arg \left( \sum_{m=1}^n \alpha_m \exp \left[ \underbrace{\phi_m + 2\pi \mathbf{v}_m \cdot \mathbf{r}_{\perp}}_{\text{position}} - \underbrace{\frac{kr_{\perp}^2}{2F_m}}_{\text{focus}} \right] \right), \quad (6.1)$$

where we have used the notation of Eq. 5.1. This precise digital control means that we can empirically correct for small errors in the relay lens positions (the SLM pixel size sets a lower bound  $F_m > 400$  mm, which gives us several mm tolerance on the lens positions).

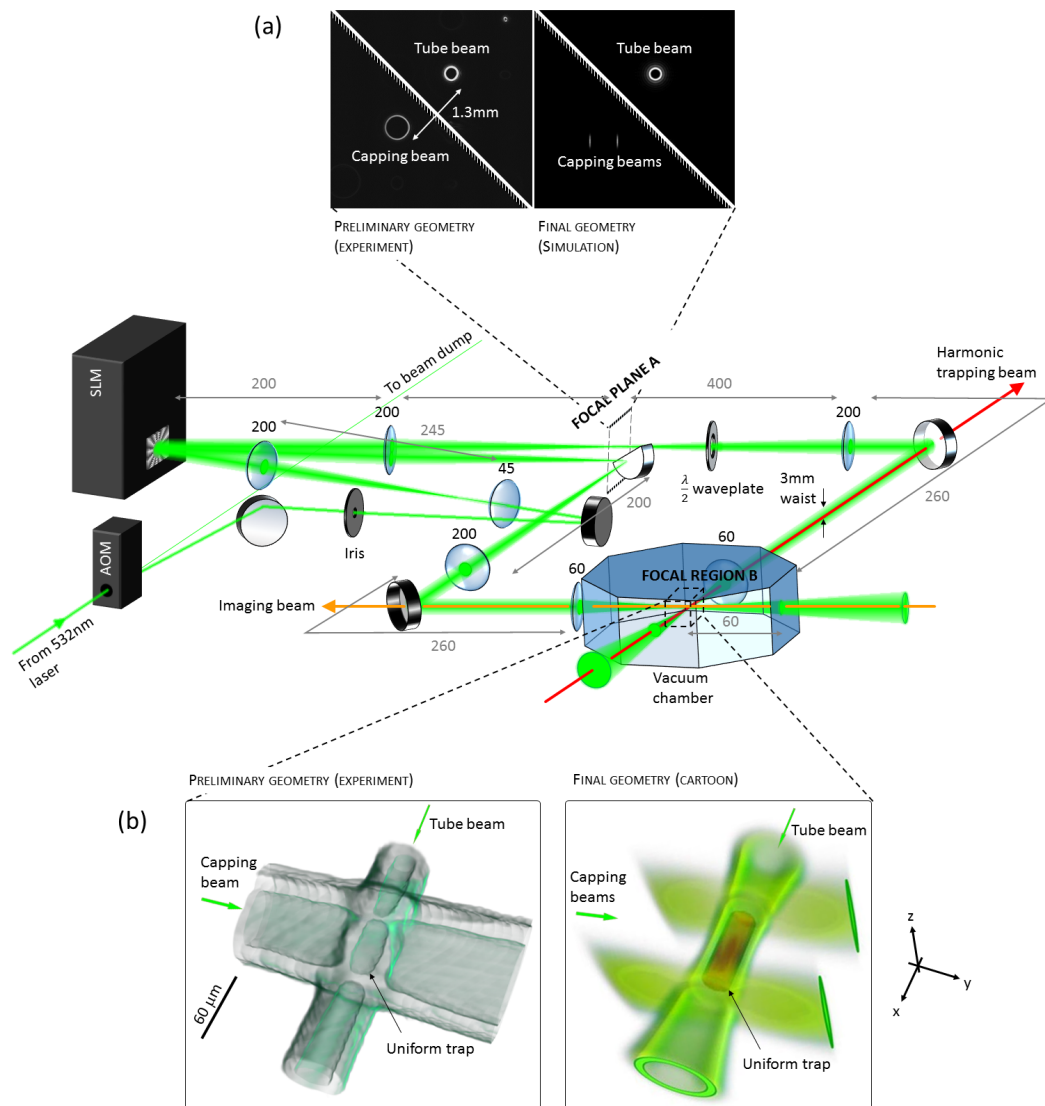


**Fig. 6.3.:** The optical apparatus used to sculpt and cross the trapping beams. We show approximate distances and focal lengths in mm. A single hologram on the SLM creates the spatially separated optical geometry for both the tube and capping beams in the focal plane A. A knife-edge mirror is used to steer the capping beam perpendicular to the tube beam. (a) We show both an experimental image of plane A for the original two-tube geometry, and a simulation of the final geometry, indicating the position of the splitting mirror in white. Simple optics image the patterns in focal plane A into focal region B. (b) By moving a CCD through region B (without the vacuum chamber in place), we can map out the 3D equipotential surface of the two-tube trap and identify the trapping volume. We also present a cartoon of the final trapping geometry with the area occupied by the atoms highlighted in red. The diffraction limited spot size in region B is  $3 \mu\text{m}$  radius, and the Rayleigh length is  $54 \mu\text{m}$ .

### 6.1.3 The final geometry

Both the tube and the capping beams were revised after observing their performance when trapping atoms. Below we highlight the major design choices and reasons for the final geometry:

#### Tube beam: Axicon vs. pseudo-LG

In table 5.1 we saw two different holograms for producing circular (tubular) beams: a spiral phase winding,  $\phi = \ell\theta$  produces a "pseudo-Laguerre-Gauss" (pseudo-LG) beam<sup>2</sup> parameterised by integer  $\ell$ , and a radial phase gradient,  $\phi = \frac{kR}{f}r_{\perp}$ , produces an "axicon" beam<sup>3</sup>. The analytical form for the diffraction pattern of these holograms in the focal plane can be found by appropriate Fourier transforms. For these calculations we imagine illuminating the hologram with a Gaussian beam,  $E_0(\mathbf{r}_{\perp}, z = 0) \propto \frac{w_0}{w} \exp\left(-\frac{r_{\perp}^2}{w^2}\right)$ , of waist  $w$  (note that we have defined  $w_0 = \frac{\lambda f}{\pi w}$  as the diffraction limited spot size in the Fourier plane). The results of the transforms are as follows:

$$\text{Pseudo-LG} \quad E_{\text{LG}}(\mathbf{r}_{\perp}, z = 2f) \propto \frac{r_{\perp}}{w_0} \exp\left(-\frac{r_{\perp}^2}{2w_0^2}\right) \left[ I_{\frac{\ell-1}{2}}\left(\frac{r_{\perp}^2}{2w_0^2}\right) - I_{\frac{\ell+1}{2}}\left(\frac{r_{\perp}^2}{2w_0^2}\right) \right] \exp(i\ell\theta)$$

$$\text{Axicon} \quad E_{\text{ax}}(\mathbf{r}_{\perp}, z = 2f) \propto \int_0^{\infty} e^{-\frac{(\rho-iR)^2}{w_0^2}} J_0\left(\frac{2\rho r_{\perp}}{w_0}\right) \rho d\rho$$

where  $J_n(z)$  is a Bessel function, and  $I_n(z)$  is a modified Bessel functions of the first kind. We also consider a hybrid beam, produced by the phase pattern  $\phi = \frac{kR}{f}r_{\perp} + \ell_{\text{ax}}\theta$ , which we refer to as the "spiral-axicon". In the limit  $R/w_0 \gg 0.5\ell_{\text{ax}}$ , a spiral-axicon beam still resembles an axicon beam, but, unlike a pure axicon beam, a spiral-axicon is truly dark at  $r_{\perp} = 0$ , which satisfies our desire for a strictly dark trap.

$$\text{Spiral-axicon} \quad E_{\text{ax}}^{\text{sp}}(\mathbf{r}_{\perp}, z = 2f) \propto \exp(i\ell_{\text{ax}}\theta) \int_0^{\infty} e^{-\frac{(\rho-iR)^2}{w_0^2}} J_{\ell_{\text{ax}}}\left(\frac{2\rho r_{\perp}}{w_0}\right) \rho d\rho$$

<sup>2</sup>The origin of this name is the Laguerre-Gauss solution to the cylindrically symmetric paraxial Helmholtz equation describing laser beam propagation. Pure Laguerre-Gauss laser modes are indexed by integers  $\ell$  and  $p$  where  $\ell$  determines the azimuthal phase winding number of the beam, and  $p$  determines the number of radial nodes [122]. Since we imprint a phase winding onto a Gaussian beam, we obtain a beam which is a superposition of several  $p$  modes all with the same  $\ell$ . The dominant mode is  $p = 0$ , but since our beam is not a pure Laguerre-Gauss mode, we refer to it as a pseudo-LG beam.

<sup>3</sup>The origin of this name is the refractive optical element, known as an axicon. An axicon is a glass cone which can be modelled as a thin optical element which imprints a radial phase gradient onto an incident beam.

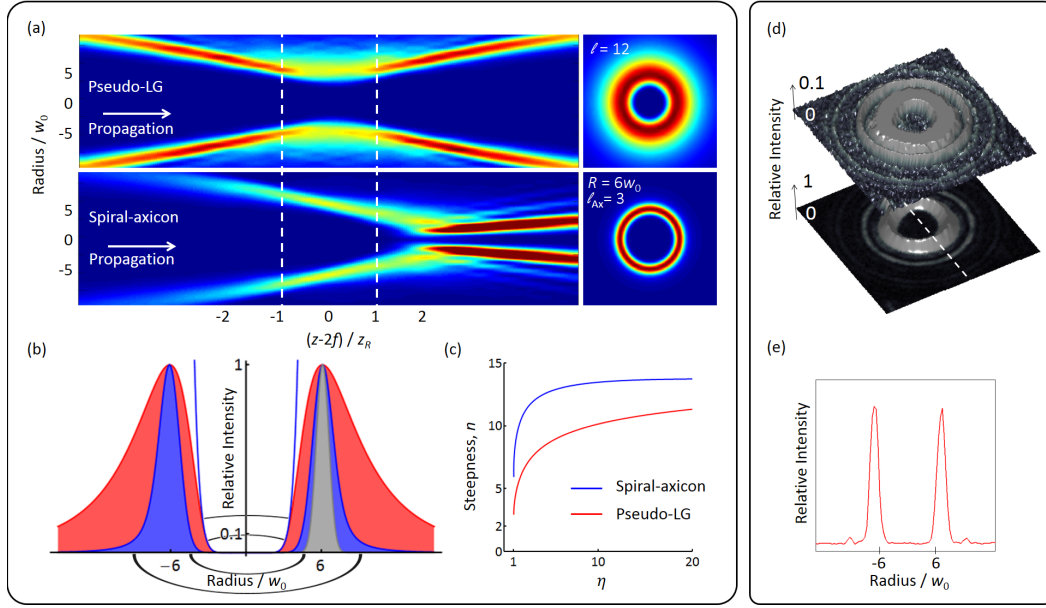


**Fig. 6.4.:** A theoretical comparison between the  $\ell = 12$  pseudo-LG beam and the  $R = 6w_0, \ell_{ax} = 3$  spiral-axicon beam. (a) The profiles of the two beams in the direction of propagation and in the focal plane. Here  $z_R$  is the Rayleigh length. (b) Analysis of the wall thickness and steepness for a fixed peak radius. The pseudo-LG beam (red shading) has much broader walls than the spiral-axicon (blue shading), and therefore requires more laser power to achieve the same trap depth. For reference, we show a diffraction limited spot (gray shading) and an  $r^{10}$  power law fit (blue line) to the pseudo-LG for  $\eta = 10$ . (c) Comparison of the fitted steepness,  $r^n$  for different  $\eta$ . (d) Experimental focal plane of an  $\ell = 12$  pseudo-LG beam with a zoom showing the level of noise in the bottom of the trap. The circular fringes around the main peak come from a circular aperture that we impose on the hologram to eliminate the Fourier components of the square edge of the SLM screen (see Fig. 6.6). (e) A plot of the potential along the dashed line in (d) showing  $< 1\%$  noise on the trap floor.

Fig. 6.4 shows a comparison between pseudo-LG and spiral-axicon beams, with  $\ell$  and  $R$  set appropriately to achieve the trap dimensions we will use later. There are three main beam properties to consider when comparing these two methods of generating tubes. These are considered separately below:

1. **Wall steepness:** A perfectly uniform trap would have infinitely steep walls. This can never be achieved for any real optical system with a finite diffraction limit. To assess how close our beams come to the ideal case, we fit the analytic intensity patterns with a radial power law  $|E|^2 \propto r_{\perp}^n$ . As  $n \rightarrow \infty$ , we approach the ideal uniform case, and for  $n \rightarrow 2$  we have the traditional case of a parabolic trap. Fig. 6.4(c) compares the fitted power  $n(\eta)$  for spiral-axicon and pseudo-LG beams with radii  $6w_0$ . Note that  $\eta$  is a parameter which describes how far up the sides of the wall we explore with the fit. If the peak depth of the trap (i.e. the height of the walls) is  $U_{\text{peak}} = \eta k_B T$  where  $T$  is the temperature of the trapped cloud then we are only concerned with fitting the region explored by the bulk of the atoms, i.e. up to  $\sim U_{\text{peak}}/\eta$ . We find that for  $\eta \gg 1$ , both

beams are very much steeper than parabolic, but the spiral-axicon beam is steeper for all  $\eta$ .

2. *Efficiency*: Both beams produce rings of light of finite thickness. If the ring is too thick then we will not have enough laser power to reach high  $\eta$  traps. Numerically examining the beam profiles reveals that the radius of a pseudo-LG beam is  $r_{\perp}^{\text{LG}} \approx 0.5 \ell w_0$ , and from a parabolic expansion around this radius of peak intensity, we obtain the ring thickness as  $\delta r_{\perp} \approx 0.35 \ell w_0$ . For a spiral-axicon, these values are  $r_{\perp}^{\text{ax}} \approx R$  and  $\delta r \approx 1.66 w_0$ . Therefore, the ratio of the trap depths created by the two beams is:  $U_{\text{peak}}^{\text{ax}}/U_{\text{peak}}^{\text{LG}} \approx 0.4R/w_0$ . Since we will be working at  $R \approx 6 w_0$ , the spiral-axicon will produce deeper traps for a given total laser power.
3. *3D profile*: Using the Helmholtz propagator in Eq. B.2 we can simulate the propagation of the shaped beams near  $z = 2f$ . We find that the pseudo-LG beam produces the expected tube of roughly constant radius over a Rayleigh length,  $z_R$ , on either side of the focus. However, the radius of the axicon tube monotonically falls with  $z$  near the focus (see Fig. 6.4(a)). This varying radius does not threaten the uniformity of our trap, but the loss of symmetry does make analysing our images more difficult and is an unnecessary complication to the otherwise simple message of our atom cloud images (see Fig. 6.5(a)).

In summary, the spiral-axicon wins points 1 and 2: the beam is steeper and more efficient than the pseudo-LG beam. However, for clarity of presentation, we choose to make our trap using a pseudo-LG tube beam which has a more favorable 3D structure (point 3). In the final experiment, we use an  $\ell = 12$  beam, which gives a tube of diameter  $\ell w_0 \approx 35 \mu\text{m}$  ( $w_0 \approx 3 \mu\text{m}$ ).

### Capping beam: Tube vs sheets

To cap the tube, we can either use a second, larger diameter tube or two line beams. Both of these arrangements are shown in Fig. 6.3.

Experimentally, we find that if we try to perform evaporative cooling in the two-tube arrangement, then atoms which evaporate radially out of the inner tube get stuck in the larger outer tube (see Fig. 6.5(a),(b)). Since evaporating atoms need to completely escape the trap, this confinement in the capping tube may affect evaporation and distorts the images we take. Therefore we choose to use two line beams to cap the tube. This geometry is achieved by compositing two  $F = 7.5 \text{ m}$  cylindrical lens patterns,  $\phi = -\frac{ky^2}{2F}$ , with different horizontally displacing phase gradients. This produces two sheet beams  $54 \mu\text{m}$  tall and  $3 \mu\text{m}$  wide separated horizontally by an easily adjustable  $70 \mu\text{m}$  (see Fig. 6.3(a)).

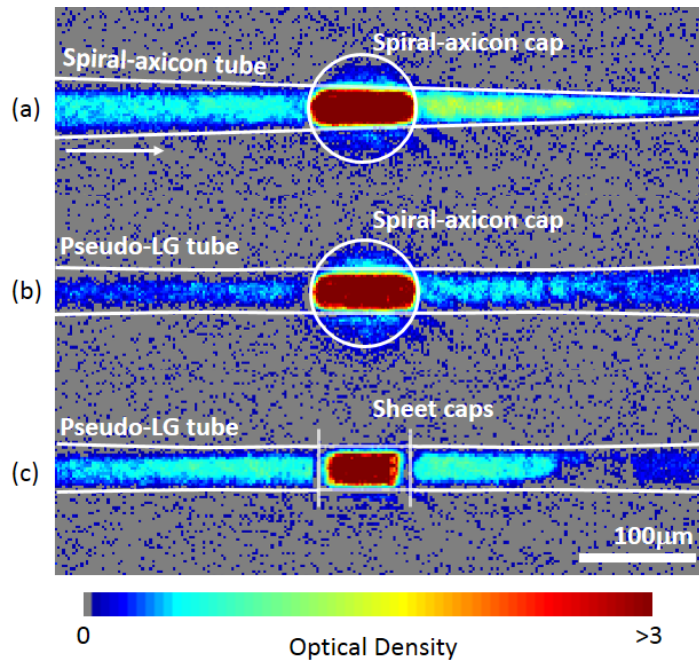


**Fig. 6.5.:** Evolution of the final trap geometry. The main trap is the dense, red region in the centre of each image, and we have ramped down the trap depth to spill atoms which map out the path of the laser beams. The white lines show the inferred points of peak light intensity. (a) and (b) show that the cloud shape formed with a spiral-axicon tube beam is distorted by the converging beam walls, and a pseudo-LG tube beam does not show any distortion. In (a) and (b), some radially evaporating atoms escape from the tube beam but are still trapped in the larger diameter capping beam. Since our picture integrates atom density along the capping beam propagation direction, these externally trapped atoms will distort our images. To avoid this, we choose to cap the beam with two sheets of light. The final geometry is shown in (c).

The final hologram to produce the tube and two linear capping beams is shown in Fig. 6.6. Note that this hologram includes the empirically selected phase gradients and lens terms which correct for the imperfect placement of the relay optics. Simulations of the pattern produced by this hologram in Focal plane A are shown in Fig. 5.5 and 6.3(a).

## 6.2 First realisation with atoms

Having established the optical technique for producing a uniform trap, we now describe the results of the experiment using this apparatus to create the first (quasi)homogeneous atomic BEC. We briefly describe the loading procedure, and then verify that we have succeeded in our aim of (a) producing a uniform cloud and (b) condensing that cloud.

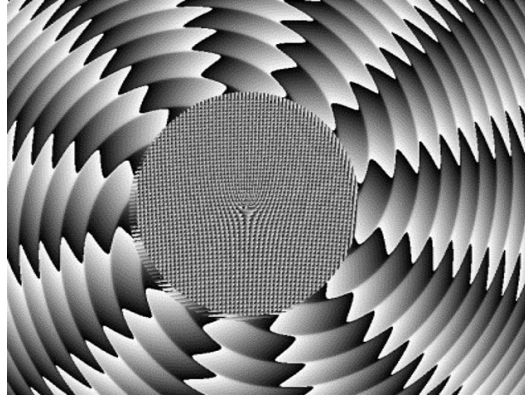


**Fig. 6.6.:** The phase hologram used to produce both the tube and capping beam geometry. To prevent distortion by the Fourier components of the sharp corners of the SLM screen, we only apply the phase ramps,  $2\pi\mathbf{v}_m \cdot \mathbf{r}_\perp$ , inside the circular region which is the same radius as the incident beam waist and centered on the incident beam.

### 6.2.1 Loading procedure

Using the apparatus described in [118], we cool a gas of  $^{87}\text{Rb}$  atoms in a harmonic hybrid magneto-optical trap until the cloud is small enough to fit inside our cylindrical uniform box trap. At this point, the cloud of  $\sim 7 \times 10^5$  atoms is partially condensed at a temperature  $T = 120 \text{ nK}$ . To transfer these atoms into our uniform trap, we ramp on the  $532 \text{ nm}$  laser as illustrated in Fig. 6.7 to create the uniform optical box surrounding the harmonically trapped cloud. Out of the  $1 \text{ W}$  of power from the green laser source,  $700 \text{ mW}$  reach the atoms, achieving a maximum trap depth of  $U_{\text{peak}} = k_B \times 2 \mu\text{K}$ . Once the green laser is on we ramp down the harmonic trapping beam.

At this point we need to counter the effect of gravity, which if left uncompensated will turn our uniform trap into a linear trap with potential  $U = mgz$ . We use a magnetic field gradient of  $15.276 \text{ G/cm}$  produced by the combination of a quadrupole field and a uniform bias field to cancel gravity at the  $10^{-4}$  level. The transfer into the uniform box is completed once the harmonic trap has fully turned off and the anti-gravity field is fully on.

Approximately 80% of the atoms originally in the harmonic trap are successfully transferred into the uniform trap, but the transfer is not adiabatic. After the transfer, the temperature of the gas is  $130 \text{ nK}$ . Under these conditions, the cloud is no longer condensed. Nevertheless, it is sufficiently degenerate to show the effects of Bose statistics. In the next section, we use this non-condensed gas to verify the uniformity of the trap. We will then progress to the task of condensing in the uniform trap in section 6.2.3.

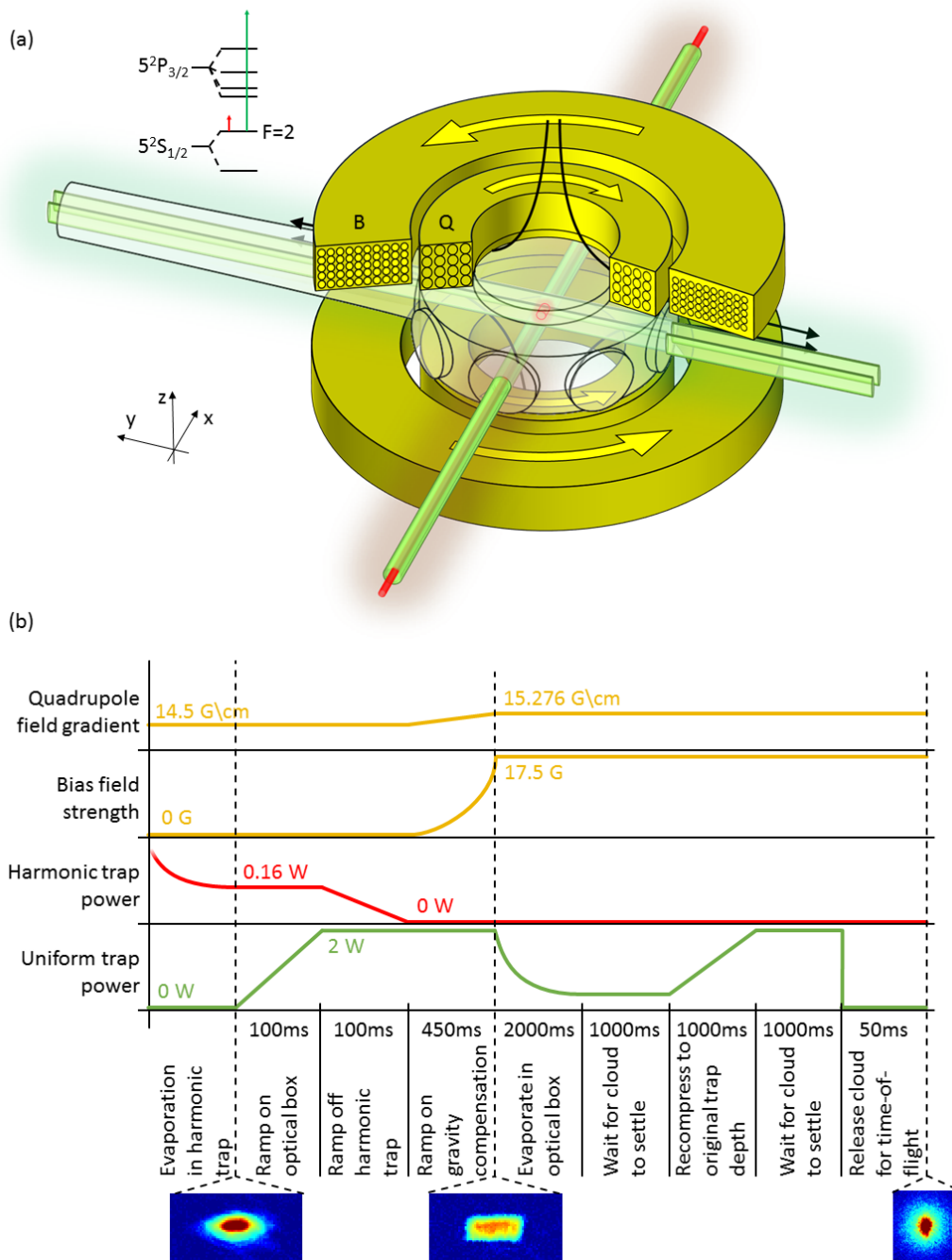


**Fig. 6.7.:** Experimental apparatus for preparing a uniform BEC. (a) A schematic of the optical and magnetic components of the trap showing the 532 nm green (uniform) and 1070 nm red (harmonic) lasers and the quadrupole (Q) and bias (B) coils. The location of the atoms is shown by the central red cylinder, and the laser detunings are shown (not to scale) on a cartoon of the  $^{87}\text{Rb}$   $D_2$  lines. (b) The experimental sequence used to create and probe the uniform BEC. The uniform box trap is loaded from a harmonic trap, and a magnetic field gradient cancels gravity. Images from Figs. 6.8 and 6.10 are shown (not to scale) to indicate when in the sequence these pictures are taken.

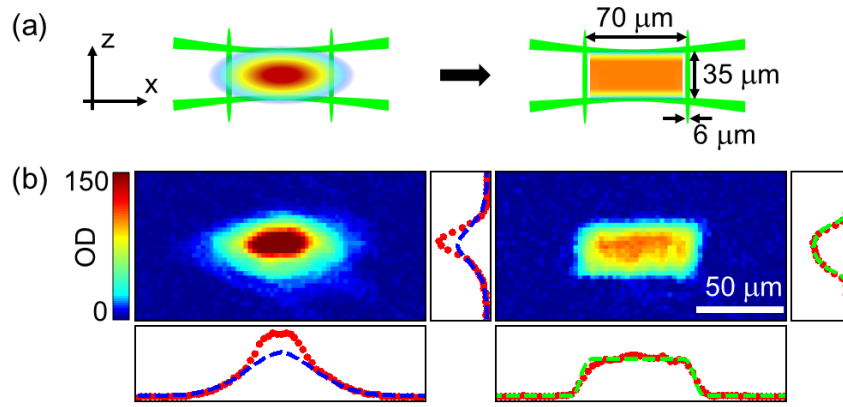


**Fig. 6.8.:** Preparing a quasiuniform Bose gas. (a) The atoms are loaded into the box trap after precooling in a harmonic trap. (b) In situ images of the cloud just before (left) and after (right) loading into the box and corresponding line-density profiles along  $x$  (bottom plots) and  $z$  (side plots) directions. The line densities along  $x$  ( $z$ ) are obtained by integrating the images along  $z$  ( $x$ ). The blue dashed lines in the left panel are fits to the thermal component of the harmonically trapped gas. The green dashed lines in the right panel are fits based on the expected profiles for a uniform-density gas. The rounding off of these profiles is due to the imaging resolution, which is taken into account in the fits.

## 6.2.2 Non-condensed atoms in a uniform potential

The non-condensed cloud produced immediately after transfer into the uniform trap can be investigated either *in situ* or after release from the trap to gather both qualitative and quantitative evidence for the uniformity of our optical box. These two cases are considered below:

### *In situ* images – Qualitative uniformity

We take images of the optically dense clouds immediately before and after the transfer using a 500 ns exposure of intense laser light with saturation parameter  $I/I_S = 150$ . These high intensity images are analysed using the full form of Eq. 2.4 [113, 114, 123] to give the optical density,  $OD = \sigma_0 \int n dz$  profiles shown in Fig. 6.8. The contrast between the shape of the atom cloud in a harmonic trap and our trap is our first qualitative evidence that the novel trap is indeed uniform.

For each image, we show the line-density profiles,  $\tilde{n}$ , obtained by integrating the image along either  $x$  (across) or  $z$  (down). For a perfectly cylindrical volume of length  $L$  and radius  $R$  uniformly filled with atoms, the profiles in these two directions would be:

$$\tilde{n}(x) = \int OD dy \propto \text{TH} \left( \frac{x}{L} \right) \otimes \text{PSF} \quad (6.2)$$

$$\tilde{n}(z) = \int OD dx \propto \sqrt{1 - \left(\frac{z}{R}\right)^2} \otimes PSF, \quad (6.3)$$

where  $\text{TH}(x)$  is a top hat function which is unity for  $-1/2 < x < 1/2$  and zero elsewhere, and  $\otimes PSF$  indicates convolution with the imaging point spread function (which we take to be a Gaussian of waist  $5 \mu\text{m}$ ). The green dashed lines in Fig. 6.8(b) are fits to the data using the functions above. These fits describe the data well, and give  $L = 63 \pm 2 \mu\text{m}$  and  $R = 15 \pm 1 \mu\text{m}$ , which are consistent with the calculated separation of the green walls based on the hologram in Fig 6.6, reduced by the diffraction-limited wall thickness.

### Time-of-flight images – Quantitative uniformity

We now turn to a more quantitative study of the uniformity of our gas, which we access via the momentum distribution of trapped thermal clouds. To measure the momentum distribution, we release the non-condensed cloud from the uniform trap and image it after 50 ms ballistic expansion in ToF (see in section 2.2). For a thermal cloud, this gives an image of the momentum distribution of the atoms convolved with the (relatively large) initial density distribution in the box<sup>4</sup>.

For a quantum gas, the momentum distribution of a cloud contains the fingerprint of the uniformity of the trap from which that cloud was released. To quantitatively extract this fingerprint, we parameterise our trap by considering it to be an effective *isotropic*<sup>5</sup> potential of the form  $U_0 r^n$ . Under this assumption<sup>6</sup>, the momentum distribution is:

$$\begin{aligned} f(p) &= \int d^3\mathbf{r} \frac{1}{\exp\left(\frac{1}{k_B T} \left[ \frac{p^2}{2m} + U_0 r^n - \mu \right]\right) - 1} \\ &= \frac{4\pi}{n} \frac{U_0}{k_B T} \Gamma\left(\frac{3}{n}\right) g_{3/n} \left( e^{\frac{1}{k_B T} \left( \mu - \frac{p^2}{2m} \right)} \right). \end{aligned} \quad (6.4)$$

<sup>4</sup>Note that we ignore the interaction effects for these non-condensed clouds. The interaction energy per particle is  $\sim k_B \times 10 \text{ nK}$  which is much less than the cloud temperature (refer forward to Fig. 7.5)

<sup>5</sup>The anisotropy of the potential does not affect the scalings discussed here: for an anisotropic trap of the form  $\sum_i U_i r^{n_i}$ , the parameter  $\alpha$  (defined after Eq. 6.5) becomes  $\alpha = 1 + \sum_i 1/n_i$ , and the remainder of the subsequent analysis is unchanged.

<sup>6</sup>Note that we have also used the semi-classical approximation (replacing a sum over eigenstates with an integral over momenta). We used this approximation for harmonic traps in Part I of this thesis. In the context of a uniform box-trap is exact in the case of an infinite box size. Performing a numerical comparison between an exact eigenstate summation and the semi-classical momentum integral for a finite box [39] shows that semi-classical approximation reproduces the momentum state occupations to within 1% relative error for experimentally relevant parameters.

Note that the trap parameter  $n$  has a strong influence on the form of the momentum distribution (as  $n$  increases,  $g_{3/n}(e^{-x^2})$  becomes more sharply peaked). Using the fact that an atom with momentum  $\mathbf{p}$  will travel a distance  $\mathbf{x}' = \mathbf{p}t/m$  in time  $t$ , we can calculate the line-density profile for the cloud (ignoring the initial size of the box) as:

$$\begin{aligned}\tilde{n}_{\text{ToF}}(z) &= \int f\left(\mathbf{p} = \frac{\mathbf{x}m}{t}\right) dydx \\ &= \sqrt{\frac{m}{2t^2k_B T}} \left(\frac{T}{\theta_\alpha}\right)^{\alpha+1/2} g_\alpha\left(e^{\frac{1}{k_B T}\left(\mu - \frac{mz^2}{2t^2}\right)}\right),\end{aligned}\quad (6.5)$$

where  $\alpha = 1 + 3/n$  and the constant  $\theta_\alpha$  absorbs various factors such as the imaging magnification and cross section. To account for the initial size of the uniform box, we convolve  $\tilde{n}_{\text{ToF}}$  with the *in situ* profile from Eq. 6.3.

The limiting cases of a parabolic trap ( $n = 2$ ) and a truly uniform trap ( $n \rightarrow \infty$ ) correspond to  $\alpha = 5/2$  and  $\alpha = 1$  respectively. In Fig. 6.9(a), we attempt to fit our ToF images with these two limiting cases, using  $\theta_\alpha$ ,  $\mu$  and  $T$  as free parameters. The  $g_1$  function fits  $\tilde{n}_{\text{ToF}}$  very well, with the reduced  $\chi^2 \approx 1$ . The  $g_{5/2}$  fit is comparatively poor:  $\chi^2 \approx 7$  and the systematic patterns in the fitting residuals  $\Delta\tilde{n} = \tilde{n}_{\text{ToF}} - \tilde{n}_{\text{fit}}$  clearly show that this is fundamentally a wrong functional form. Qualitatively, the measured momentum distribution is more "peaky" than that of a harmonically trapped degenerate gas (this arises because the density of states in a uniform box allows a greater occupation of low energy states than in a harmonic trap).

As shown in the inset of Fig. 6.9(a), the measured  $\tilde{n}$  can be fitted well using  $\alpha$  in the range  $1 - 1.7$ , whereas higher values can be clearly excluded. Note, however, that  $\theta_\alpha$  was one of our free parameters in these fits. Allowing this theoretical constant to vary gives the fitting function an unphysical freedom and overestimates the range of suitable  $\alpha$  values. Crucially, only for the correct  $\alpha$  is the best-fit value of  $\theta_\alpha$  a temperature-independent constant. Below we use this fact to accurately determine the leading-order correction to the flatness of our trapping potential.

### Cooling in the uniform trap – Precise evaluation of flatness

Above, we have looked at qualitative evidence from *in-situ* density profiles and simple quantitative evidence from ToF images which suggest that our box is uniform to within  $\alpha < 1.7$  (i.e. a power law certainly steeper than  $r^4$ ). However, we have noted that we used too many degrees of freedom in these simple fits, and we can extract a better estimate of the true uniformity by finding the value of  $\alpha$  for which the fit parameter  $\theta_\alpha$  (theoretically constant for fixed  $\alpha$ ) does not vary with temperature.

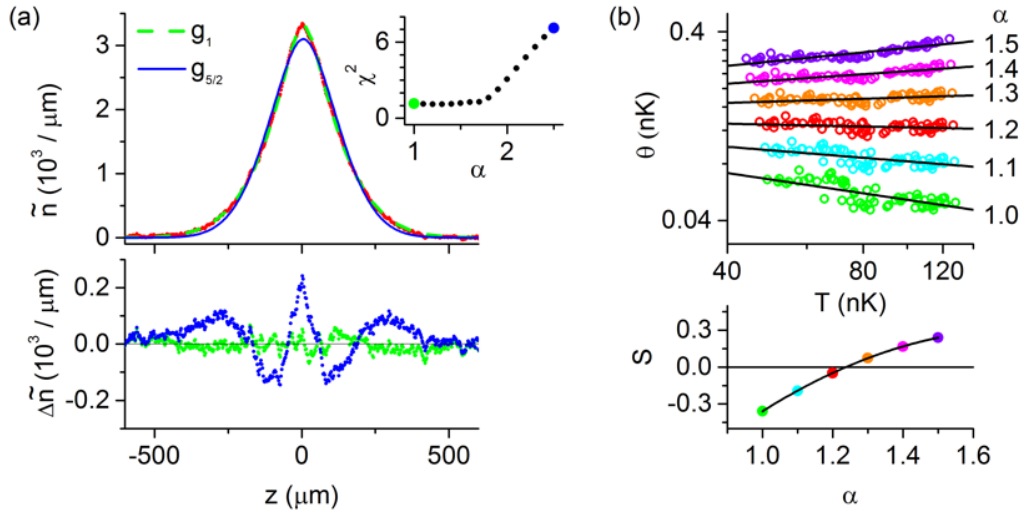


**Fig. 6.9.:** Momentum distribution in a (quasi)uniform degenerate Bose gas. (a) ToF profile  $\tilde{n}(z)$  of a noncondensed cloud (red) and  $g_\alpha$  fits to the data, with  $\alpha = 1$  (green) and  $5/2$  (blue). We also show the fitting residuals  $\Delta\tilde{n}$ . Inset: fitting  $\chi^2$  versus  $\alpha$ . (b) Flatness of the box potential: the condition  $S = d[\log(\theta)]/d[\log(T)] = 0$  (see text) gives  $\alpha = 1.23 \pm 0.03$ , corresponding to an effective  $r^{13 \pm 2}$  potential.

This process is outlined below to reveal that the trap is in fact uniform up to a leading order correction of the form  $\sim r^{13}$ .

To vary the temperature of the cloud, we cool the atoms by forced evaporation (i.e. we reduce the green laser intensity to lower the trap walls and let high energy atoms escape). Since  $\theta_\alpha$  varies with the total depth of the trap (i.e. with  $U_0$ ), we always recompress the trap back to a depth of  $2 \mu\text{K}$  to keep  $\theta_\alpha$  theoretically constant, before releasing the atoms to take ToF images<sup>7</sup>.

The drift of the fitted  $\theta_\alpha$  with the corresponding temperature,  $T$ , is shown for different values of  $\alpha$  in Fig. 6.9(b) (each point represents a single experimental run). We empirically observe that this drift is described well by a constant slope  $S_\alpha = d[\log(\theta_\alpha)]/d[\log(T)]$ , and we see that  $S_\alpha$  varies monotonically<sup>8</sup> with  $\alpha$ . From the no-drift condition,  $S_\alpha = 0$ , we get  $\alpha = 1.23 \pm 0.03$ , and therefore conclude that the leading-order correction to the flatness of our box is captured by an effective  $r^{13 \pm 2}$  power law.

<sup>7</sup>At sufficiently low temperatures, a condensate may form in the trap which will appear as a sharp peak at low momentum in the centre of our ToF image. Since we do not want to address the additional complication of the condensate until the next section, we exclude the central  $180 \mu\text{m}$  region of the cloud (i.e. a region larger than all the BECs observed below) from the fits in this section.

<sup>8</sup>Physically, if the  $\alpha$  used for fitting is too high, as the gas cools the actual momentum distribution narrows faster than  $g_\alpha$ . The fit then increasingly underestimates  $T$  and compensates by decreasing  $\theta_\alpha$ . Conversely, if  $\alpha$  is too low, the fitted  $\theta_\alpha$  increases as the gas is cooled. The fitted temperatures also show the expected systematic drifts.

In reality, our trap is anisotropic: from Fig. 6.4(c), we theoretically expect our potential to resemble  $U_0^{\text{LG}} r_{\perp}^{10} + U_0^{\text{cap}} x^{n_x}$  for  $\eta \approx 10$ , where  $n_x$  is the steepness parameter of the capping beams which we numerically find to be  $n_x \gg 10$ . These values predict  $\alpha \approx 1.2$ , which corresponds to an effective  $r^{-15}$  power law, consistent with the experimental observation.

Although our careful analysis has enabled us to distinguish an  $r^{-13}$  power law from the ideal case, we will see in section 7.1 that this distinction is minor for most thermodynamic and many-body studies.

### 6.2.3 A BEC of atoms in a uniform potential

Having verified the uniformity of our trap, we now turn our attention to observing evidence that a phase transition to a condensed state occurs when we evaporatively cool the cloud using the full experimental sequence in Fig. 6.7. Below, we discuss two pieces of evidence which indicate that a phase transition does indeed occur when we cool.

#### Evidence for BEC – Aspect ratio inversion in time-of-flight

The most immediate evidence for a BEC in our uniform box comes from the sharp increase in occupation of low momentum states after evaporative cooling. We observe these states as a dense central peak when we release the cloud for 50 ms ToF. This macroscopic occupation is obvious in momentum space (ToF) pictures, but importantly, it cannot be seen *in situ*. Such behaviour is expected for a uniform system, where the condensate is delocalised across the entire trap volume, and cannot be easily discerned from the homogeneous thermal atoms *in situ*. This phenomenon of condensation in momentum space but not in real space is shown in Fig. 6.10(b), where it is contrasted with the harmonic case which shows obvious signs of condensation in both spaces.

In ToF images from our homogeneous trap, the thermal cloud expands with an isotropic velocity distribution, while the BEC peak undergoes an aspect ratio inversion from the wide, short trap to a narrow, tall ToF peak. This inversion is characteristic of a condensed state<sup>9</sup>.

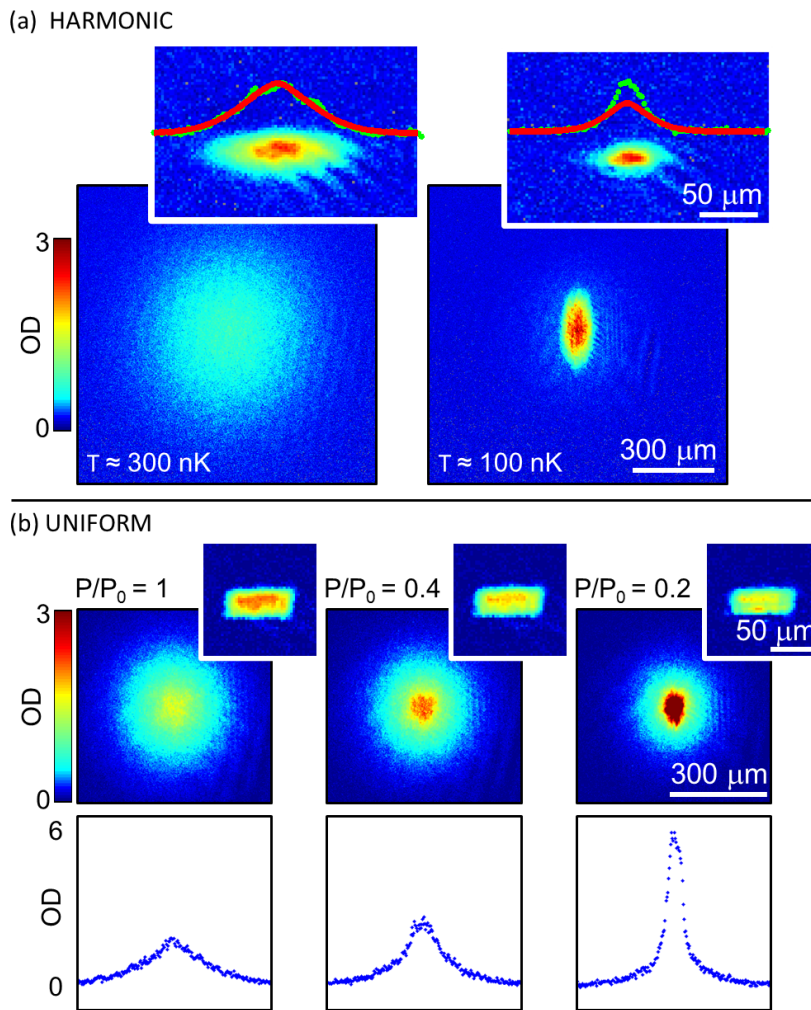


**Fig. 6.10.:** Condensation in real space and/or momentum space. (a) *Harmonic* trap. We show absorption images taken after 50 ms of ToF (main panels) and *in situ* (inset panels, with the same colour scale as in Fig. 6.8). The top panels show cuts through the *in situ* distributions (green points) together with fits to the thermal wings (red line). The condensate is revealed in the colder cloud as a sharp peak rising above the thermal cloud in both real space and momentum space, with the aspect ratio of the BEC inverting during ToF. (b) *Uniform* trap. Cooling is achieved by lowering the trapping laser power  $P$ . Again, we show images after 50 ms of ToF and *in situ* (insets). The bottom panels show cuts through the momentum distributions recorded in ToF. In contrast to the case of a harmonic trap, no dramatic effects of cooling are observed *in situ*. However, BEC is clearly seen in the anisotropic expansion.

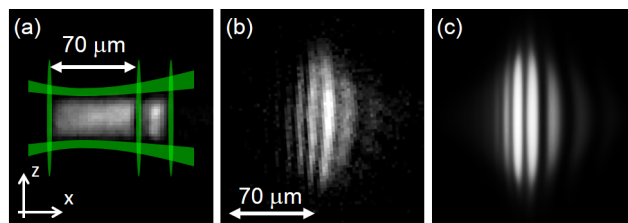


**Fig. 6.11.:** Matter-wave interference with a (quasi)uniform BEC. (a) *In situ* image of a two-trap configuration, together with a sketch of the green-light arrangement used to create it. (b) Interference pattern observed after 100 ms of ToF expansion. (c) Numerical simulation of the expected interference pattern.

## Evidence for coherence – Interference

A BEC is a phase-coherent object, and we prove the presence of coherence by observing interference fringes when we overlap our BEC with another coherent matter-wave. This is very easily achieved in our apparatus as follows:

The versatility of our vector-hologram method allows us to digitally insert a third capping wall further down the tube beam. This traps a small satellite cloud next to the large uniform cloud (see Fig. 6.11(a)). We can fill both of these dark traps with atoms and then simultaneously evaporate in the green light to produce two spatially separated condensates. Since the satellite trap is very small, the rounding of the potential by the diffraction limit means that it is not uniform. Nevertheless, the satellite BEC is a coherent object which we can use to interferometrically probe the coherence of the larger, uniform BEC.

We produce a quasi-pure BEC in both traps ( $T < 30$  nK), and then release the atoms, allowing the two clouds to overlap in ToF. After 100 ms ToF, we observe the interference fringes seen in Fig. 6.11(b). The contrast of these fringes is up to  $\approx 50\%$ , limited by our imaging resolution and the fact that the satellite BEC contains considerably fewer atoms than the uniform BEC. This contrast, and the shape of the fringes are reproduced in a numerical simulation of the Gross-Pitaevskii equation (see Appendix C) shown in Fig. 6.11(c).

Note that the fringes become narrower from right to left in Fig. 6.11. This can be qualitatively understood by considering that the uniform BEC expands very slowly in the  $x$  direction, meaning that we can just consider the expansion of the satellite BEC, which expands rapidly in all directions. When we take an image after time  $t_{\text{ToF}}$  of time-of-flight, the momentum component,  $\hbar k_x$ , originating in the satellite will have moved a distance  $\delta x = \hbar k_x t_{\text{ToF}}/m$ . This gives a parabolic variation of phase  $k\delta x \approx (m/\hbar t_{\text{ToF}})\delta x^2$  for the components of the satellite BEC in the  $x$  direction. When this interferes with the uniform BEC (which is essentially not expanding along  $x$ ), we obtain fringes with parabolic spacing.

Observation of interference is firm evidence that the cloud in our trap is a coherent condensate. We will return to the opportunities that this versatile interferometric technique offers for future experiments in section 9.3.

---

<sup>9</sup>The inversion can be caused either by the anisotropic momentum distribution of an anisotropic spatial wavefunction or by interactions which tend to expand the cloud fastest in the most constrained trapping direction where the interaction force  $-V_0\nabla n$  is largest. In our case, interaction effects dominate the BEC expansion because the interaction energy of the our BEC with  $10^5$  atoms is  $\sim k_B \times 1$  nK, which is much greater than the kinetic energy of the box ground state (approximately  $k_B \times 10^{-2}$  nK).

## 6.3 Conclusion

In this chapter, we have discussed the first realisation of an atomic BEC in a uniform potential. So far, we have simply outlined the novel apparatus, illustrated the profiles of thermal clouds in our trap, and verified that we can produce BECs by evaporative cooling. Furthermore, we have benchmarked the uniformity of our trap by measuring the leading order correction from a flat potential to be a steep power law  $\sim r^{13}$ . This new system has great potential for new experiments where parabolic trapping geometries complicate or entirely mask many fundamental many-body phenomena which we wish to investigate. In the next chapter, we will summarise a series of experiments which probe the equilibrium properties of Bose gases in our uniform trap both near and far below the critical BEC transition temperature. Throughout these experiments, we will contrast our homogeneous gas results with the more traditional harmonic trap experiments.

# Observing Equilibrium Properties of a Homogeneous Bose Gas

While benchmarking our novel trap we immediately saw considerable contrast between the behaviour of our homogeneous gas and that of a harmonically trapped sample. Most notably, in the previous chapter we observed that the momentum distribution of a degenerate homogeneous gas is "more sharply peaked" at any given temperature and chemical potential, and we saw that condensation occurs in momentum space only. In this chapter we will continue to highlight the *equilibrium* properties of a gas trapped in our novel system and contrast these with the behaviour of gases in more conventional harmonic traps.

Our discussion will be split into two parts (see Fig. 4.2): Section 7.1 will concentrate on the equilibrium thermodynamics of a thermal or partially condensed homogeneous Bose gas, while 7.2 will specifically study the equilibrium properties of the ground state BEC. Since we designed our homogeneous gas as an idealised system, the experiments discussed in this chapter can all be described accurately by textbook theories, and they will not highlight many unexpected surprises (except perhaps section 7.1.3). This allows us to progress rapidly through many topics with the aim of with creating a solid foundation on which to build more complex experiments later (see chapter 8).

## 7.1 Thermodynamic experiments

The thermodynamic studies that we present here will concentrate on a central concept in BEC theory: Einstein's textbook picture of condensation as a purely statistical phase transition. Using our new trap, we are able to give the best experimental observation of the statistically-driven phenomenon of excited-state saturation (section 7.1.1), and we uncover experimental evidence for a novel cooling effect driven by quantum statistics - the quantum Joule-Thomson effect - which was theoretically predicted more than 70 years ago [124] (section 7.1.3). Both of these effects were previously obscured by the inhomogeneity of parabolic traps.

## 7.1.1 Saturation of a Bose gas

We will begin our discussion with a theoretical summary of Einstein's picture of a non-interacting Bose gas in a potential  $U(r)$ , and present our experimental support for this picture in later subsections. Einstein said that the density of atoms in the excited states is given by:

$$n'(r) = \int \frac{d^3\mathbf{p}}{2\pi\hbar} \frac{1}{\exp\left(\frac{1}{k_B T} \left[ \frac{p^2}{2m} + U(r) - \mu \right]\right) - 1}$$

$$\implies n'(r)\lambda_T^3 = g_{3/2}\left(e^{[\mu - U(r)]/k_B T}\right), \quad (7.1)$$

where  $g_\alpha(z)$  is the polylogarithm function, and the remaining symbols are the standard notation of the semi-classical approximation.

Inspecting Eq. 7.1, we find that the excited state density (in a infinite<sup>1</sup>, non interacting gas) cannot rise above  $n_c\lambda_T^3 = \zeta(3/2) = 2.612$ . This sets a strict limit on the excited state populations at a given temperature, which occurs for the case  $\mu \rightarrow \min[U(r)]$ . Once the excited states are saturated in this way, any additional atoms must pile up in the ground state, leaving the excited state population constant at constant temperature (see Fig. 7.1(a)). This capping of the thermal population is Einstein's saturation picture.

The trapping geometry can modify this picture in the following way: The critical density,  $n_c$  is first achieved at the point(s) satisfying  $U(\mathbf{r}) = \min[U(\mathbf{r})]$ , and adding further atoms will cause a condensate to form at these points. The mean field interaction between the thermal cloud and the newly-formed dense condensate modifies the effective potential experienced by the thermal atoms. Hartree-Fock theory gives the modification as [3] (see also footnote 8).

$$V_{\text{eff}}(\mathbf{r}) = U(\mathbf{r}) + 2V_0[n'(\mathbf{r}) + n_0(\mathbf{r})], \quad (7.2)$$

<sup>1</sup>Here we ignore the zero-point energy of the trap which shifts the critical value of  $\mu$  in traps with a finite atom number [3]

where  $n_0$  is the condensate density and  $V_0(> 0)$  is the interaction pseudo-potential strength defined in Eq. 1.2. Ignoring the dilute thermal-thermal interaction term, and inserting the Thomas-Fermi solution  $n_0(\mathbf{r}) = [\mu - U(\mathbf{r})]/V_0$  gives:

$$V_{\text{eff}} = |U(\mathbf{r}) - \mu| + \mu. \quad (7.3)$$

Now we make the contrast between the harmonic and uniform cases:

### Harmonic case

If  $U(\mathbf{r}) = \frac{1}{2}m\omega_{\text{ho}}^2 r^2$ , then Eq. 7.3 describes a ‘‘Mexican hat’’ potential (see Fig. 7.1(b)). Crucially as the condensate appears (i.e. as  $\mu$  changes sign) the locus of points  $U(\mathbf{r}) = \min[V_{\text{eff}}(\mathbf{r})]$  changes from a single point ( $\mu < 0$ ) to a 3D shell of points ( $\mu > 0$ ). Therefore, the growing condensate effectively pushes the critical region into a larger volume, and hence more thermal atoms must be added to maintain the critical density  $n_c$ . Due to the geometry of the trap, as the condensate grows, the critical region is pushed further out of the trap and by the volumetric argument presented above, more and more thermal atoms are required to support the growing condensate. The growth of the thermal occupation as the condensate grows means we cannot say that the excited states are saturated on a global scale<sup>2</sup>. The trap geometry has played a key role in this non-saturation argument [45].

For completeness, we briefly quantify this non-saturation to first order by modelling the thermal atoms as entirely excluded from the region  $r < R_{\text{TF}}$  occupied by the condensate [25, 26]. Under this assumption, integrating 7.1 gives:

$$N' \lambda_T^3 = 4\pi \int_{R_{\text{TF}}}^{\infty} g_{3/2} \left( e^{[\mu - \frac{1}{2}m\omega_{\text{ho}} r^2]/k_B T} \right) r^2 dr \quad (7.4)$$

where  $R_{\text{TF}}^2 = 2\mu/m\omega_{\text{ho}}^2$  is the Thomas-Fermi radius of the condensate. Making the substitution  $R^2 = r^2 - R_{\text{TF}}^2$  and expanding  $r$  to first order<sup>3</sup> in  $R_{\text{TF}}/R$  allows us to evaluate this integral as:

$$\frac{N'}{N_c^0} \approx 1 + 2.02 \frac{\hbar\omega_{\text{ho}}}{k_B T} \left( \frac{N_0 a}{a_{\text{ho}}} \right)^{2/5}, \quad (7.5)$$

<sup>2</sup>Note that the excited states are *locally* saturated

<sup>3</sup>The main contribution to the integral comes from  $r \approx \sqrt{2kT/m\omega_{\text{ho}}}$ , so this expansion is valid in the regime  $kT \gg \mu$ .

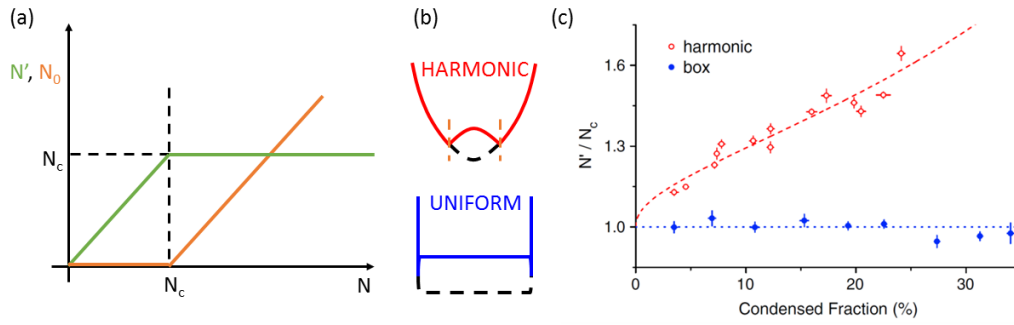


**Fig. 7.1.:** Saturation of the thermal component. (a) Einstein's textbook picture of saturation in a uniform Bose-gas at fixed temperature. Once the total atom number,  $N$  passes a temperature dependent critical number,  $N_c$ , the excited state population,  $N'$  saturates and all additional atoms appear in the condensate. (b) Mean-field repulsion of thermal atoms from the dense condensate. We present cartoons of the effective potential (solid line) experienced by thermal atoms in the presence of a condensate. The black dotted lines are the potential shapes in the absence of a condensate. The orange dotted lines mark the radial extent of the condensate in the harmonic case and the condensate spans the box in the uniform case. (c) In the box trap, a partially condensed gas follows the ideal prediction,  $N_0 = N_c$ , whereas in the harmonic trap the thermal component is strongly non-saturated. Each point represents the average of approximately six experimental runs with error bars indicating the uncertainty on the mean. The dashed red line shows the theoretical prediction for the harmonic trap. (For the harmonic-trap data  $T \approx 110$  nK and  $N_c \approx 65 \times 10^3$ .)

where we have used the Thomas-Fermi result  $\mu = \frac{15^{2/5}}{2} \left( \frac{Na}{a_{\text{ho}}} \right)^{2/5} \hbar\omega_{\text{ho}}$  [3],  $a_{\text{ho}}$  is the harmonic oscillator length, and  $N_0^c$  is the non-interacting critical atom number (compare this result with Eq. 2.16). This completes our demonstration that the combination of geometrical and interaction effects cause  $N'$  to increase with  $N_0$  for  $a < 0$  in a harmonic trap.

### Uniform case

In contrast to the harmonic case, there is no geometrical change to a uniform potential as  $\mu$  varies in Eq. 7.3. The presence of a condensate only causes a global shift in  $V_{\text{eff}}$  (see Fig. 7.1(b)). This means that there is no geometrical argument for non-saturation in a homogeneous Bose gas. A full treatment of an interacting homogeneous gas, should strictly replace  $p^2/2m$  in the Bose factor in Eq. 7.1 with the full Bogoliubov dispersion relation  $\epsilon(\mathbf{p}) = [(p^2/2m + V_0 n_0)^2 - (V_0 n_0)^2]^{1/2}$ . This leads to the thermal phase-space density actually dropping *below*  $n_c \lambda^3$  once the BEC forms in a uniform system [125–127]. For our parameters this effect is small, and we do not hope to measure it in our experiment [39, 125–127]. Therefore, we hope to observe a saturated gas even at finite interaction strengths in our system.

We experimentally test this saturation of a homogeneous gas as follows: By varying the number of atoms initially captured in the magneto-optical trap from the background gas (see Fig. 6.1), we can change the number of atoms loaded into the uniform trap. We then evaporate to empirically chosen points such that we

achieve clouds at a constant temperature of  $45 \pm 1$  nK with different condensed fractions  $N_0/N$ . The thermal atom number is counted by fitting the  $g_\alpha$  form to a ToF image, excluding the condensate peak, and we then count  $N_0$  by and integrating the residual of this fit at low momenta. We find, in stark contrast to the harmonic case, that  $N'$  does not increase as  $N_0$  increases (i.e. the dashed blue line in Fig. 7.1(c) is horizontal to within our experimental errorbars), indicating that our gas is globally saturated. This is the best demonstration of Einstein's picture of excited state saturation to date.

Two further thermodynamic experiments arise from this saturation property. These are briefly outlined below:

### 7.1.2 The critical condition

By varying the final depth of the evaporation in the uniform trap during the sequence in Fig. 6.7, we simultaneously vary the temperature and condensed fraction of the final cloud. We can extract a critical point by plotting  $N'$  and  $N_0$  vs.  $T$  in Fig. 7.2, and looking at the conditions at which the condensate first appears. For the experimental sequence shown, we find the critical point to be when  $N' \approx 5 \times 10^5$  atoms, and  $T_c = 92 \pm 3$  nK. From the measured box volume, we get a consistent theoretical value for a critical temperature,  $T_c^0 = 98 \pm 10$  nK. This calculation includes a small numerically calculated finite-size shift and an interaction shift of  $T_c^0$  [128–130], of about 6% and 1%, respectively on top of the ideal gas result  $n\lambda_T^3 = \zeta(3/2)$ . The error

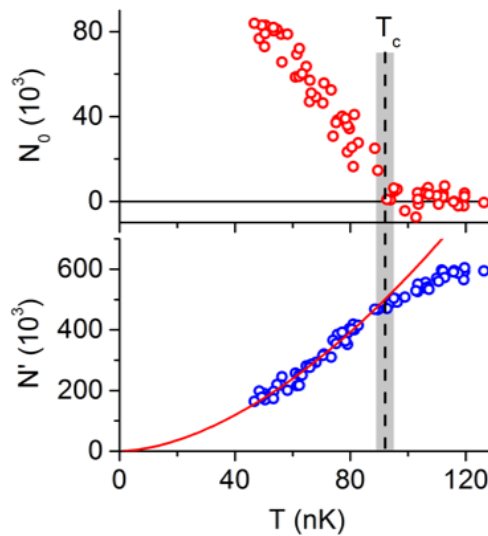


**Fig. 7.2.:** The number of condensed ( $N_0$ ) and thermal ( $N'$ ) atoms versus  $T$ . The critical temperature  $T_c = 92 \pm 3$  nK is in agreement with the prediction for a uniform Bose gas. Below  $T_c$ , a power-law fit (solid red line) gives  $N_0 \propto T^{1.73 \pm 0.06}$ . (single experimental run per point; scatter indicates random error scale)

on the theoretical value includes the 10% uncertainty in our absolute atom-number calibration (calibrated by measuring  $T_c$  in a harmonic trap [41]).

Now we harness the saturation of our gas to verify Einstein's prediction  $N_c \propto \lambda_T^{-3}$  in Eq. 7.1. Cooling beyond the critical point gives a gas with  $N_0 > 0$  and  $N' = N_c$  (i.e. saturation). We measure  $N'$  and  $T$  as we cool and fit our experimental data below  $T_c$  to obtain  $N_c \propto T^{1.73 \pm 0.06}$ . The measured exponent of  $1.73 \pm 0.06$  is close to the perfectly uniform behaviour of  $3/2$ , and agrees very well with the predicted power law in an  $r^{13}$  potential (for a trap of fixed  $\alpha$ , we expect<sup>4</sup>  $N_c \propto T^{\alpha+1/2}$ , so our power law is consistent with our value of  $\alpha \approx 1.23$ ).

### 7.1.3 The quantum Joule-Thomson effect

So far, we have presented studies which give the best experimental evidence for the well known phenomenon of saturation at  $n_c \lambda_T^3 = \zeta(3/2)$ . While working on these experiments, we uncovered a more surprising effect: when a condensed cloud is held in the imperfect vacuum of our apparatus, it spontaneously cools down.

This phenomenon again boils down to the saturation of the gas: If we remove an atom from the thermal cloud in a partially condensed sample, then, instantaneously,  $N' < N_c$ . This inequality is not allowed for a saturated gas with  $N_0 > 0$ , and so the balance  $N' = N_c$  must be restored by transferring an atom from the condensate to the thermal cloud. This transfer alone does not conserve energy (the condensate atom is gaining energy), and must be accompanied by a redistribution of the existing thermal atoms into a lower energy state (see Fig. 7.3). In summary, this means that if we hold a saturated cloud and remove particles in an energy-independent way, then the cloud temperature will decrease. In our imperfect vacuum, it is collisions with the background gas which removes atoms from our sample.

We can phrase this process as the quantum analogue of the classical Joule-Thomson rarefaction of a gas. The Joule-Thomson effect (which is used in industrial refrigerators) describes the change in temperature of an *interacting* classical gas when it undergoes isoenthalpic rarefaction:  $(\partial T / \partial P)_H$ . In an ideal classical gas, the enthalpy,  $H$ , depends only on  $T$ , and thus  $(\partial T / \partial P)_H = 0$ . Therefore, classically, only *interacting* gases can show any change in temperature in an isoenthalpic process. On the other hand, a *quantum* Bose gas will show Joule-Thomson cooling as a purely quantum-statistical effect even in the absence of interactions (see below) [124]. We therefore refer to the process in which  $(\partial T / \partial P)_H \neq 0$  in a system without interactions as the *quantum* Joule-Thomson effect. This quantum-mechanical cooling effect was predicted more than 70 years ago [124], and it is only with the experimental

<sup>4</sup>This scaling can be obtained by integrating Eq. 6.5 over  $z$

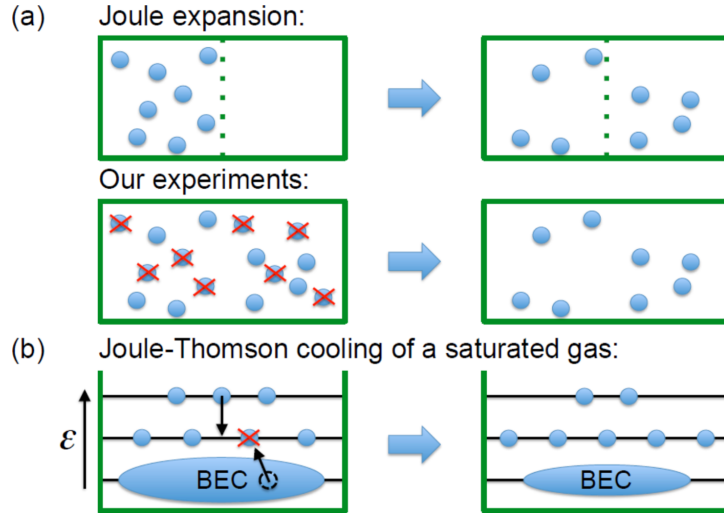


**Fig. 7.3:** A cartoon of the quantum Joule-Thomson effect (a) Isoenthalpic rarefaction. In a classical Joule-Thomson process the system volume is increased, whereas in our experiment, the atom number is reduced. For an ideal gas, both processes conserve specific enthalpy and are thermodynamically equivalent. (b) Microscopic origin of JT cooling in a saturated quantum gas. Removal of a thermal atom requires a zero-energy particle to come out of the BEC in order to maintain  $N_0 = N_c$ , while energy conservation requires redistribution of atoms between energy levels. Cooling is seen in the change of the relative populations of the excited states (in this cartoon we neglect the fact that  $N_c$  also slowly decreases).

advantages of our uniform system that it has been finally experimentally observed (see also [131] for the fermionic case).

### Predicted cooling trajectory

For a non-interacting equilibrium Bose gas, the process of atom loss by background gas collisions is isoenthalpic by the following argument: Within the ideal-gas approximation, the pressure is  $P = \frac{2}{3} E/V$  [3], where  $E$  is the total energy of the system. The enthalpy is then  $H = \frac{5}{3} E$ . Since the collisions with the background gas are not energy selective, the average energy per particle,  $E/N$ , remains constant, so the specific enthalpy,  $h = H/N$ , is conserved.

We can calculate the temperature change as atoms are lost in this isoenthalpic process by starting with the expression for the energy of a partially condensed ideal Bose gas:  $E = (\alpha + 1/2) \frac{\zeta(\alpha+3/2)}{\zeta(\alpha+1/2)} N_c k_B T$  [3], and substituting in  $N_c = T^{\alpha+1/2}$ , to obtain:

$$\begin{aligned} \frac{E}{N} \propto \frac{T^{\alpha+3/2}}{N} &\implies \left( \frac{\partial T}{\partial N} \right)_h = \frac{1}{\alpha + 3/2} \frac{T}{N} \\ &\implies \frac{T}{T_i} = \left( \frac{N}{N_i} \right)^{1/(\alpha+3/2)}. \end{aligned} \quad (7.6)$$

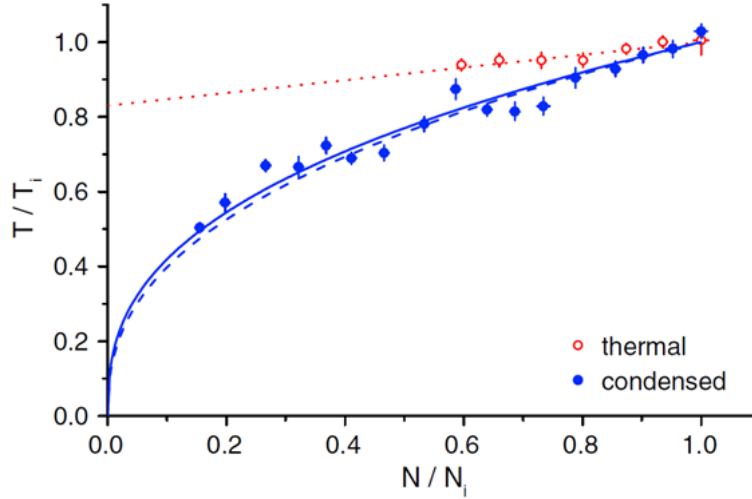


**Fig. 7.4.:** The quantum Joule Thomson effect in a partially condensed and a thermal, weakly degenerate Bose gas. Each point represents the average of approximately five experimental runs with error bars indicating the uncertainty on the mean. The dashed and solid blue line are predictions based on  $\alpha = 1$  (Eq. 7.6) and a more realistic  $\alpha \sim 1.2$  for our trap, respectively. The dotted red line is a numerical calculation (see text).

This provides a theoretical prediction for the cooling phenomenon that we observe.

### Experimental results

Fig. 7.4 shows the cooling trajectory for an experiment in which we hold a partially condensed cloud at initial temperature  $T_i = 45$  nK in a uniform trap with a vacuum lifetime<sup>5</sup> of  $\tau \approx 10$  s. The cooling as  $N$  varies in this plot from  $N_i = 1.7N_c(T_i)$  to  $0.3N_c(T_i)$  is well captured by Eq. 7.6.

Classically, the Joule-Thomson effect is often phrased in terms of a coefficient  $\mu_{\text{JT}} = (\partial T / \partial P)_h$ . For our quantum system, we write:

$$\begin{aligned} \mu_{\text{JT}} &= \left( \frac{\partial T}{\partial N} \right)_h \left( \frac{\partial N}{\partial P} \right)_h = \frac{3}{2} V \frac{N}{E} \left( \frac{\partial T}{\partial N} \right)_h \\ \implies \mu_{\text{JT}} &= \frac{2}{5} \frac{\lambda_T^3}{\zeta(5/2) k_B}. \end{aligned} \quad (7.7)$$

<sup>5</sup>Note that due to the low particle density ( $< 5 \times 10^{12} \text{ cm}^{-3}$ ) the three body recombination rate is negligible [48], and throughout the decay, the elastic scattering rate remains sufficiently high for the gas to re-equilibrate on a timescale  $\leq 2 \text{ s} \ll \tau$  [36]. This ensures that we do not form a superheated state.

where we have taken the perfectly uniform case ( $\alpha = 1$ ). At our lowest temperature,  $\mu_{JT} \approx 4 \times 10^9$  K/bar, which is 10-11 orders of magnitude larger than typical values observed in classical gases [132].

The effect we observe is purely quantum mechanical ( $\mu_{JT} \rightarrow 0$  as  $\hbar \rightarrow 0$ ) and driven by Bose statistics (not by interactions<sup>6</sup>). Note that this physics is masked in the case of a harmonic trap because (a) the gas is not saturated for any experimentally accessible interaction strengths, and (b) the increased densities at the centre of the trap lead to greater three-body effects which heat the cloud faster than the Joule-Thomson effect cools it (see the equilibrium decay curves in chapter 2).

We do not expect this dramatic cooling to occur in a non saturated cloud since the qualitative understanding we gave relies on the clamping  $N' = N_c$ . A minor complication to this picture is that for a degenerate but not condensed cloud, we do expect some cooling effect from energy-unselective atom loss. This arises from the fact that the ratio  $\xi \equiv E/[(\alpha + 1/2)Nk_B T]$  decreases from 1 to  $\frac{\zeta(\alpha+3/2)}{\zeta(\alpha+1/2)}$  ( $\approx 0.514$  for  $\alpha = 1$ ) between the classical limit and the critical point. As background collisions reduce  $N$ , the gas becomes less degenerate, and  $\xi$  grows. Hence, if  $E/N$  is kept constant  $T$  must slightly decrease. The dotted red line in Fig. 7.4 shows a numerical calculation of this effect for a thermal cloud with  $N_i = 0.6 N_c(T_i)$  [124], and again, this fits the data very well.

## 7.2 Ground state measurements

We now shift our attention away from the thermodynamics of thermal and partially condensed homogeneous gases to concentrate on the BEC itself. In order to investigate this low energy state, we will introduce the technique of Bragg spectroscopy. Bragg spectroscopy is a valuable tool for accessing precise information on the momentum distribution of our trapped gas. This will allow us to perform more complex studies such as the dynamical study in chapter 8. Before embarking on these dynamical studies, we will invest time in this section to discuss and benchmark our Bragg spectroscopy apparatus in a simple equilibrium context. We start with the theory of Bragg spectroscopy (section 7.2.1), and then briefly illustrate this with experimental applications in static equilibrium (section 7.2.2 and 7.2.3).

<sup>6</sup>The total drop in temperature of 22 nK cannot be explained by the  $< 4$  nK change in interaction energy (calculated from the upper bound  $\frac{8\pi\hbar^2\alpha}{m} \frac{N_i - N}{V}$ ). In fact the interaction energy change actually predicts a small increase in temperature.

## 7.2.1 Bragg spectroscopy

Throughout our thermodynamic studies, we were able to extract quantitative information from ToF profiles of partially condensed gases. This is because the kinetic energy of the excited states in a cloud near the critical temperature is much higher than the interaction energy (see fig: 7.5), meaning the time-of-flight dynamics is dominated by the kinetic energy. Therefore, after an experimentally achievable time-of-flight we can obtain a reasonable measure of the excited-state momentum distribution of the partially condensed gas.

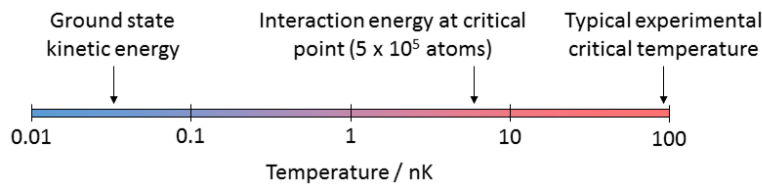


**Fig. 7.5.:** Typical energy scales for the experiments in this chapter. For thermal and partially condensed clouds, ToF expansion is governed by the atoms' kinetic energy (when we cross  $T_c$ , we have  $\sim 5 \times 10^5$  atoms). For a pure BEC of  $\sim 10^5$  atoms, the interaction energy dominates.

However, if we have a pure BEC, the interaction energy dominates the time-of-flight dynamics, so we cannot directly image the momentum distribution of a BEC in an interacting system. Instead, interactions drive the BEC to adopt a characteristic diamond shape in ToF for which we have no analytical form. So far we only understand this shape in numerical simulations (see Fig. 7.6), and through the qualitative argument that that the expansion occurs fastest where the contours of  $|\nabla n_0|$  have least curvature.

The difficulty in extracting the momentum distribution can be overcome using Bragg spectroscopy [133–139]. The essence of the technique is to pick out and spatially separate the atoms in a particular momentum state from the bulk cloud, allowing us to count the occupation of that individual momentum state. By addressing different momenta in turn, we can reconstruct the complete *in-situ* momentum distribution of the cloud. For a pure condensate, this will give the ground state momentum wave-function,  $|\psi(\mathbf{p})|^2$ .

Below we will describe how this momentum selection can theoretically be achieved using two light beams, and later we will outline the apparatus required for Bragg spectroscopy.

### The theory of Bragg spectroscopy

Since a photon's energy/momentum ratio is much larger than that of a non-relativistic atom, single photon interactions produce "near vertical" transitions on an energy-

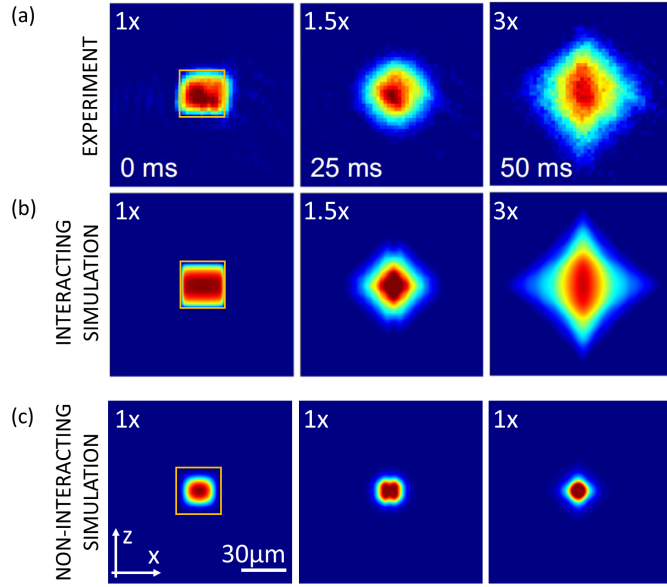


**Fig. 7.6.:** ToF expansion of a gas from a uniform box. (a) Experimental images of a freely expanding gas taken 0, 25 and 50 ms after release from the box (delineated in orange). Since the cloud becomes more dilute as it expands, we adjust the colour scale as shown by the multiplicative factor in the top left of each panel. (b) A simulation based on the Gross-Pitaevskii equation including realistic interactions for  $1.5 \times 10^5$  atoms (see Appendix C) matches the experiment well. (c) Simulation of a non-interacting gas under the same conditions as (b). This illustrates that the ground state expansion in our experiment is dominated by interaction effects.

momentum diagram (see Fig. 7.7(a)). However, combining *two* laser beams with wavevectors  $\mathbf{k}_1$  and  $\mathbf{k}_2 = \mathbf{k}_1 + \Delta\mathbf{k}$ , we can arrange "near horizontal" transitions which impart momentum  $\hbar\Delta\mathbf{k}$  to the atom (the atom absorbs a photon from the first beam and emits into the second). Importantly, energy and momentum conservation ensure that for fixed  $\mathbf{k}_1$  and  $\mathbf{k}_2$  there is only one class of momentum states (a single plane in momentum space<sup>7</sup>) which is resonant with this two photon transition. In this way, a two photon transition can be used to precisely select atoms in a particular momentum class and kick them out of the bulk cloud.

Two photon transitions have been discussed in section 4.1.2 in the context of Raman scattering in a system with three *discrete* levels. For the present application, the wavefunction of the condensate can be written in a *continuous* momentum basis (i.e. plane waves) which can all be coupled by the two lasers. To develop an intuition for the effect of the two laser beams on the occupations of this continuum, we artificially select one particular momentum state  $|\mathbf{p}\rangle$  and its corresponding state  $|\mathbf{p} + \hbar\Delta\mathbf{k}\rangle$  and imagine applying our Raman theory to only these states. In our experiments,  $|\mathbf{p}\rangle$  and  $|\mathbf{p} + \hbar\Delta\mathbf{k}\rangle$  are in the  $F = 2$  internal state, and the intermediate state,  $|i\rangle$ , in the Raman process will be played by states in the  $F' = 3$  hyperfine level (see Fig. 7.7(a)).

<sup>7</sup>The resonant plane is given by  $\mathbf{p} \cdot \Delta\mathbf{k} = 2\pi m(f - f_r - f_{\text{int}})$  using symbols defined in Eq. 7.8

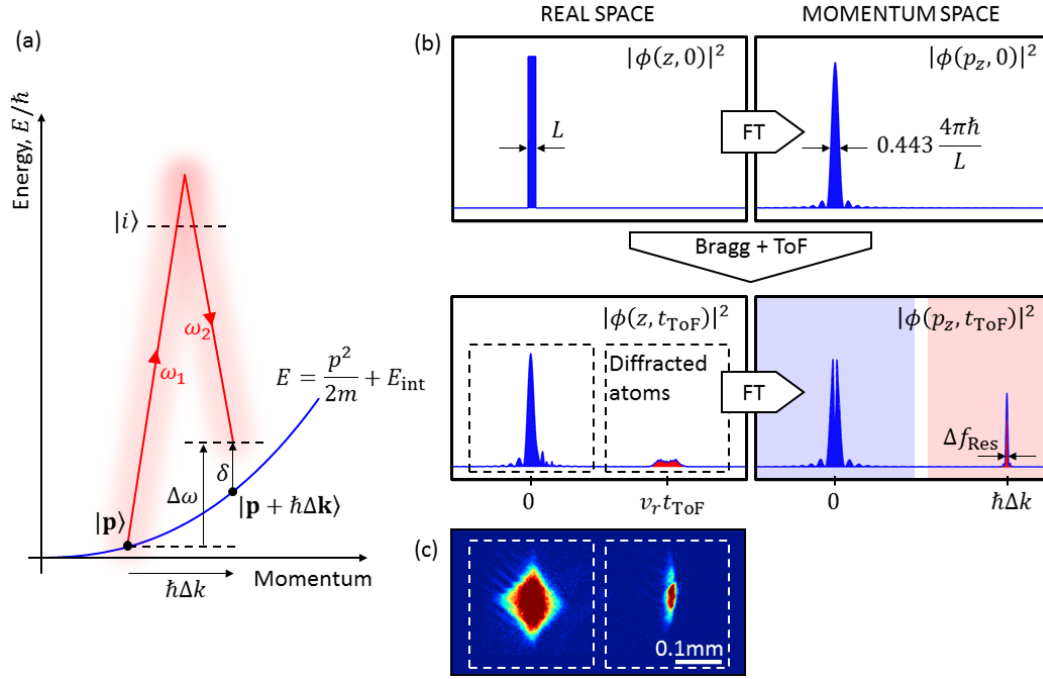


**Fig. 7.7.:** Theoretical picture for Bragg spectroscopy. (a) The laser arrangement for transferring momentum  $\hbar\Delta\mathbf{k}$ . (b) A non-interacting 1D numerical (Gross-Pitaevskii) simulation illustrating the real and momentum space effect of a resonant Bragg pulse with  $\Omega/2\pi = 8$  Hz,  $t = 35$  ms on a top-hat wavefunction of width  $L$ . After  $t_{\text{ToF}} = 140$  ms ToF (bottom panels) diffracted cloud (red) is at position  $v_r t_{\text{ToF}}$ . In momentum space, the Bragg pulse has transferred a very narrow band of momenta out of the states  $\{\mathbf{P}\}$  (blue shading) to the states  $\{\mathbf{P} + \hbar\Delta\mathbf{k}\}$  (red shading). Thus, by counting the diffracted atoms as we address different momenta with the Bragg pulse, we obtain the momentum distribution to a momentum resolution of  $\sim \Delta f_{\text{Res}}$ . (c) A (3D) experimental image corresponding to the (1D) simulation in (b).

As shown in Fig. 4.1(bii.), the detuning  $\delta$  is a key parameter defining the Rabi oscillations between the coupled states (note that we will use two lasers with equal intensities such that  $\delta' = \delta$  in the notation of Eq. 4.10). From Fig. 7.7(a), we can write  $\delta$  as:

$$\begin{aligned} \delta &= \Delta\omega + \frac{1}{\hbar} \left( \frac{p^2}{2m} + E_{\text{int}}^0 \right) - \frac{1}{\hbar} \left( \frac{(\mathbf{p} + \hbar\Delta\mathbf{k})^2}{2m} + E_{\text{int}}^\Delta \right) \\ &= 2\pi(f - f_r - f_{\text{int}} - f_{\mathbf{p}}), \end{aligned} \quad (7.8)$$

where:

- $f$  is the frequency difference between the two laser beams:  $2\pi f = (\omega_1 - \omega_2)$
- $f_r$  is the recoil energy  $E_r = \hbar^2|\Delta\mathbf{k}|^2/2m$  expressed in frequency units:  $f_r = E_r/h$

- $f_{\text{int}} = (E_{\text{int}}^{\Delta} - E_{\text{int}}^0)/\hbar$  is the difference in per-particle interaction energy for the two momentum states expressed in frequency units
- $f_{\mathbf{p}}$  is the atomic momentum expressed in Bragg frequency units:  $2\pi f_{\mathbf{p}} = \Delta\mathbf{k} \cdot \mathbf{p}/m$

Inserting Eq. 7.8 into Eq. 4.12 gives the population of state  $|\mathbf{p} + \hbar\Delta\mathbf{k}\rangle$  after illuminating state  $|\mathbf{p}\rangle$  with light for time  $t$  as:

$$|\tilde{c}_{\mathbf{p}+\hbar\Delta\mathbf{k}}(t)|^2 = |\tilde{c}_{\mathbf{p}}(0)|^2 \left(\frac{\Omega_R t}{2}\right)^2 \underbrace{\text{sinc}^2\left(\frac{t}{2}\sqrt{\Omega_R^2 + 4\pi^2(f - f_r - f_{\text{int}} - f_{\mathbf{p}})^2}\right)}_{\text{"Resolution kernel", Res}(f - f_{\mathbf{p}})}. \quad (7.9)$$

This describes Rabi oscillations in time in our artificial 3-level system. When we return to the continuous momentum picture, we can interpret this result by dividing the continuum into two relevant sets of states:

- States  $\{\mathbf{P}\}$ , which are significantly occupied by atoms in the trap (for a pure BEC, we expect this set to extend  $\sim \hbar/L$  either side of zero momentum, where  $L$  is the trap length).
- States  $\{\mathbf{P} + \hbar\Delta\mathbf{k}\}$ , which are the displacement of  $\{\mathbf{P}\}$  by  $\hbar\Delta\mathbf{k}$  in momentum space.

For  $\Delta\mathbf{k} \gg 1/L$ , these two sets can be treated as entirely separate (i.e. orthogonal) (see Fig. 7.7(b)), and we further posit that we can treat two photon interactions with the continuum of momentum states as a set of independent Raman interactions between each state in  $\{\mathbf{P}\}$  exclusively with its corresponding state in  $\{\mathbf{P} + \hbar\Delta\mathbf{k}\}$ . Under these assumptions, the total occupation of the states  $\{\mathbf{P} + \hbar\Delta\mathbf{k}\}$  after a Bragg pulse of time  $t$  is:

$$N_{\{\mathbf{P}+\hbar\Delta\mathbf{k}\}}(f) = \left(\frac{\Omega_R t}{2}\right)^2 \int_{\{\mathbf{P}\}} |\psi(\mathbf{p})|^2 \text{Res}(f - f_{\mathbf{p}}) d^3\mathbf{p}, \quad (7.10)$$

where, in the continuum limit, we have identified  $|\tilde{c}_{\mathbf{p}}(0)|^2$  with the initial momentum wavefunction,  $|\psi(\mathbf{p})|^2$ . By symmetry, we can separate  $\psi(\mathbf{p}) = \sqrt{N}\varphi(p_r, p_\theta)\phi(p_x)$  where  $p_r$ ,  $p_\theta$  and  $p_x$  are momentum space cylindrical polar coordinates aligned with the symmetries of our cylindrical trap,  $\varphi$  and  $\phi$  are both normalised to unity, and

$N$  is the total atom number. If we align  $\Delta\mathbf{k}$  parallel to the  $p_x$  axis, we can write the bragg-diffracted fraction as the convolution:

$$\frac{N_{\{\mathbf{P}+\hbar\Delta\mathbf{k}\}}(f)}{N} = \left(\frac{\Omega_R t}{2}\right)^2 \int |\phi(p_x)|^2 \text{Res}(f - \Delta k p_x/m) dp_x. \quad (7.11)$$

Therefore, plotting the diffracted fraction as a function of the relative laser detuning,  $f$ , we obtain the momentum wave-function,  $|\phi(p_x)|^2$ , at a resolution set by the convolution kernel,  $\text{Res}(f)$ .  $\text{Res}(f)$  is a function centered at  $f = f_c = f_r + f_{\text{int}}$  with a zero-zero width,  $\Delta f_{\text{Res}}$ , of:

$$\Delta f_{\text{Res}} = \frac{1}{\pi} \sqrt{\left(\frac{2\pi}{t}\right)^2 - \Omega_R^2}. \quad (7.12)$$

For maximum momentum space resolution, we want  $\text{Res}(f) \rightarrow \delta(f)$  (i.e.  $\Delta f_{\text{Res}} \rightarrow 0$ ). Therefore we minimize  $\Omega_R$  and maximise  $t$  while empirically ensuring that (i) we maintain a measurable diffracted fraction and (ii) the bragg pulse remains shorter than any characteristic time for the free evolution of  $\phi(p_x)$  (this is particularly relevant for the ToF measurements in section 7.2.3).

The diffracted atoms move at velocity  $v_r \approx \hbar\Delta k/m$ , which is much faster than the ground state BEC expansion velocity by virtue of the arranged  $\Delta\mathbf{k} \gg 1/L$ . Therefore, after sufficient ToF, the diffracted atoms appear as a cloud separated from the non-diffracted atoms. This allows us to simply count  $N_{\{\mathbf{P}+\hbar\Delta\mathbf{k}\}}(f)$  and  $N$  (see Fig. 7.7(c)), and by changing the relative frequency  $f$  of the two lasers, we achieve our initial goal of mapping out  $|\phi(p_x)|^2$  via Eq. 7.11.

### Apparatus for Bragg spectroscopy

We now put the theory outlined above on a more concrete footing by outlining the apparatus used to realise Bragg spectroscopy in our experiment.

We use two 3 mm diameter, intensity stabilized [40] laser beams of approximately 780 nm which are  $\sim 6.6$  GHz blue-detuned from the  $|F = 2\rangle \rightarrow |F' = 3\rangle$  transition. The frequencies of these beams are further shifted one by  $-80$  MHz and the other by  $(-80 + f)$  MHz using AOMs. They are then steered with mirrors to intersect at the atoms at a total angle of  $30^\circ$  (see Fig. 7.8). This arrangement gives  $v_r \approx 3$  mm/s and  $f_r \approx 1$  kHz.

Unless otherwise stated, we will apply the Bragg pulse *in situ* and allow the diffracted atoms to escape by lowering the walls of the uniform trap below the recoil energy,

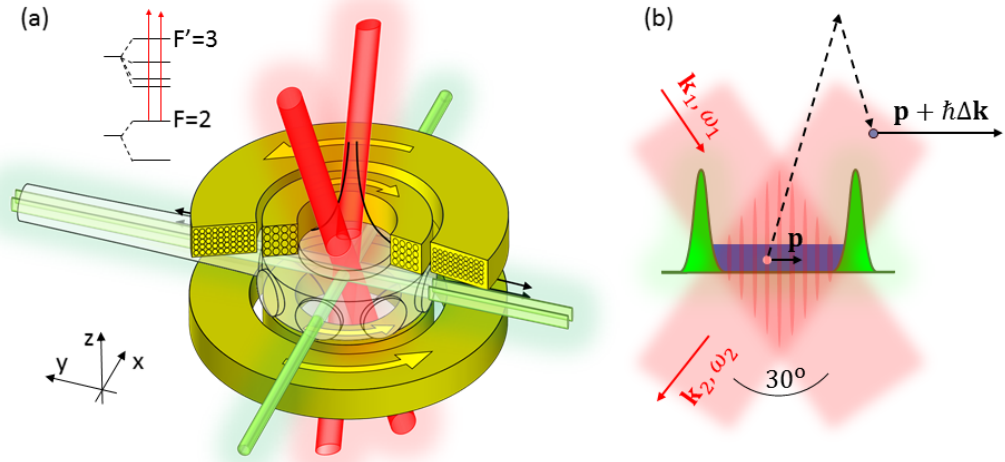


**Fig. 7.8.:** Apparatus for Bragg spectroscopy. (a) The arrangement of the bragg beams (red) illuminating the uniform trap. The detunings of the lasers are shown (not to scale) on a cartoon of the  $^{87}\text{Rb}$   $D_2$  line. (b) A trapped atom with initial momentum  $\mathbf{p}$  absorbs recoil momentum  $\hbar\Delta\mathbf{k}$  aligned with  $x$ -axis. The trap wall height (green) is lower than the energy of the recoiling atoms. The Bragg beams and interference lattice are not drawn to scale; in reality the beams are much larger than the box and the lattice spacing is much smaller.

$E_r$ , while still trapping the BEC (see Fig. 7.8(b)). Atoms diffracted out of the trap are then easily counted. Since the trapped BEC momentum distribution does not evolve with time (ignoring the Bragg perturbation), we can apply long Bragg pulses ( $t = 35$  ms) with a low Rabi-frequency ( $\Omega_R = 8$  Hz) to minimize  $\Delta f_{\text{Res}}$ . In dynamical experiments (e.g. probing  $|\phi(p_x)|$  in ToF) we will reduce the length of the Bragg pulse and increase  $\Omega_R$  to improve the time resolution of our measurements while sacrificing spectral resolution.

The experimental results using this apparatus to probe an equilibrium BEC are outlined in the next sections.

## 7.2.2 Ground-state wavefunction & The Heisenberg limit

We will start our experimental discussion with a simple example of a momentum spectrum recorded for an *in situ* homogeneous BEC in a trap of length  $L = 30 \pm 1 \mu\text{m}$  and radius  $R \approx 16 \mu\text{m}$  (see Fig. 7.9(a)). Depending on the interaction strength, there are two limits for the shape of this ground state wavefunction, summarised in table 7.1. Referring to Fig. 7.5, we expect our BEC to be deeply in the Thomas-Fermi regime. This is supported experimentally by both *in situ* images which reveal the top-hat profile of the trapped condensate, and by the Bragg spectrum which closely fits the  $\text{sinc}^2$  profile,  $|\phi^{\text{TF}}(p_x)|$ , defined in table 7.1 convolved with  $\text{Res}(f)$ . As expected for a fully coherent BEC spanning the uniform box-trap, we find that

	Non-interacting	Thomas-Fermi
Real Space	$\phi^0(x) = \cos\left(\frac{\pi x}{L}\right) \text{TH}\left(\frac{x}{L}\right)$	$\phi^{\text{TF}}(x) = \text{TH}\left(\frac{x}{L}\right)$
Momentum Space	$ \phi^0(p_x) ^2 = \frac{4L}{\pi^3} \left( \frac{\cos(\pi f_p L/v_r)}{1 - (2f_p L/v_r)^2} \right)^2$	$ \phi^{\text{TF}}(p_x) ^2 = \frac{L}{2\pi} \text{sinc}^2\left(\frac{\pi f_p L}{v_r}\right)$
FWHM	$W^0 \approx 1.19 \frac{v_r}{L}$	$W^{\text{TF}} \approx 0.89 \frac{v_r}{L}$

**Tab. 7.1.:** Key results for the real and momentum space wave functions in the non-interacting and Thomas-Fermi limits.  $\text{TH}(z)$  is a top hat function equal to unity for  $-1/2 < z < 1/2$  and zero elsewhere. FWHM indicates the full-width-at-half-maximum for the absolute-squared momentum space wave functions.

the full-width-at-half-maximum (FWHM),  $W = 100 \pm 3$  Hz, is independent of  $N$  and closely matches the expected width (after convolution with  $\text{Res}(f)$ ) of 93 Hz. Note that since  $\text{Res}(f)$  is centered at  $f_c \approx 1$  kHz, we plot the spectrum against Bragg beam detuning relative to  $f_c$ .

In Fig. 7.9(b), we plot the FWHM of the Bragg spectra measured for different box sizes,  $L$  (we use the SLM techniques in chapter 5 to move the walls of the optical box). This reveals the expected Heisenberg  $1/L$  scaling of the momentum width for the range of boxes studied.

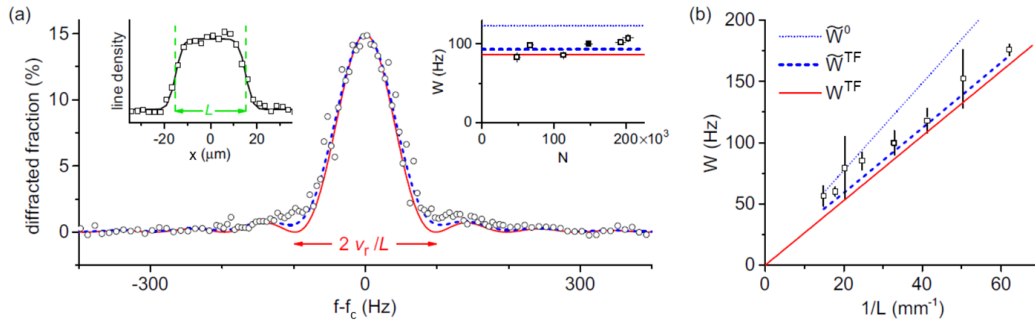


**Fig. 7.9.:** Heisenberg-limited momentum spread in a uniform interacting BEC. (a) Main panel: Bragg spectrum of a trapped BEC of length  $L = 30 \mu\text{m}$ . The solid red line shows the theoretical Heisenberg-limited spectrum  $|\phi^{\text{TF}}(p_x)|^2$  and the dashed blue line shows the theoretical spectrum after convolution with the Bragg resolution kernel,  $\text{Res}(f)$ . Left inset:  $L$  is determined by fitting the in-trap BEC density profile, accounting for the imaging resolution. Right inset: FWHM of the spectrum,  $W$ , versus the atom number,  $N$ , for the same  $L$ . The filled square corresponds to the data in the main panel, with  $W = (100 \pm 3)$  Hz. The solid red line shows  $W^{\text{TF}} = 0.89v_r/L = 87$  Hz and the dashed blue line shows the FWHM after convolution:  $\tilde{W}^{\text{TF}} = 93$  Hz. The dotted blue line shows  $\tilde{W}^0 = 123$  Hz, expected for a noninteracting BEC. (b)  $W$  versus inverse box length,  $1/L$ , showing the expected Heisenberg scaling. Solid red, dashed blue, and dotted blue lines show  $W^{\text{TF}}$ ,  $\tilde{W}^{\text{TF}}$ , and  $\tilde{W}^0$  respectively. (All error bars represent  $1\sigma$  fitting uncertainty on  $W$ ).

### 7.2.3 Ground state interaction energy

So far, we have only looked at the widths of the Bragg spectrum. However, information can also be extracted from the position  $f_c = f_r + f_{\text{int}}$  of the spectral peak. Since the peak position depends on  $f_{\text{int}}$ , we can use shifts in the peak position to monitor variations in the ground state interaction energy. From exchange symmetry, the interaction energy between atoms in distinguishable states is twice that of atoms in the same state<sup>8</sup>. Therefore we can evaluate the shift  $f_{\text{int}}$  as:

$$\begin{aligned} hf_{\text{int}} &= E_{\text{int}}^{\Delta} - E_{\text{int}}^0 \\ &= (2V_0n_0 + 2V_0n') - (V_0n_0 + 2V_0n') \\ &= V_0n_0, \end{aligned} \quad (7.13)$$

where  $V_0$  is the interaction parameter defined in Eq. 1.2,  $n_0$  is the density of atoms in the BEC, and  $n'$  is the thermal atom density. We rewrite this expression as  $f_{\text{int}} = \alpha N$  where  $N$  is the total atom number, and

$$\alpha = \frac{N_0}{N} \frac{2\hbar a}{m\pi R^2 L}. \quad (7.14)$$

We can estimate the condensed fraction  $N_0/N$  by numerically simulating the expected diffracted fraction for a pure condensate at  $f = f_c$  (see Appendix C) and comparing this to the experimental value ( $\sim 15\%$ ) measured in Fig. 7.9(a). This method gives  $N_0/N = 0.8 \pm 0.1$ , which is also supported by "BEC filtering" experiments [40, 140] (the uncertainty indicates variation between experimental runs). This allows us to calculate the theoretical value for  $\alpha$  as  $\alpha = (24 \pm 2) \times 10^{-5}$  Hz/atom.

#### Experimental Results

To experimentally measure the slope  $\alpha = df_{\text{int}}/dN$  we can vary the final value of  $N$  by changing the time during which we catch atoms from the background gas at the start of an experimental run (i.e. the duration of the magneto-optical trap step in Fig. 6.1). Plotting measured values of  $f_{\text{int}}$  as a function of  $N$  gives an empirical value  $\alpha = (20 \pm 1) \times 10^{-5}$  Hz/atom (see Fig. 7.10(a)). This is slightly below the theoretical

<sup>8</sup>Briefly, this 'Bosonic factor of 2' can be derived in the two-particle case by comparing the expectation of the interaction potential  $V_0\delta(\mathbf{r}_1 - \mathbf{r}_2)$  for atoms in identical states  $|\phi_1(\mathbf{r}_1)\rangle |\phi_1(\mathbf{r}_2)\rangle$  and different states  $2^{-1/2}[|\phi_1(\mathbf{r}_1)\rangle |\phi_2(\mathbf{r}_2)\rangle + |\phi_1(\mathbf{r}_2)\rangle |\phi_2(\mathbf{r}_1)\rangle]$ . In the latter case, exchange terms of the form  $\langle \phi_1(\mathbf{r}_1) | \langle \phi_2(\mathbf{r}_2) | V_0\delta(\mathbf{r}_1 - \mathbf{r}_2) | \phi_2(\mathbf{r}_1)\rangle | \phi_1(\mathbf{r}_2)\rangle$  contribute a total additional energy  $V_0/V$  where  $V$  is the box volume. It is simple to extend this to the  $n_0$ -particle case to explain extra interaction energy  $V_0n_0$ .

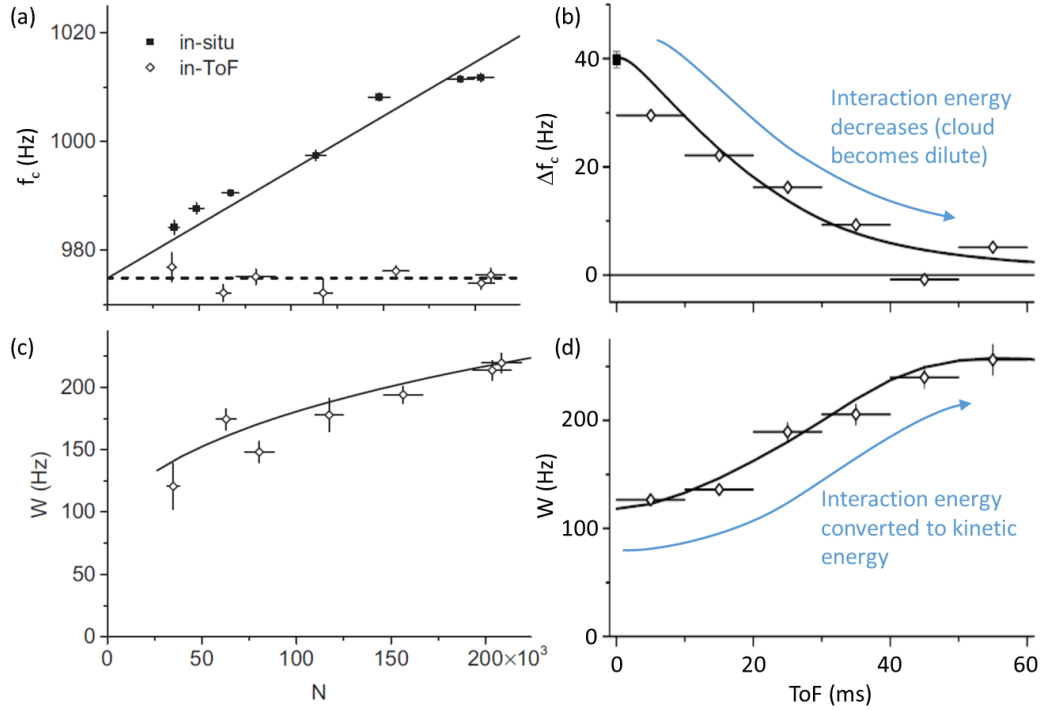


**Fig. 7.10.:** Bragg spectrum shifts and widths as functions of  $N$  and ToF. (a) We plot  $f_c$  versus  $N$  for Bragg pulses applied *in situ* (solid squares) and after 50 ms of ToF (open diamonds) for  $L = 30 \mu\text{m}$ . Dashed line:  $f_c \approx f_r \approx 975$  Hz, solid line:  $f_c = f_r + \alpha N$ , with  $\alpha \approx 20 \times 10^{-5}$  Hz/atom. (b) Evolution of  $f_c$  during ToF. The solid square corresponds to the in-trap data from Fig. 3. The horizontal error bars indicate our temporal resolution, limited by the Bragg-pulse duration, and vertical error bars indicate fitting uncertainties. (c) Spectral width for the ToF data presented in panel (a). The solid line shows a numerical simulation based on the Gross-Pitaevskii equation. (d) Spectral width during ToF for the data in panel (b). In (b) and (d), the solid lines show numerical simulations based on the GP equation for  $N = 1.25 \times 10^5$  atoms.

value due to the  $\approx 15\%$  depletion of the condensate atom number during the Bragg pulse<sup>9</sup>.

To obtain the baseline (i.e.  $\lim_{N \rightarrow 0} f_c$ ) in Fig. 7.10(a), we perform a different experiment where we release the cloud in ToF before applying the Bragg pulse. Fig. 7.10(b) shows that the interaction energy (as measured by  $f_c$ ) drops as the cloud becomes more dilute in ToF<sup>10</sup>. This allows us to assume that after 50 ms ToF, the interaction energy is negligible. Experimentally, we observe this effect in the independence of  $f_c$  on  $N$  after 50 ms ToF in Fig. 7.10(a). These measurements give us an accurate measurement of the recoil energy  $f_r = f_c(N = 0) \approx 975$  Hz, and a baseline for the *in situ* measurements.

<sup>9</sup>We can repeat the measurement with a reduced  $\Omega_R$  and extrapolate to the vanishing diffracted-fraction limit to obtain an improved estimate  $\alpha = (23 \pm 1) \times 10^{-5}$  Hz/atom [40].

<sup>10</sup>Note that since the BEC momentum distribution evolves with time in ToF, we must apply shorter pulses ( $t = 10$  ms) with a higher Rabi-frequency ( $\Omega_R = 28$  Hz) to "instantaneously" measure the momentum. We thus sacrifice spectral resolution to gain temporal resolution in the data in Figs 7.10(b) and (d).

For completeness, we finally show the FWHM,  $W$ , of the Bragg spectrum as a function of  $N$  after 50 ms ToF and as a function of ToF for  $N = 1.25 \times 10^5$  atoms in Figs 7.10(c) and (d) respectively. These again show the conversion of interaction energy to kinetic energy (i.e. broadening of the momentum distribution) in ToF, with the size of the effect increasing with  $N$ . Furthermore, they demonstrate the excellent agreement of our experimental system with simple GP simulations<sup>11</sup> (see Appendix C).

Before leaving this topic, it is worth briefly contrasting our results with those obtained for a harmonically trapped system [141, 142]. The most striking difference is that in an inhomogeneous cloud,  $f_{\text{int}}$  is a function of position, and therefore the Bragg spectrum is broadened by the spread of  $f_{\text{int}}$  in the cloud. This makes interpreting Bragg spectra of inhomogeneous systems more difficult than the homogeneous case: the true momentum distribution is only recovered by processing out the interaction broadening. Hence we claim that the measurements presented in these sections have been the clearest demonstration of Heisenberg scaling in cold atomic gases. Furthermore, we have seen that without any post-processing we have been able to resolve interaction energies with an astonishing precision of  $\approx h \times 2Hz$  (corresponding to a temperature scale of 100pK).

## 7.3 Conclusion

This section has provided a brief review of the first experiments carried out with a homogeneous atomic Bose gas. We have discussed both the equilibrium thermodynamics of thermal and partially condensed gases, and also the quantum mechanical properties of the ground state in equilibrium. These experiments have already shown that the uniform system has great potential for new experiments where parabolic trapping geometries complicate or entirely mask fundamental many-body phenomena which we wish to investigate. In the next chapter, we will perform a more sophisticated experiment which again requires our uniform system, and also employs the technique of Bragg diffraction introduced here.

---

<sup>11</sup>note that we include a residual 1.5Hz harmonic trapping potential in the simulations to model the curvature of the imperfect gravity compensating magnetic field



# Critical Dynamics of Spontaneous Symmetry Breaking in a Homogeneous Bose gas

Prehistoric cultures long perfected the art of cooling metals across the liquid-solid phase transition. Crucially, they found that it is not only the transition itself but also the approach to the transition (via different quenching, tempering and annealing protocols) which is important for defining the mechanical properties of the final solid. Nowadays, we interpret these metallic properties in terms of the grain structure of the material (i.e. the size of the domains of common crystallographic axes), and we know that the dynamics of the nucleation and growth of grains during a specific cooling trajectory dictates the properties of the resulting solid phase.

This metallurgic example concerns a first order phase transition, but we have already seen that dynamics are also important for determining the properties of systems near second order transitions. For example, in chapter 2, we saw that a superheated state can be dynamically generated when the phase equilibrium point moves from the ordered to disordered state at a rate faster than the system can follow. In this chapter, we consider crossing the BEC transition in the opposite direction: we will drive a homogeneous Bose gas below the critical temperature at a finite rate and explore the coherence properties of the resulting BEC. Importantly, we will observe that the growth of correlations is stalled by the systems diverging response time near the critical point. This leads to the formation of finite sized domains of phase coherence in the condensate, with each domain choosing a different value for the symmetry breaking phase of the BEC order parameter. Note that unlike the metallic grains formed in the thermal quench of a metal, we expect the domain boundaries in a quenched BEC to be a smooth region in which the phase interpolates from one area (domain) of approximately constant phase to another area (domain) of approximately constant phase. We will measure the size of these domains using an adaptation of the spectroscopic techniques introduced in the previous chapter.

The chapter is organised as follows: In section 8.1 we describe the theory of domain formation in quench-cooled homogeneous BECs, then in section 8.2 we present an experimental method for accurately extracting the size of these domains. We will compare the experimentally measured domain sizes to the theoretical predictions in

8.3 and 8.4, ultimately allowing us to extract the first measurement of the dynamical critical exponent for the universality class of the homogeneous 3D BEC transition.

## 8.1 Domain size in Kibble-Zurek theory

The key result in this chapter will be experimental verification of a link between the rate at which we cool a homogeneous Bose gas through the BEC transition and the size of the domains of phase coherence in the resulting condensate. Theoretically, a simple framework for predicting this link is provided by the Kibble-Zurek (KZ) mechanism [143, 144]. Signatures of this theory have already been studied in a range of experimental systems, including liquid crystals [145], liquid helium [146, 147], superconductors [148–150], atomic BECs [151–156], multiferroics [157] and trapped ions [158–160]. We will briefly discuss the KZ theory below before presenting our experimental results on homogeneous BECs.

When performing a thermal quench through the transition we define the "distance" to the critical point as the reduced temperature  $\epsilon = (T - T_c)/T_c$ . A fundamental characteristic of second order transitions is that as  $\epsilon \rightarrow 0$  several macroscopic observables diverge as scale-invariant power laws in  $\epsilon$ . Since short-range physics becomes largely irrelevant near the critical point (due to long-range fluctuations of the order parameter) all second-order transitions can be classified into a small number of universality classes depending on their generic features such as symmetries, dimensionality and range of interactions [161, 162]. All transitions within a universality class display the same critical exponents for the power-law divergences. In particular, we will be interested in the critical behaviour of two quantities:

- The asymptotic divergence of the correlation length,  $\xi$ , as  $\epsilon$  approaches 0:

$$\xi \sim \begin{cases} X_+ \epsilon^{-\nu} & \epsilon > 0 \quad (\text{disordered}) \\ X_- \epsilon^{-\nu} & \epsilon < 0 \quad (\text{ordered}) \end{cases}, \quad (8.1)$$

where the exponent  $\nu$  and the ratio of the critical amplitudes  $X_+/X_-$  are universal quantities within a universality class.

- The characteristic rate at which correlations can build up in our system. This rate is given by the inverse of the relaxation time,  $\tau$ , which by the dynamical

scaling hypothesis [163] follows another universal power law near the critical point:

$$\tau \sim \xi^z. \quad (8.2)$$

Combining Eq. 8.1 and 8.2, we see that the system exhibits a critical slowing down as it approaches the transition. This means that if we cool quickly across the transition, correlations cannot grow fast enough to span the system before the BEC forms. The system is then frozen in a condensed state with a finite phase coherence length given by the equilibrium correlation length at the freeze time (see Fig. 8.1(a)).

To predict the frozen coherence length within the KZ theory, we imagine driving the system through the critical point with a linear quench of  $\epsilon$ :

$$\epsilon = \frac{t_c - t}{\tau_Q}, \quad (8.3)$$

where the time  $t = t_c$  is the time at which we cross the critical point, and the timescale  $\tau_Q$  parametrises the rate of the quench. The KZ hypothesis states that the system dynamics become frozen when the rate of change of  $\xi$  is faster than the system's relaxation rate:

$$\left| \frac{\dot{\xi}}{\xi} \right| > \frac{1}{\tau}. \quad (8.4)$$

Using Eq. 8.1, 8.2 and 8.3, we can solve for the time  $t_{\text{freeze}} = |t_c - \hat{t}|$  at which the system freezes:

$$\hat{t}_{\pm} \sim (X_{\pm}^{1/\nu} |\tau_Q|)^{\nu z / (1 + \nu z)}. \quad (8.5)$$

Within  $\hat{t}$  of  $t_c$ , the correlation length can no longer adiabatically grow in accordance with Eq. 8.1. In the KZ framework, we assume that  $\xi$  is frozen at the length,  $d = \xi|_{t=t_c - \hat{t}_+}$ , and coherence length (i.e. the size of the domains) for  $\epsilon < 0$  will be given by  $d$ . Inserting Eq. 8.5 and 8.3 into 8.1 gives:

$$d = \lambda_0 \left( \frac{\tau_Q}{\tau_0} \right)^b \quad b = \frac{\nu}{1 + \nu z}, \quad (8.6)$$

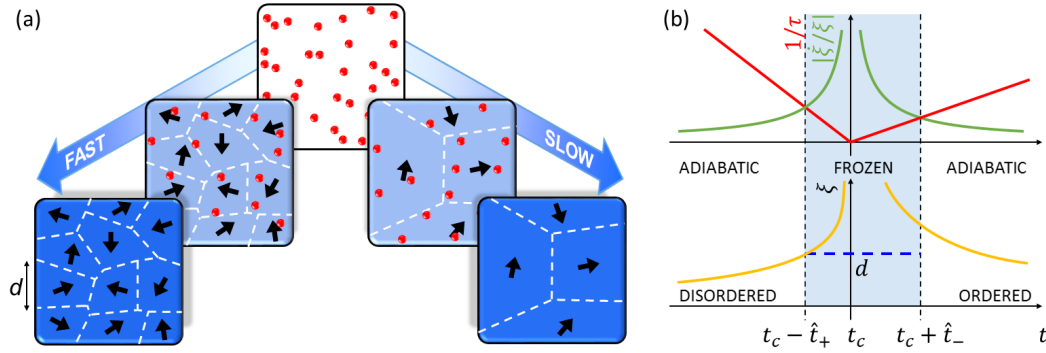


**Fig. 8.1.:** Domain formation during spontaneous symmetry breaking in a homogeneous Bose gas. (a) Red circles depict thermal atoms and blue areas coherent domains, in which the  $U(1)$  gauge symmetry is spontaneously broken. The black arrows indicate the independently chosen condensate phase at different points in space, and dashed lines delineate domains over which the phase is approximately constant. The average size  $d$  of the domains formed at the critical point depends on the cooling rate. Further cooling can increase the population of each domain before the domain boundaries evolve. (b) Cartoons illustrating the calculation of the Kibble-Zurek scaling law. The system is frozen in the blue shaded region where  $|\dot{\xi}/\xi| > 1/\tau$ . The lower panel shows the equilibrium value of  $\xi$  (orange), and the Kibble-Zurek hypothesis states that  $\xi$  stalls at the value  $\sim d$  (blue dashed line) when the system is frozen

where we have explicitly inserted dimensionful constants  $\lambda_0$  and  $\tau_0$ , which depend on the microscopic details of a particular system. In our system  $\lambda_0$  is expected to be set by the thermal wavelength at the critical point, and  $\tau_0$  by the elastic scattering time  $\tau_{\text{el}}$  [152, 164]; for our experimental parameters,  $\lambda_c \approx 0.7 \mu\text{m}$ , and a classical estimate gives  $\tau_{\text{el}} \approx 30 \text{ ms}$ .

Fig. 8.1(b) graphically summarises the steps in the derivation of Eq. 8.6. In essence, we have shown that due to the phenomenon of critical slowing down, crossing the BEC transition at a finite rate causes domains of predictable size to form with independent choices of the symmetry-breaking order parameter<sup>1</sup> (i.e. the BEC phase).

Our ultimate aim is to quantitatively measure the power-law  $d \sim \tau_Q^b$  for the homogeneous 3D BEC transition. This transition resides in the same universality class as the 3D XY model and the lambda transition of liquid  $^4\text{He}$ , for which the critical exponents can be calculated in a mean-field (i.e. Ginzburg-Landau) theory [163, 166], or in a beyond mean-field dynamical critical model, known as the F Model [163]. The relevant exponents in these theories are summarized in table 8.1.

<sup>1</sup>Note that at the domain boundaries, rare long lived topological defects can also form [165], their nature and density depending on the physical system. We will not explicitly consider these defects in our discussion.

	Mean Field	Beyond Mean Field
$z$	2	3/2
$\nu$	1/2	2/3
$X_+/X_-$	0	$\sim 0.3$
$b$	1/4	1/3

**Tab. 8.1.:** Critical exponents and amplitude ratios for time-dependent-Ginzburg-Landau mean field (MF) [163, 166] and beyond MF [163] models. The beyond MF critical exponents are calculated according to the so-called F Model, and the amplitude ratio is calculated numerically [167].

We hope to measure these critical exponents in later sections, however it is useful to first discuss the qualitative evidence for domain formation and introduce the basic experimental parameters. This will be the task for the next section.

### 8.1.1 Qualitative evidence for domain formation

Experimentally, we will use our uniform box trap to study the Kibble-Zurek theory. Using individual ToF images it is remarkably simple to observe the *qualitative* message of Fig. 8.1(a) - i.e. the faster the temperature quench, the smaller the domains. The procedure for this qualitative study is outlined below:

We prepare a homogeneous Bose gas by loading  $3 \times 10^5$   $^{87}\text{Rb}$  atoms into our cylindrical optical-box trap with length  $L \approx 26 \mu\text{m}$  along the horizontal  $x$ -axis, and radius  $R \approx 17 \mu\text{m}$ . Initially  $T \approx 170$  nK, corresponding to  $T/T_c \approx 2$ . We then evaporatively cool the gas by lowering the trap depth linearly from  $\sim 2 \mu\text{K}$  to  $\sim 30$  nK in time  $t_Q$ . We cross  $T_c \approx 70$  nK with  $2 \times 10^5$  atoms, and at the end of the cooling we have  $10^5$  atoms at  $T \lesssim 10$  nK ( $T/T_c \lesssim 0.2$ ).

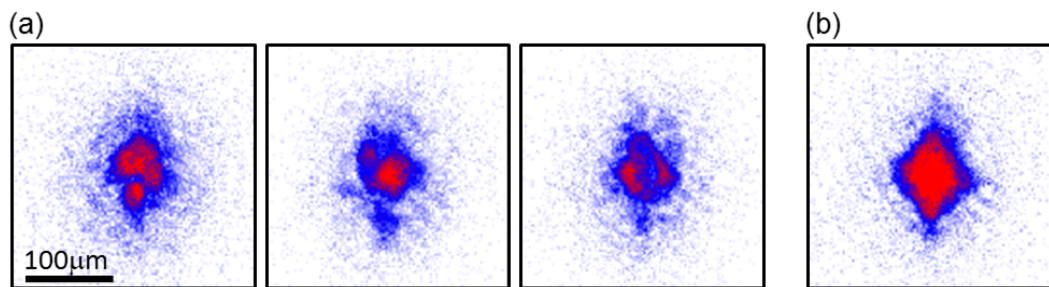


**Fig. 8.2.:** Phase inhomogeneities in a deeply degenerate gas are revealed in time-of-flight expansion as density inhomogeneities. (a) The gas is cooled in 1 s from  $T \approx 170$  nK, through  $T_c \approx 70$  nK, to  $\lesssim 10$  nK. Each realization of the experiment results in a different pattern, and averaging over many images results in a smooth featureless distribution. (b) Preparing a  $T \lesssim 10$  nK gas more slowly (over 5 s) results in an essentially pure BEC with a spatially uniform phase.

When we release this condensate from the trap, any phase inhomogeneities are revealed in ToF expansion as density inhomogeneities [153, 168]. In Fig. 8.2, we compare the ToF profiles for a gas cooled to  $T \ll T_c$  "quickly" ( $t_Q \approx 1$  s) and "slowly" ( $t_Q \gtrsim 5$  s). Gases cooled quickly reveal density modulations in ToF indicative of the presence of small domains *in situ*. In contrast, in our finite-sized box, slow cooling can produce an essentially pure and fully coherent (single-domain) BEC which develops the characteristic diamond shape in ToF (c.f. Fig. 7.6). This contrast supports the qualitative picture illustrated in Fig. 8.1(a).

## 8.2 Quantitative measurement of domain sizes

We now study the KZ mechanism more quantitatively. Specifically, we will develop an experimental technique for measuring the size,  $d$ , of the domains in our quench-cooled clouds.

To measure the size of the domains, imagine a pure condensate described in the classical field approximation<sup>2</sup> by the complex wavefunction  $\psi(\mathbf{r})$ , and consider inspecting this wavefunction at two points separated by  $\mathbf{r}'$ . If  $|\mathbf{r}'| < d$  then the two points may lie in the same domain, so there will be a correlation between the phases of  $\psi(\mathbf{r})$  and  $\psi(\mathbf{r} + \mathbf{r}')$ . Conversely if  $|\mathbf{r}'| > d$ , we expect little correlation between the phases. These phase correlations which decay over the length-scale  $d$  can be captured by the spatially averaged two point first order correlation function, defined as

$$C_1(\mathbf{r}') = \frac{\int \langle \psi(\mathbf{r})^* \psi(\mathbf{r} - \mathbf{r}') \rangle d^3\mathbf{r}}{\sqrt{\int \langle |\psi(\mathbf{r})|^2 \rangle d^3\mathbf{r} \int \langle |\psi(\mathbf{r} - \mathbf{r}')|^2 \rangle d^3\mathbf{r}}} = \frac{1}{N} \int \langle \psi(\mathbf{r})^* \psi(\mathbf{r} - \mathbf{r}') \rangle d^3\mathbf{r}, \quad (8.7)$$

where  $\langle \dots \rangle$  denotes averaging over different domain configurations of  $\psi$ , and  $\psi$  is normalised to  $\int d^3\mathbf{r} |\psi|^2 = N$ .

In our experiment,  $\psi$  is only non-zero inside our uniform cylindrical box trap. This artificially introduces the length scales of the finite-sized box,  $L$  and  $R$ , into the problem which complicates the extraction of  $d$  from the decay of  $C_1$ . Below, we outline a technical derivation of how the finite sized box affects the measurement of  $d$ . While we attempt to be as formally correct as possible at each step, it is only the final result in Eq. 8.13 which is important for the later sections. This final result is

<sup>2</sup>Note that we could treat the Bose gas using the field operators  $\hat{\Psi}(\mathbf{r})$  and inspect the spatially averaged first order correlation function proportional to  $\int d^3\mathbf{r} \langle \hat{\Psi}(\mathbf{r})^\dagger \hat{\Psi}(\mathbf{r} - \mathbf{r}') \rangle$ . However for large occupation of the BEC, it is simpler to approximate  $\hat{\Psi}(\mathbf{r})$  as a complex function  $\psi(\mathbf{r})$  (i.e. ignore the field operator commutator).

relatively intuitive when one considers the limits of  $d \rightarrow L$  and  $d \ll L$ , and simple experiments reproduce these intuitive limits (see Fig. 8.6).

### 8.2.1 Infinite system correlations from a finite-sized experiment

We begin by constructing a function  $\psi_\infty(\mathbf{r})$  defined in a homogeneous system of volume  $V_\infty \rightarrow \infty$  with a constant modulus  $\sqrt{N/\pi R^2 L}$  and a phase  $\Theta(\mathbf{r})$ :

$$\psi_\infty = \sqrt{\frac{N}{\pi R^2 L}} \exp[i\Theta(\mathbf{r})]. \quad (8.8)$$

The function  $\Theta$  is chosen such that  $\psi_\infty$  everywhere has the same characteristic phase correlations as  $\psi$ . This means that we can obtain  $\psi$  from  $\psi_\infty$  by "masking out" all points not inside the cylindrical trap:

$$\psi(\mathbf{r}) = \text{Cyl}(\mathbf{r})\psi_\infty(\mathbf{r}) \quad (8.9)$$

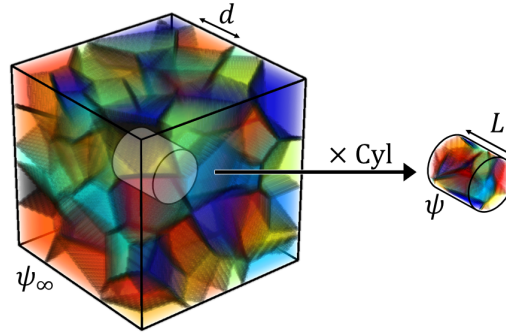


**Fig. 8.3.:** The relationship between  $\psi_\infty$  and  $\psi$ . We imagine cutting a finite sized cylinder out of an infinite system  $\psi_\infty$  to obtain  $\psi$ . The infinite system has characteristic domain size  $d$  (phase domains are illustrated in different colours).

where  $\text{Cyl}(\mathbf{r})$  is a unity inside the cylindrical trap and zero elsewhere. Inserting Eq. 8.9 into 8.7 gives:

$$C_1(\mathbf{r}') = \frac{1}{N} \int_{V_\infty} \text{Cyl}(\mathbf{r})\text{Cyl}(\mathbf{r} - \mathbf{r}') \langle \psi_\infty^*(\mathbf{r})\psi_\infty(\mathbf{r} - \mathbf{r}') \rangle d^3\mathbf{r}, \quad (8.10)$$

By symmetry, since  $\psi_\infty$  describes an infinite homogeneous system, we can replace  $\langle \psi_\infty^*(\mathbf{r})\psi_\infty(\mathbf{r} - \mathbf{r}') \rangle$  with its spatial average:

$$\langle \psi_\infty^*(\mathbf{r})\psi_\infty(\mathbf{r} - \mathbf{r}') \rangle = \frac{1}{V_\infty} \int_{V_\infty} \langle \psi_\infty^*(\mathbf{s})\psi_\infty(\mathbf{s} - \mathbf{r}') \rangle d^3\mathbf{s}. \quad (8.11)$$

Now, noting from Eq. 8.8 that  $\int_{V_\infty} d^3\mathbf{s} |\psi_\infty(\mathbf{s})|^2 = NV_\infty/\pi R^2 L$ , we can insert Eq. 8.11 into Eq. 8.10 to obtain:

$$C_1(\mathbf{r}') = \frac{1}{\pi R^2 L} \frac{\int_{V_\infty} \langle \psi_\infty^*(\mathbf{s}) \psi_\infty(\mathbf{s} - \mathbf{r}') \rangle d^3\mathbf{s}}{\underbrace{\sqrt{\int_{V_\infty} \langle |\psi_\infty(\mathbf{s})|^2 \rangle d^3\mathbf{s} \int_{V_\infty} \langle |\psi_\infty(\mathbf{s} - \mathbf{r}')|^2 \rangle d^3\mathbf{s}}}_{C_1^\infty(\mathbf{r}')}} \int_{V_\infty} \text{Cyl}(\mathbf{r}) \text{Cyl}(\mathbf{r} - \mathbf{r}') d^3\mathbf{r}, \quad (8.12)$$

Where we have identified the central term as the infinite system correlation function  $C_1^\infty(\mathbf{r})$ . For the case  $\mathbf{r}' = x\hat{\mathbf{x}}$  (where  $\hat{\mathbf{x}}$  is a unit vector along the axis of the cylindrical trap) we can calculate the geometric overlap integral in Eq. 8.12 under the assumption of a perfectly uniform trap with no healing length. This gives the final result:

$$C_1(x\hat{\mathbf{x}}) = C_1^\infty(x\hat{\mathbf{x}}) \times \left(1 - \frac{x}{L}\right). \quad (8.13)$$

I.e. if we measure  $C_1$  (as described in the next section), then we will be measuring the infinite system correlation function,  $C_1^\infty$  (which contains the length-scale  $d$ ) modulated by a linear geometric envelope arising from the finite trap size.

## 8.2.2 Homodyne interference for measuring domain size

So far we have said that the length scale  $d$  which we want to measure is encoded in the decay of  $C_1^\infty$ , and we have shown that  $C_1^\infty$  can be deduced from  $C_1$ . Now we must find a way to experimentally measure  $C_1$  itself.

Inserting the Fourier transform of  $\psi(\mathbf{r})$  into Eq. 8.7 immediately gives  $C_1$  as the Fourier transform of the momentum distribution of the BEC. Therefore, it is tempting to refer to our momentum-space measurements chapter 7 and say that we can simply Fourier transform a Bragg spectrum to obtain  $C_1$ . However, for very fast quenches ( $\tau_Q \sim \tau_0$ ), we expect  $d \sim \lambda_c$ , corresponding to a Bragg spectrum spread over  $W \sim 3$  kHz. Such a wide spectrum requires the Bragg pulse to have a large  $\Omega_R t$  in order to diffract a measurable fraction of atoms. From Eq. 7.12, this generally leads to broadening of the Bragg spectrum for experimentally achievable values of  $t$ . This broadening begins to significantly affect the spectrum as  $d$  grows (i.e.  $W$  shrinks), and it was found to be difficult to find a suitable protocol which could measure both large ( $\sim 30 \mu\text{m}$ ) and small ( $\sim 0.7 \mu\text{m}$ ) domains. For this reason, we devise an alternative experimental approach based on homodyne interference.

The approach is inspired by [142], and is based on three steps:

<i>"Copy"</i>	Create a "copy" of $\psi(\mathbf{r})$	$\{\psi(\mathbf{r}), \psi(\mathbf{r})\}$
<i>Arrange</i>	Displace one copy by $x\hat{\mathbf{x}}$	$\{\psi(\mathbf{r}), \psi(\mathbf{r} - x\hat{\mathbf{x}})\}$
<i>Interfere</i>	Create a superposition of the displaced copies	$\psi(\mathbf{r}) + \psi(\mathbf{r} - x\hat{\mathbf{x}})$

If we count the number of atoms in the homodyne interference pattern arising in the final step, we recover  $C_1(x\hat{\mathbf{x}})$ :

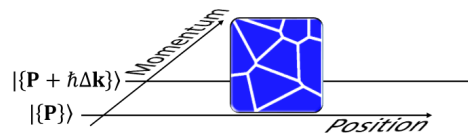
$$\int |\psi(\mathbf{r}) + \psi(\mathbf{r} + x\hat{\mathbf{x}})|^2 d^3\mathbf{r} = 2N \{1 + \text{Re}[C_1(x\hat{\mathbf{x}})]\}. \quad (8.14)$$

In the next subsections, we will describe how the steps above can be achieved using two separated Bragg pulses.

### Step 1: "Copy"

After releasing the cloud from the trap, suppose we apply a very short, powerful pulse of Bragg light with  $\Omega_R/2\pi \approx 700$  Hz and  $t = 0.1$  ms. With these parameters, the Bragg resolution kernel in Eq. 7.9 becomes very broad with  $\Delta f_{\text{res}} \approx 20$  kHz. Even for correlations of size  $\lambda_c$ , the Bragg spectrum of the atomic cloud is 3 kHz  $\ll 20$  kHz wide. Therefore, the resolution kernel can be treated as flat, and all momenta in the cloud experience the same population transfer in time  $t$ .

Since the Bragg process is now effectively momentum-independent, we can treat the system as a two level system with the lower level,  $|\{\mathbf{P}\}\rangle$ , representing the band of states in the stationary cloud and a higher level  $|\{\mathbf{P} + \hbar\Delta\mathbf{k}\}\rangle$  representing the diffracted atoms. In this basis, we write the initial state as  $\psi(\mathbf{r}) |\{\mathbf{P}\}\rangle \equiv (\psi(\mathbf{r}), 0)^T$ , which we represent pictorially as follows:

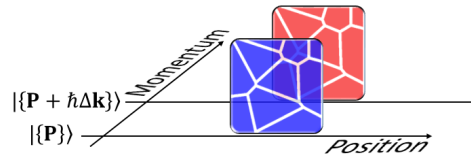


Now we can set the frequency difference between the Bragg lasers as  $f = f_c \approx 1$  kHz such that  $\delta = 0$  in Eq. 4.11. The Bragg pulse then couples the  $|\{\mathbf{P}\}\rangle$  and  $|\{\mathbf{P} + \hbar\Delta\mathbf{k}\}\rangle$  states according to the matrix

$$\mathbf{B}(\Omega_R) = \begin{pmatrix} \cos\left(\frac{\theta}{2}\right) & -i \sin\left(\frac{\theta}{2}\right) \\ -i \sin\left(\frac{\theta}{2}\right) & \cos\left(\frac{\theta}{2}\right) \end{pmatrix}, \quad (8.15)$$

where for our parameters,  $\theta = \Omega_R t \approx \pi/7$ . Therefore, after the first Bragg pulse, we have the state:

$$\mathbf{B}(\Omega_R) \begin{pmatrix} \psi(\mathbf{r}) \\ 0 \end{pmatrix} = \begin{pmatrix} \cos\left(\frac{\theta}{2}\right) \psi(\mathbf{r}) \\ -i \sin\left(\frac{\theta}{2}\right) \psi(\mathbf{r}) \end{pmatrix} \quad (8.16)$$



Thus we have "copied" the wavefunction  $\psi(\mathbf{r})$  into the state(s)  $|\{\mathbf{P} + \hbar\Delta\mathbf{k}\}\rangle$ .

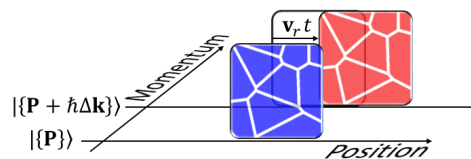
### Step 2: Arrange

If we turn off the Bragg beams and wait for time  $t_A$ , then the diffracted cloud in the moving states  $|\{\mathbf{P} + \hbar\Delta\mathbf{k}\}\rangle$  moves by  $\mathbf{v}_r t_A$ . We represent the action of this wait using the matrix:

$$\mathbf{A}(t_A) = \begin{pmatrix} 1 & 0 \\ 0 & \hat{T}_{t_A} \end{pmatrix} \quad (8.17)$$

where  $\hat{T}$  is the translation operator defined by  $\hat{T}_t f(\mathbf{x}) = f(\mathbf{x} - \mathbf{v}_r t)$ . After the wait,  $t_A$ , we have the state

$$\mathbf{A}(t_A)\mathbf{B}(\Omega_R) \begin{pmatrix} \psi(\mathbf{r}) \\ 0 \end{pmatrix} = \begin{pmatrix} \cos\left(\frac{\theta}{2}\right) \psi(\mathbf{r}) \\ -i \sin\left(\frac{\theta}{2}\right) \psi(\mathbf{r} - \mathbf{v}_r t_A) \end{pmatrix}, \quad (8.18)$$

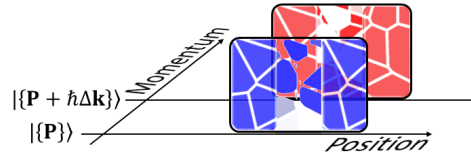


And thus we have achieved the aim of displacing one of the copies.

### Step 3: Interfere

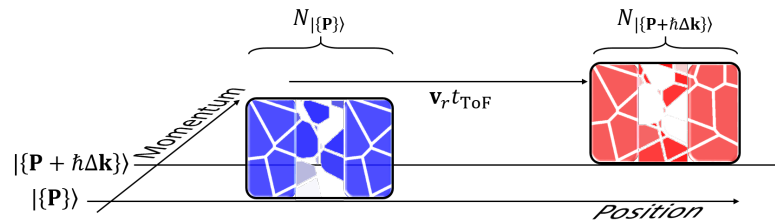
Finally, we interfere the displaced copies by applying a second Bragg pulse identical to and in phase with the first pulse. This gives the final state:

$$\mathbf{B}(\Omega_R)\mathbf{A}(t_A)\mathbf{B}(\Omega_R) \begin{pmatrix} \psi(\mathbf{r}) \\ 0 \end{pmatrix} = \begin{pmatrix} \cos^2\left(\frac{\theta}{2}\right)\psi(\mathbf{r}) - \sin^2\left(\frac{\theta}{2}\right)\psi(\mathbf{r} - \mathbf{v}_r t_A) \\ -i \sin\left(\frac{\theta}{2}\right)\cos\left(\frac{\theta}{2}\right)[\psi(\mathbf{r}) + \psi(\mathbf{r} - \mathbf{v}_r t_A)] \end{pmatrix}, \quad (8.19)$$



In the region where the copies overlap, the final density of atoms in the  $|\{\mathbf{P} + \hbar\Delta\mathbf{k}\}\rangle$  state depends on the relative phase of the overlapping domains in the two copies. If we wait a further time-of-flight of  $t_{\text{ToF}} = 140$  ms (i.e. apply  $\mathbf{A}(t_{\text{ToF}})$ ) we obtain the interference term  $\propto [\psi(\mathbf{s}) + \psi(\mathbf{s} - \mathbf{v}_r t_A)]$  in state  $|\{\mathbf{P} + \hbar\Delta\mathbf{k}\}\rangle$  spatially separated by  $\mathbf{v}_r t_{\text{ToF}}$  from the stationary cloud in state  $|\{\mathbf{P}\}\rangle$ . Therefore, we can count the fraction of atoms in this diffracted cloud, and using Eq. 8.14 and 8.13, we obtain:

$$\frac{N_{|\{\mathbf{P} + \hbar\Delta\mathbf{k}\}\rangle}}{N} = \frac{1}{2} \left\{ 1 + \left(1 - \frac{x}{L}\right) \text{Re} [C_1^\infty(x\hat{\mathbf{x}})] \right\} \sin^2(\theta), \quad (8.20)$$



where  $x\hat{\mathbf{x}} = \mathbf{v}_r t_A$ . Eq. 8.20 is the key result of this section, stating that we can measure the  $C_1^\infty$  correlation function (encoding the length scale  $d$ ) by simply counting the fraction of atoms diffracted by our homodyne interferometric scheme. We will use this technique in our quantitative studies in sections 8.3 and 8.4, however, first we will outline one final technical point in the section below.

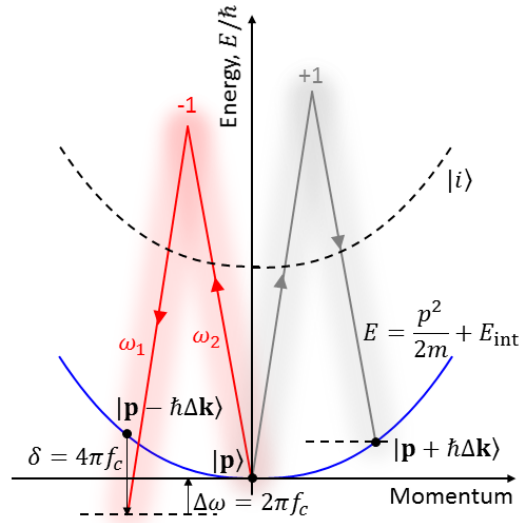


**Fig. 8.4.:** Level diagram for the -1 Bragg diffraction order (red). The lasers are tuned such that a stationary atom is resonant with the +1 order transition (shown in gray). This results in a large detuning,  $\delta$ , for the -1 order.

### Aside: Bragg diffraction orders

Note that so far we have only considered transitions from  $\{\mathbf{P}\}$  to  $\{\mathbf{P} + \hbar\Delta\mathbf{k}\}$  (the so-called +1 order). Using the same laser beams but swapping the roles of absorption and stimulated emission, it is possible to couple  $\{\mathbf{P}\}$  to  $\{\mathbf{P} - \hbar\Delta\mathbf{k}\}$  (the -1 order). Since the lasers are resonant with the +1 transition, the -1 transition is detuned by  $\delta/2\pi = 2f_c$  (see Fig. 8.4). To find the population of the -1 order, we can repeat the analysis above with  $\delta \neq 0$  using the full matrix  $\mathbf{B}(\Omega_R, \delta)$  from Eq. 4.11 and including the free evolution of the states<sup>3</sup> in  $\mathbf{A}(\Omega_R, \delta)$ . This gives the diffracted fraction in the -1 order as:

$$\frac{N_{\{\mathbf{P}-\hbar\Delta\mathbf{k}\}}}{N} = \frac{2\Omega_R^2}{\delta^2} \left\{ 1 + \cos \left[ \delta \left( t + \frac{x}{v_r} \right) \right] \left( 1 - \frac{x}{L} \right) C_1^\infty(x\hat{\mathbf{x}}) \right\} \sin^2 \left( \frac{\delta t}{2} \right) \quad (8.21)$$

where we have assumed  $\sqrt{\Omega_R^2 + \delta^2} \approx |\delta|$  and that  $C_1^\infty$  is a real function (which is true for any system with an even momentum distribution). We can draw two conclusions from Eq. 8.21:

<sup>3</sup>It is important to note that when the lasers are off ( $\Omega_R = 0$ ) during the wait time  $t_A$ ,  $\mathbf{B}(\Omega_R = 0, \delta)$  does not reduce to the identity for  $\delta \neq 0$ . Therefore, in the rotating frame, we must include the evolution of the states at relative frequency  $\delta$  during the "arrange" step:

$$\mathbf{A}(t_A, \delta) = \underbrace{\begin{pmatrix} \exp\left(\frac{i\delta t_A}{2}\right) & 0 \\ 0 & \exp\left(\frac{-i\delta t_A}{2}\right) \end{pmatrix}}_{\mathbf{B}(\Omega_R=0, \delta)|_{t \rightarrow t_A}} \begin{pmatrix} 1 & 0 \\ 0 & \hat{T}_{t_A} \end{pmatrix}.$$

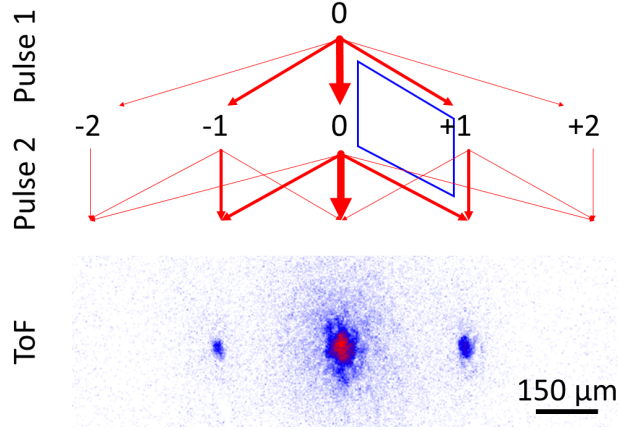


**Fig. 8.5.:** Relevant Bragg diffraction orders. The arrows show the cumulative population transfer between the orders with the lines of decreasing thickness indicating relative populations  $\mathcal{O}(1)$ ,  $\mathcal{O}[(\Omega_R t)^2]$ , and  $\mathcal{O}[(\Omega_R t)^4]$  respectively. Note that the homodyne interference circuit (highlighted in blue) is only affected to  $\mathcal{O}[(\Omega_R t)^4]$  by the presence of other Bragg orders. The ToF image shows the result of an experimental run from section 8.3 in which we cool the gas in  $t_Q = 0.8$  s, apply Bragg pulses separated by  $t_A = 0.4$  ms, and then wait 140 ms ToF.

- The population in the  $-1$  order cloud oscillates with  $t_A = x/v_r$  at frequency  $\delta$ .
- The population in the  $-1$  order is as significant as the  $+1$  order (ignoring oscillations). This can be seen by taking the envelope of the oscillations of  $N_{|\{\mathbf{P}-\hbar\Delta\mathbf{k}\}\rangle}/N$ , and expanding  $\sin(\theta)$  for small angles, giving  $N_{|\{\mathbf{P}\pm\hbar\Delta\mathbf{k}\}\rangle}/N \sim (\Omega_R t)^2$ . Qualitatively, the symmetry in the amplitude of the  $\pm 1$  orders is a result of the broad Bragg resolution kernel  $2\pi \times \Delta f_{\text{res}} \gg 2\delta$ .

The significance of the  $-1$  order brings into question the validity of our treatment of  $\{\mathbf{P}\}$  and  $\{\mathbf{P} + \hbar\Delta\mathbf{k}\}$  as a closed two-level system coupled by  $\mathbf{B}$ . However, following the schematic diagram in Fig. 8.5, we see that the  $-1$  order only modifies our expression in Eq. 8.20 by terms  $\mathcal{O}(\Omega_R^4 t^4)$ , provided that we count all the  $-1$ ,  $0$  and  $+1$  orders in  $N$ . Since  $(\Omega_R t)^2 \approx 0.2 \ll 1$ , we ignore all these higher order terms (4-photon processes and depletion of the zero-order cloud) and work to just first order with Eq. 8.20.

This concludes our technical discussion of the derivation and validity of Eq. 8.20 which is key to the experimental work discussed in the remainder of this chapter.

### 8.2.3 Experimental measurement of $C_1$

In this section, we introduce the various forms for  $C_1$  which we observe in the experiment using our homodyne interference scheme. Fig. 8.6 shows  $C_1(x\hat{\mathbf{x}})$

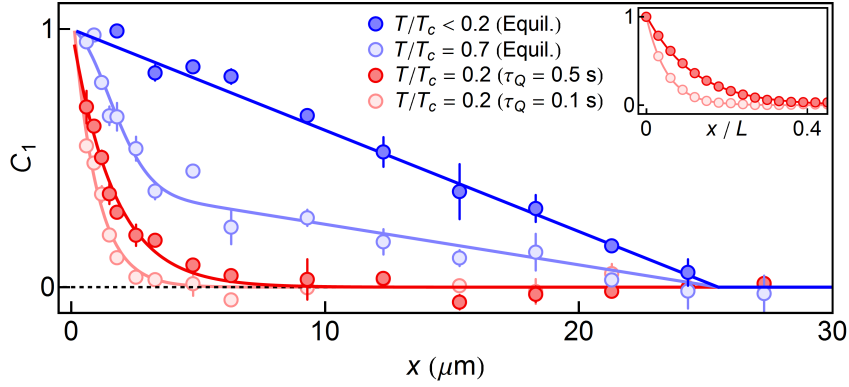


**Fig. 8.6.:** Correlation function  $C_1(x) = (1 - x/L)C_1^\infty(x)$  measured in equilibrium (blue) and after a quench (red) for, respectively, two different  $T/T_c$  values and two different quench times (four experimental runs per point; error bars indicate standard deviation in mean). Inset: 1D calculation of  $G_1$  for a fragmented BEC containing  $D = 10$  (red) and 20 (light red) domains of random sizes and phases. The solid lines correspond to  $C_1^\infty = \exp(-xD/L)$

functions measured in equilibrium (blue) and after a quench (red), and we compare three experimental cases:

*Pure BEC* In an essentially pure equilibrium BEC (prepared slowly, as for Fig. 8.2(b)),  $C_1^\infty(x\hat{x}) = 1$  and  $C_1(x\hat{x})$  is simply given by the linear overlap function  $1 - x/L$  (dark blue line).

*Partial BEC* Cooling slowly in equilibrium, but stopping at  $T/T_c \approx 0.7$ , gives a  $C_1$  with a fast initial decay, corresponding to the significant thermal fraction. Importantly, the coherence still spans the whole system, with the slope of the long-ranged part of  $C_1$  giving the condensed fraction (light blue line is a guide to the eye).

*Quenched clouds* By comparison, the  $C_1$  functions for quenched clouds have no equilibrium interpretation. For the curves shown,  $T/T_c \approx 0.2$ , corresponding to a phase space density  $> 25$ , and yet coherence extends over only a small fraction of  $L$ . Furthermore, in Fig. 8.6, we immediately see agreement with the qualitative picture that faster quenches lead to  $C_1$  functions with a shorter decay length.

The data for the quenched clouds are fitted well by  $C_1^\infty \propto \exp(-x/\ell)$  (red lines), which provides a simple and robust way to extract the coherence length. This exponential form is further supported by a 1D calculation shown in the inset of Fig. 8.6. Here we generate a wavefunction with a fixed number of domains  $D$ , randomly positioning the domain walls and assigning each domain a random phase. Averaging over many realizations, we obtain  $C_1^\infty(x)$  that is fitted very well by an exponential with  $\ell = L/D = d$ . (In our 3D experiments the total number of domains is  $\sim D^3$  and  $C_1(x)$  is effectively averaged over  $\sim D^2$  1D distributions.)

Since the exponential fit gives us direct access to  $\ell = d$ , we can now move on to a fully quantitative study of the KZ theory.

## 8.3 Direct observation of Kibble-Zurek freeze-out

We are hoping to observe the scaling of  $d$  with  $\tau_Q$ , but as we will see, in our experiment we also directly observe the freeze-out phenomenon central to the KZ hypothesis. For the KZ scaling law of Eq. 8.6, a crucial assumption is that  $\xi$  is essentially frozen within  $\hat{t}_{\pm}$  of  $t_c$ . While intuitively appealing, this assumption is in principle only approximate, and the dynamics of the system coarsening (i.e., merging of the domains) at times  $t > t_c$  is still a subject of theoretical work [169].

In our experiment we use two different quench protocols outlined in Fig. 8.7. We start by describing the first quench protocol, QP1, where we vary only the total time  $t_Q$  over which we ramp down the trap depth.

### 8.3.1 Quench protocol 1: Basic KZ scaling and its breakdown

In QP1 we restrict  $t_Q$  to values between 0.2 s and 3.5 s, for which we observe that the cooling curves are self-similar<sup>4</sup>. We find that we always cross  $T_c = (70 \pm 10)$  nK at time

$$t_c = (0.72 \pm 0.05) t_Q, \quad (8.22)$$

and always have the same atom number (within  $\pm 20\%$ ) at the end of cooling. The self-similarity of the measured cooling trajectories and the essentially constant evaporation efficiency indicate that for this range of  $t_Q$  values the system is always sufficiently thermalised for the temperature (as determined from the thermal wings in ToF) to be well defined during the quench<sup>5</sup>. Furthermore, from the definition of  $\epsilon$ , we can linearise the cooling trajectory near  $t_c$  and calculate  $\tau_Q$  from the derivative as follows:

$$\left. \frac{d\epsilon}{dt} \right|_{t \approx t_c} = -\frac{1}{\tau_Q}, \quad (8.23)$$

<sup>4</sup>Note that we empirically find that for  $t_Q < 0.2$  s the evaporation is less efficient and the cooling trajectories are no longer self-similar

<sup>5</sup>Near  $T_c$  the mean free path for classical elastic collisions is about four times larger than the size of the box. Hence, while the evaporation takes place at the box walls, we can also safely assume that  $T$  is uniform across the sample.

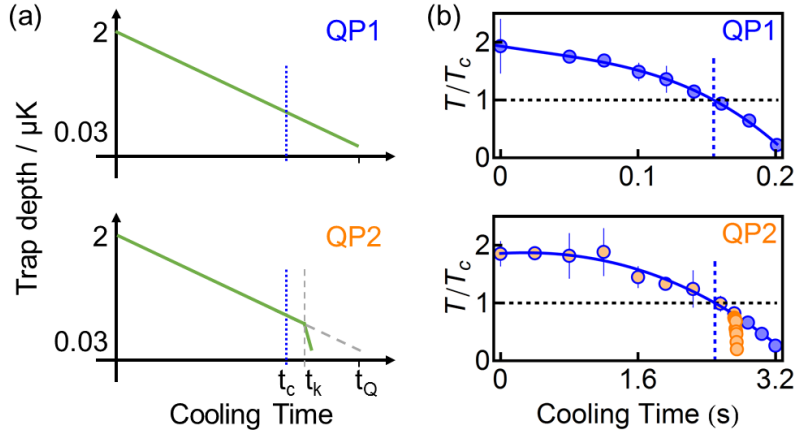


**Fig. 8.7.:** Quench protocols. (a) In QP1, the laser power is ramped down linearly over time  $t_Q$  to reduce the trap depth. In QP2 the laser power is ramped faster (at a slope characteristic of  $t_Q = 0.2$  s) after  $t_k \gtrsim t_c$ . (b) The self-similar QP1 cooling trajectories are shown in blue for total cooling time  $t_Q = 0.2$  s (upper panel) and 3.2 s (lower panel) (four experimental runs per point; error bars indicate standard deviation in mean). We use polynomial fits to the data (such as shown by the solid lines) to deduce  $t_c$  and  $\tau_Q$ . QP2 is shown in the lower panel by the orange points, with the kink at  $t_k = 0.85 t_Q$ .

and due to the self similarity, we find that to good approximation<sup>6</sup>

$$\tau_Q \propto t_Q. \quad (8.24)$$

It is worth briefly commenting on this result in light of the non-linearity of the cooling trajectories in Fig. 8.7:

### The definition of $\tau_Q$ for a non-linear quench

The KZ theory is built upon the assumption of a linear quench for which the derivative in Eq. 8.23 is constant and  $\tau_Q$  is unambiguously defined. Experimentally, we do not perform linear temperature quenches and for a quench which is not truly linear, there is some uncertainty over exactly where the derivative should be evaluated (hence we write  $t \approx t_c$  in Eq. 8.23). According to the KZ hypothesis, the domain size is determined by the system properties at the freeze-out point. Therefore, it is most reasonable to define  $\tau_Q$  from the derivative at the point,  $t_c - \hat{t}_+$ , given by the solution to the (non-linearised) equation  $|\dot{\xi}/\xi| = 1/\tau$ .

In Appendix D, we use a simple numerical model for our non-linear quench to investigate whether evaluating  $\tau_Q$  from the slope at the freeze time rather than at the critical time affects the simple proportionality in 8.24 (see Fig. 8.8). The model confirms two important results:

<sup>6</sup>When the derivative is evaluated at exactly at  $t = t_c$ , we find a constant of proportionality  $\tau_Q = (0.41 \pm 0.02) t_Q$ .

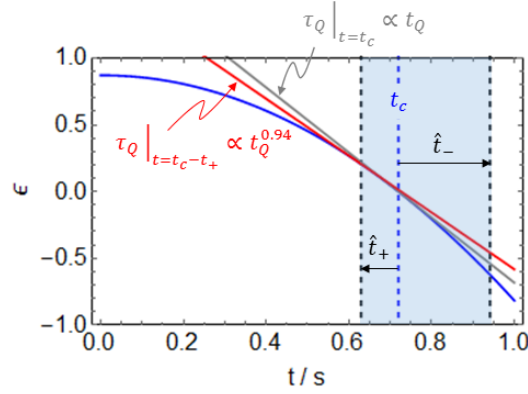


**Fig. 8.8.:** Technical details of our non-linear quench trajectory. We parameterise the self-similar shape of the QP1 cooling curves by the quadratic curve shown in blue. In a numerical model in Appendix D we calculate the freeze-out conditions (blue shaded region) and illustrate the  $t_Q = 1$  s case above (assuming F-Model critical exponents). To link this non-linear curve to the linearised KZ theory, we can define  $\tau_Q$  as the inverse slope of  $\epsilon(t)$  evaluated at either  $t = t_c$  (gray) or  $t = t_c - \hat{t}$  (red). See text for a discussion of these two scenarios.

- The KZ scaling law for the domain size at the critical point is only recovered exactly if we use  $\tau_Q$  defined by the slope of the quench trajectory at  $t_c - \hat{t}_+$ .
- There is a small non-linearity between the  $\tau_Q$  evaluated from the slope at the freeze time and at the critical time. A numerical power-law fit in both the MF and F Model for characteristic parameters in our experiment gives  $\tau_Q|_{t=t_c-\hat{t}_+} \approx 1.1(\tau_Q|_{t=t_c})^{0.94}$ , i.e.  $\tau_Q|_{t=t_c-\hat{t}_+} \propto t_Q^{0.94}$ . This non-linearity means that we must be careful when replacing  $\tau_Q$  with  $t_Q$  when evaluating any exponents.

In summary, the numerical analysis tells us that if we were to ignore all complications arising from our non-linear quench and evaluate the derivative in Eq. 8.24 at  $t = t_c$ , then we would recover a value of the exponent  $b$  which is 6% smaller than the true value. Since this correction is small (considerably smaller than the difference between the values of  $b$  in the MF and the F-Model), we will proceed with the assumption of a linear quench (i.e. that the proportionality in Eq. 8.24 always holds). Only once we have experimentally evaluated the exponent  $b$  under this assumption will we attempt to account for any corrections arising from the non-linearity of our cooling curve.

With this assumption in mind, we now inspect the size of the domains formed at the end of a QP1 quench:

### QP1 Results

In Fig. 8.9(a) we plot  $\ell(= d)$  vs.  $t_Q(\propto \tau_Q)$ , for experiments using QP1. For  $t_Q \leq 1$  s we observe a slow power-law growth of  $\ell$  with  $t_Q$ , in good agreement with the

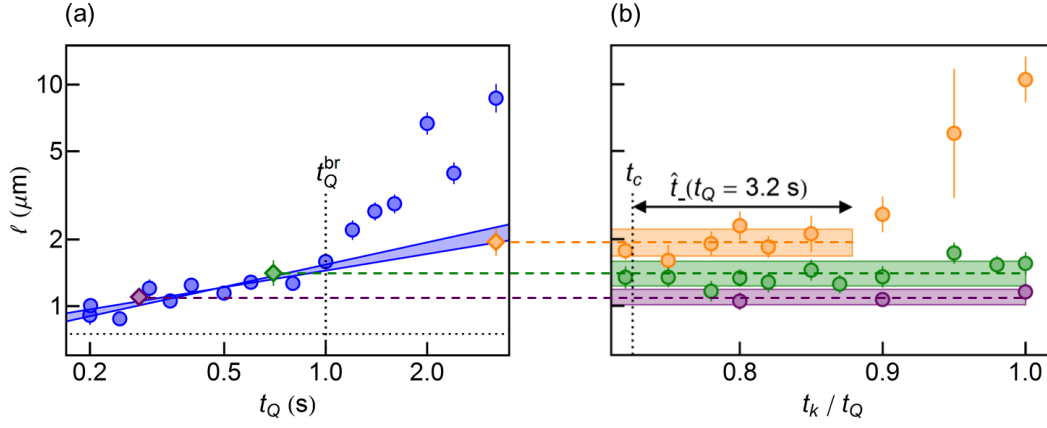


**Fig. 8.9.:** Kibble-Zurek scaling and the freeze-out hypothesis. (a) Coherence length  $\ell$  as a function of  $t_Q$ . Blue points correspond to QP1, error bars indicate fitting errors on  $\ell$ . The shaded blue area shows power-law fits with  $1/4 < b < 1/3$  to the data with  $t_Q \leq t_Q^{\text{br}} = 1$  s. The horizontal dotted line indicates our instrumental resolution (arising from the finite Bragg pulse time). (b) Coherence length  $\ell$  measured following QP2, as a function of  $t_k/t_Q$ , for  $t_Q = 3.2$  s (orange), 0.7 s (green), and 0.3 s (purple) (four experimental runs per point; error bars indicate standard deviation in mean). The shaded areas correspond to the essentially constant  $\ell$  (and its uncertainty) in the freeze-out period  $t_k - t_c < \hat{t}_-$ . (For  $t_Q < t_Q^{\text{br}}$  the system never unfreezes). The (average)  $\ell$  values within these plateaux are shown in their respective colours as diamonds in panel (b).

expected KZ scaling. However, for  $t_Q > t_Q^{\text{br}} \approx 1$  s this scaling breaks down and  $\ell$  grows faster, quickly approaching the system size.

For quenches longer than  $t_Q^{\text{br}}$ , we suggest that the breakdown of the KZ scaling is due to the system unfreezing and healing significantly *during* the quench and before it is observed. We note from Eq. 8.22 that the time between crossing  $T_c$  and the end of cooling is  $t_Q - t_c \approx 0.28 t_Q \propto t_Q$ , while the KZ freeze-out time is  $\hat{t}_- \propto t_Q^{\nu z / (1 + \nu z)}$  (assuming Eq. 8.24). Due to the different scaling of these two times with  $t_Q$ , it is always possible to perform slow enough quenches such that  $t_Q - t_c$  exceeds  $\hat{t}_-$  for  $\nu z > 0$  (see Fig. 8.10). Solving for the intersection  $\hat{t}_- \approx 0.28 t_Q^{\text{br}}$  in Fig. 8.10, we obtain an estimate of the absolute value of  $\hat{t}_-$  without *a priori* knowledge of  $\tau_0$  or  $\lambda_0$ .

$$\hat{t}_- \approx 0.28 t_Q^{\text{br}} \left( \frac{t_Q}{t_Q^{\text{br}}} \right)^{\nu z / (1 + \nu z)}. \quad (8.25)$$

Since  $\nu z = 1$  holds at both the mean field and F Model level, we can say that for both models  $\hat{t}_- \approx 0.28 \sqrt{t_Q t_Q^{\text{br}}}$ . In the next section we will have an opportunity to directly measure  $\hat{t}_-$  for comparison with this expression.

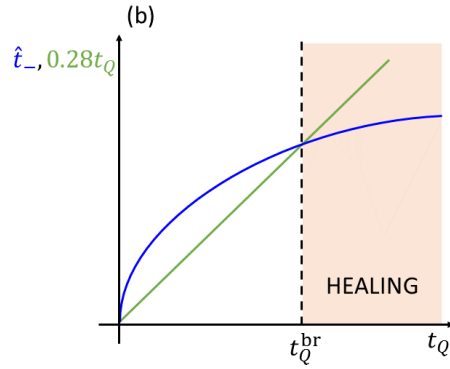


**Fig. 8.10.:** Proposed mechanism for the breakdown of the KZ scaling in Fig. 8.9(b). We plot  $t_Q - t_c$  and  $\hat{t}_-$  as a function of  $t_Q$  and suggest that beyond the intersection point,  $t_Q^{\text{br}}$  (orange shaded region), the system unfreezes and begins to heal during the QP1 quench. To explore this region we must use QP2.

### 8.3.2 Quench Protocol 2: Directly observing the KZ freeze-out

Our second quench protocol consists of two steps as shown in Fig. 8.7. This protocol allows us to directly observe the freezing of the system and to fully understand the breakdown of the scaling law at  $t_Q^{\text{br}}$  in the QP1 results. Once this breakdown is understood, we can also use QP2 measurements to extend the range of  $t_Q$  over which we can fit a power law. Using this extended range we will experimentally distinguish the MF and F Model critical exponents.

In QP2 we initially follow the QP1 trajectory for a given  $t_Q$ , but then at a variable "kink" time  $t_k \gtrsim t_c$  we accelerate the cooling. The last part of the trajectory always corresponds to the final portion of our fastest, 0.2 s cooling trajectory. This way, even for  $t_Q > t_Q^{\text{br}}$  we can complete the cooling and measure  $C_1$  before the system has time to unfreeze.

In Fig. 8.9(b), the orange points show the QP2 measurements of  $\ell$  for  $t_Q = 3.2$  s and various values of the kink position  $t_k/t_Q$ . These data reveal two remarkable facts:

- For a broad range of  $t_k$  values,  $\ell$  is indeed constant (within errors), and the width of this plateau agrees with our estimate from Eq. 8.25,  $\hat{t}_- \approx 0.5$  s for  $t_Q = 3.2$  s, indicated by the horizontal arrow.
- The value of  $\ell$  within the plateaued region falls in line with the KZ scaling law in Fig. 8.9(a).

We also show analogous QP2 measurements for  $t_Q = 0.7$  s (green) and 0.3 s (purple); in these cases  $t_Q < t_Q^{\text{br}}$ , so  $\hat{t}_-$  is longer than  $t_Q - t_c$ , the system never

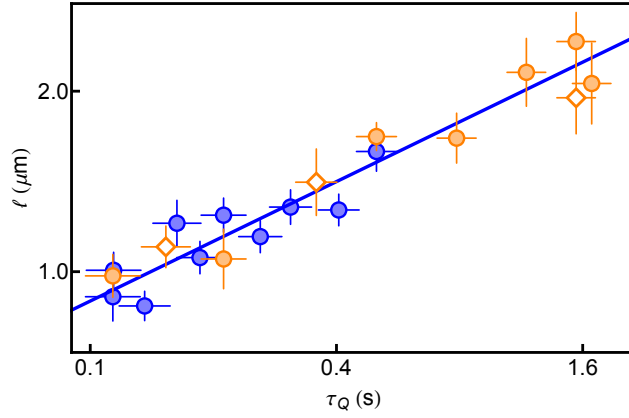


**Fig. 8.11.:** Critical exponents of the interacting BEC transition. Orange circles and diamonds show  $\ell$  values obtained using QP2, as in Fig. 8.9(b); the diamonds show the same three data points as in Fig. 8.9(a). Blue circles show the same QP1 data with  $t_Q \leq 1$  s as in Fig. 8.9(a). The horizontal error bars indicate the systematic uncertainty in  $\tau_Q$  based on evaluation of  $-(\dot{\epsilon})^{-1}$  over the range  $t = t_c - \hat{t}_+ \rightarrow t_c$ . We obtain  $b = 0.33_{\pm 0.03}^{\pm 0.02 \text{ sys.}}$  (solid line), in agreement with the F model prediction  $b \approx 1/3$ , corresponding to  $\nu \approx 2/3$  and  $z = 3/2$ , and excluding the mean-field value  $b = 1/4$ .

unfreezes, and thus the acceleration of the cooling has no effect on  $\ell$ . These plateaux provide direct support for the KZ freeze-out hypothesis.

## 8.4 Kibble-Zurek scaling and universal critical exponents

To accurately determine the KZ exponent  $b$ , we have made extensive measurements following QP2, extracting  $\ell$  from the plateaued regions of width  $\min[\hat{t}_-, t_Q - t_c]$ , as in Fig. 8.9(b). In Fig. 8.11 we combine these data with the QP1 measurements for  $t_Q \leq t_Q^{\text{br}}$ , and plot  $\ell$  versus  $\tau_Q$ . To construct this plot we must return to the problem raised in section 8.3 of exactly where on the non-linear cooling trajectory we should evaluate  $\tau_Q = -(\dot{\epsilon})^{-1}$ . There are two routes to proceed which we deal with separately below:

### Evaluate $\tau_Q$ at $t_c$

The simplest analysis which ignores the non-linearity of the cooling trajectory is to accept the proportionality  $\tau_Q \propto t_Q$  and find  $b$  as the slope of a plot of  $\log(\ell)$  vs.  $\log(t_Q)$ . This gives  $b = 0.31 \pm 0.03$ , which is in agreement with the F Model ( $b = 1/3$ ) and excludes the MF prediction ( $b = 1/4$ ). Furthermore, note that this approach gives a lower bound on the value of  $b$ , and the numerical simulation in Appendix D suggests that we should include a 6% systematic correction to this value (because  $\tau_Q \propto t_Q^{0.94}$ ). Applying this correction (which is smaller than the statistical error on

b) hints at a value  $b = 0.33$  which is in even better agreement with the F Model prediction.

### Evaluate $\tau_Q$ at $t_c - \hat{t}_+$

The study above gave considerable support to the beyond mean-field F Model exponents, however rather than accessing  $b$  directly, it only provided a tight lower bound to  $b$  and relied on numerical simulations to indicate the true value of  $b$ . Ideally, we would not rely on any simulations, but instead estimate  $\hat{t}_+$  directly from the experiment, and evaluate  $\tau_Q$  at  $t_c - \hat{t}_+$ . Measuring  $\hat{t}_+$  is experimentally challenging, however we proceed with the following assumptions:

- First we assume from Eq. 8.5 that  $\hat{t}_+/\hat{t}_- = (X_+/X_-)^{z/(1+\nu z)} \approx 0.4$ , where we assume F Model results for  $\nu$ ,  $z$  and  $X_+/X_-$  in the hope of self-consistently measuring  $b$ .
- Next we assume that the value of  $\hat{t}_- = 0.28\sqrt{t_Q t_Q^{\text{br}}}$  suggested in section 8.3.1 is a good estimate of  $\hat{t}_-$  from which we can evaluate  $\hat{t}_+ = 0.4\hat{t}_-$ .

These assumptions are difficult to justify rigorously. In particular, the second assumption requires that the microscopic time and length scales  $\tau_0$  and  $\lambda_0$  do not change when a BEC is present. Nevertheless, we can follow this protocol with  $t_Q^{\text{br}} = 1$  s to achieve an estimate  $b = 0.35 \pm 0.03$ . This is again consistent with the F Model, and gives us a way to assess the systematic error in our value of  $b$ .

One could even combine the values of  $b$  for the two methods above to give  $b = 0.33_{\pm 0.03 \text{ stat.}}^{\pm 0.02 \text{ sys.}}$ . It is reassuring to note that the systematic variation on  $b$  as we analyse the data in different ways is not larger than the statistical uncertainty on any given analysis, and is also significantly smaller than the difference between the F Model and MF theory.

## 8.4.1 Dynamical critical exponent, $z$

Having observed excellent agreement with the KZ theory, we now discuss the implications of our measurements for the critical exponents of the interacting BEC phase transition, which is in the same universality class as the  $\lambda$ -transition of  $^4\text{He}$ . While  $\nu \approx 0.67$  has been measured in both liquid helium (see [170]) and atomic gases [171], the dynamical exponent  $z$  has, to our knowledge, never been measured before (see [163, 172]). Using the well-established  $\nu = 0.67$  and Eq. 8.6, we obtain  $z = 1.5_{\pm 0.3 \text{ stat.}}^{\pm 0.2 \text{ sys.}}$ . In contrast, MF theory does not provide a self-consistent interpretation of our results, since fixing  $\nu = 1/2$  yields an inconsistent  $z = 1.0_{\pm 0.3 \text{ stat.}}^{\pm 0.2 \text{ sys.}}$ . Interestingly, if we instead fix  $\nu z = 1$ , which holds at both MF and F-model level,

from Eq. 8.6 we obtain a slightly more precise  $z = 1.5^{\pm 0.1 \text{ sys.}}_{\pm 0.1 \text{ stat.}}$  and also recover  $\nu = 0.67^{\pm 0.04 \text{ sys.}}_{\pm 0.06 \text{ stat.}}$ .

## 8.5 Conclusion

This chapter has presented an experiment which is the culmination of all the work in the second half of this thesis. We developed a versatile trapping technique in chapter 5, applied this to make a uniform system in chapter 6, introduced bragg spectroscopy to benchmark the equilibrium ground state properties in chapter 7, and now finally applied this in a dynamical study of the KZ freeze-out mechanism and measurement of the dynamical critical exponent for our universality class.

Note that our uniform trapping potential was essential for the clean observation of the KZ mechanism presented here. In an inhomogeneous potential  $U(\mathbf{r})$ , the critical temperature is a function of position. This means that  $\epsilon$  is position dependent and as we decrease  $T$ , the critical point  $\epsilon(x, t) = 0$  is reached at different points at different times. Condensation happens first at the point(s)  $\mathbf{r}_0 = \arg \min[U(\mathbf{r})]$ , and then a "transition front" radiates out from this(these) point(s) at speed:

$$v_F = \left| \frac{\partial \epsilon / \partial t}{\partial \epsilon / \partial x} \right| \quad (8.26)$$

Independent phase domains will only form if this front travels faster than the speed  $v_s$  at which the choice of symmetry breaking phase can be communicated<sup>7</sup>. Whereas in a uniform system,  $v_F$  diverges (because  $\partial \epsilon / \partial x = 0$  - i.e. the entire system becomes critical at once), in an inhomogeneous system, we need to take the competition between  $v_F$  and  $v_s$  into account. This means that we cannot directly observe the KZ freeze-out (only local regions of the system are frozen at any time), and the (local) size of the domains and is generally not given by any simple power law. Instead, a harmonically trapped system is described the so-called inhomogeneous KZ theory [165], which is only able to predict approximate scaling laws with  $b \geq 1$  holding near  $\mathbf{r}_0$ . Hence, our uniform system was essential for the observation of the fundamental mechanism and consequences of KZ theory that we have described here.

<sup>7</sup>Intuitively,  $v_s$  can be bounded by the velocity scale  $v_s < \hat{\xi} / \hat{\tau}$  given by the local frozen quantities  $\hat{\xi}$  and  $\hat{\tau}$

## Conclusions and Outlook

The experiments in Part I and Part II of this thesis were carried out on two separate machines. The first machine is able to tune inter-atomic interactions and allowed us to study dynamical effects of superheating and three-body loss in regimes of very weak and very strong interactions respectively. The second machine is specialised for producing novel optical geometries, and specifically we created the worlds first atomic Bose gas in a uniform potential. The chapters presented here reviewed a series of equilibrium and dynamical experiments performed so-far in this uniform trap.

In the future, we plan to combine the two key features of both machines in a third machine which will allow us to tune interactions and geometry on the same experiment. Work has already started on this machine, and several proof-of-principle experiments have been carried out on our existing machines to lay the ground-work for when the third machine is fully operational. The uniform system in chapter 6 offers such a rich range of experimental paths that our investigations in the immediate future will concentrate on this simple geometry rather than expanding to more elaborate trap shapes. There are four experiments which we envisage for the near future, which are described in the sections below. The first two are extensions to chapters 7 and 8, and the last two involve small additions to our uniform trap geometry.

### 9.1 Thermodynamics with tuneable interactions

The first proposed experiment continues our strand of thermodynamic experiments from chapter 7. In particular, we first wish to investigate the effect of interactions on the the critical temperature ( $T_c$ ) for condensation.

In a harmonically trapped gas,  $T_c$  is shifted relative to the ideal gas value by a mean-field effect arising from the inhomogeneity of the trap. It was recently possible to also measure a more interesting  $T_c$ -shift arising from interaction-driven critical correlations on top of this much larger mean-field shift [41] (see Eq. 2.11). Further accurate measurement is not possible in a harmonic trap because the large mean-field effect dominates over any interesting physics. In a homogeneous gas, there is no mean-field  $T_c$ -shift, and any  $T_c$ -shifts due to critical correlations become the highest order effects [173]. This means that experiments on our uniform system

will give us an immediate handle on the fundamental critical phenomena driving the beyond-mean field  $T_c$  shift, which has been the focus of theoretical debates for many years (see [26] for a historical summary).

## 9.2 Kibble-Zurek with tuneable interactions

In chapter 8, we observed behaviour of a thermally quenched Bose gas consistent with the beyond mean-field critical exponents of the F Model. The reason for the failure of mean-field is that fluctuations in the order parameter become as large as the value of order parameter near the critical point. It is possible to derive a criterion (the so-called Ginzburg criterion) for the point at which critical fluctuations cause the breakdown of mean-field theory as [171]:

$$\xi > \xi_G = \frac{\lambda_c^2}{\sqrt{128\pi^2 a}} \quad (9.1)$$

where  $a$  is the s-wave scattering length. In our experiment in chapter 8,  $\xi_G \approx 0.8$ , and since the freeze-out values of  $\ell$  are consistently higher than this value, our observation of beyond mean-field exponents is consistent with the Ginzburg criterion. When we tune the interaction strength,  $a$ , in our new machine we will be able to increase  $\xi_G$  and repeat our Kibble-Zurek measurements in this weakly interacting gas to try to measure mean-field exponents in a regime where  $\xi < \xi_G$ .

Another interesting future study could focus on the dynamics of domain coarsening after unfreezing on the ordered side, or on the variance and distribution of domain sizes formed after the quench.

## 9.3 Interferometry

In Fig. 6.11 we saw how simple it is to apply our digital holographic methods to create trapped-atom interferometers. Atom interferometers can be used to detect any external stimulus (e.g. a magnetic field gradient) which causes the phase of one of the interfering clouds to evolve at a different rate to the other. Interfering two BECs in uniform traps offers the following fundamental advantages over interferometers constructed using locally harmonic potentials:

1. Our trap is dark, and therefore there is no dephasing between the trapped condensates arising from a differential AC Stark effect caused by small trap asymmetries.

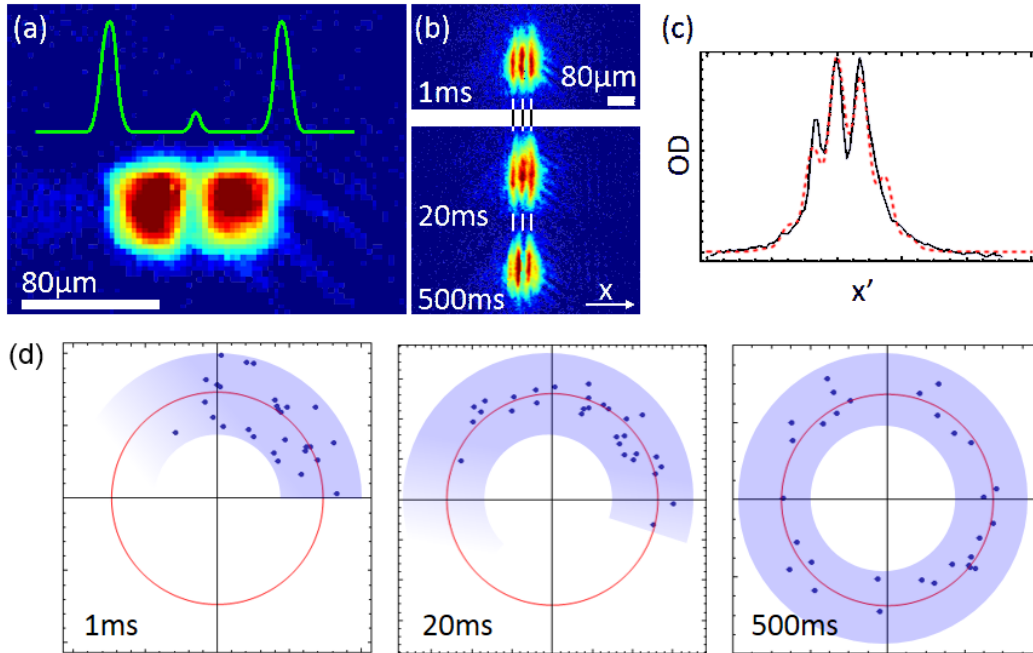


**Fig. 9.1.:** Trapped atom interferometry using our uniform system (preliminary). (a) *In situ* image of a single condensate split into two halves using the three-wall potential illustrated in the green profile. (b) Typical ToF images showing interference fringes when the condensates have been held in their separate halves for 1, 20 and 500 ms. We mark the locations of the fringe peaks after 1 ms hold time with vertical lines. We obtain the same pattern with high probability after 20 ms hold time, but the fringe phase is randomised after 500 ms. (c) We quantitatively extract the phase and amplitude of the fringes using a fit (red dotted line) to a cut through the fringes in the  $x$  direction (blue line). (d) Interferometric measurement of decoherence time. We hold the gas in the split trap for 1, 20 or 500 ms and then observe the interference in ToF. Repeating this many times, we can extract the distribution of the phase,  $\phi$ , and amplitude,  $A$ , of the fringes and plot them on a polar plot. We find that for hold times greater than  $\sim 100$  ms, the phase is fully randomised.

2. The peak atom density in uniform traps is low compared to a cloud of the same number of atoms in locally harmonic traps. This allows us to put enough atoms in our uniform interferometer to achieve a good signal-to-noise ratio, while maintaining a low density such that dephasing from differential mean-field shifts significantly reduced. Mean-field dephasing can be further reduced by turning off interatomic interactions.

Dephasing from the AC Stark shift and the mean-field shift can severely limit the integration time of traditional trapped-atom interferometers [174, 175]. To indicate the advantages of our homogeneous arrangement, we carried out the following proof-of-principle experiment:

We create a uniform BEC with a small central wall running up the middle of the trap (see Fig 9.1(a)). Initially, this wall is sufficiently low with respect to the chemical potential of the BEC to allow a single, connected BEC to form in the entire trap. We then ramp up the green laser power to raise the wall, and split the BEC in two.

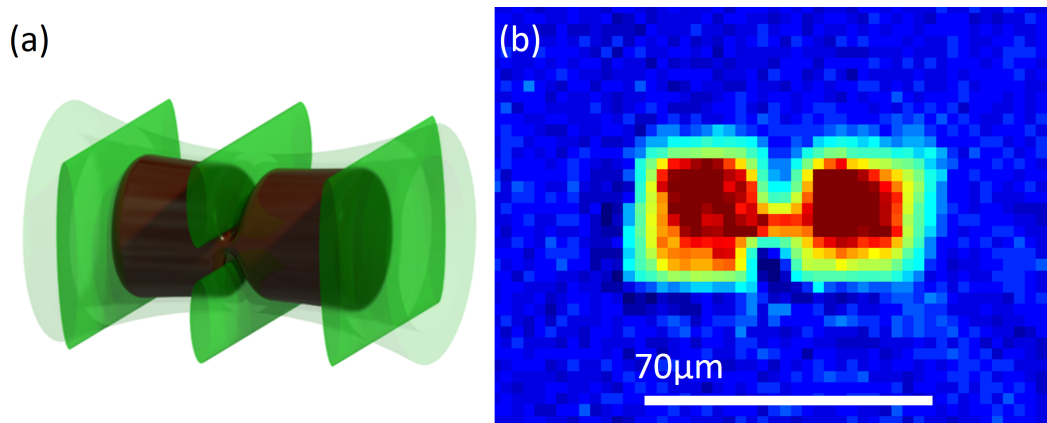


**Fig. 9.2.:** Transport phenomena in an ultracold Bose gas (preliminary). (a) A cartoon of the optical geometry for creating a narrow channel for investigation of quantum transport properties. The central green wall is split to create a channel which can be as narrow as the diffraction limit. The atoms are shown in red, and for clarity, we suppress the appearance of the tube beam. (b) An experimental image using the apparatus of chapter 6 to load atoms into this potential.

Since the two BECs were formed from a single common ancestor, they are initially phase-locked with each other. Therefore if we immediately release the green trap, we should always observe the same fringe pattern when they interfere. We can detect any dephasing of the two condensates after a hold time  $t$  as a randomisation of the fringe pattern in repeated realisations at the same hold time. Figure 9.1(d) shows the distribution of phases and amplitudes of the interference fringe pattern after  $t = 1, 20$  or  $500$  ms. We can see that the dephasing time is at least  $20$  ms in our apparatus, and further experiments gave evidence that the dephasing time is longer than  $\sim 100$  ms. This is similar to state-of-the-art trapped atom interferometers using squeezed states or non-interacting gases which achieve dephasing times of a few hundred milliseconds [49, 174].

### 9.3.1 Transport and thermomechanical phenomena

There has been a recent growth in interest in transport [76, 77, 176–178] and thermomechanical [179, 180] effects in ultracold gases. We note that our holographic methods make it very simple to construct a geometry in which two uniform reservoirs are connected by a thin channel (see Fig. 9.2). Using a magnetic field gradient, we can load all the atoms into one reservoir, and then watch the atoms diffuse through the channel when we turn off the gradient. For our bosonic gas, we should see two different transport effects: the thermal atoms should move ballistically through the channel, while the BEC should show superfluid properties. We suggest that it may be possible to tune the parameters of the channel (e.g. by changing the channel width or inserting a tunnelling barrier) such that the superflow is much faster than the ballistic thermal diffusion. This will allow us to create a "superleak" which only allows

superfluid through. We will use this to explore thermomechanical effects in our Bose gas [179–181] similar to those observed in superfluid helium experiments [182].

Other transport effects could be observed by shaking our optical box (e.g. using an oscillating magnetic field gradient) and observing the superfluid response using bragg spectroscopy.



# Appendices



# Experimental Sequence Overview

During this thesis, we have not dwelt on the preparatory stages of laser- and evaporative-cooling required to reach condensation. Instead, we have concentrated on experiments performed when the cloud is already near degeneracy or deeply condensed. It is somewhat humbling to note that all the techniques and experiments presented in this thesis take place only in the final few moments of a long experimental sequence. The bulk of the sequence was built up by previous students and is summarised in their theses: [25, 26, 33] (Part I machine) and [39, 40] (Part II machine). For specific details of the early experimental procedure, the reader is directed towards these theses. Here we will just provide a brief overview of the key concepts of the simpler Part II machine in a manageable two-page cartoon. It is hoped that this overview will be a useful first roadmap for any future students tasked with extending upon this work.

## A.1 Rubidium-87 $D_2$ Lines

Throughout the cartoons on the following pages, we will illustrate the relevant laser transitions on a skeleton of the  $^{87}\text{Rb}$   $D_2$  line. For clarity, labels are omitted from this skeleton, and a labelled level spectrum is included in Fig. A.1 for reference.

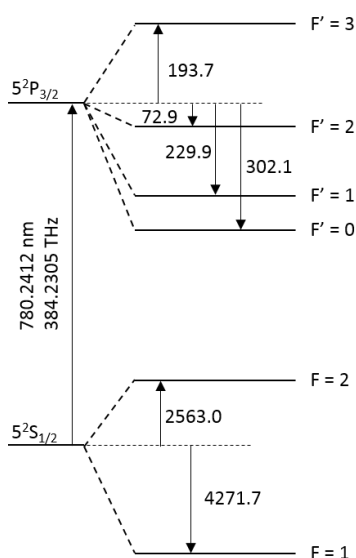
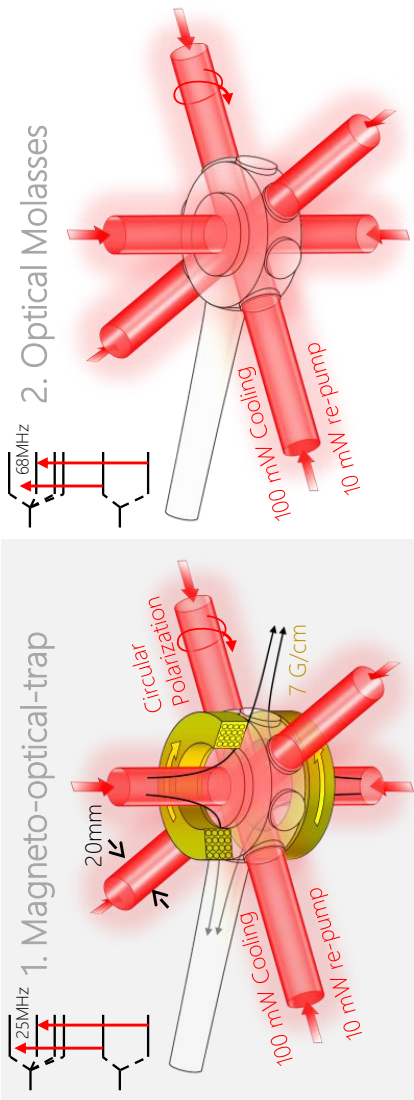
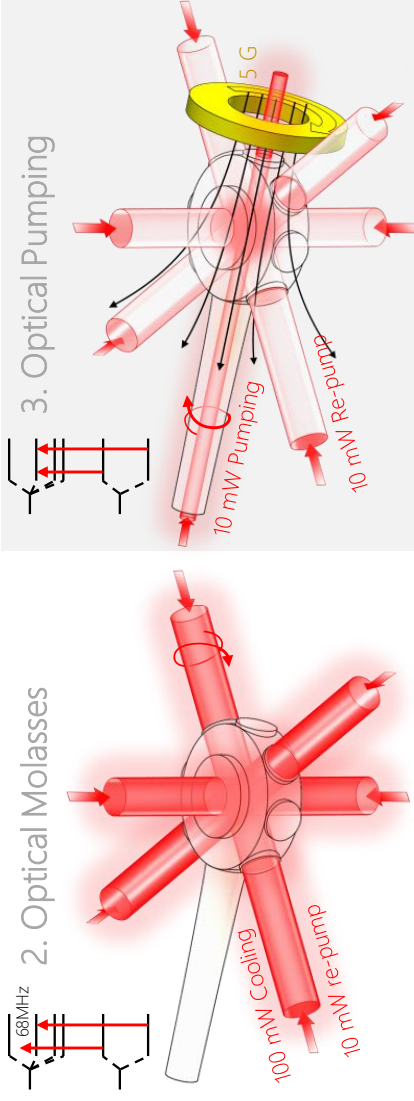


**Fig. A.1.:** Hyperfine structure of the  $^{87}\text{Rb}$   $D_2$  lines. Data (reported in MHz) reproduced from [183].

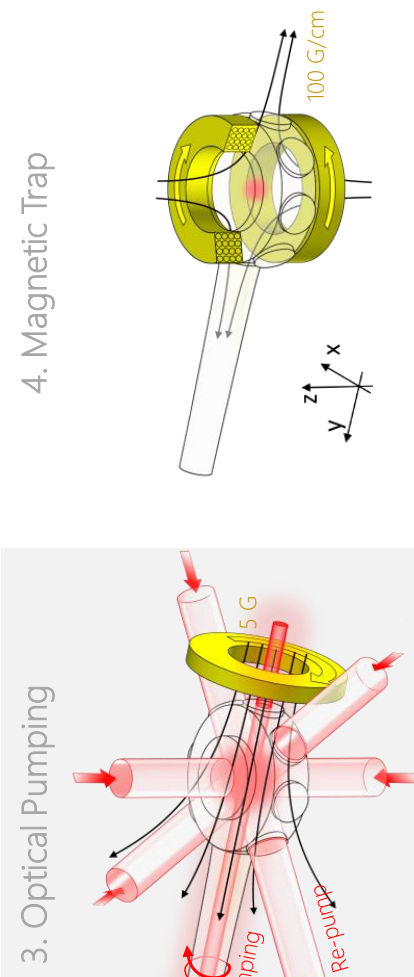
### 1. Magneto-optical-trap



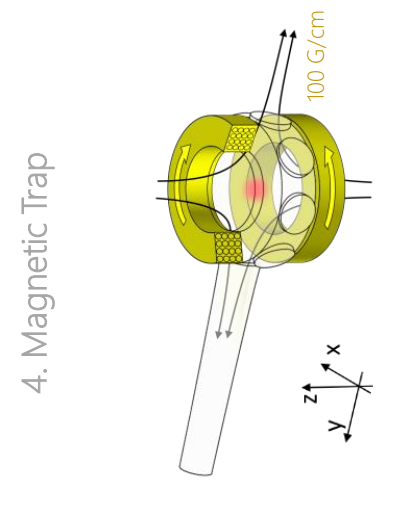
### 2. Optical Molasses



### 3. Optical Pumping



### 4. Magnetic Trap

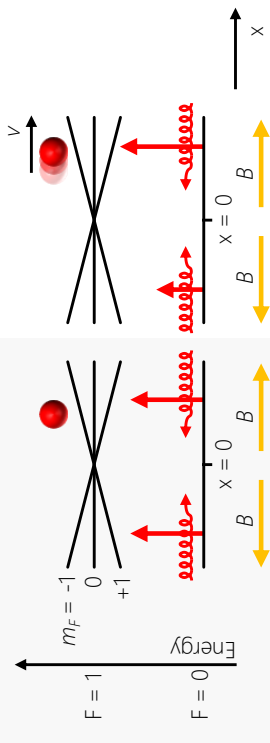


### Laser Cooling: Capturing and cooling a <sup>87</sup>Rb atoms from a background vapour.

1. **Magneto-optical-trap:** A combination of circularly polarized laser beams along each coordinate direction and a quadrupole magnetic field provide a position- and velocity-dependent trapping force. In practice, we use lasers  $\delta_0=25\text{MHz}$  detuned from the  $F=2 \rightarrow F=3$  transition, but the principle is best understood by considering a system with a simpler  $F=0 \rightarrow F=1$  transition. The detuning of the laser light from this transition has three contributions:

1. The static detuning,  $\delta_0$ , of the laser from the zero-field  $F=0 \rightarrow F=1$  transition.
2. The Doppler-shift,  $\mathbf{k} \cdot \mathbf{v}$ , due to the atoms' velocity.
3. The Zeeman-shift,  $g_F \mu_B B / \hbar$ , of the  $m_F = +1, 0, -1$  hyperfine levels.

The diagrams below illustrate the detuning of the lasers (red) from the atomic levels (black) for a stationary and moving atom:



For a *stationary* atom at  $x > 0$ , the  $|0,0\rangle \rightarrow |1,-1\rangle$  ( $\sigma^-$ ) transition is closest to resonance. We can arrange a restoring force by choosing circularly polarized light such that photons are preferentially scattered from the beam propagating in the  $-x$  direction. This restoring force provides a position-dependent trapping potential.

For atoms *moving* the  $+x$  direction, the beam propagating in the  $-x$  direction is blue-shifted towards resonance. This produces a velocity-dependent damping force which cools the trapped atomic cloud.

### Magnetic Trapping: Confining the atoms in a strong quadrupole magnetic field which splits the hyperfine levels ready for radio-frequency evaporation.

1. **Optical pumping:** Puts atoms in the magnetically trappable  $|2,2\rangle$  state by driving the  $\sigma^+$   $|F=2, m_F\rangle \rightarrow |F'=2, m_{F'}+1\rangle$  transition using circularly polarized light propagating along a quantization axis defined by a single coil. Atoms pumped into the excited states spontaneously decay back to the ground states to be pumped again until the population builds up in the dark  $|F=2, m_F=2\rangle$  state. Any atoms which decay into the  $F=1$  manifold are re-pumped back into the cycling transition by re-pump lasers resonant with  $|F=1\rangle \rightarrow |F'=2\rangle$ .

2. **Magnetic trapping:** The low-field-seeking  $|2,2\rangle$  state is confined by a strong quadrupole field.

With appropriately polarized beams in all 6 directions, the atoms are trapped and cooled in a 3D.

When cooling on the  $F=2 \rightarrow F=3$  transition, spontaneous emission to the  $F=1$  ground state is possible via higher order transitions. Atoms in the  $F=1$  level are brought back into  $F=2$  using re-pump light resonant with the  $F=1 \rightarrow F'=2$  transition.

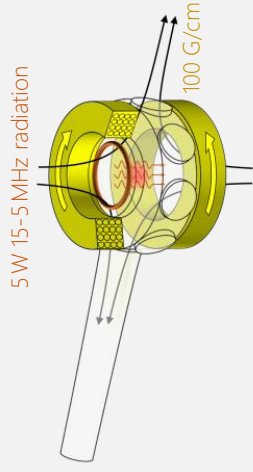
2. **Optical Molasses:** The quadrupole field is turned off and the cloud is allowed to cool in the presence of only the velocity-dependent damping force. Without the magnetic field, additional, 'sub-Doppler' cooling mechanisms (Sisyphus cooling) can significantly reduce the temperature of the cloud.

### Laser cooling limits:

1. **Doppler cooling limit:** Spontaneous emission at a rate given by the inverse excited state linewidth,  $\Gamma^{-1}$ , heats at a rate  $(\hbar k)^2 / (2m\Gamma)$ . Balancing this with the laser cooling damping rate  $(-\mathbf{F} \cdot \mathbf{v} \sim \mathbf{v} \cdot \mathbf{v})$  gives an equilibrium temperature of  $k_B T = \hbar / 2$  ( $\sim 150 \mu\text{K}$  for  $^{87}\text{Rb}$ ).
2. **Recoil limit:** Absorption/emission of photons only affects the atom's momentum in units of  $\hbar k$ . This discretisation gives a 'recoil limit' for laser cooling  $k_B T = (\hbar k)^2 / (2m)$  ( $\sim 200 \text{nK}$  for  $^{87}\text{Rb}$ ).

Evaporative cooling is used in later steps to beat the recoil limit

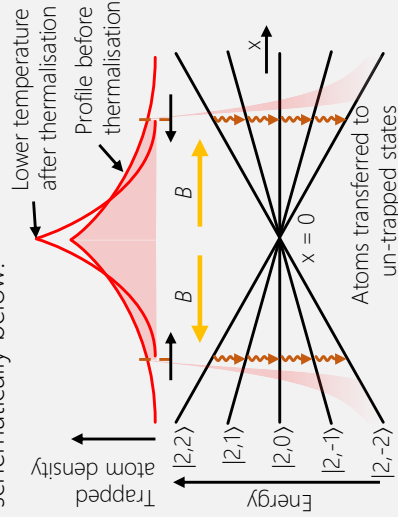
## 5. Radio-frequency Evaporation



### Radio-Frequency Evaporation:

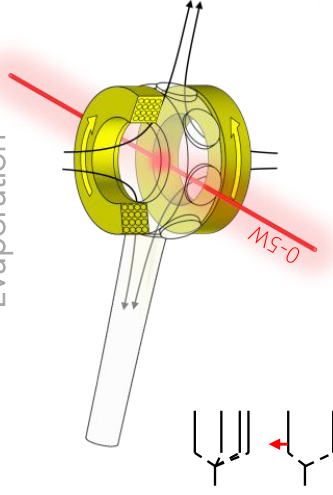
Removing the highest energy atoms to allow the remaining atoms to re-thermalise at a lower temperature.

Zeeman splitting of the  $F=2$  manifold in the quadrupole field allows us to address atoms in different regions of the trap by tuning the frequency of radio-wave radiation flooding the apparatus. By targeting the highest energy atoms (at large radius from the magnetic zero) and transferring them from the trapped  $|2,2\rangle$  state into un-trapped states, we allow the remaining atoms to re-thermalise at a lower temperature. This is illustrated schematically below:



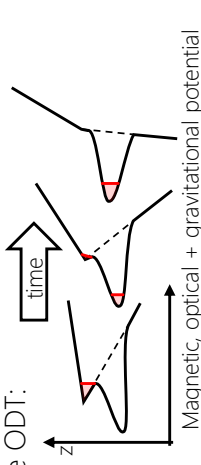
Sweeping the radiation from 15  $\rightarrow$  5 MHz in 2 s, cools the cloud to 90  $\mu$ K.

## 6. Hybrid-trap & Optical Evaporation



### Hybrid-trap & Optical Evaporation:

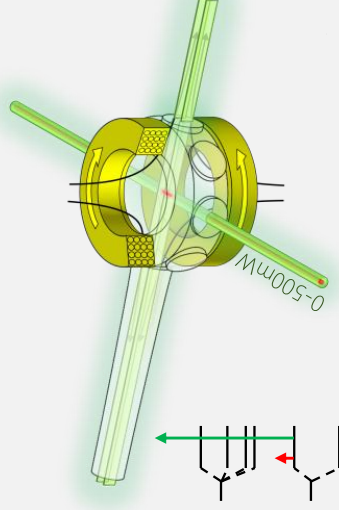
Majorana spin-flips occur at the quadrupole magnetic zero where the atom's spin (precessing at a vanishing Larmor frequency) cannot adiabatically follow the change in magnetic field direction. These flips eject low energy atoms dwelling near the magnetic zero. To cool below the  $\mu$ K level, we transfer the atoms into a single-beam (harmonic) optical dipole trap (ODT) far red-detuned (1070nm) from all resonances and positioned 60  $\mu$ m (1 optical waist) below the magnetic zero. Reducing the quadrupole field 'pours' the atoms into the ODT:



In the ODT, the atoms are confined along the beam by the residual 7.4 G/cm quadrupole field. Off axis this field provides an approximately harmonic potential with trapping frequency 30Hz.

**Optical Evaporation:** The ODT is ramped down from 5W exponentially over 7s. This evaporatively cools the gas, achieving condensation at 0.16W (2  $\mu$ K trap depth, 90Hz radial frequency)

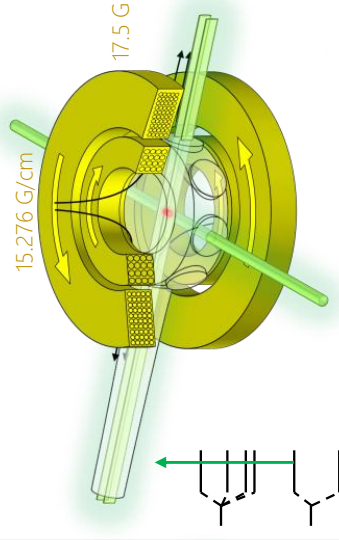
## 7. Uniform trap loading



### Uniform-trap Transfer atoms into and condense in novel trap geometry

**Trap loading:** 532 nm shaped uniform trap beams are ramped on as the ODT is ramped down. To release atoms into the box. A uniform bias field is added to the quadrupole field to create a uniform anti-

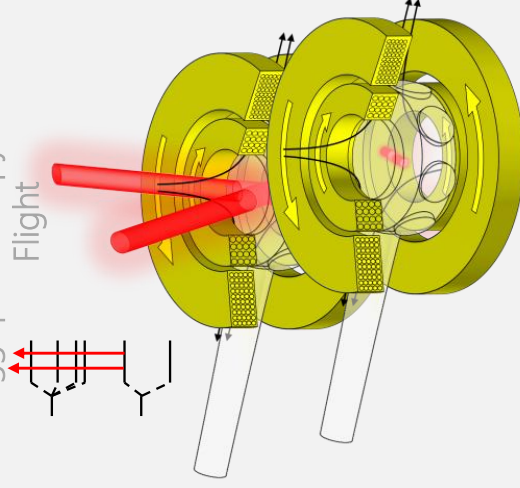
## 8. Uniform trap evaporation



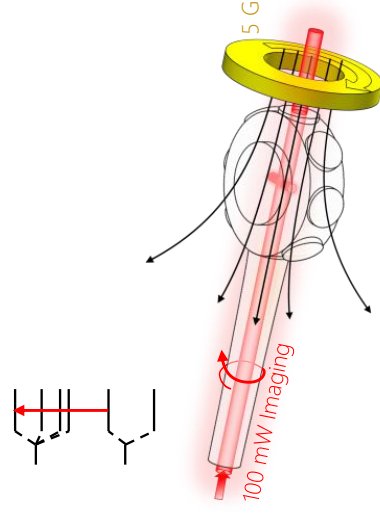
gravity magnetic field gradient 15.276 G/cm. **Optical evaporation:** The green laser power is ramped down exponentially over 2s to achieve condensation

See chapter 6

## 9. Bragg spectroscopy & Time-of-Flight



## 10. Absorption Imaging



### Query cloud properties via momentum distribution

Either by Bragg-spectroscopy (pure BEC) or time-of-flight (anti-gravity field left on)

See chapter 7

### Absorption Imaging

Circularly polarized light drives the  $\sigma^+$   $|2, 2\rangle \rightarrow |3, 3\rangle$  transition in the presence of a 5G guide field. A camera captures the shadow in the profile of the atoms as they absorb photons.



# Raster Holography

In Fig 5.7(b), we saw the Gerchberg-Saxton algorithm for generating raster holograms. The Gerchberg-Saxton algorithm calculates a phase hologram by linking the known moduli in the SLM and trapping planes through simulation of the light propagation back and forth between these planes. After each propagation, we manually impose the modulus constraints while leaving the phase to converge on the required solution. The convergence of this algorithm is problematic (see Fig. 5.8), and in this section, we describe improvements to this computational method, building on the work of Pasienski and DeMarco [103]. In addition, we present experimental results which indicate that the traps produced by our method are of sufficient quality to integrate into cold atom experiments.

## B.1 MRAF: Mixed-region amplitude freedom

To combat the fact that the Gerchberg-Saxton algorithm generally fails to converge correctly, Pasienski and DeMarco devised the MRAF algorithm. The idea of MRAF is to enhance convergence of the Gerchberg-Saxton algorithm in one region of the trapping plane by giving up control of the remaining regions [103–106]. More precisely, MRAF defines a "drawing"  $\mathcal{D}$  in the trapping plane containing all the points in which the desired potential is non-zero, and an additional "canvas" region,  $\mathcal{C}$ , of zero potential around the drawing (see Fig. 5.8). The modulus constraint is then manually imposed only inside  $\mathcal{C}$  and  $\mathcal{D}$  at each iterative step, thus reducing the number of constraints the algorithm aims to satisfy. It is hoped that with the additional freedom of amplitude outside  $\mathcal{C}$  the algorithm will correctly converge onto the desired diffraction pattern inside  $\mathcal{C}$  and  $\mathcal{D}$ . Meanwhile, a complex pattern of fringes and speckles develop in the unconstrained region outside  $\mathcal{C}$ ,

In the original MRAF paper, region  $\mathcal{C}$  is limited to a tight border around  $\mathcal{D}$  (with a typical width of  $\approx 1\%$  of the trapping region length scales). Although  $\mathcal{C}$  is a featureless region of zero potential, it is an integral part of the trap since it defines the zero to which all the pixels in  $\mathcal{D}$  are referenced. For practical purposes, such a small canvas can be a severe limitation because the fringes and speckles in the unconstrained region could greatly complicate the process of loading atoms into the desired region,  $\mathcal{D}$ . Therefore, our method aims to expand  $\mathcal{C}$  to approach its theoretical limit, which is set by Nyquist's theorem to be 25% of the area of the

simulated trapping plane<sup>1</sup>. In this large canvas regime, MRAF suffers the same fate as the Gerchberg-Saxton algorithm: convergence stagnates to produce poor solutions even after many iterations.

## B.2 Optical vortices

The reason for the failure of the MRAF algorithm in the extended canvas regime is the formation of large populations of optical vortices during the early iterations (approximately 1 vortex for every 10 pixels in Fig. B.2). Optical vortices are topological features of the light field corresponding to a phase winding around a point of zero intensity. Large vortex populations are problematic because individual vortices are difficult to eliminate in subsequent iterations of the algorithm. Unwinding a vortex requires global disruption of the hologram, which cannot be achieved in late iterations of Gerchberg-Saxton-type algorithms which monotonically reduce the mean square deviation from the target [184, 185]. Therefore any erroneous vortices are “frozen in” early on, and the algorithm gets stuck in a local optimum corresponding to a particular vortex distribution.

### B.2.1 Offset-MRAF

One possibility for handling vortices is by pairwise creation and annihilation, which requires only local operations; computational algorithms which encourage such pairwise operations are given in [186]. However, here we consider a much simpler solution. Our method simply offsets the trapping pattern inside  $\mathcal{C}$  and  $\mathcal{D}$  by a uniform intensity,  $|\Delta|^2$ , to remove all points of zero light intensity. This redefines the zero of the potential but does not change the physics of the trap. The aim is to ensure the phase of all points inside  $\mathcal{C}$  and  $\mathcal{D}$  is well defined for all iterations. If a point of zero intensity is generated, then the phase becomes ambiguous, and we risk forming a vortex in later iterations (see Fig. B.1). To ensure  $|\Delta|^2$  is sufficiently large to prevent vortex formation, we perform a single iteration of the algorithm and count the number of vortices produced. This first iteration starts from a parabolic phase hologram which defocuses the light into a vortex-free patch of characteristic size set by  $\mathcal{C}$ . We then gradually increase  $|\Delta|^2$  until a single iteration from this starting point does not introduce any vortices. We call this method of introducing an offset to prevent vortex formation the “offset-MRAF” (OMRAF) algorithm.

---

<sup>1</sup>The Nyquist argument proceeds as follows: An  $N \times N$  SLM plane can be fast-Fourier-transformed to an  $N \times N$  trapping plane with a diffraction limited spot size of exactly 1 pixel. The Nyquist limit states that the diffraction limit should be reduced to *half* a pixel (the smallest feature in the trap is 1 pixel). This can be achieved by padding the computer-simulated SLM plane with zeros to increase its size to  $2N \times 2N$ . This means that only 25% of the simulated SLM plane is covered by the physical SLM, so we can at best control only 25% of the trapping plane.

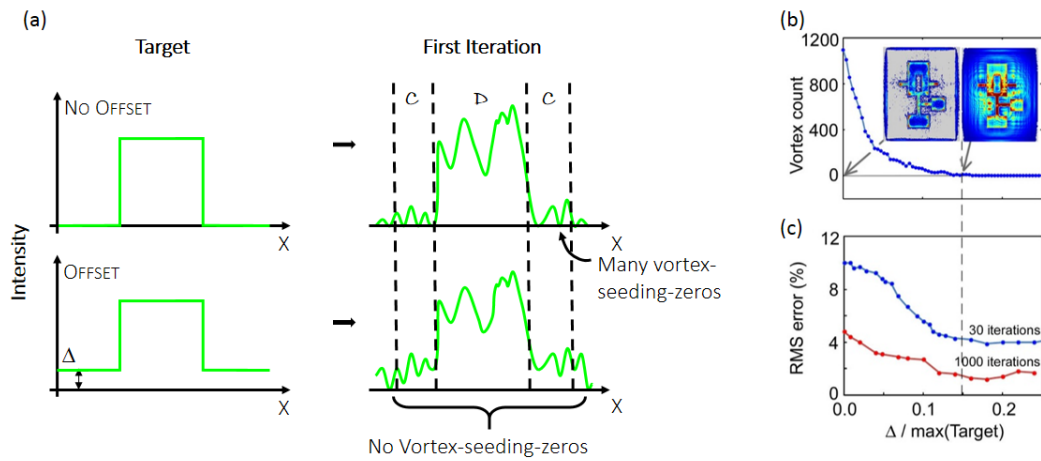


**Fig. B.1.:** Choosing the optimal offset intensity. (a) Clarification of the role of the offset as a means to eliminate vorticies and points of zero intensity which could develop into vortices. (b) The method for picking the optimal offset,  $\Delta$ , measured in units of the peak amplitude in the target pattern. We perform a single iteration of the algorithm, for different offsets, to produce patterns such as those shown in the insets. We then choose the lowest value of  $\Delta$  (indicated by the dashed line) which gives no vortices within  $\mathcal{C}$  or  $\mathcal{D}$  in this first iteration. (c) Improvement in the trap reconstruction associated with the offset.)

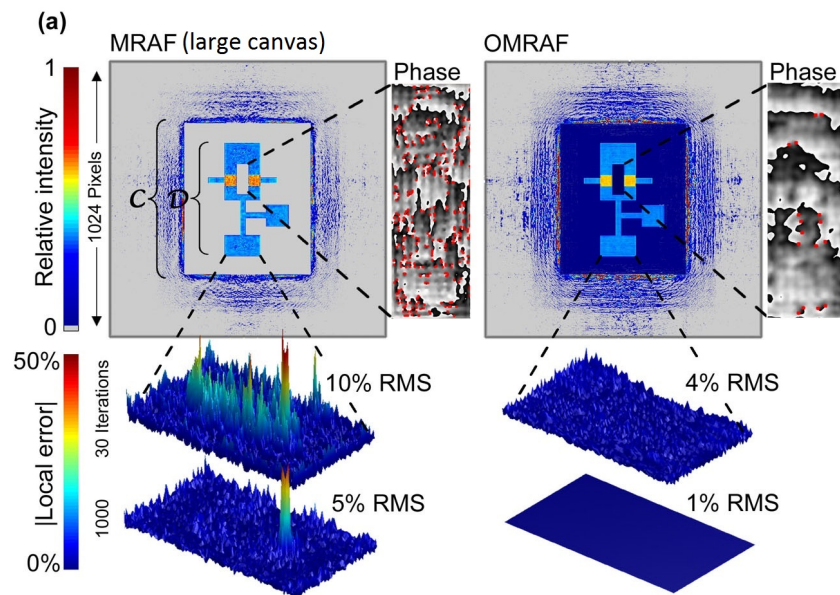


**Fig. B.2.:** Computational results for traps with a well defined zero potential background. We present reconstructions of the test trap with MRAF and OMRAF methods. We also show details of the local reconstruction error (bottom insets) and the local phase (right insets). In the phase plots (obtained after 30 iterations) we use black to white to represent 0 to  $2\pi$  and red dots to mark vortex cores.

For maximum light-usage efficiency, we want to minimise the proportion of the incident light which is steered into the featureless background, i.e. choose the minimal  $|\Delta|$  which gives satisfactory results. We find that for all the patterns we tested a suitable offset was  $|\Delta| \sim 10-15\%$  of the maximum amplitude in the trapping plane (i.e.  $|\Delta|^2 \sim 1\%$  of the maximum intensity). A computational simulation of the trapping potential produced using the OMRAF algorithm is shown in Fig. B.2. Our method reduces the number of vortices seen in  $\mathcal{C}$  after 30 iterations by a factor of  $\sim 20$  compared to MRAF in the large-canvas limit. This allows excellent convergence of the algorithm, leaving only 4% RMS error between the desired trap and the OMRAF result after 30 iterations and 1% RMS after 1000.

### B.2.2 Efficiency

One compromise associated with the OMRAF method is a reduction in the efficiency of light use. We define efficiency as the ratio of the integral of the trap intensity above the background offset to the total integral across the trapping plane. Including the non-zero  $\Delta$  causes a drop in efficiency by a factor of approximately 2 relative to MRAF, from 43% to 24%, for the trap shape shown in Fig. B.2. Nevertheless, our method remains more efficient than intensity-masking methods such as [187], which report 3% efficiency for simple patterns. We calculate that for more complex patterns such as our test trap shape, intensity masking would be less than 1% efficient.

## B.3 Experimental realisation with laser light

We test our OMRAF algorithm experimentally by producing light patterns using 532 nm laser light in the arrangement shown in Fig. 5.2. Throughout this section, we use the following techniques to improve the quality of our final traps:

- We use the standard SLM-based Shack-Hartmann algorithm [188] to correct for the low spatial frequency phase aberrations in the optical system and characterise our input laser beam.
- We use an active feedback algorithm [8] to optimise the final experimental patterns. This feedback routine is essential to remove the “sinc envelope” caused by the pixellation of the SLM, which would otherwise globally modulate the intensity pattern.
- Finally, in practice, we find that when we try to produce experimental patterns with  $\mathcal{C}$  covering the maximum theoretically permitted area (25% of the trapping plane), we cannot achieve patterns with less than 20% RMS fluctuations. This

is significantly improved in the results presented below by reducing  $\mathcal{C}$  to cover only 10% of the trapping plane.

Unfortunately, even with these precautions, we are not immediately able to generate traps with the low RMS errors predicted by our simulations. Below we suggest a further improvement which leads to traps of sufficient quality to consider integration into cold atom experiments.

## B.4 Fourier vs Helmholtz

In the previous section, we presented computational results generated under the paraxial approximation in which the propagator mapping the light in the SLM plane to the trapping plane is given by a scaled Fourier transform. Using this approach in our experiments with an  $f = 200$  mm lens, we are able to produce a trapping pattern with RMS error of  $\approx 11\%$  (see Fig. B.3). As highlighted in Fig. B.3(b), the most prominent form of error is semi-regular fringing. We suggest that the source of this error is the inadequacy of the paraxial approximation, and we use a numerical Helmholtz solver to test this hypothesis.

The Helmholtz equation for light propagation in free space gives that the Fourier transform of a light field,  $E(\mathbf{x}; z)$ , is modified by a phase factor  $\Theta(\xi; z)$  as it propagates in the  $+z$  direction [87]:

$$\mathcal{F}[E(\mathbf{r}; 0); \xi] = \mathcal{F}[E(\mathbf{r}; z); \xi] \underbrace{\exp\{ikz\sqrt{1 - (\lambda\xi)^2}\}}_{\Theta(\xi; z)}, \quad (\text{B.1})$$

where  $\mathcal{F}[g(\mathbf{r}); \xi]$  denotes the Fourier transform (FT) of  $g$ , making the Fourier variable pairing  $\mathbf{r} \leftrightarrow \xi$  explicit, and  $k = 2\pi/\lambda$  denotes the wave vector of the light. The routine for propagation of  $E_0$  via the apparatus in Fig. 5.2 can then be conceptually decomposed into 3 stages:

$$\begin{aligned} \text{"Propagate FT from SLM to lens"} & \quad \psi_1(\xi) = \mathcal{F}[E_0(\mathbf{r}); \xi] \Theta(\xi; f) \\ \text{"Apply Lens in Fourier space"} & \quad \psi_2(\eta) = [\psi_1 \otimes \tilde{L}](\eta) \\ \text{"Propagate FT to trapping plane"} & \quad \psi_3(\eta) = \psi_2(\eta) \Theta(\eta; f) \end{aligned}$$

$$\text{Then:} \quad \mathcal{P}_{\text{Helmholtz}}[E_0(\mathbf{r}); \mathbf{R}] = \mathcal{F}^{-1}[\psi_3(\eta); \mathbf{R}], \quad (\text{B.2})$$

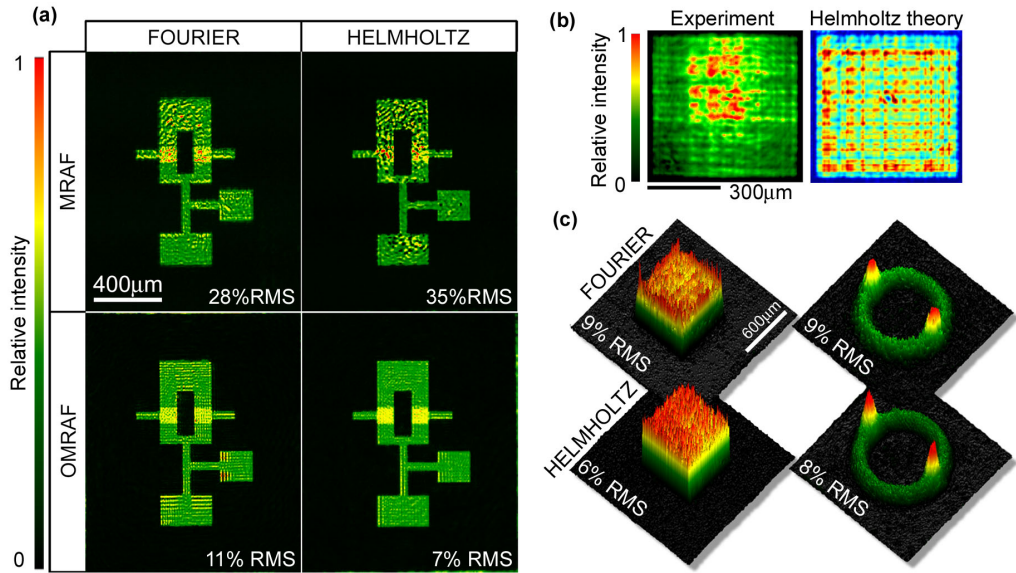


**Fig. B.3.:** Experimental results with 532 nm laser light. (a) Experimental patterns based on four different computational methods (for display we crop the trapping plane around region  $\mathcal{C}$ ). We observe low quality traps with the MRAF algorithm, and we are unable to improve them by adjusting the propagator (indeed, in this high RMS error regime, the additional complexity of the Helmholtz propagator can be detrimental). However, incorporating a Helmholtz propagator into our OMRAF algorithm allows us to produce the test pattern with only 7% RMS error. (b) Illustrates the need for a beyond-paraxial propagator. The left panel shows an experimental pattern based on OMRAF calculation under the paraxial approximation. The right panel shows that similar fringing is reproduced when the same paraxial kinoform is fed into a Helmholtz propagator to simulate the experiment. (c) To test the universality of our method, we also show experimental OMRAF patterns cropped to the boundary of  $\mathcal{C}$  for a uniform square trap and an annular BEC stirrer [8, 103].

where  $\mathcal{P}_{\text{Helmholtz}}$  represents the overall Helmholtz propagator,  $\otimes$  represents convolution, and  $\tilde{L}$  represents the FT of the phase pattern imprinted by the lens, which, after aberration correction, we assume to be:

$$\tilde{L}(\xi) \approx \mathcal{F} \left[ \exp \left( \frac{ikr^2}{2f} \right); \xi \right]. \quad (\text{B.3})$$

To show that the Helmholtz propagator is required, we use the OMRAF algorithm under the Fourier approximation to produce a “Fourier-generated” kinoform, and then input this kinoform into our numerical Helmholtz propagator to simulate the experimental apparatus. This indeed produces the fringing pattern similar to that observed experimentally, which gives us confidence to continue with the Helmholtz method (Fig. B.3(b)). We thus replace all instances of the Fourier propagator in the OMRAF algorithm with a Helmholtz propagator. In this way, we are able to eliminate the erroneous fringing, and reduce the RMS error of the experimental pattern to 7%. As shown in Fig. B.3, we can produce other trap shapes with similar fidelity. Thus, even for traps with sharp edges and an extended canvas region, we achieve RMS variation comparable to the 4% fluctuations previously seen only for simple

smooth traps with negligible canvas [8]. In [189], it has already been shown that 5% RMS errors are sufficiently low for superfluid circuit and atomtronic applications. We therefore believe that our methods show great promise for future applications.



# Graphics Card Acceleration of Computations for Ultracold Atom Experiments

Computers play a central role in almost every aspect of a cold atom experiment. In particular, there are two large computational jobs:

- *Data Analysis*: The amount of data produced by the experimental machines is intractable without a concerted computational effort
- *Physical Simulations*: Often even "simple" calculations (e.g. determination of the ToF profile after release from a uniform trap in Fig. 7.6) must be performed numerically.

These applications generally require a large number of relatively simple operations to be performed on a large data set. Such tasks are ideally suited to a graphical-processing-unit (GPU), which can be visualised as a large team of very basic processors which all operate concurrently on separate parts of the data set (see Fig. C.1). In the sections below we will give one example from each two categories above in which the use of a GPU has had a significant impact.

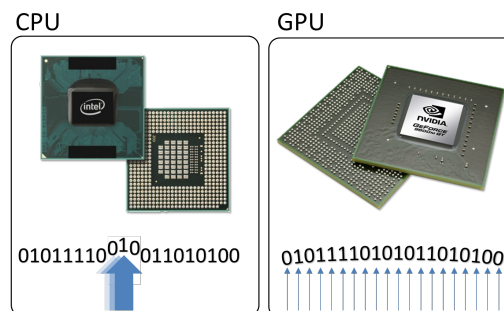


**Fig. C.1.:** Comparison of a computer's central-processing-unit (CPU) and graphical-processing-unit (GPU). The CPU can be visualised as running a heavy-duty thread sequentially through the data to be processed, whereas a GPU uses multiple light-weight threads running in parallel on different parts of the data.

## C.1 Image processing: AnalysisGpUI

A typical project may require upwards of  $10^5$  experimental runs from the first planning stages to the final publication. This corresponds to approximately 1TB of raw data in the form of camera images which need to be processed. Image processing is not only required in the final stages of data analysis: more often, image processing must be performed instantaneously while the machine is running such that an optical component or machine setting can be adjusted with near real-time feedback. For this reason, we harness massively parallel GPU for rapid processing of experimental images. In particular, we usually want to fit a theoretical model to the atomic profile in the images in order to extract atom numbers and temperatures. This requires an efficient technique for non-linear least-squares fitting, as discussed in the next section.

### GPU Levenberg-Marquardt least squares fitting

A GPU based Levenberg-Marquardt non-linear least-squares solver library<sup>1</sup> was written and embedded in a user friendly interface<sup>2</sup> shown in Fig. C.2 (note that the software name, AnalysisGpUI, is a play on the acronyms GPU and GUI (graphical-user-interface)). The Levenberg-Marquardt algorithm finds the parameter set  $\beta$  for a model function  $f_i(\beta)$  which minimizes the sum of the square deviation from data  $y_i$  over all points,  $i$ :  $\arg \min_{\beta} (\sum_i |y_i - f_i(\beta)|^2)$ . This algorithm proceeds by iteratively solving for an improved parameter set  $\beta' = \beta + \delta$  given by:

$$[\mathbf{J}^T \mathbf{J} + \lambda \text{diag}(\mathbf{J}^T \mathbf{J})] \delta = \mathbf{J}^T [\mathbf{y} - \mathbf{f}(\beta)] \quad (\text{C.1})$$

where  $J_{ij} = \partial f_i / \partial \beta_j$ ,  $\text{diag}(\mathbf{M})$  indicates the square matrix constructed from the diagonal of  $\mathbf{M}$ , and  $\lambda$  is a tuning parameter which is decreased when the computer detects it is approaching convergence. Solving Eq. C.1 is not computationally demanding (the dimension of the matrices is equal to the number of fitting parameters in the set  $\beta$ ). However, constructing the objects (particularly  $\mathbf{J}^T \mathbf{J}$ ) in this expression from the experimental images can require a very large number ( $\sim 10^{10}$ ) of very basic floating point operations per image. This is where we can profit from the parallel GPU architecture.

---

<sup>1</sup>Written in CUDA/C++

<sup>2</sup>Written in C#/OpenGL

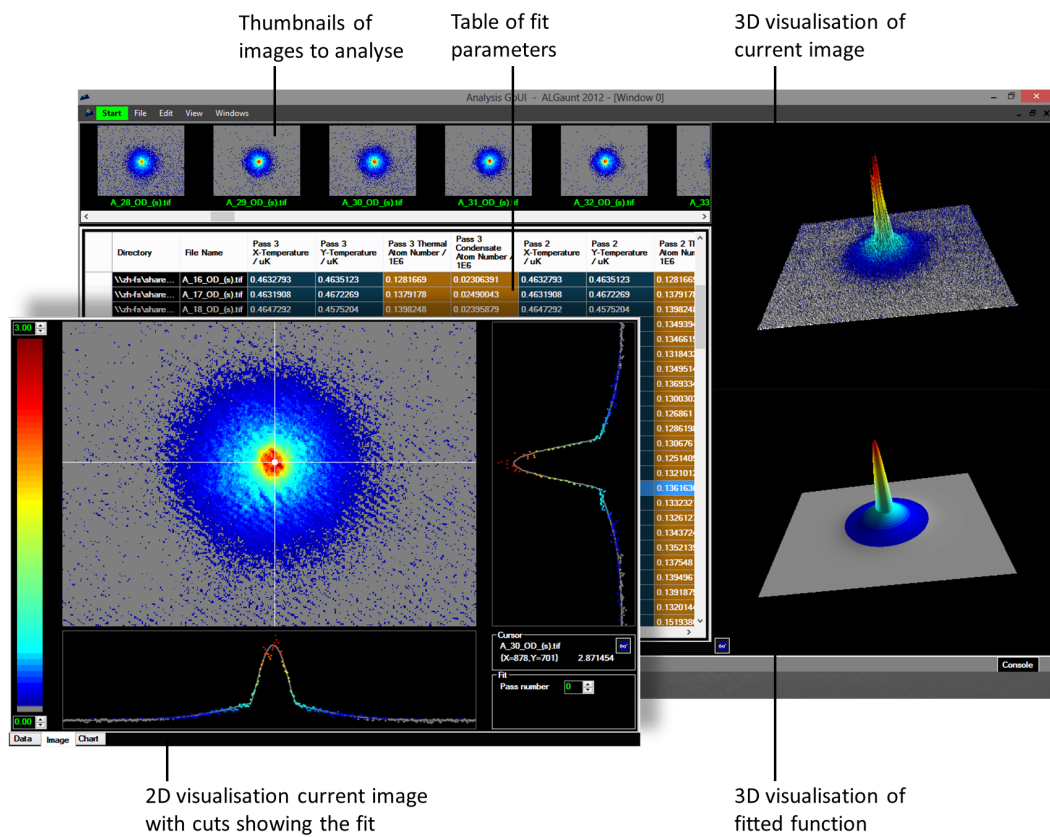
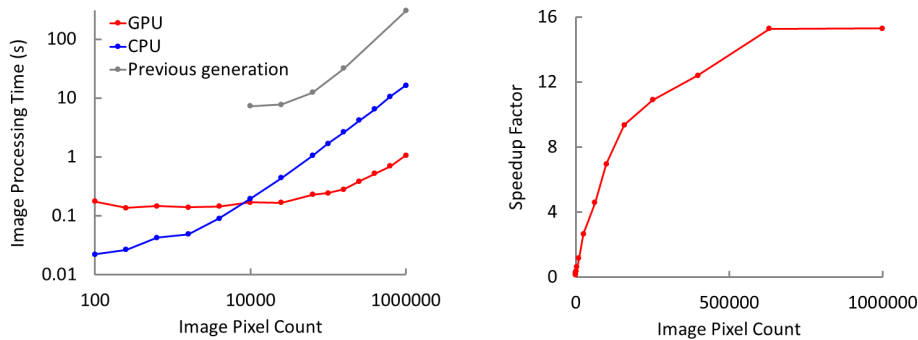


Fig. C.2.: AnalysisGpUI user interface.



**Fig. C.3.:** Performance analysis of our GPU algorithm. (a) Image processing time as a function of image size. The 0.1 s GPU initialisation time per image makes it slower than the CPU for very small tasks, but (b) the GPU is up to  $\times 16$  faster than the CPU for large tasks in our test rig.

### GPU performance

In Fig. C.3, we compare the performance of our GPU implementation with the same code running on a CPU (we also compare the speed to a previous-generation MATLAB-based fitting software [26]). The hardware used for this comparison was:

	Memory Bandwidth	Peak giga-FLOPS
CPU (Intel Core 2 Duo T9400)	3.2 GB/s	20
GPU (NVIDIA GeForce 9600M GT)	25.6 GB/s	120

As expected, the GPU performs much better than the CPU for large problem sizes, with a speedup of up to  $16\times$ . Since performing this benchmark test, we have upgraded to an NVIDIA GTX 550Ti card which provides up to  $64\times$  speedup, and the fitting process is now primarily limited by the process of loading the image file from the network.

## C.2 Physical simulation: EvolveGPuE

Throughout this thesis, there have been several occasions when we have had to resort to numerical simulations to make a quantitative comparison with experiments (see e.g. Fig. 7.6 and 7.10). Here we will briefly outline how these simple simulations of pure condensates can be quickly performed on a graphics card.

We consider a condensate described by the classical field  $\psi(\mathbf{x}, t)$  in the Gross-Pitaevskii equation (GPE):

$$i\hbar \frac{\partial \psi}{\partial t} = \left[ \underbrace{-\frac{\hbar^2}{2m} \nabla^2}_{\hat{H}_{\text{Kin}}} + \underbrace{U(\mathbf{r}, t) + V_0 |\psi|^2}_{\hat{H}_1} \right] \psi \quad (\text{C.2})$$

The formal solution to this equation is [190]:

$$\begin{aligned} \psi(\mathbf{r}, t + \Delta t) &= \exp\left(-\frac{i\Delta t}{\hbar} (\hat{H}_{\text{Kin}} + \hat{H}_1)\right) \psi(\mathbf{r}, 0) \\ &= \underbrace{\exp\left(-\frac{i\Delta t}{2\hbar} \hat{H}_1\right)}_{\hat{X}} \underbrace{\exp\left(-\frac{i\Delta t}{\hbar} \hat{H}_{\text{Kin}}\right)}_{\hat{K}} \underbrace{\exp\left(-\frac{i\Delta t}{2\hbar} \hat{H}_1\right)}_{\hat{X}} \psi(\mathbf{r}, t) + \mathcal{O}(\Delta t^3) \end{aligned} \quad (\text{C.3})$$

Where in the last line we will drop commutators scaled by  $\sim \Delta t^3$  and higher. Since  $\hat{X}$  is diagonal in position space ( $\hat{X}f(\mathbf{x}) = X(\mathbf{x})f(\mathbf{x})$ ) and  $\hat{K}$  is diagonal in momentum space ( $\hat{K}f(\mathbf{p}) = K(\mathbf{p})f(\mathbf{p})$ ), we can perform appropriate (scaled) Fourier transforms to write Eq. C.3 in a form which can be calculated on a computer:

$$\psi(\mathbf{x}, t + \Delta t) = X(\mathbf{x}) \times \mathcal{F}^{-1} [K(\mathbf{p}) \times \mathcal{F} [X(\mathbf{x}) \times \psi(\mathbf{x}, t)]], \quad (\text{C.4})$$

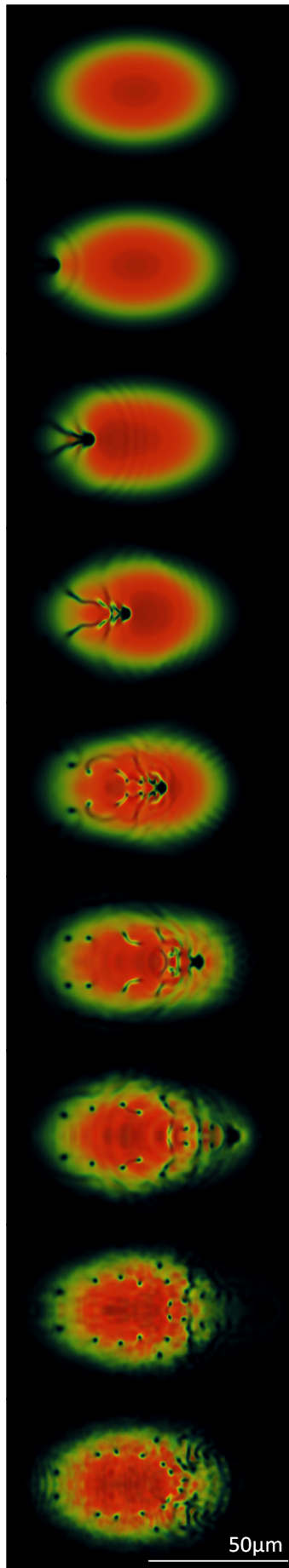
where  $\mathcal{F}$  denotes an appropriately scaled Fourier transform to map from position to momentum space.

Note that if we choose an imaginary value for  $\Delta t$ , Eq. C.3 describes the decay of all excited components of  $\psi$  in imaginary time, and  $\psi(\mathbf{r}, t)$  asymptotes to the ground state of the system. Therefore, to simulate the time-of-flight dynamics of an equilibrium system, we start with any  $\psi(\mathbf{x}, 0)$  which has finite overlap with the ground state and propagate in-trap in imaginary time until the system converges on the ground state. Then we release the trap and propagate in real time.

### The GPE on a GPU

We simulate the GPE with arbitrary  $U(\mathbf{r}, t)$  using our program `Evo1veGPuE` (a play on the acronyms GPU and GPE) to perform the parallelisable operations highlighted in blue in Eq. C.4 on the GPU. Since we are often interested in watching the dynamical evolution of our system (e.g. in ToF or as a response to a change of trap geometry), `Evo1veGPuE`, is purpose-built to display  $\psi(\mathbf{r}, t)$  immediately as it is calculated (see

**Fig. C.4:** An example dynamical simulation. A cylindrical obstacle is dragged at  $\approx 1$  mm/s through an anisotropic harmonically trapped cloud with trapping frequencies of approximately 60, 14 and 9 Hz in the three coordinate directions. The cloud contains  $5 \times 10^5$   $^{87}\text{Rb}$  atoms. Snapshots of the cloud are illustrated every 15 ms showing the development of quantized vortices (seen as tubes of zero density) in the wake of the object. This simulation is carried out on a  $256 \times 256 \times 256$  grid, and with a time discretisation of  $\Delta t = 0.04$  ms, we obtain a simulation speed of 1.4 seconds per 1 ms of evolution.



e.g. Fig. C.4). Since an NVIDIA GTX 680 graphics card takes  $\sim 0.06$  s to calculate the update  $t \rightarrow t + \Delta t$  on a spatial grid of  $256 \times 256 \times 256$  points, the frame rate of the calculation is fast enough to play as a continuous movie as the calculation proceeds, and the user can interact with this movie by changing the camera angle to inspect the 3D cloud as it evolves (see real-time videos at [191, 192]). To ensure that the dynamically updating display does not significantly slow down the calculation, the calculation is done directly in part of the GPU's memory already belonging to the OpenGL display pipeline. This minimises the movement of the large array of numbers representing  $\psi$  in memory.

Note that a CPU based calculation is  $> 10$  times slower than our GPU calculation, and the overhead of transferring this data to the GPU for display makes it impractical to run a continuous movie of the CPU calculation in real time. The main limitation of our GPU solution is the limited graphical memory resources available. High end consumer graphics cards have up to 4 GB of RAM which (once the memory overheads of the fast-Fourier transform routine are subtracted) allows us to work with grid dimensions up to  $485^3$  (in this limit  $\psi \sim 1$  GB).

### Volumetric display of $\psi$

The calculation of  $\psi$  is performed in 3D, but the results must be displayed on the 2D screen. This is achieved by sampling the volume occupied by  $\psi$  on  $\approx 200$  equally spaced planes perpendicular to the viewing direction. The value of  $|\psi|^2$  is interpolated onto these planes and translated into a colour and transparency (denser regions being more opaque). The semi-transparent stack of planes is then rendered onto the screen one by one with the colours blending according to the transparency of the added plane. This gives the illusion of a semi-transparent cloud in 3D space (see Fig. C.5).

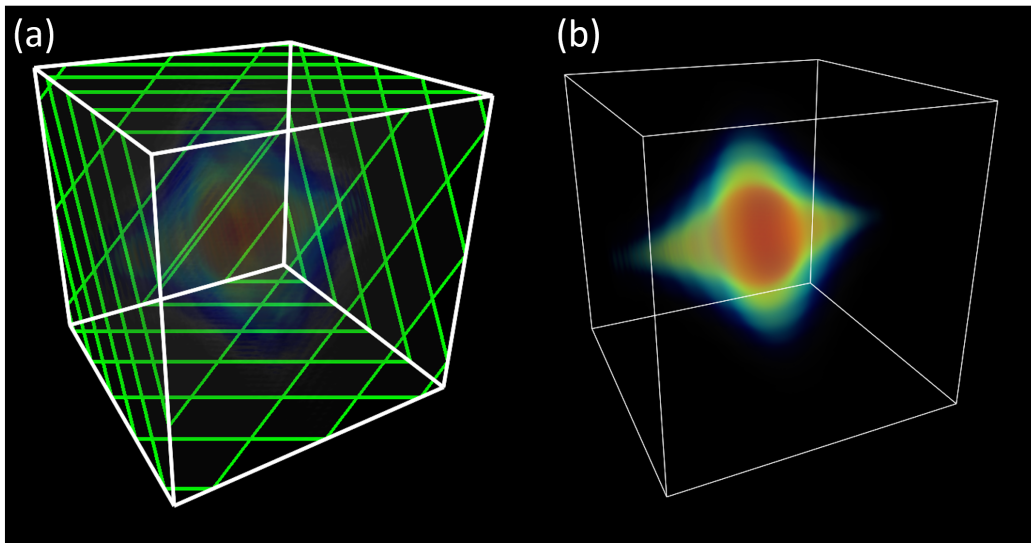


**Fig. C.5.:** Volumetric rendering of  $\psi$ . (a) The volume occupied by  $\psi$  is sampled by many equally spaced semi-transparent planes perpendicular to viewing direction (green - only 10 planes are shown). These planes are rendered one by one to the screen with the final pixel values being the accumulated colour and transparency. (b) When 200 planes are used, we see the illusion of a 3D cloud. The cloud shown here is the same as in Fig. 7.6 (50 ms ToF).

# Numerical Simulation of Kibble-Zurek Dynamics

Kibble-Zurek theory is deliberately very simple and very general, making only broad claims about the exponents of the power laws governing the frozen properties of a system as its dynamics slows near the critical point. To give definite numerical values to the microscopic length- and time-scales  $\lambda_0$  and  $\tau_0$  is certainly not in the spirit of the original formulation, and to claim that the KZ theory should capture anything but the most basic properties of the dynamical evolution of  $\xi$  near the critical point is incorrect.

Nevertheless, in this appendix, we will break these conventions and try to directly compare the KZ predictions to a simple numerical model of the system's dynamics near the critical point. Our motivation for performing this study is to assess the extent to which the non-linear form of our temperature quench, illustrated in Fig. 8.7, affects our interpretation of the experiment in chapter 8 where we evaluate parameters based on a linear KZ theory.

Since this section is an abuse of the intended purpose of KZ theory, there will be many questions which arise during the formulation of our dynamic model. These questions are highlighted in blue below, and it must be remembered that our answers to these questions are sensible but not rigorously justified. Although the assumptions are uncontrolled, we include the full details of our model here because it reproduces the KZ predictions remarkably well.

## D.1 Dynamical evolution of $\xi$

We are fundamentally interested in the size of phase coherent domains in our BEC, but critical phenomena are all phrased in terms of the correlation length  $\xi$ . Therefore, our first question is:

*Question 1: How does the correlation length on the approach to the critical point relate to the size of the BEC domains on the ordered side?*

We simply assume  $\xi(t_c) = d$ , and thus to evaluate  $d$  we must simulate the evolution of  $\xi$  up to the critical point. This evolution is governed by the relaxation timescale,

$\tau$ , however there is some question over the exact form of the dynamical equation linking  $\xi$  and  $\tau$ :

*Question 2: What is the functional form linking  $\xi/\dot{\xi}$  and  $\tau$ ?*

Here we assume a simple form inspired by the nomenclature "relaxation time".

$$\dot{\xi} = -\frac{\xi - \xi^{\text{eq}}}{\tau} \quad (\text{D.1})$$

where  $\xi^{\text{eq}} = \lambda_0 X |\epsilon|^{-\nu}$  and  $X = X_+$  for  $\epsilon > 0$  and  $X = X_-$  for  $\epsilon < 0$ . In equilibrium, the dynamical scaling hypothesis says that we can write down a "dispersion relation" between  $\tau^{\text{eq}}$  and  $\xi^{\text{eq}}$

$$\tau^{\text{eq}} = \tau_0 (\xi^{\text{eq}}/\lambda_0)^z \propto |\epsilon|^{-\nu z} \quad (\text{D.2})$$

Note that we were careful to include the critical amplitude ratio,  $X_{\pm}$ , in the expression for  $\xi$ , but we leave it as an open question whether there is such a ratio for  $\tau$ :

*Question 3: Is there a critical amplitude ratio associated with  $\tau$ ?*

When the system is far from equilibrium, it is not obvious that  $\tau = \tau^{\text{eq}}$ . Instead, it is possible that  $\tau$  is given by an extension of the dispersion relation to non-equilibrium scenarios:

$$\tau^{\text{dyn}} = \tau_0 (\xi/\lambda_0)^z \quad (\text{D.3})$$

These two possible definitions of  $\tau$  lead us to another question:

*Question 4: Is the relaxation dynamics governed by the distance to the critical point (i.e. by  $\tau = \tau^{\text{eq}}$ ) or by the instantaneous  $\xi$  and the non-equilibrium dispersion relation (i.e. by  $\tau = \tau^{\text{dyn}}$ )?*

We answer this question by noting that inserting the (finite)  $\tau^{\text{dyn}}$  into Eq. D.1 leads to  $\dot{\xi}/\xi \rightarrow \infty$  at the critical point, which is not in the spirit of a "critical slowing down". Therefore, we believe that the choice  $\tau = \tau^{\text{eq}}$  is more realistic. For interest we also show calculations with and  $\tau = \tau^{\text{dyn}}$  in Fig. D.1.

The full numerical model for a quench with a quadratic non-linearity matching our experimental cooling trajectory (see Fig. 8.8) is written explicitly below. For the

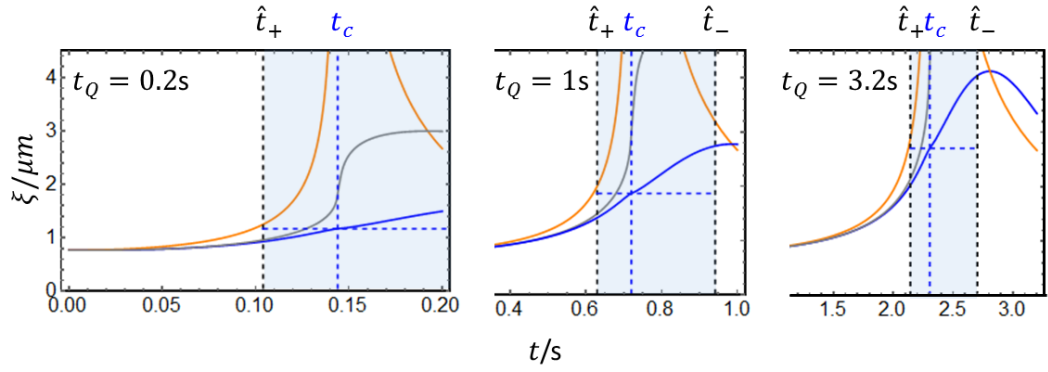


**Fig. D.1.:** Numerical simulations for the dynamics during a non-linear quench self similar to the example shown in Fig. 8.8. We show separate simulations for  $t_Q = 0.2$  s, 1 s and 3.2 s. The orange line shows  $\xi^{\text{eq}}$  and the blue line shows the dynamically evaluated  $\xi$  based on  $\tau^{\text{eq}}$  (for interest, we also show  $\xi$  evaluated base on  $\tau^{\text{dyn}}$  in gray). The vertical blue dashed line indicates  $t_c$  and the horizontal line marks  $\xi(t_c)$ . The frozen region is shaded blue. Note that  $\xi^{\text{eq}}(t_c - \hat{t}_+) = \xi(t_c)$  as expected from KZ theory.

purposes of illustration, we run the simulation with the F Model critical parameters. We have checked that inserting general  $\nu$  and  $z$  leads to consistent results.

Cooling trajectory	$\epsilon = -\frac{t-t_c}{\tau_Q^0} \left(1 - \gamma \frac{t-t_c}{t_Q}\right)$	$t_c = 0.72 t_Q$	$\tau_Q^0 = 0.41 t_Q$	$\gamma = 0.7$
Dynamical equations	$\dot{\xi} = -(\xi - \xi^{\text{eq}})/\tau^{\text{eq}}$	$\xi^{\text{eq}} = \lambda_0 X  \epsilon ^{-\nu}$	$\tau^{\text{eq}} = \tau_0 (\xi^{\text{eq}}/\lambda_0)^z$	
Freeze-out	$\left  \frac{\dot{\xi}^{\text{eq}}(\hat{t}_{\pm})}{\xi^{\text{eq}}(\hat{t}_{\pm})} \right  = \frac{1}{\tau^{\text{eq}}(\hat{t}_{\pm})}$	$d = \xi(t_c)$		
Critical Exponents	$\nu = 2/3$	$z = 3/2$	$X_+ = 1$	$X_+/X_- = 0.3$
Microscopics	$\lambda_0 = 0.7 \mu\text{m}$	$\tau_0 = 30 \text{ ms}$		

## D.2 Simulation results

The simulation produces a number of reassuring conclusions for our non-linear cooling curve which are briefly enumerated below:

- The model with no free parameters captures the size  $d$  of the domains measured in the experiment remarkably well (see Fig. D.2)
- The model correctly predicts  $t^{\text{br}} \approx 1$  s (see Fig. D.1)
- $\xi^{\text{eq}}(t_c - \hat{t}_+)$  is very close to the dynamical value  $\xi(t_c)$ , which numerically justifies the KZ hypothesis that the system's correlation length as it crosses the critical point is equal to the equilibrium correlation length at the freeze-out time.

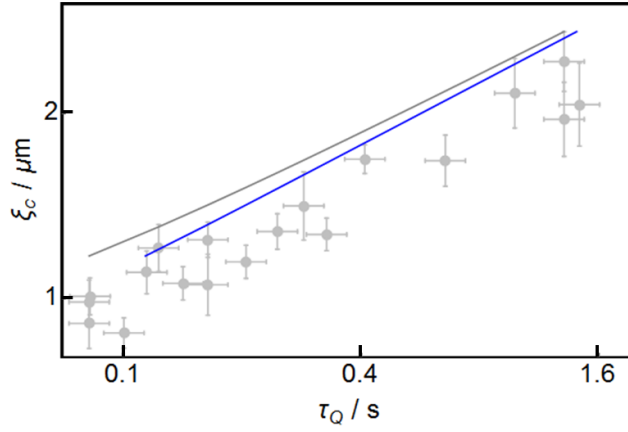


**Fig. D.2.:** The effect of calculating  $\tau_Q$  at  $t_c - \hat{t}_+$ . When we run the simulation and plot  $\xi(t_c)$  vs.  $\tau_Q$  evaluated at  $t_c$ , we obtain the gray line which is (i) not perfectly linear and (ii) gives a KZ exponent of  $0.94\nu/(1 + \nu z)$ . If we instead evaluate  $\tau_Q$  at  $t_c - \hat{t}_+$ , we obtain the blue line, which is (i) linear and (ii) gives  $b = \nu/(1 + \nu z)$ . To compare the absolute values of  $\xi(t_c)$  we plot the experimentally measured domain sizes as grey points. These points are shown "un-processed" (i.e. with  $\tau_Q$  evaluated at  $t_c$ ) for comparison with the grey line. Note that here we used  $\tau_0 = \tau_{e1} = 30$  ms and  $\lambda_0 = \lambda_c = 70$   $\mu\text{m}$ , which were independently estimated. The fact that the *absolute* values of the experimentally measured  $\ell$  are close to our prediction with no free parameters is remarkable because there could be several numerical factors of order 1 which we have omitted.

- For a linear quench ( $\gamma = 0$ ) we recover  $b = \nu/(1 + \nu z)$  to three digit precision
- For  $\gamma = 0.7$  (corresponding to our experiment) we only recover  $b = \nu/(1 + \nu z)$  when we evaluate  $\tau_Q$  at  $t_c - \hat{t}_+$ . Evaluating  $\tau_Q$  at  $t_c$  gives a strict lower bound on  $b$ .
- A power law fit to  $\tau_Q|_{t_c - \hat{t}_+}$  vs.  $t_Q$  gives  $\tau_Q|_{t_c - \hat{t}_+} \propto t_Q^{0.94}$  indicating that analysing the data with  $\tau_Q|_{t_c} \propto t_Q$  gives an underestimate of  $b$  by 6% (see Fig. D.2).

One surprising prediction from our simulation is the observation that  $\xi$  continuously evolves during the "frozen" period. This is in contradiction with a literal interpretation of the KZ freezing hypothesis, and also in contradiction with the plateau observed in the experimentally measured value of  $d$  after  $t_c$  (see Fig. 8.9). We suggest that this contradiction could be due to the fact that the experiment measures the phase coherence length and not the correlation length. Although we assume that the coherence length is set by the correlation length at the critical point it does not necessarily evolve in the same way as the correlation length. This can be particularly seen in the long-time limit where the coherence length will increase as the system unfreezes and cools further, while the correlation length of the fluctuations will reduce. Since the evolution of the coherence length is not captured by our model, it is surprising that the experimental breakdown time  $t^{\text{br}} = 1$  s is still approximately consistent with the quench time for which  $t_c + \hat{t}_- = t_Q$  in our simulation. The fact that

the simulation correctly predicts  $t^{\text{br}}$  gives us some reassurance that  $\hat{t}_-$  calculated from Eq. 8.25 is a relevant unfreezing time for the KZ theory.

In conclusion, although there are still many open questions, this simulation produces results which are reassuringly similar to the experimental values. Most importantly, it justifies our analysis of the data when extracting critical exponents in chapter 8.



# Bibliography

- [1] Feynman RP. Simulating physics with computers. *Int J Theor Phys* **21**, 467–488 (1982).
- [2] Bloch I, Dalibard J, Nascimbène S. Quantum simulations with ultracold quantum gases. *Nature Phys* **8**, 267–276 (2012).
- [3] Pethick CJ, Smith H. *Bose-Einstein condensation in dilute gases* (Cambridge University Press, 2002).
- [4] Smith RP, Hadzibabic Z. Effects of interactions on Bose-Einstein condensation of an atomic gas. In: Bramati A, Modugno M, editors, *Physics of Quantum Fluids* (Springer Berlin Heidelberg, 2013), volume 177 of *Springer Series in Solid-State Sciences*. pp. 341-359.
- [5] Lin YJ, Compton R, Perry A, Phillips W, Porto J, et al. Bose-Einstein condensate in a uniform light-induced vector potential. *Phys Rev Lett* **102**, 130401 (2009).
- [6] Lin YJ, Compton RL, Jimenez-Garcia K, Porto JV, Spielman IB. Synthetic magnetic fields for ultracold neutral atoms. *Nature* **462**, 628–632 (2009).
- [7] Lin YJ, Compton RL, Jiménez-García K, Phillips WD, Porto JV, et al. A synthetic electric force acting on neutral atoms. *Nature Phys* **7**, 531–534 (2011).
- [8] Bruce GD, Mayoh J, Smirne G, Torralbo-Campo L, Cassetari D. Smooth, holographically generated ring trap for the investigation of superfluidity in ultracold atoms. *Phys Scripta* **T143**, 8 (2010).
- [9] Moulder S, Beattie S, Smith RP, Tammuz N, Hadzibabic Z. Quantized supercurrent decay in an annular Bose-Einstein condensate. *Phys Rev A* **86**, 013629 (2012).

- [10] Beattie S, Moulder S, Fletcher RJ, Hadzibabic Z. Persistent currents in spinor condensates. *Phys Rev Lett* **110**, 025301 (2013).
- [11] Bloch I. Ultracold quantum gases in optical lattices. *Nature Phys* **1**, 23–30 (2005).
- [12] Bakr WS, Peng A, Tai ME, Ma R, Simon J, et al. Probing the superfluid–to–Mott insulator transition at the single-atom level. *Science* **329**, 547–550 (2010).
- [13] Uehlinger T, Jotzu G, Messer M, Greif D, Hofstetter W, et al. Artificial graphene with tunable interactions. *arXiv:13084401* (2013).
- [14] Foot C. *Atomic physics* (Oxford University Press, 2008).
- [15] Landau L, Lifshitz E. *Quantum Mechanics* (Elsevier, 2007), 3 edition.
- [16] Dalibard J. Collisional dynamics of ultra-cold atomic gases. In: Proceedings of the International School of Physics-Enrico Fermi. volume 321 (1999).
- [17] Inouye S, Andrews M, Stenger J, Miesner HJ, Stamper-Kurn D, et al. Observation of Feshbach resonances in a Bose–Einstein condensate. *Nature* **392**, 151–154 (1998).
- [18] Köhler T, Góral K, Julienne PS. Production of cold molecules via magnetically tunable Feshbach resonances. *Rev Mod Phys* **78**, 1311 (2006).
- [19] Chin C, Grimm R, Julienne P, Tiesinga E. Feshbach resonances in ultracold gases. *Rev Mod Phys* **82**, 1225 (2010).
- [20] Roati G, Zaccanti M, D’Errico C, Catani J, Modugno M, et al.  $^{39}\text{K}$  Bose-Einstein condensate with tunable interactions. *Phys Rev Lett* **99**, 010403 (2007).
- [21] De Sarlo L, Maioli P, Barontini G, Catani J, Minardi F, et al. Collisional properties of sympathetically cooled  $^{39}\text{K}$ . *Phys Rev A* **75**, 022715 (2007).
- [22] D’Errico C, Zaccanti M, Fattori M, Roati G, Inguscio M, et al. Feshbach resonances in ultracold  $^{39}\text{K}$ . *New J Phys* **9**, 223 (2007).
- [23] Zaccanti M, Deissler B, D’Errico C, Fattori M, Jona-Lasinio M, et al. Observation of an Efimov spectrum in an atomic system. *Nature Phys* **5**, 586–591 (2009).

- [24] Campbell RL, Smith RP, Tammuz N, Beattie S, Moulder S, et al. Efficient production of large  $^{39}\text{K}$  Bose-Einstein condensates. *Phys Rev A* **82**, 063611 (2010).
- [25] Campbell RL. *Thermodynamic Properties of a Bose Gas with Tuneable Interactions*. Ph.D. thesis, University of Cambridge (2011).
- [26] Tammuz N. *Thermodynamics of Ultracold  $^{39}\text{K}$  Atomic Bose Gases With Tuneable Interactions*. Ph.D. thesis, University of Cambridge (2011).
- [27] Ruprecht P, Holland M, Burnett K, Edwards M. Time-dependent solution of the nonlinear Schrödinger equation for Bose-condensed trapped neutral atoms. *Phys Rev A* **51**, 4704 (1995).
- [28] Gerton JM, Strekalov D, Prodan I, Hulet RG. Direct observation of growth and collapse of a Bose–Einstein condensate with attractive interactions. *Nature* **408**, 692–695 (2000).
- [29] Donley EA, Claussen NR, Cornish SL, Roberts JL, Cornell EA, et al. Dynamics of collapsing and exploding Bose–Einstein condensates. *Nature* **412**, 295–299 (2001).
- [30] Landini M, Roy S, CarcagníL, Trypogeorgos D, Fattori M, et al. Sub-doppler laser cooling of potassium atoms. *Phys Rev A* **84**, 043432 (2011).
- [31] Landini M, Roy S, Roati G, Simoni A, Inguscio M, et al. Direct evaporative cooling of  $^{39}\text{K}$  atoms to bose-einstein condensation. *Phys Rev A* **86**, 033421 (2012).
- [32] Salomon G, Fouché L, Wang P, Aspect A, Bouyer P, et al. Gray molasses cooling of  $^{39}\text{K}$  to a high phase-space density. *arXiv:13104014* (2013).
- [33] Moulder S. *Persistent Currents in Bose-Einstein Condensates*. Ph.D. thesis, University of Cambridge (2013).
- [34] Griffin A, Nikuni T, Zaremba E. *Bose-condensed gases at finite temperatures* (Cambridge University Press, 2009).
- [35] Fedichev P, Shlyapnikov G, Walraven J. Damping of low-energy excitations of a trapped Bose-Einstein condensate at finite temperatures. *Phys Rev Lett* **80**, 2269 (1998).
- [36] Monroe CR, Cornell EA, Sackett CA, Myatt CJ, Wieman CE. Measurement of Cs-Cs elastic scattering at  $T = 30 \mu\text{K}$ . *Phys Rev Lett* **70**, 414–417 (1993).

- [37] DeMarco B, Bohn JL, Burke JP, Holland M, Jin DS. Measurement of  $p$ -wave threshold law using evaporatively cooled fermionic atoms. *Phys Rev Lett* **82**, 4208–4211 (1999).
- [38] Smith RP, Beattie S, Moulder S, Campbell RL, Hadzibabic Z. Condensation dynamics in a quantum-quenched Bose gas. *Phys Rev Lett* **109**, 105301 (2012).
- [39] Gotlibovych I. *Degenerate Bose Gases in a Uniform Potential*. Ph.D. thesis, University of Cambridge (2011).
- [40] Schmidutz T. *In preparation*. Ph.D. thesis, University of Cambridge (2011).
- [41] Smith RP, Campbell RL, Tammuz N, Hadzibabic Z. Effects of interactions on the critical temperature of a trapped Bose gas. *Phys Rev Lett* **106**, 250403 (2011).
- [42] Smith RP, Tammuz N, Campbell RL, Holzmann M, Hadzibabic Z. Condensed fraction of an atomic Bose gas induced by critical correlations. *Phys Rev Lett* **107**, 190403 (2011).
- [43] Gardiner C, Lee M, Ballagh R, Davis M, Zoller P. Quantum kinetic theory of condensate growth: Comparison of experiment and theory. *Phys Rev Lett* **81**, 5266 (1998).
- [44] Dalfovo F, Giorgini S, Pitaevskii LP, Stringari S. Theory of Bose-Einstein condensation in trapped gases. *Rev Mod Phys* **71**, 463–512 (1999).
- [45] Tammuz N, Smith RP, Campbell RL, Beattie S, Moulder S, et al. Can a Bose gas be saturated? *Phys Rev Lett* **106**, 230401 (2011).
- [46] Gardiner C, Zoller P, Ballagh R, Davis M. Kinetics of Bose-Einstein condensation in a trap. *Phys Rev Lett* **79**, 1793 (1997).
- [47] Bransden BH, Joachain CCJ. *Physics of atoms and molecules* (Pearson Education India, 2003).
- [48] Söding J, Guéry-Odelin D, Desbiolles P, Chevy F, Inamori H, et al. Three-body decay of a rubidium Bose–Einstein condensate. *Appl Phys B* **69**, 257–261 (1999).
- [49] Fattori M, Roati G, Deissler B, D’errico C, Zaccanti M, et al. Magnetic dipolar interaction in a Bose-Einstein condensate atomic interferometer. *Phys Rev Lett* **101**, 190405 (2008).

- [50] Taylor E, Randeria M. BCS-BEC crossover and the unitary fermi gas. *Annu Rev Cond Mat Phys* **5** (2013).
- [51] Huang K. *Statistical mechanics* (Wiley, 1987).
- [52] Braaten E, Hammer HW, Kusunoki M. Efimov states in a Bose-Einstein condensate near a Feshbach resonance. *Phys Rev Lett* **90**, 170402 (2003).
- [53] Kraemer T, Mark M, Waldburger P, Danzl J, Chin C, et al. Evidence for Efimov quantum states in an ultracold gas of caesium atoms. *Nature* **440**, 315–318 (2006).
- [54] Braaten E, Hammer HW. Efimov physics in cold atoms. *Ann Phys* **322**, 120–163 (2007).
- [55] Hammer HW, Platter L. Universal properties of the four-body system with large scattering length. *Eur Phys J A* **32**, 113–120 (2007).
- [56] Braaten E, Hammer HW, Kang D, Platter L. Three-body recombination of identical bosons with a large positive scattering length at nonzero temperature. *Phys Rev A* **78**, 043605 (2008).
- [57] Massignan P, Stoof HT. Efimov states near a Feshbach resonance. *Phys Rev A* **78**, 030701 (2008).
- [58] Ferlaino F, Knoop S, Berninger M, Harm W, D’Incao JP, et al. Evidence for universal four-body states tied to an Efimov trimer. *Phys Rev Lett* **102**, 140401 (2009).
- [59] Gross N, Shotan Z, Kokkelmans S, Khaykovich L. Observation of universality in ultracold  ${}^7\text{Li}$  three-body recombination. *Phys Rev Lett* **103**, 163202 (2009).
- [60] von Stecher J, D’Incao JP, Greene CH. Signatures of universal four-body phenomena and their relation to the Efimov effect. *Nature Phys* **5**, 417–421 (2009).
- [61] Pollack SE, Dries D, Hulet RG. Universality in three- and four-body bound states of ultracold atoms. *Science* **326**, 1683–1685 (2009).
- [62] Ferlaino F, Zenesini A, Berninger M, Huang B, Nägerl HC, et al. Efimov resonances in ultracold quantum gases. *Few-Body Syst* **51**, 113–133 (2011).
- [63] Wild R, Makotyn P, Pino J, Cornell E, Jin D. Measurements of Tan’s contact in an atomic Bose-Einstein condensate. *Phys Rev Lett* **108**, 145305 (2012).

- [64] Roy S, Landini M, Trenkwalder A, Semeghini G, Spagnolli G, et al. Test of the universality of the three-body Efimov parameter at narrow Feshbach resonances. *Phys Rev Lett* **111**, 053202 (2013).
- [65] Fedichev PO, Reynolds MW, Shlyapnikov GV. Three-body recombination of ultracold atoms to a weakly bound  $s$  level. *Phys Rev Lett* **77**, 2921–2924 (1996).
- [66] Weber T, Herbig J, Mark M, Nägerl HC, Grimm R. Three-body recombination at large scattering lengths in an ultracold atomic gas. *Phys Rev Lett* **91**, 123201 (2003).
- [67] Rem B, Grier A, Ferrier-Barbut I, Eismann U, Langen T, et al. Lifetime of the Bose gas with resonant interactions. *Phys Rev Lett* **110**, 163202 (2013).
- [68] Greene CH, Esry B, Suno H. A revised formula for 3-body recombination that cannot exceed the unitarity limit. *Nucl Phys A* **737**, 119–124 (2004).
- [69] D’Incao JP, Suno H, Esry BD. Limits on universality in ultracold three-boson recombination. *Phys Rev Lett* **93**, 123201 (2004).
- [70] Mehta N, Rittenhouse ST, D’Incao J, Von Stecher J, Greene CH. General theoretical description of  $n$ -body recombination. *Phys Rev Lett* **103**, 153201 (2009).
- [71] Braaten E, Hammer HW. Universality in few-body systems with large scattering length. *Phys Rep* **428**, 259–390 (2006).
- [72] Gross N, Shotan Z, Kokkelmans S, Khaykovich L. Nuclear-spin-independent short-range three-body physics in ultracold atoms. *Phys Rev Lett* **105**, 103203 (2010).
- [73] Jonsell S. Efimov states for systems with negative scattering lengths. *Europhys Lett* **76**, 8 (2006).
- [74] Makotyn P, Klauss CE, Goldberger DL, Cornell E, Jin DS, et al. Universal dynamics of a degenerate unitary Bose gas. *arXiv:13083696* (2013).
- [75] Claussen N, Kokkelmans S, Thompson S, Donley E, Hodby E, et al. Very-high-precision bound-state spectroscopy near a  $^{85}\text{Rb}$  Feshbach resonance. *Phys Rev A* **67**, 060701 (2003).

- [76] Brantut JP, Meineke J, Stadler D, Krinner S, Esslinger T. Conduction of ultracold fermions through a mesoscopic channel. *Science* **337**, 1069–1071 (2012).
- [77] Lee JG, McIlvain BJ, Lobb C, Hill III W. Analogs of basic electronic circuit elements in a free-space atom chip. *Sci Rep* **3** (2013).
- [78] Han R, Khoon Ng H, Englert BG. Raman transitions without adiabatic elimination: A simple and accurate treatment. *J Mod Optic* **60**, 255–265 (2013).
- [79] Bruce GD, Bromley SL, Smirne G, Torralbo-Campo L, Cassetari D. Holographic power-law traps for the efficient production of Bose-Einstein condensates. *Phys Rev A* **84**, 053410 (2011).
- [80] Gaunt AL, Schmidutz TF, Gotlibovych I, Smith RP, Hadzibabic Z. Bose-einstein condensation of atoms in a uniform potential. *Physical Review Letters* **110**, 200406 (2013).
- [81] Meyrath T, Schreck F, Hanssen J, Chuu CS, Raizen M. Bose-einstein condensate in a box. *Physical Review A* **71**, 041604 (2005).
- [82] Hinds EA, Hughes IG. Magnetic atom optics: mirrors, guides, traps, and chips for atoms. *J Phys D Appl Phys* **32**, R119 (1999).
- [83] Reichel J, Hänsel W, Hänsch TW. Atomic micromanipulation with magnetic surface traps. *Phys Rev Lett* **83**, 3398–3401 (1999).
- [84] Retter JA. *Cold Atom Microtraps above a Videotape Surface*. Ph.D. thesis, University of Sussex (2002).
- [85] Fortágh J, Zimmermann C. Magnetic microtraps for ultracold atoms. *Rev Mod Phys* **79**, 235–289 (2007).
- [86] Gabor D. A new microscopic principle. *Nature* **161**, 777–778 (1948).
- [87] Ersoy OK. *Diffraction, Fourier Optics and Imaging*. Wiley Series in Pure and Applied Optics (Wiley, 2007), 414 pp.
- [88] Kozma A, Kelly DL. Spatial filtering for detection of signals submerged in noise. *Appl Optics* **4**, 387–392 (1965).
- [89] Huang T, Burnett J, Deczky A. The importance of phase in image processing filters. *IEEE T Acoust Speech* **23**, 529–542 (1975).

- [90] Oppenheim AV, Lim JS. The importance of phase in signals. *P IEEE* **69**, 529–541 (1981).
- [91] Tadmor Y, Tolhurst D. Both the phase and the amplitude spectrum may determine the appearance of natural images. *Vision Res* **33**, 141–145 (1993).
- [92] Millane R, Hsiao W. On apparent counterexamples to phase dominance. *J Opt Soc Am A* **20**, 753–756 (2003).
- [93] Liesener J, Reicherter M, Haist T, Tiziani H. Multi-functional optical tweezers using computer-generated holograms. *Opt Commun* **185**, 77–82 (2000).
- [94] Di Leonardo R, Ianni F, Ruocco G, et al. Computer generation of optimal holograms for optical trap arrays. *Opt Express* **15**, 1913–1922 (2007).
- [95] Spalding GC, Courtial J, Di Leonardo R. Holographic optical tweezers. In: DL A, editor, *Structured Light and Its Applications* (Academic Press, 2008). pp. 139–168.
- [96] Seldowitz MA, Allebach JP, Sweeney DW. Synthesis of digital holograms by direct binary search. *Appl Optics* **26**, 2788–2798 (1987).
- [97] Boyer V, Chandrashekar C, Foot C, Laczik Z. Dynamic optical trap generation using FLC SLMs for the manipulation of cold atoms. *J Mod Optic* **51**, 2235–2240 (2004).
- [98] Boyer V, Godun RM, Smirne G, Cassetari D, Chandrashekar CM, et al. Dynamic manipulation of Bose-Einstein condensates with a spatial light modulator. *Phys Rev A* **73**, 031402 (2006).
- [99] Zhou G, Chen Y, Wang Z, Song H. Genetic local search algorithm for optimization design of diffractive optical elements. *Appl Optics* **38**, 4281–4290 (1999).
- [100] Gerchberg BRW, Saxton WO. A practical algorithm for the determination of phase from image and diffraction plane pictures. *Optik* **35**, 237–246 (1972).
- [101] Levi A, Stark H. Image restoration by the method of generalized projections with application to restoration from magnitude. *J Opt Soc Am A* **1**, 932–943 (1984).
- [102] Bauschke HH, Combettes PL, Luke DR. Phase retrieval, error reduction algorithm, and Fienup variants: a view from convex optimization. *J Opt Soc Am A* **19**, 1334–1345 (2002).

- [103] Pasienski M, DeMarco B. A high-accuracy algorithm for designing arbitrary holographic atom traps. *Opt Express* **16**, 2176–2190 (2008).
- [104] Wyrowski F. Diffractive optical elements: iterative calculation of quantized, blazed phase structures. *J Opt Soc Am A* **7**, 961 (1990).
- [105] Akahori H. Spectrum leveling by an iterative algorithm with a dummy area for synthesizing the kinoform. *Appl Optics* **25**, 802–811 (1986).
- [106] Aagedal H, Schmid M, Beth T, Teiwes S, Wyrowski F. Theory of speckles in diffractive optics and its application to beam shaping. *J Mod Optic* **43**, 1409–1421 (1996).
- [107] Raman C, Köhl M, Onofrio R, Durfee DS, Kuklewicz CE, et al. Evidence for a critical velocity in a Bose-Einstein condensed gas. *Phys Rev Lett* **83**, 2502–2505 (1999).
- [108] Perali A, Palestini F, Pieri P, Strinati GC, Stewart JT, et al. Evolution of the normal state of a strongly interacting Fermi gas from a pseudogap phase to a molecular Bose gas. *Phys Rev Lett* **106**, 060402 (2011).
- [109] Nascimbène S, Navon N, Pilati S, Chevy F, Giorgini S, et al. Fermi-liquid behavior of the normal phase of a strongly interacting gas of cold atoms. *Phys Rev Lett* **106**, 215303 (2011).
- [110] Ho TL, Zhou Q. Obtaining the phase diagram and thermodynamic quantities of bulk systems from the densities of trapped gases. *Nature Phys* **6**, 131–134 (2010).
- [111] Nascimbène S, Navon N, Jiang K, Chevy F, Salomon C. Exploring the thermodynamics of a universal Fermi gas. *Nature* **463**, 1057–1060 (2010).
- [112] Navon N, Nascimbène S, Chevy F, Salomon C. The equation of state of a low-temperature Fermi gas with tunable interactions. *Science* **328**, 729–732 (2010).
- [113] Hung CL, Zhang X, Gemelke N, Chin C. Observation of scale invariance and universality in two-dimensional Bose gases. *Nature* **470**, 236–239 (2011).
- [114] Yefsah T, Desbuquois R, Chomaz L, Günter KJ, Dalibard J. Exploring the thermodynamics of a two-dimensional Bose gas. *Phys Rev Lett* **107**, 130401 (2011).

- [115] Ku MJ, Sommer AT, Cheuk LW, Zwierlein MW. Revealing the superfluid lambda transition in the universal thermodynamics of a unitary Fermi gas. *Science* **335**, 563–567 (2012).
- [116] Drake TE, Sagi Y, Paudel R, Stewart JT, Gaebler JP, et al. Direct observation of the Fermi surface in an ultracold atomic gas. *Phys Rev A* **86**, 031601 (2012).
- [117] Sagi Y, Drake TE, Paudel R, Jin DS. Measurement of the homogeneous contact of a unitary Fermi gas. *Phys Rev Lett* **109**, 220402 (2012).
- [118] Gotlibovych I, Schmidutz TF, Moulder S, Campbell RL, Tammuz N, et al. A compact single-chamber apparatus for Bose-Einstein condensation of  $^{87}\text{Rb}$ . *arXiv:12124108* (2012).
- [119] Isenhower L, Williams W, Dally A, Saffman M. Atom trapping in an interferometrically generated bottle beam trap. *Opt Lett* **34**, 1159–1161 (2009).
- [120] Cacciapuoti L, De Angelis M, Pierattini G, Tino G. Single-beam optical bottle for cold atoms using a conical lens. *Eur Phys J D* **14**, 373–376 (2001).
- [121] Wei MD, Shiao WL, Lin YT. Adjustable generation of bottle and hollow beams using an axicon. *Opt Commun* **248**, 7–14 (2005).
- [122] Pampaloni F, Enderlein J. Gaussian, Hermite-Gaussian, and Laguerre-Gaussian beams: A primer. *arXiv:0410021* (2004).
- [123] Reinaudi G, Lahaye T, Wang Z, Guéry-Odelin D. Strong saturation absorption imaging of dense clouds of ultracold atoms. *Opt Lett* **32**, 3143–3145 (2007).
- [124] Kothari D, Srivasava B. Joule-Thomson effect and quantum statistics. *Nature* **140**, 970–971 (1937).
- [125] Goldman VV, Silvera IF. Atomic-hydrogen in an inhomogeneous magnetic-field-density profile and Bose-Einstein condensation. *Phys Rev B* **24**, 2870–2873 (1981).
- [126] Huse DA, Siggia ED. The density distribution of a weakly interacting Bose gas in an external potential. *J Low Temp Phys* **46**, 137–149 (1982).
- [127] Minguzzi A, Tosi M. Linear density response in the random-phase approximation for confined Bose vapours at finite temperature. *J Phys-Condens Mat* **9**, 10211 (1997).

- [128] Grossmann S, Holthaus M. Bose-Einstein condensation in a cavity. *Z Phys B Con Mat* **97**, 319–326 (1995).
- [129] Arnold P, Moore G. BEC transition temperature of a dilute homogeneous imperfect Bose gas. *Phys Rev Lett* **87**, 120401 (2001).
- [130] Kashurnikov V, Prokof'ev N, Svistunov B. Critical temperature shift in weakly interacting Bose gas. *Phys Rev Lett* **87**, 120402 (2001).
- [131] Timmermans E. Degenerate Fermion gas heating by hole creation. *Phys Rev Lett* **87**, 240403 (2001).
- [132] Roebuck J, Osterberg H. The Joule-Thomson effect in helium. *Phys Rev* **43**, 60 (1933).
- [133] Kozuma M, Deng L, Haglely E, Wen J, Lutwak R, et al. Coherent splitting of Bose-Einstein condensed atoms with optically induced Bragg diffraction. *Phys Rev Lett* **82**, 871 (1999).
- [134] Steinhauer J, Ozeri R, Katz N, Davidson N. Excitation spectrum of a Bose-Einstein condensate. *Phys Rev Lett* **88**, 120407 (2002).
- [135] Richard S, Gerbier F, Thywissen JH, Hugbart M, Bouyer P, et al. Momentum spectroscopy of 1d phase fluctuations in bose-einstein condensates. *Phys Rev Lett* **91**, 010405 (2003).
- [136] Ozeri R, Katz N, Steinhauer J, Davidson N. Colloquium: Bulk Bogoliubov excitations in a Bose-Einstein condensate. *Rev Mod Phys* **77**, 187–205 (2005).
- [137] Papp SB, Pino JM, Wild RJ, Ronen S, Wieman CE, et al. Bragg spectroscopy of a strongly interacting  $^{85}\text{Rb}$  Bose-Einstein condensate. *Phys Rev Lett* **101**, 135301 (2008).
- [138] Ernst PT, Götze S, Krauser JS, Pyka K, Lühmann DS, et al. Probing superfluids in optical lattices by momentum-resolved Bragg spectroscopy. *Nature Phys* **6**, 56–61 (2009).
- [139] Lingham MG, Fenech K, Hoinka S, Vale CJ. Local observation of pair condensation in a fermi gas at unitarity. *Phys Rev Lett* **112**, 100404 (2014).
- [140] Gerbier F, Thywissen JH, Richard S, Hugbart M, Bouyer P, et al. Experimental study of the thermodynamics of an interacting trapped Bose-Einstein condensed gas. *Phys Rev A* **70**, 013607 (2004).

- [141] Stenger J, Inouye S, Chikkatur AP, Stamper-Kurn D, Pritchard D, et al. Bragg spectroscopy of a Bose-Einstein condensate. *Phys Rev Lett* **82**, 4569 (1999).
- [142] Hagley E, Deng L, Kozuma M, Trippenbach M, Band Y, et al. Measurement of the coherence of a Bose-Einstein condensate. *Phys Rev Lett* **83**, 3112 (1999).
- [143] Kibble TW. Topology of cosmic domains and strings. *J Phys A-Math Gen* **9**, 1387 (1976).
- [144] Zurek WH. Cosmological experiments in superfluid helium? *Nature* **317**, 505–508 (1985).
- [145] Chuang I, Durrer R, Turok N, Yurke B. Cosmology in the laboratory: Defect dynamics in liquid crystals. *Science* **251**, 1336–1342 (1991).
- [146] Bäuerle C, Bunkov YM, Fisher S, Godfrin H, Pickett G. Laboratory simulation of cosmic string formation in the early Universe using superfluid  $^3\text{He}$ . *Nature* **382**, 332–334 (1996).
- [147] Ruutu V, Eltsov V, Gill A, Kibble T, Krusius M, et al. Vortex formation in neutron-irradiated superfluid  $^3\text{He}$  as an analogue of cosmological defect formation. *Nature* **382**, 334–336 (1996).
- [148] Carmi R, Polturak E. Search for spontaneous nucleation of magnetic flux during rapid cooling of  $\text{YBa}_2\text{Cu}_3\text{O}_{7-\delta}$  films through  $t_c$ . *Phys Rev B* **60**, 7595 (1999).
- [149] Carmi R, Polturak E, Koren G. Observation of spontaneous flux generation in a multi-Josephson-junction loop. *Phys Rev Lett* **84**, 4966 (2000).
- [150] Monaco R, Mygind J, Rivers R. Zurek-Kibble domain structures: the dynamics of spontaneous vortex formation in annular Josephson tunnel junctions. *Phys Rev Lett* **89**, 080603 (2002).
- [151] Sadler LE, Higbie JM, Leslie SR, Vengalattore M, Stamper-Kurn DM. Spontaneous symmetry breaking in a quenched ferromagnetic spinor Bose-Einstein condensate. *Nature* **443**, 312–315 (2006).
- [152] Weiler CN, Neely TW, Scherer DR, Bradley AS, Davis MJ, et al. Spontaneous vortices in the formation of Bose-Einstein condensates. *Nature* **455**, 948–951 (2008).

- [153] Chen D, White M, Borries C, DeMarco B. Quantum quench of an atomic Mott insulator. *Phys Rev Lett* **106**, 235304 (2011).
- [154] Lamporesi G, Donadello S, Serafini S, Dalfovo F, Ferrari G. Spontaneous creation of Kibble-Zurek solitons in a Bose-Einstein condensate. *Nature Phys* **9**, 656-660 (2013).
- [155] Braun S, Friesdorf M, Hodgman S, Schreiber M, Ronzheimer J, et al. Emergence of coherence and the dynamics of quantum phase transitions. *arXiv:14037199* (2014).
- [156] Corman L, Chomaz L, Bienaimé T, Desbuquois R, Weitenberg C, et al. Quench-induced supercurrents in an annular two-dimensional Bose gas. *arXiv:14064073* (2014).
- [157] Chae S, Lee N, Horibe Y, Tanimura M, Mori S, et al. Direct observation of the proliferation of ferroelectric loop domains and vortex-antivortex pairs. *Phys Rev Lett* **108**, 167603 (2012).
- [158] Ulm S, Roßnagel J, Jacob G, Degünther C, Dawkins S, et al. Observation of the Kibble-Zurek scaling law for defect formation in ion crystals. *Nat Commun* **4**, 2290 (2013).
- [159] Pyka K, Keller J, Partner H, Nigmatullin R, Burgermeister T, et al. Topological defect formation and spontaneous symmetry breaking in ion Coulomb crystals. *Nat Commun* **4**, 2291 (2013).
- [160] Ejtemaee S, Haljan P. Spontaneous nucleation and dynamics of kink defects in zigzag arrays of trapped ions. *Phys Rev A* **87**, 051401 (2013).
- [161] Kardar M. *Statistical physics of fields* (Cambridge University Press, 2007).
- [162] Altland A, Simons BD. *Condensed matter field theory* (Cambridge University Press, 2010).
- [163] Hohenberg PC, Halperin BI. Theory of dynamic critical phenomena. *Rev Mod Phys* **49**, 435–479 (1977).
- [164] Anglin JR, Zurek WH. Vortices in the wake of rapid Bose–Einstein condensation". *Phys Rev Lett* **83**, 1707 (1999).
- [165] del Campo A, Zurek WH. Universality of phase transition dynamics: Topological defects from symmetry breaking. *Int J Mod Phys A* **29** (2014).

- [166] Täuber UC. *Critical dynamics: a field theory approach to equilibrium and non-equilibrium scaling behavior* (Cambridge University Press, 2014).
- [167] Cucchieri A, Engels J, Holtmann S, Mendes T, Schulze T. Universal amplitude ratios from numerical studies of the three-dimensional  $o(2)$  model. *Journal of Physics A: Mathematical and General* **35**, 6517 (2002).
- [168] Dettmer S, Hellweg D, Ryyty P, Arlt JJ, Ertmer W, et al. Observation of phase fluctuations in elongated Bose–Einstein condensates. *Phys Rev Lett* **87**, 160406 (2001).
- [169] Biroli G, Cugliandolo LF, Sicilia A. Kibble–Zurek mechanism and infinitely slow annealing through critical points. *Phys Rev E* **81**, 050101 (2010).
- [170] Pogorelov A, Suslov I. On the critical exponents for the  $\lambda$  transition in liquid helium. *JETP Letters* **86**, 39–45 (2007).
- [171] Donner T, Ritter S, Bourdel T, Ottl A, Köhl M, et al. Critical behavior of a trapped interacting Bose gas. *Science* **315**, 1556–1558 (2007).
- [172] Folk R, Moser G. Critical dynamics: a field-theoretical approach. *J Phys A* **39**, R207 (2006).
- [173] Zobay O, Metikas G, Kleinert H. Nonperturbative effects on  $T_c$  of interacting bose gases in power-law traps. *Phys Rev A* **71**, 043614 (2005).
- [174] Jo GB, Shin Y, Will S, Pasquini T, Saba M, et al. Long phase coherence time and number squeezing of two bose-einstein condensates on an atom chip. *Phys Rev Lett* **98**, 030407 (2007).
- [175] Grond J, Hohenester U, Mazets I, Schmiedmayer J. Atom interferometry with trapped bose–einstein condensates: impact of atom–atom interactions. *New J Phys* **12**, 065036 (2010).
- [176] Stadler D, Krinner S, Meineke J, Brantut JP, Esslinger T. Observing the drop of resistance in the flow of a superfluid fermi gas. *Nature* **491**, 736–739 (2012).
- [177] Brantut JP, Grenier C, Meineke J, Stadler D, Krinner S, et al. A thermoelectric heat engine with ultracold atoms. *arXiv:13065754* (2013).
- [178] Krinner S, Stadler D, Meineke J, Brantut JP, Esslinger T. Superfluidity with disorder in a thin film of quantum gas. *Phys Rev Lett* **110**, 100601 (2013).

- [179] Karpiuk T, Gremaud B, Miniatura C, Gajda M. Superfluid fountain effect in a Bose-Einstein condensate. *Phys Rev A* **86**, 033619 (2012).
- [180] Papoular D, Ferrari G, Pitaevskii L, Stringari S. Increasing quantum degeneracy by heating a superfluid. *Phys Rev Lett* **109**, 084501 (2012).
- [181] Marques G, Bagnato V, Muniz S, Spehler D. Mechanocaloric and thermomechanical effects in Bose-Einstein-condensed systems. *Phys Rev A* **69**, 053808 (2004).
- [182] Allen J, Jones H. New phenomena connected with heat flow in helium II. *Nature* **141**, 243-244 (1938).
- [183] Steck DA. Rubidium 87 D line data (2001) <http://george.ph.utexas.edu/~dsteck/alkalidata/rubidium87numbers.pdf>.
- [184] Fienup JR. Phase retrieval algorithms: a comparison. *Appl Opt* **21**, 2758–2769 (1982).
- [185] Wyrowski F, Bryngdahl O. Iterative Fourier-transform algorithm applied to computer holography. *J Opt Soc Am A* **5**, 1058–1065 (1988).
- [186] Senthilkumaran P, Wyrowski F, Schimmel H. Vortex stagnation problem in iterative Fourier transform algorithms. *Opt Laser Eng* **43**, 43–56 (2004).
- [187] Scherer DR, Weiler CN, Neely TW, Anderson BP. Vortex formation by merging of multiple trapped Bose-Einstein condensates. *Phys Rev Lett* **98**, 110402 (2007).
- [188] Bowman RW, Wright AJ, Padgett MJ. An SLM-based Shack-Hartmann wavefront sensor for aberration correction in optical tweezers. *J Opt* **12**, 124004 (2010).
- [189] Wright K, Blakestad R, Lobb C, Phillips W, Campbell G. Driving phase slips in a superfluid atom circuit with a rotating weak link. *Phys Rev Lett* **110**, 025302 (2013).
- [190] Feit M, Fleck Jr J, Steiger A. Solution of the schrödinger equation by a spectral method. *J Comput Phys* **47**, 412–433 (1982).
- [191] Gaunt AL. Laser spoon through a condensate (2013) [https://www.youtube.com/watch?v=37IZq\\_uUBI8](https://www.youtube.com/watch?v=37IZq_uUBI8).

[192] Gaunt AL. Double well tunnelling (2013) <https://www.youtube.com/watch?v=9EKguw1bqhk> .

